Antenna Diagnostics for Spherical Near-Field Antenna Measurements

Cappellin, Cecilia

Publication date:
2008

Document Version
Publisher's PDF, also known as Version of record

ANTENNA DIAGNOSTICS FOR SPHERICAL NEAR-FIELD ANTENNA MEASUREMENTS

Ph.D. Thesis

Cecilia Cappellin

September 2007

Supervisors:

Olav Breinbjerg, Professor, Ph.D.
Ørsted · DTU, Technical University of Denmark

Aksel Frandsen, Ph.D.
TICRA

Version revised in June 2008, where printing errors have been corrected and the list of publications updated.

Abstract

Antenna Diagnostics for Spherical Near-Field Antenna Measurements

A new antenna diagnostics technique for spherical near-field antenna measurements is presented. The technique is based on the transformation of the Spherical Wave Expansion (SWE) to the Plane Wave Expansion (PWE), and allows an accurate computation of the extreme near-field of the antenna under test.
The relation between the SWE and the PWE is first investigated. It is shown that the plane wave spectrum (PWS) can be computed from the coefficients of the SWE through a rigorous transformation, in the visible as well as in the invisible region of the spectral domain.
The antenna diagnostics technique is then developed on the basis of the SWE-to-PWE transformation and the necessary additional steps to obtain the extreme near-field from a spherical near-field measurement are taken into account. The fundamental properties of the transformation are discussed, with emphasis on their theoretical as well as practical implications. In particular, the convergence mechanism of the series expressing the PWS is studied. It is shown that the infinite series can be truncated at a finite value N, which depends on the size of the antenna, the origin of the measurement coordinate system and the part of spectral domain where the PWS is computed. When convergence of the series is reached in part of the invisible region, a resolution higher than the traditional value of half a wavelength can be obtained in the extreme near-field.
The computation of the extreme near-field from the plane wave spectrum is described. It is recalled that the PWS generally possesses a singularity at the border between the visible and invisible regions. Though the singularity is integrable, a straightforward application of the Fast Fourier Transform does not normally provide accurate results. A singularity extraction technique for computation of antenna extreme near-fields from singular plane wave spectra is thus developed and presented. Next, the effects of finite measurement accuracy on the proposed antenna diagnostics technique are studied through numerical simulations. It is concluded that, in practice, electrical inaccuracies, and in particular amplitude noise, limit the spectral region where the PWS reaches convergence. Under typical measurement conditions the recovery of the PWS is generally obtained in the visible region and at the border where the singularity exists. For electrically small antennas a part of the invisible region of the PWS can be reconstructed, but for electrically large antennas the entire invisible region must normally be disregarded.
The SWE-to-PWE antenna diagnostics technique is finally verified by two experimental test cases employing real measurements data. Measurements are conducted at the DTU-ESA Spherical Near-Field Antenna Test Facility located at the Technical University of Denmark (DTU). First, a commercially available offset reflector antenna is considered. Three mechanical errors are intentionally introduced and the ability and accuracy of the diagnostics technique to identify them are tested. Second, the antenna system of the satellite-based Soil Moisture and Ocean Salinity (SMOS) radiometer is investigated, in particular the diagnostics technique is used to successfully identify the sources of the anomalies detected in 2 of the 138 measured antenna far-field patterns.

Resumé

Antenne-Diagnose for Sfæriske Nærfelts-Målinger af Antenner

En ny antenne-diagnoseteknik for sfæriske nærfelts-målinger af antenner præsenteres. Teknikken er baseret på transformationen af den sfæriske vektorbølge-udvikling til den plane vektorbølge-udvikling, og den tillader en nøjagtig beregning af det ekstreme nærfelt af testantennen.
Først undersøges relationen mellem den sfæriske vektorbølge-udvikling og den plane vektorbølge-udvikling. Det vises, at planbølge-spektret kan beregnes udfra koefficienterne til den sfæriske udvikling gennem en eksakt transformation, både i det synlige og usynlige område af det spektrale domæne.
Derefter udvikles antenne-diagnoseteknikken på basis af transformationen fra den sfæris-ke til den plane udvikling, og de nødvendige trin for at beregne det ekstreme nærfelt fra en sfærisk nærfelts-måling undersøges. Grundlæggende egenskaber ved transformationen undersøges med vægt på deres teoretiske såvel som praktiske konsekvenser. Konvergens-forholdene ved udviklingen som beskriver planbølge-spektret, bliver især undersøgt. Det vises, at den uendelige række kan afsluttes for en bestemt værdi N, som afhænger af antenne størrelsen, origo for måle-koordinatsystemet og den del af det spektrale domæne, hvor spektret ønskes beregnet. En opløsning højere end den traditionelle halve bølgelængde kan opnås i det ekstreme nærfelt, hvis konvergensen af rækken bliver nået i en del af det usynlige område.
Beregningen af det ekstreme nærfelt fra planbølge-udviklingen bliver dernæst beskrevet. Planbølge-spektret har normalt en singularitet på grænsen mellem det synlige og usynlige område. Selvom singulariteten kan integreres, giver almindelig brug af Fast Fourier Transform ikke nøjagtige resultater. En singularitet-ekstraktions-teknik for beregningen af antennens ekstreme nærfelt fra singulære planebølge-spektra udvikles og diskuteres. Til sidst undersøges effekten af målenøjagtigheden på antenne-diagnoseteknikken gennem numeriske beregninger. Det konkluderes, at elektriske unøjagtigheder, især amplitudestøj, i praksis begrænser det spektrale område, hvor planbølge-spektret opnår konvergens. Under typiske målinger bliver planbølge-spektret generelt rekonstrueret i det synlige område og på grænsen, hvor singulariteten findes. En del af det usynlige område af planbølge-spektret bliver normalt rekonstrueret for elektrisk små antenner, men hele det usynlige område må ignoreres for elektrisk store antenner.
Antenne-diagnoseteknikken baseret på transformationen fra den sfæriske vektorbølge-udvikling til den plane vektorbølge-udvikling bliver afslutningsvis verificeret med to eksperimentelle test, hvor rigtige måledata bliver anvendt. Målingerne er udført i DTU-ESA Spherical Near-Field Antenna Test Facility på Danmarks Tekniske Universitet (DTU). Først undersøges en kommerciel offsetreflektorantenne. Tre mekaniske fejl er forsætligt introduceret og anvendeligheden og nøjagtigheden af antenne-diagnoseteknik-ken til at identificere disse afprøves. Derefter bliver antennesystemet i radiometret for den satellitbaserede Soil Moisture and Ocean Salinity (SMOS) mission undersøgt. Specielt bliver diagnoseteknikken brugt til succesfuldt at identificere kilderne til uregelmæssigheder, der blev påvist i 2 af de 138 målte antenne-diagrammer.

Preface

The work presented in this thesis was carried out at TICRA and at the department of ElectroScience at the Technical University of Denmark (DTU), between October 2004 and September 2007. The study was financed by TICRA with the support of the Danish Industrial Ph.D. Programme.
There are several people who encouraged me and assisted me in these three years, and I would like to thank them all. First and foremost my two supervisors from DTU and TICRA, Olav Breinbjerg and Aksel Frandsen. Without them this work would not have been possible. Their inspiring and always constructive attitude, continuous support and patience have been an invaluable source of motivation. Their extensive knowledge and a perfect balance between theory and practice made my Ph.D. a challenging experience that definitely was worth the efforts. Thank you for sharing with me the passion for your work, the humility and the habit of always aiming at improving.
I would like to thank all of TICRA for showing trust by accepting me as industrial Ph.D. student and by allocating its resources to me. The way a relaxed and simple working environment can be successfully combined with advanced and high level work is something I really admire. A special thanks goes to Michael Lumholt who became the official proofreader of this thesis and gave me useful and generous suggestions.
I would then like to extend my deep gratitude to all the people that closely helped me in settling down in Denmark and enjoyed moments with me that I will never forget. Emiliano, Enrica for all personal and scientific advice that often cheered me up, Ania for being there during all these years, Sara, John and Sid for the countless chats and laughs in the corridor, the lunches in the kitchen, the cineforum and the joy of spending time together, and Samel for the long talks about life.
And thanks to all my friends that, though scattered around the world, are always very close...the list would be long, but I shall try anyway...Elisa, Paolo, Alessia, Paola, Giulia, Valerio, Caterina, Sara, Stefano, Mauro...
And last, but not least, my family. I thank my parents for their precious and invaluable support, for always believing in me and in my dreams and for their wonderful ability to shorten geographic distances...and my sister Giulia, a source of continuous inspiration, lovely discussions and affection.

List of publications

Journal publications

[J1] C. Cappellin, O. Breinbjerg, A. Frandsen, "Properties of the transformation from the spherical wave expansion to the plane wave expansion", Radio Science, 43, RS1012, doi:10.1029/2007RS003696, February 2008.

[J2] C. Cappellin, O. Breinbjerg, A. Frandsen, "A singularity extraction technique for computation of antenna aperture fields from singular plane wave spectra", Microwave and Optical Technology Letters, Vol. 50, No. 5, pages 1308-1312, May 2008.

Conference publications

[C1] C. Cappellin, J. M. Nielsen, O. Breinbjerg, "A high-resolution antenna diagnostics technique for spherical near-field antenna measurements", *JINA 2004, International Symposium on Antennas*, Nice, France, November 2004.

[C2] C. Cappellin, O. Breinbjerg, A. Frandsen, "A high-resolution antenna diagnostics technique for spherical near-field measurements", *28th ESA Antenna Workshop on Space Antenna Systems and Technologies*, ESTEC, Noordwijk, The Netherlands, May 2005.

[C3] C. Cappellin, A. Frandsen, O. Breinbjerg, "On the relationship between the spherical wave expansion and the plane wave expansion for antenna diagnostics", *Antenna Measurements Technique Association, AMTA Europe Symposium*, Munich, Germany, May 2006.

[C4] C. Cappellin, O. Breinbjerg, A. Frandsen, "The influence of finite measurement accuracy on the SWE-to-PWE antenna diagnostics technique", *European Conference on Antennas and Propagation, EuCAP*, Nice, France, November 2006.

[C5] C. Cappellin, A. Frandsen, O. Breinbjerg,"Application of the SWE-to-PWE antenna diagnostics technique to an offset reflector antenna", *Antenna Measurements Technique Association Symposium, AMTA*, St. Louis, USA, November 2007.

[C6] C. Cappellin, A. Frandsen, S. Pivnenko, G. Lemanczyk, O. Breinbjerg, "Diagnostics of the SMOS radiometer antenna system at the DTU-ESA spherical near-field antenna test facility", *European Conference on Antennas and Propagation, EuCAP*, Edinburgh, UK, November 2007.

Contents

Chapter 1

Introduction

Accurate and advanced antenna measurements techniques have in recent years attracted the interest of the antenna community due to considerable improvements in computational methods and antenna design, in particular within space applications. It may happen, however, that the measured radiation pattern differs from the designed one, for the presence of some anomalies, the causes of which can often not be explained immediately. The need to perform an accurate diagnostics of the antenna under test has thus grown in parallel. While the presence of electrical or mechanical errors in an antenna is detected in the measured far-field, their identification is normally possible only through an inspection of the extreme near-field, or equivalently called aperture field, of the antenna. Examples of such errors, which can originate from the manufacturing as well as the operation of the antenna, are excitation of higher-order modes in a waveguide antenna, malfunction of microwave components in the feed network of an array and surface distortions in a reflector antenna. A plot of the near-field amplitude on a plane in front of the antenna can help identifying higher-order waveguide modes, while a plot of the near-field phase can reveal feed network malfunctions and reflector surface deviations.

The most widely used antenna diagnostics technique is based on the well-established relation that allows the computation of the visible region of the plane wave spectrum (PWS) from the antenna far-field pattern, see Booker and Clemmow [1]. Through the inverse Fourier transform of the plane wave spectrum, the antenna extreme near-field is obtained. The technique is called backward transformation method (BTM), see Bucci et al. [2], is applicable to general antennas, it provides satisfactory results and is simple and computationally very efficient due to the use of the inverse Fast Fourier Transform. When applied to diagnostics of planar arrays, the BTM provides not only the extreme near-field but, with few additional steps, also the array excitations, see Lee et al. [3] and Langsford et al. [4]. However, in this case the accuracy is limited since the mutual coupling between the antenna elements is neglected and the a priori knowledge of the element factor is assumed. An alternative technique to reconstruct the elements' excitation has

been recently proposed by Bucci et al. [2] for non planar arrays, by solving the linear system that relates the excitation coefficients to the field at the measurement points.
The inverse Fourier transform also expresses the relation between the far-field and the current distribution on the surface of large reflectors, under some mathematical and geometrical assumptions. From the phase of the inverse Fourier transform of the far-field, the deviation of the reflector surface from its ideal geometry can be obtained if the reflector antenna is a paraboloid of known focus, and if the surface distortion is small with respect to the wavelength, as done by Rochblatt [5][6] and by Rahmat-Samii [7][8].
Generally, the far-field pattern is measured in amplitude and phase directly in the far-field region or is obtained from a near-field measurement. Alternatively, several numerical techniques are available to retrieve the phase of the far-field pattern from measurements of only amplitude. A good review is given by Taylor in [9], while specific algorithms are described by Yaccarino and Rahmat-Samii in [10] and by Smith et al. in [11]. Once the far-field pattern is known in amplitude and phase, all authors employ a traditional BTM to compute the antenna extreme near-field for diagnostics purposes. If measurements are done at a compact range or spherical near-field range, the complex far-field pattern is known in the entire half sphere. This provides information of the plane wave spectrum in the entire visible region and thus a spatial resolution of theoretically half a wavelength in the reconstructed near-field. Interpolation from the spherical to the rectangular coordinates system is however needed in order to use the inverse Fast Fourier Transform. If planar near-field measurements are used, Hanfling et al. [12], interpolation is not necessary but the spatial resolution is smaller, since the obtained far-field is reliable only within the angular region determined by the finite dimensions of the scan plane and the antenna aperture, see Yaghjian [13].
Particular interest has been shown in the past thirty years in methods to extend the reliable region of far-field patterns obtained from truncated measurements, in order to increase the spatial resolution of the aperture field computed with the BTM. The most successful is based on the iterative technique discussed by Gerchberg [14] and Papoulis [15] for a bandlimited scalar signal. The technique was extended to the electromagnetic vectorial case by Rahmat-Samii [7] and tested with simulated far-field patterns. The same iterative algorithm was used for array synthesis by Narasimhan and Kumar [16] with simulated data, and for array diagnostics by Johansson and Svensson [17] with real measurements data, to compute the array excitations with the assumption of knowing the element factor and neglecting the mutual coupling between the elements. It has been shown that, while the iterative technique converges very fast and to the correct solution when working with simulated data, the algorithm becomes less robust in presence of noise. A promising technique that deals with noisy data has been recently proposed by Martini et al. [18] by combining the iterative algorithm with the a priori knowledge of the antenna geometry and by working at the same time on the electric and magnetic fields. The idea of using the iterative technique of Gerchberg and Papoulis to recover, from the visible region of the plane wave spectrum, part of the invisible region has been taken into consideration by Sanchez-Escuderos et al. [19]

using simulated data and very simple antenna configurations. Results are however preliminary and following investigations are necessary.
A resolution higher than half a wavelength requires a measurement of propagating as well as evanescent plane waves in order to recover part of the invisible region of the plane wave spectrum. Since evanescent waves decrease exponentially with increasing distance from the antenna, an accurate measurement can only be realized at a distance less than approximately one wavelength from the source, see Wang [20]. At this distance, multiple reflections between the antenna and the probe strongly limit the measurement accuracy. Even in the case of measuring some of the evanescent waves, the back-propagation process of the BTM is anyway delicate since measurement errors increase exponentially and corrupt the invisible region of the plane wave spectrum and the useful information which can be deduced from it, Hanfling et al. [12] and Joy and Guler [21].
The only case of resolution higher than half a wavelength with real measurements data was reported by Joy et al. [22] using an antenna diagnostics technique called spherical microwave holography (SMH) developed and extensively studied at the Georgia Institute of Technology. The technique uses spherical near-field measurements and is based on the spherical wave expansion (SWE) of the radiated field. From the SWE of the field on the measurement sphere, the field is evaluated on a smaller and concentric spherical surface closer to the antenna. The method was applied to detect anomalies in radomes of spherical shape, like wall thickness variations and dielectric constant changes. The relation between the spatial resolution on the evaluation sphere, normally coinciding with the radome surface, and the number of spherical modes contained in the SWE was also studied. In order to do that, a constant phase or amplitude perturbation, modeled as a two-dimensional rectangular function, of a known field was considered over a disk-shaped region of the evaluation sphere. Resolution was defined as the diameter of the perturbation region, measured along the circumference of the evaluation sphere, for which a maximum mode N in the SWE produces a perturbation with height exactly half of the actual perturbation. With r_e being the radius of the evaluation sphere and ϵ the resolution, the authors found that $N = 3.04 r_e/\epsilon$. A resolution of 0.33λ was obtained by increasing the dynamic range of the measurement system with a specially designed small aperture probe, and by using a separation distance between the radome surface and the measurement surface of 0.7λ. The technique provides satisfactory results for spherical radomes but it is strongly limited by the smallest sphere centered at the origin of the measurement coordinate system and enclosing the entire antenna, the so called minimum sphere, since the SWE is valid only outside that sphere.
Finally, it is worth mentioning a last diagnostics approach, which on the basis of the electromagnetic field on a certain measurement surface computes the equivalent currents on the surface of the antenna or radome under test. The technique is based on a Method of Moments algorithm and is less immediate than the mentioned BTM or SMH. It has been applied by Sarkar, Las-Heras and Taaghol to spherical near-field measurements [23] [24], and by Persson et al. to cylindrical near-field measurements for the scalar case [25].
In summary, it is seen that all the proposed techniques are well suited to certain

types of antennas and errors but less for others. Furthermore, some are limited in the accuracy that they can provide either because of the algorithm or the antenna measurement techniques on which they are based.

The purpose of the present work is to develop a new antenna diagnostics technique that applies to general types of antennas, that is intrinsically accurate, and that takes advantage of the high accuracy that can be provided by the spherical near-field antenna measurement technique, see Hansen [26]. The technique will be implemented at the DTU-ESA Spherical Near-Field Antenna Test Facility [27], to provide an extra capability in addition to the antenna measurement itself. Furthermore, its implementation into a commercial TICRA software can also be considered.
The central idea behind the new antenna diagnostics technique is the transformation between two different representations of the field radiated by an antenna. The first of these is the SWE, expressing the electric field as a sum of spherical waves weighted by coefficients, the second is the plane wave expansion (PWE), expressing the field as a spectrum of plane waves. A spherical near-field measurement provides the coefficients of the SWE and these are then normally used to calculate the antenna far-field pattern. They cannot be used directly to calculate the extreme near-field of the antenna since the SWE is valid only outside the antenna minimum sphere. On the other hand, the PWE is valid at an arbitrarily close distance in front of the antenna, thus also in the extreme near-field region of interest for antenna diagnostics. While it is well-known that the visible region of the plane wave spectrum can be obtained from the far-field [1], Devaney and Wolf [28] showed that a rigorous transformation from the SWE to the PWE allows the determination of the plane wave spectrum in both the visible and invisible regions from the coefficients of the SWE. This provides, once the PWS is inverse Fourier transformed, a spatial resolution in the calculated extreme near-field higher than the traditional half a wavelength and thus a more accurate identification of the errors affecting the antenna.
While the results presented in [28] were of extraordinary mathematical value, their use in practical applications was never investigated. For this purpose, the transformation from the SWE to the PWE must first be clarified in order to use the S.I. rationalized system of units and the spherical vector wave functions of [26]. Next, its fundamental properties and the influence of implementation aspects on the accuracy of the computed extreme near-field should be examined. These are aspects such as truncation to a finite number of spherical modes, use of the inverse discrete Fourier transform to calculate the extreme near-field, and obtainable spatial resolution. This will lead to guidelines and specifications for the parameters to be employed in the operational implementation of the new technique. Further, the effect of non-ideal measurements aspects, such as measurement noise and receiver drift for example, on the accuracy of the antenna diagnostics technique must be studied. Finally, the developed technique should be experimentally verified. A series of measurements at the DTU-ESA Facility should be conducted with different antennas where errors have intentionally been introduced, and the ability of the diagnostics technique to identify them must be tested.

The present thesis documents the development of the new antenna diagnostics technique. The thesis is based on six included papers, [J1] [J2] and [C3]-[C6], in this order and according to the list of publications on page iv, which constitute the main outcome of the Ph.D. study. While the general overview summarizes the main results presented in the papers, it also contains concepts and discussions which are assumed, but not covered, in the manuscripts. Specifically, Chapter 2 provides the necessary theoretical background for the following chapters and the mathematical foundation for the diagnostics technique. The theory of the spherical wave expansion and plane wave expansion is reviewed with attention on definitions, domains of validity, properties, and use in antenna measurements. Later, the transformation from the SWE to the PWE is described. Chapter 3 deals with the necessary additional steps to obtain the antenna aperture field from a spherical near-field measurement. First, the fundamental properties of the SWE-to-PWE transformation are studied, emphasizing their theoretical as well as practical implications. The computation of the extreme near-field from the plane wave spectrum is then considered, taking into account the numerical difficulties that arise in case of a singular spectrum. A technique to extract the singularity and obtain accurate field results is developed and proposed. Further, the concept of resolution is discussed by studying the factors that determine what the human eye can observe and distinguish in a near-field plot. The chapter ends with an investigation on the effects of finite measurement accuracy on the SWE-to-PWE diagnostics technique. Chapter 4 presents the experimental verification of the technique, summarizing the results of two test cases using real measurements data. A commercially available offset reflector antenna is the subject of the first part of the chapter, while the antenna system of the satellite-based Soil Moisture and Ocean Salinity (SMOS) radiometer is investigated in the second part. Finally, conclusions are drawn in Chapter 5 where also recommendations and suggestions for further work are given.

Throughout the present report the S.I. rationalized system and the suppressed $e^{-i\omega t}$ time dependence are used.

Chapter 2

SWE-to-PWE transformation

The Spherical Wave Expansion (SWE) and the Plane Wave Expansion (PWE) are two well-known techniques to express time-harmonic electromagnetic fields in source-free regions of space. The choice of employing the SWE or the PWE is determined by the geometry of the source configuration, the spatial region of interest, and the available information about the radiated fields. While the mathematical formulations of the PWE and SWE are very different, as are their respective regions of validity, it is possible to derive one expansion from the other through a rigorous transformation. The SWE-to-PWE transformation constitutes the theoretical basis for the proposed antenna diagnostics technique.
After a general review of the SWE and PWE in Sections 2.1-2.2, the transformation from one expansion to the other is described in Section 2.3. A linear, isotropic and homogeneous medium is always assumed in all sections and chapters. Though the derivation presented in Section 2.3 is based on the results of Devaney and Wolf [28], it has been extended in order to use the power-normalized spherical vector wave functions, the $k_x k_y$-PWE, and the S.I. rationalized system of units.

2.1 Spherical wave expansion

The SWE expresses the electromagnetic field in a source-free region of space as an infinite series of discrete spherical waves weighted by coefficients. The original form of the SWE was introduced by W. W. Hansen [29], while the theory was popularized a few years later by Stratton [30]. A more recent treatment was given by J. E. Hansen [26] in relation to spherical near-field antenna measurements; his notation is used in this section and throughout this work, as it is also employed at the DTU-ESA Facility.
The expression of the SWE can be derived by solving in spherical coordinates, see Fig. 2.1, the vector wave equation for the electric field $\vec{E}$ in a source-free region of space [30]

$$\nabla^2 \vec{E} + k^2 \vec{E} = 0 \tag{2.1}$$

where k is the wave number given by $k = \omega\sqrt{\epsilon\mu}$, with ϵ and μ being respectively the permittivity and permeability of the medium.

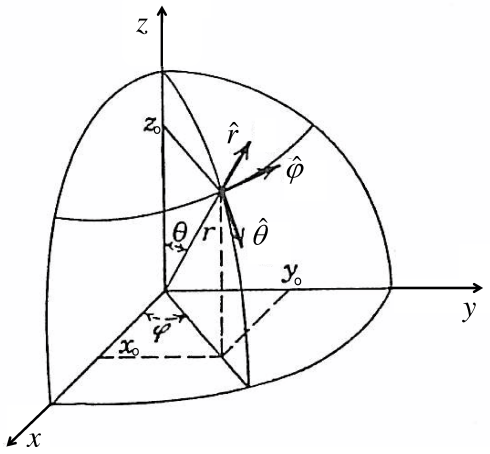

Figure 2.1: Rectangular and spherical coordinate systems.

In order to solve (2.1), the solution in spherical coordinates of the corresponding scalar equation

$$(\nabla^2 + k^2)f = 0 \tag{2.2}$$

is used. It can be shown in fact [30], that the solution of (2.2), called generating function, allows one to define two functions, $\vec{F}_1$ and $\vec{F}_2$, which satisfy (2.1) and form an orthogonal and complete basis on which the electromagnetic field in any spherical source-free region of space can be decomposed. They are given by

$$\vec{F}_1 = \nabla f \times \vec{r} \tag{2.3}$$

$$\vec{F}_2 = k^{-1}\nabla \times \vec{F}_1 \tag{2.4}$$

and are known in literature as spherical vector wave functions.
To obtain the expression of the generating function, we write f as product of independent terms,

$$f(r,\theta,\phi) = f_1(r)f_2(\theta)f_3(\phi), \tag{2.5}$$

and solve (2.2) by separation of variables, obtaining

$$f_{mn}^{(c)}(r,\theta,\phi) = \frac{1}{\sqrt{2\pi}}\frac{1}{\sqrt{n(n+1)}}\Big(-\frac{m}{|m|}\Big)^m z_n^{(c)}(kr)\bar{P}_n^{|m|}(\cos\theta)e^{im\phi} \tag{2.6}$$

according to [26], with $n = 1,2,3,...$, $m = -n,-n+1,...,0,1,2,...n$ and with $\bar{P}_n^{|m|}(\cos\theta)$ being the normalized associated Legendre function related to the Legendre function $P_n^{|m|}(\cos\theta)$ through

$$\bar{P}_n^{|m|}(\cos\theta) = \sqrt{\frac{2n+1}{2}\frac{(n-|m|)!}{(n+|m|)!}}P_n^{|m|}(\cos\theta). \tag{2.7}$$

The upper index c specifies the radial function $z_n^{(c)}(kr)$ as one among

$z_n^{(1)}(kr) = j_n(kr)$ spherical Bessel function of first kind,

$z_n^{(2)}(kr) = n_n(kr)$ spherical Neumann function of first kind,

$z_n^{(3)}(kr) = h_n^{(1)}(kr)$ spherical Hankel function of the first kind,

$z_n^{(4)}(kr) = h_n^{(2)}(kr)$ spherical Hankel function of the second kind,

with $h_n^{(1)}(kr) = j_n(kr) + in_n(kr)$ and $h_n^{(2)}(kr) = j_n(kr) - in_n(kr)$. The index c indicates standing waves which are finite at the origin of the coordinate system for $c = 1$, standing waves which are infinite at the origin of the coordinate system for $c = 2$, outward traveling waves for $c = 3$ and inward traveling waves for $c = 4$. From (2.3), (2.4) and (2.6), the spherical vector wave functions defined by [26] and used throughout this work become

$$\begin{aligned}\vec{F}_{1mn}^{(c)}(r,\theta,\phi) &= \nabla f_{mn}^{(c)}(r,\theta,\phi) \times \vec{r} \; = \\ &= \frac{1}{\sqrt{2\pi}} \frac{1}{\sqrt{n(n+1)}} \Big(- \frac{m}{|m|} \Big)^m \Big[z_n^{(c)}(kr) \frac{im\bar{P}_n^{|m|}(\cos\theta)}{\sin\theta} e^{im\phi}\hat{\theta} \\ &- z_n^{(c)}(kr) \frac{d\bar{P}_n^{|m|}(\cos\theta)}{d\theta} e^{im\phi}\hat{\phi} \Big]\end{aligned} \tag{2.8}$$

and

$$\begin{aligned}\vec{F}_{2mn}^{(c)}(r,\theta,\phi) &= k^{-1}\nabla \times \vec{F}_{1mn}^{(c)}(r,\theta,\phi) = \\ &= \frac{1}{\sqrt{2\pi}} \frac{1}{\sqrt{n(n+1)}} \Big(- \frac{m}{|m|} \Big)^m \Big[\frac{n(n+1)}{kr} z_n^{(c)}(kr) \bar{P}_n^{|m|}(\cos\theta) e^{im\phi}\hat{r} + \\ &\frac{1}{kr} \frac{d}{d(kr)} \Big(kr z_n^{(c)}(kr) \Big) \frac{d\bar{P}_n^{|m|}(\cos\theta)}{d\theta} e^{im\phi}\hat{\theta} + \\ &\frac{1}{kr} \frac{d}{d(kr)} \Big(kr z_n^{(c)}(kr) \Big) \frac{im\bar{P}_n^{|m|}(\cos\theta)}{\sin\theta} e^{im\phi}\hat{\phi} \Big].\end{aligned} \tag{2.9}$$

The final SWE valid by proper choice of the index c in any source-free region of space limited by spherical surfaces and centered at the origin of the coordinate system, see Fig. 2.2, is thus given by

$$\vec{E}(\vec{r}\,) = \frac{k}{\sqrt{\eta}} \sum_{cmn} Q_{1mn}^{(c)} \vec{F}_{1mn}^{(c)}(\vec{r}\,) + Q_{2mn}^{(c)} \vec{F}_{2mn}^{(c)}(\vec{r}\,), \tag{2.10}$$

for the electric field, and by

$$\vec{H}(\vec{r}\,) = -ik\sqrt{\eta} \sum_{cmn} Q_{1mn}^{(c)} \vec{F}_{2mn}^{(c)}(\vec{r}\,) + Q_{2mn}^{(c)} \vec{F}_{1mn}^{(c)}(\vec{r}\,), \tag{2.11}$$

for the magnetic field, with $\eta = \sqrt{\epsilon/\mu}$ being the intrinsic admittance of the medium, and $Q_{1mn}^{(c)}$ and $Q_{2mn}^{(c)}$ being the coefficients. For the example depicted in Fig. 2.2 of an antenna radiating in presence of a scatterer, $c = 1$ is used in

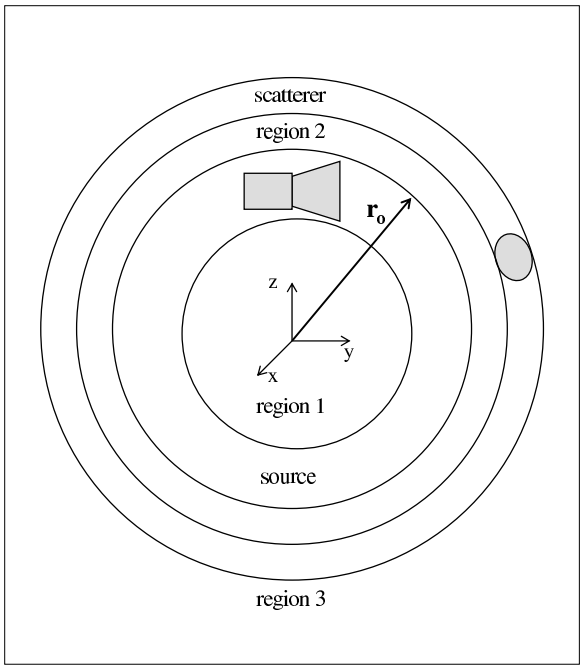

Figure 2.2: Source-free regions 1, 2 and 3, where the SWE of the electromagnetic field is valid.

region 1, $c = 1, 2$ or equivalently $c = 3, 4$ in region 2 and $c = 3$ in region 3.
The expression obtained by [26] in (2.6) is slightly different from the one introduced by [30]. The choice of defining the generating function like in (2.6) turns out to be computationally convenient when the SWE is obtained from a spherical near-field measurement, i.e., from the samples of the radiated field on a sphere centered at the origin of the coordinate system and circumscribing the antenna. An overview of the theory of spherical near-field measurements is besides the scope of the present section, however, it is worth mentioning that the fundamentals of the spherical near-field technique were established in the Seventies by a joint effort between TICRA, DTU and the National Bureau of Standards [31], resulting in a textbook [26] and in a commercial software, SNIFTD [32], which are today regarded as the de facto standards within spherical near-field antenna testing.

We now restrict our attention to the case of a single antenna radiating in free-space, i.e., we remove the scatterer in Fig. 2.2, and consider the source-free region defined by $r > r_o$, with r_o being the radius of the smallest sphere centered at the origin of the coordinate system and circumscribing the antenna, see Fig. 2.2, the so called *antenna minimum sphere*. Unless otherwise stated, this is the antenna

configuration treated in the rest of the thesis. For this source only modes with $c = 3$ exist and (2.10) becomes

$$\vec{E}(\vec{r}\,) = \frac{k}{\sqrt{\eta}} \sum_{n=1}^{\infty} \sum_{m=-n}^{n} Q_{1mn}^{(3)} \vec{F}_{1mn}^{(3)}(\vec{r}\,) + Q_{2mn}^{(3)} \vec{F}_{2mn}^{(3)}(\vec{r}\,) \qquad r > r_o \tag{2.12}$$

which constitutes the definition of SWE introduced by [26] that will be used in the present report.
It is noted that the generating function of (2.6) introduces in (2.12) a power-normalization, such that any single $c = 3$ spherical wave with amplitude 1 radiates a power of 1/2 watt. Moreover, the factors in front of the summation signs in (2.12) allow one to derive a simple relation for the total power in watts radiated by the antenna, according to [26]

$$P_{rad} = \frac{1}{2} \sum_{mn} |Q_{1mn}^{(3)}|^2 + |Q_{2mn}^{(3)}|^2 = \sum_{n} P_{rad}(n), \tag{2.13}$$

with $P_{rad}(n)$ being the power spectrum

$$P_{rad}(n) = \frac{1}{2} \sum_{m} |Q_{1mn}^{(3)}|^2 + |Q_{2mn}^{(3)}|^2 \tag{2.14}$$

which will be widely used in the following sections.

The series of (2.12) is in principle infinite, however some observations can be made. It is noted that the space outside the antenna minimum sphere can be viewed as a spherical waveguide, with radius from r_o to infinity, where spherical waves propagate in the radial direction with modes $\vec{F}_{1mn}^{(3)}(\vec{r}\,)$ and $\vec{F}_{2mn}^{(3)}(\vec{r}\,)$. For increasing r the cross-section of the spherical waveguide increases, while the cut-off frequency decreases, allowing in principle an infinite number of spherical modes to propagate along the guide. Every mode presents however a transition between propagation and evanescence around a radial distance $r_n = n/k$, since the mode decays rapidly with increasing r for $r << r_n$, corresponding to an evanescent wave, while it decays as r^{-1} for $r >> r_n$, corresponding to a propagating wave. This can easily be visualized by plotting the amplitudes of the two radial functions for $c = 3$, $h_n^{(1)}(kr)$ and $\frac{1}{kr}\frac{d}{d(kr)}(krh_n^{(1)}(kr))$, in respect of kr for different n, see Fig. 2.3 according to [26]. Though all modes are propagating in the far-field, the transition property implies that, for an antenna with a minimum sphere radius r_o, modes with $n > kr_o$ are highly suppressed outside the minimum sphere and only modes with $n < kr_o$ contribute with not negligible amplitude to the far-field and at the distance where a near-field measurement is usually taken. Thus, for an antenna with minimum sphere r_o, the SWE of the radiated field can in practice be truncated at some $n = N$. The value of N, which ensures the convergence of the series of (2.12) can be found by applying the following empirical rule introduced by [26]

$$N = \lfloor kr_o \rfloor + n_1, \tag{2.15}$$

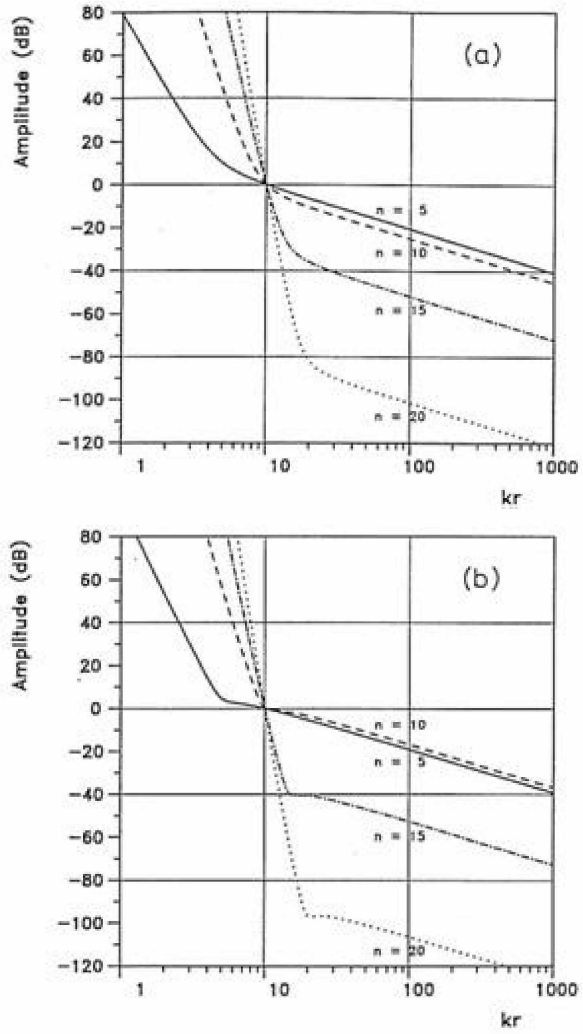

Figure 2.3: Amplitude of (a) the function $h_n^{(1)}(kr)$ and (b) the function $\frac{1}{kr}\frac{d}{d(kr)}(krh_n^{(1)}(kr))$, for $n = 5, 10, 15, 20$ normalized to 0 dB at $kr = kr_o = 10$.

where n_1 depends on the position of the source in the coordinate system and on the desired accuracy in the measurement. In particular, if the antenna is centered at the coordinate system so that r_o is as small as possible, if the measurement sphere is more than 5 wavelengths from the minimum sphere and if 4 correct digits in the field computation are sufficient, n_1 can be set equal to 10, obtaining

$$N = \lfloor kr_o \rfloor + 10. \tag{2.16}$$

If the measurement sphere is closer, a larger n_1 has to be chosen [26]. A more accurate value of N has been recently proposed by Jensen and Frandsen [33] by studying the effect of the truncation of the spherical nm-modes in (2.12) with the storage capacity and computational speed of today's computers. They found that the value of n_1 is generally not a constant but depends on the radius of the antenna minimum sphere and the amount of truncated power P_{tr}

$$P_{tr} = P_{rad} - \sum_{n=1}^{N} P_{rad}(n), \tag{2.17}$$

where the power spectrum is computed with (2.14) and a total radiated power $P_{rad} = 1$ is assumed. The new expression of N to be used in (2.12) is given by

$$N = \lfloor kr_o \rfloor + 0.045\sqrt[3]{kr_o}(-P_{tr}). \tag{2.18}$$

If for example a truncated power of P_{tr} =-80 dB is allowed, (2.18) becomes

$$N = \lfloor kr_o \rfloor + 3.6\sqrt[3]{kr_o}. \tag{2.19}$$

The truncation value N determines the sampling in θ and ϕ which allows the SWE to be obtained from the discrete values of the electric field measured on a sphere centered at the origin of the measurement coordinate system and concentric with the minimum sphere, according to

$$\Delta\theta = \frac{2\pi}{2N+1} = \Delta\phi. \tag{2.20}$$

If the smallest cylinder parallel to the measurement z-axis and enclosing the antenna under test has a radius $\rho_c < r_o$, a different sampling can be used in ϕ

$$\Delta\phi = \frac{2\pi}{2M+1}, \tag{2.21}$$

with M being

$$M = \lfloor k\rho_c \rfloor + 10. \tag{2.22}$$

2.2 Plane wave expansion

The PWE expresses the electromagnetic field in a source-free region of space as an infinite continuous spectrum of plane waves, of different complex amplitudes and different wave propagation vectors. The original PWE was introduced by Whittaker and Watson [34], reformulated by Stratton [30] and employed for the first time by Kerns [35] in planar near-field antenna measurements. A more recent treatment can be found in [36]. Since the proposed definitions do not show substantial differences or computational advantages, the notation used in [36] is chosen and used throughout this report.
The expression of the PWE can be derived by solving Maxwell's equations in cartesian coordinates [37]. For this purpose, we consider the electromagnetic field

radiated by a source distribution in the cartesian coordinate system of Fig. 2.4, with z_o being the largest z-coordinate of the source on the positive z-axis. Unless otherwise stated, this will be the case considered in the entire thesis. We then write in the source-free region of space $z > z_o$ the vector wave equation for the electric field $\vec{E}$

$$(\nabla^2 + k^2)\vec{E}(\vec{r}\,) = 0 \tag{2.23}$$

and the divergence of $\vec{E}$

$$\nabla \cdot \vec{E}(\vec{r}\,) = 0. \tag{2.24}$$

Next, we decompose the position vector $\vec{r}$ and the electric field $\vec{E}$ along the carte-

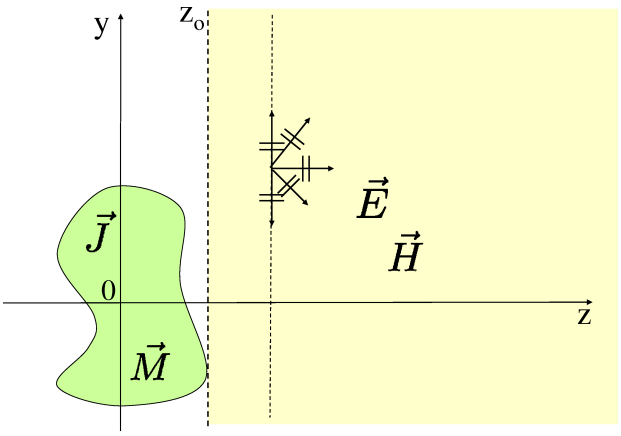

Figure 2.4: Spatial domain of validity $z > z_o$ of the PWE of Eqs. (2.35) and (2.36).

sian unit vectors and substitute them into (2.23) and (2.24), obtaining respectively

$$\Big(\frac{\partial^2}{\partial x^2} + \frac{\partial^2}{\partial y^2} + \frac{\partial^2}{\partial z^2} + k^2\Big)\vec{E}(x,y,z) = 0 \tag{2.25}$$

$$\frac{\partial E_x(x,y,z)}{\partial x} + \frac{\partial E_y(x,y,z)}{\partial y} + \frac{\partial E_z(x,y,z)}{\partial z} = 0. \tag{2.26}$$

We then introduce the two-dimensional Fourier transform of the electric field in respect of the x- and y-spatial variables according to [36][1] as

$$\vec{T}(k_x,k_y,z) = \frac{1}{2\pi}\int_{-\infty}^{+\infty}\int_{-\infty}^{+\infty}\vec{E}(x,y,z)e^{-i(k_x x + k_y y)}dxdy, \tag{2.27}$$

with $\vec{T}(k_x,k_y,z)$ being the plane wave spectrum (PWS) of the electric field on the z-plane of interest, and $k_x k_y$ being the spectral variables. If both (2.25) and (2.26)

[1] The authors' relations, valid for the time Fourier transform of the electric and magnetic field, can be applied also to the phasors of the fields, since phasors and time domain Fourier quantities satisfy the same set of Maxwell's equations

are Fourier transformed with respect to x and y they become respectively

$$\Big[-k_x^2 - k_y^2 + \frac{\partial^2}{\partial z^2} + k^2 \Big] \vec{T}(k_x, k_y, z) = 0 \tag{2.28}$$

$$k_x T_x(k_x, k_y, z) + k_y T_y(k_x, k_y, z) - i \frac{\partial}{\partial z} T_z(k_x, k_y, z) = 0, \tag{2.29}$$

where the PWS is the unknown.
By defining

$$k_z^2 = k^2 - k_x^2 - k_y^2, \tag{2.30}$$

and substituting (2.30) into (2.28) we then obtain

$$\frac{\partial^2 \vec{T}(k_x, k_y, z)}{\partial z^2} + k_z^2 \vec{T}(k_x, k_y, z) = 0, \tag{2.31}$$

whose solution is of the form $\vec{T}(k_x, k_y) e^{\pm i k_z z}$. Since we are considering the source-free region $z > z_o$, only outgoing waves propagating along the positive z-axis described by $e^{i k_z z}$ have physical meaning.
The expression of the PWS thus becomes

$$\vec{T}(k_x, k_y, z) = \vec{T}(k_x, k_y) e^{i k_z z}. \tag{2.32}$$

It is important to note, looking at (2.32), that the particular z-dependence of the PWS allows the computation of $\vec{T}(k_x, k_y, z)$ on any z-plane $z > z_o$ by simply varying the value of z once the function $\vec{T}(k_x, k_y)$ is known.
By substituting (2.32) into (2.29) we find

$$k_x T_x(k_x, k_y) + k_y T_y(k_x, k_y) + k_z T_z(k_x, k_y) = 0, \tag{2.33}$$

which, being equal to

$$\vec{k} \cdot \vec{T}(k_x, k_y) = 0, \tag{2.34}$$

indicates that from the knowledge of two components of the spectrum $\vec{T}(k_x, k_y)$ the third one can be obtained. Normally T_x and T_y are considered independent and T_z is derived.
From (2.32), (2.27) can thus be rewritten as

$$\vec{T}(k_x, k_y) e^{i k_z z} = \frac{1}{2\pi} \int_{-\infty}^{+\infty} \int_{-\infty}^{+\infty} \vec{E}(x, y, z) e^{-i(k_x x + k_y y)} dx dy, \qquad z > z_o \tag{2.35}$$

which once reversed provides

$$\vec{E}(x, y, z) = \frac{1}{2\pi} \int_{-\infty}^{+\infty} \int_{-\infty}^{+\infty} \vec{T}(k_x, k_y) e^{i k_z z} e^{i(k_x x + k_y y)} dk_x dk_y \qquad z > z_o \tag{2.36}$$

which is the PWE in the $k_x k_y$-domain of the electric field $\vec{E}(x, y, z)$ valid for every $z > z_o$ which will be used in the entire thesis. Equivalently, (2.36) is the inverse Fourier transform of the PWS $\vec{T}(k_x, k_y, z)$, while (2.35) constitutes the Fourier

transform of the electric field $\vec{E}(x,y,z)$.
In an similar way we can write for the magnetic field

$$\vec{H}(x,y,z) = \frac{1}{2\pi}\int_{-\infty}^{+\infty}\int_{-\infty}^{+\infty}\vec{T}^H(k_x,k_y)e^{i(k_x x+k_y y+k_z z)}dk_x dk_y \qquad z > z_o \quad (2.37)$$

with $\vec{T}^H(k_x,k_y)$ given by

$$\vec{T}^H(k_x,k_y) = \sqrt{\frac{\epsilon}{\mu}}\hat{k}\times\vec{T}(k_x,k_y). \quad (2.38)$$

The variables k_x, k_y, k_z are the cartesian components of the wave propagation vector $\vec{k}$, i.e., $\vec{k} = k_x\hat{x} + k_y\hat{y} + k_z\hat{z} = k\hat{k}$, and divide the spectral domain in two regions, the visible region for $k_x^2 + k_y^2 \leq k^2$, and the invisible region for $k_x^2 + k_y^2 > k^2$, see Fig. 2.5. While the spectral variables k_x and k_y are real everywhere, k_z is real in the visible region, $k_z = \sqrt{k^2 - k_x^2 - k_y^2}$, and purely imaginary with a positive imaginary part in the invisible region, $k_z = i\sqrt{k_x^2 + k_y^2 - k^2}$. Real values of k_z correspond to propagating plane waves, while imaginary values of k_z correspond to evanescent plane waves that are exponentially attenuated with z. Their contribution is usually negligible at distances larger than one wavelength from the antenna, [38] and [20].

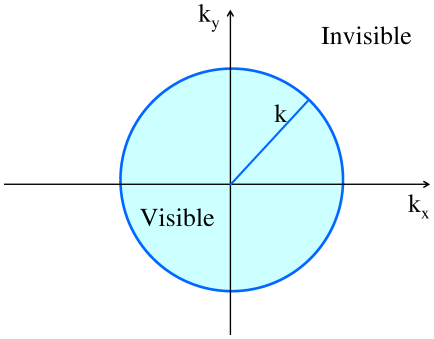

Figure 2.5: Visible and invisible regions of the spectral $k_x k_y$-domain.

An alternative expression of the spectrum, which will be used in the following sections, can be found from the triple Fourier transform of the volume current source $\vec{J}(\vec{r}\,)$ [36]

$$\vec{T}(k_x,k_y) = \frac{1}{4\pi k k_z}\sqrt{\frac{\mu}{\epsilon}}\vec{k}\times\left(\vec{k}\times\int_V \vec{J}(\vec{r}\,)e^{-i(k_x x+k_y y+k_z z)}dV\right). \quad (2.39)$$

It is finally recalled that a simple relation exists between the far-field and the visible region of the plane wave spectrum, according to [36] and [1],

$$\lim_{kr\to\infty}\vec{E}(r,\theta,\phi) = -\frac{e^{ikr}}{r}ik\cos\theta\vec{T}(k\sin\theta\cos\phi, k\sin\theta\sin\phi) \quad (2.40)$$

$$= \vec{E}_{far}(r,\theta,\phi) \qquad \theta \in [0,\pi/2] \quad \phi \in [0,2\pi]$$

The PWS is an analytic function on the entire spectral domain except at the border between the visible and invisible region where $k_z = 0$ and a singularity of the type $1/k_z$ is usually present in at least one of its components [36]. This constitutes the only possible singularity and the necessary but not sufficient condition to prevent it is a null in the antenna far-field pattern in the xy-plane ($\theta = \pi/2$). While the singularity does not appear explicitly in (2.35), the $1/k_z$-term is seen when $\vec{T}(k_x,k_y)$ is written in terms of the volume current source, (2.39), and when the visible region of $\vec{T}(k_x,k_y)$ is expressed in terms of the far-field pattern, (2.40), by noticing that $k\cos\theta = k_z$. In practice, the k_x- and k_y-integrals are truncated at finite values $\pm k_{xmax}$ and $\pm k_{ymax}$ respectively. In some cases, e.g. when the PWE is determined from a planar near-field measurement over a finite scan plan, the PWE is reliable only over the central part of the visible region of the spectral domain [13], while the part of the domain where the singularity exists must be disregarded. In other cases however, i.e., when the PWE is determined from a far-field measurement, a compact range measurement or a spherical near-field measurement, the PWE at, or close to, the border between the visible and invisible regions can be determined and the singularity is thus known. A very good overview of planar near-field antenna measurements, discussing sampling theorems and efficient computational methods, is given in [38].

In contradiction with (2.40), several scientists claimed that evanescent waves contribute to any direction of the far-field [39]-[40]-[41]. This statement was strongly contested by Wolf and Foley in [42]-[43] by using some of the general results reported in [44]. As stated in [44], it can be shown by the use of the theorem of stationary phase that the far-field is given in any direction by the contribution of the stationary point belonging to the visible region, (2.40). However, when the far-field $\vec{E}_{far}(\vec{r})$ is written by $\vec{E}_{far}(\vec{r}) = \vec{E}_{farvis}(\vec{r}) + \vec{E}_{farinvis}(\vec{r})$, with $\vec{E}_{farvis}(\vec{r})$ and $\vec{E}_{farinvis}(\vec{r})$ being the asymptotic approximation of the inverse Fourier transform of the spectrum, see (2.36), respectively performed over the only visible and only invisible region, three regions of space need then to be defined. In the region $0 < \theta < \pi/2$, equivalent to $0 < k_z < 1$, it can be proved that $\vec{E}_{far}(\vec{r}) \simeq \vec{E}_{farvis}(\vec{r})$, since $\vec{E}_{farinvis}(\vec{r})$ only provides terms of order higher than $(kr)^{-1}$ which can be neglected in the asymptotic region. However, for $\theta = 0$ and $\theta = \pi/2$, corresponding respectively to $k_z = 1$ and $k_z = 0$, $\vec{E}_{farinvis}(\vec{r})$ generally provides a term of order $(kr)^{-1}$ which needs to be considered in the asymptotic region. These terms have an opposite sign compared to the terms of the same order provided by $\vec{E}_{farvis}(\vec{r})$ for $\theta = 0$ and $\theta = \pi/2$, and thus cancel in the final expression of $\vec{E}_{far}(\vec{r})$. This has led to the conclusion that only on the two particular directions $\theta = 0, \pi/2$ the contribution of the evanescent waves is in general not negligible, and that errors are in principle introduced in considering the inverse Fourier transform of the spectrum on the visible region alone, $\vec{E}_{farvis}(\vec{r})$, as correct approximation of the far-field. However, the two special directions where the evanescent waves contribute to the far-field form a set of measure zero, i.e. they are removable points, and thus can be disregarded in the computation of the far-field with practically no consequences

for the far-field accuracy [43].

2.3 From the spherical wave expansion to the plane wave expansion

Though the SWE and the PWE can both be derived from the homogeneous vector wave equation, their regions of validity are fundamentally different. Employing a cartesian xyz-coordinate system and the associated spherical $r\theta\phi$-coordinate system, the SWE is valid for $r > r_o$, while the PWE is valid for $z > z_o$, see Fig. 2.6. Since r_o is always larger than or equal to z_o, $r_o \geq |z_o|$, the PWE can, by a proper orientation of the coordinate system, be valid in the extreme near-field region of a planar source, while this will not be the case for the SWE. It is possible however to derive the PWE from the SWE, and vice-versa, through a rigorous transformation.

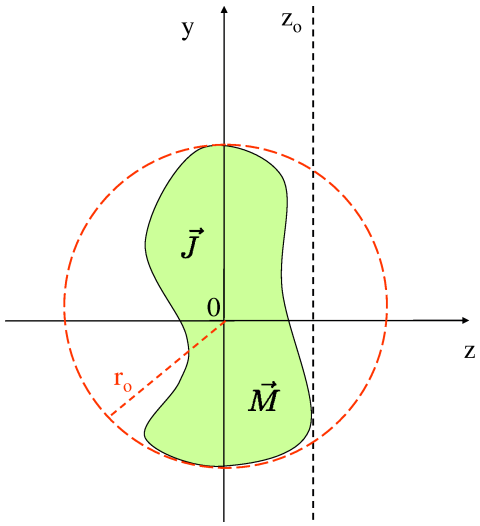

Figure 2.6: Spatial domains of validity of the SWE and PWE for a general source distribution: the PWE is valid for $z > z_o$, the SWE for $r > r_o$.

It will here be shown how the SWE of (2.12) can be transformed into the PWE of (2.36). The following derivation is based on [28], but it has been extended in order to use the power-normalized spherical vector wave functions of Eqs. (2.8)-(2.9), the $k_x k_y$-PWE of Eq. (2.36), and the S.I. system of units. This turns out to be particularly advantageous since these are the functions employed in the textbook [26] and in the software SNIFTD [32] used at the DTU-ESA Facility. An alternative derivation of the SWE-to-PWE transformation is given in Appendix A of Paper I.
The transformation is derived in 3 steps.

The first step consists of introducing the PWE of the spherical vector wave functions, which in the spectral $\alpha\beta$-domain are given by

$$\vec{F}^{(3)}_{1mn}(\vec{r}\,) = \frac{(-i)^{n+1}}{2\pi\sqrt{n(n+1)}} \int_{-\pi}^{\pi}\int_{B} \vec{Y}^{m}_{n}(\alpha,\beta) e^{ik\hat{k}\cdot\vec{r}} \sin\alpha \; d\alpha \; d\beta \tag{2.41}$$

$$\vec{F}^{(3)}_{2mn}(\vec{r}\,) = \frac{(-i)^{n}}{2\pi\sqrt{n(n+1)}} \int_{-\pi}^{\pi}\int_{B} \Big[\hat{k}\times\vec{Y}^{m}_{n}(\alpha,\beta)\Big] e^{ik\hat{k}\cdot\vec{r}} \sin\alpha \; d\alpha \; d\beta \tag{2.42}$$

with $\hat{k} = \vec{k}/k = \sin\alpha\cos\beta\hat{x} + \sin\alpha\sin\beta\hat{y} + \cos\alpha\hat{z}$, $\beta \in [-\pi,\pi]$ and $\alpha \in B$, see Fig. 2.7. Real values of α correspond to propagating waves, while complex values of α correspond to evanescent waves. The function $\vec{Y}^{m}_{n}(\alpha,\beta)$ is the vector spherical harmonics which can be expressed as

$$\vec{Y}^{m}_{n}(\alpha,\beta) = \frac{-i}{\sqrt{2\pi}}\Big(-\frac{m}{|m|}\Big)^{m}\Big(\frac{d}{d\alpha}\bar{P}^{|m|}_{n}(\cos\alpha)e^{im\beta}\hat{\beta} - \frac{im}{\sin\alpha}\bar{P}^{|m|}_{n}(\cos\alpha)e^{im\beta}\hat{\alpha}\Big) \tag{2.43}$$

with $\hat{\alpha} = \cos\alpha\cos\beta\hat{x} + \cos\alpha\sin\beta\hat{y} - \sin\alpha\hat{z}$ and $\hat{\beta} = -\sin\beta\hat{x} + \cos\beta\hat{y}$.

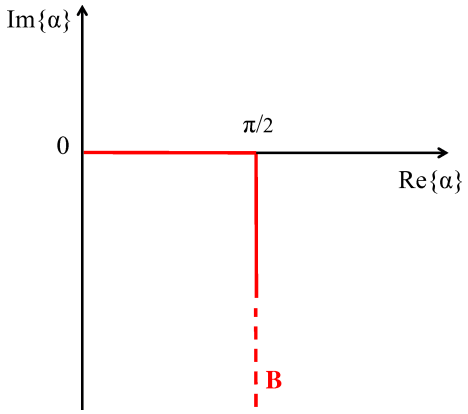

Figure 2.7: Domain of the variable α on contour B.

Second, the PWEs of (2.41)-(2.42) are substituted into the SWE of (2.12) and the order of integration and summation is interchanged, obtaining the PWE of the electric field in the spectral $\alpha\beta$-domain

$$\vec{E}(\vec{r}\,) = \frac{k}{2\pi}\int_{-\pi}^{\pi}\int_{B} \tilde{E}(\hat{k}) e^{ik\hat{k}\cdot\vec{r}} \sin\alpha \; d\alpha \; d\beta, \tag{2.44}$$

where the spectrum complex amplitude $\tilde{E}(\hat{k})$ is given by

$$\tilde{E}(\hat{k}) = \sum_{n=1}^{\infty}\sum_{m=-n}^{n} \frac{(-i)^{n}}{\sqrt{\eta}\sqrt{n(n+1)}}\Big[-iQ^{(3)}_{1mn}\vec{Y}^{m}_{n}(\alpha,\beta) + Q^{(3)}_{2mn}\hat{k}\times\vec{Y}^{m}_{n}(\alpha,\beta)\Big] \tag{2.45}$$

and can thus be calculated from the knowledge of the coefficients $Q^{(3)}_{1mn}, Q^{(3)}_{2mn}$. Third, the spectrum in the spectral $\alpha\beta$-domain, $\tilde{E}(\hat{k})e^{ik\cos\alpha z}$, is translated into the k_xk_y-domain obtaining $\vec{T}(k_x,k_y)e^{ik_z z}$. It can in fact be shown, by applying a change of integration variables in (2.44), i.e., $k_x = k\sin\alpha\cos\beta, k_y = k\sin\alpha\sin\beta, k_z = k\cos\alpha$, and by identifying the obtained result with (2.36), that

$$\vec{T}(k_x,k_y)e^{ik_z z} = \frac{1}{k_z}\tilde{E}(\hat{k})e^{ik\cos\alpha z}, \tag{2.46}$$

where α and β on the right hand side are expressed as functions of the spectral variables k_x and k_y according to

$$\alpha = \arcsin\Big(\sqrt{\frac{k_x^2+k_y^2}{k^2}}\Big) \qquad \beta = \arctan\Big(\frac{k_y}{k_x}\Big). \tag{2.47}$$

The arcsin and arctan functions must be implemented to ensure the correct contour B for the angle α and the interval $[-\pi,\pi]$ for the angle β. With (2.47), the α- and β-values corresponding to the chosen k_x- and k_y-values can be calculated exactly without any interpolation. By combining (2.45)-(2.46)-(2.47), the PWS $\vec{T}(k_x,k_y)e^{ik_z z} = \vec{T}(k_x,k_y,z)$ can finally be written as

$$\vec{T}(k_x,k_y,z) = \sum_{n=1}^{\infty}\sum_{m=-n}^{n} Q^{(3)}_{1mn}\vec{T}_{1mn}(k_x,k_y,z) + Q^{(3)}_{2mn}\vec{T}_{2mn}(k_x,k_y,z) \tag{2.48}$$

where

$$\vec{T}_{1mn}(k_x,k_y,z) = \frac{e^{ik_z z}}{k_z}\frac{(-i)^{n+1}}{\sqrt{\eta}\sqrt{n(n+1)}}\vec{Y}^m_n(\alpha,\beta) \tag{2.49}$$

$$\vec{T}_{2mn}(k_x,k_y,z) = \frac{e^{ik_z z}}{k_z}\frac{(-i)^{n}}{\sqrt{\eta}\sqrt{n(n+1)}}\hat{k}\times\vec{Y}^m_n(\alpha,\beta) \tag{2.50}$$

It is emphasized that (2.41), (2.42) and (2.45) are of fundamental importance in the theory of modal expansions and provide the theoretical justification for the SWE-to-PWE transformation. In particular we note that the spectrum complex amplitude $\tilde{E}(\hat{k})$ defined by (2.44) is an analytic function in its complex domain of definition, since it can be expressed by the spatial Fourier transform of a finite source distribution, [28] and [14]. Moreover, $\tilde{E}(\hat{k})$ is a vector function which is normal to the unit vector $\hat{k}$, i.e., $\hat{k}\cdot\tilde{E}(\hat{k}) = 0$. Since the vector spherical harmonics $\vec{Y}^m_n(\alpha,\beta)$ and $\hat{k}\times\vec{Y}^m_n(\alpha,\beta)$ constitute a complete orthogonal basis for all analytical vector functions normal to the unit vector $\hat{k}$ [28], it is possible to express $\tilde{E}(\hat{k})$ through (2.45). It is finally recalled that though we begin with a SWE that is only valid outside the minimum sphere, $r > r_o$, the obtained PWE, whose spectrum is expressed by (2.48), is valid for $z > z_o$, thus also inside the minimum sphere, see Fig. 2.6, since $\tilde{E}(\hat{k})$ does not depend on z.

To calculate the plane wave spectrum $\vec{T}(k_x,k_y,z)$ of (2.36) from the SWE of (2.12), we can thus summarize the required steps as follows:

1. Choose a certain $k_x k_y$-spectral domain.
2. For every point in the $k_x k_y$-spectral domain determine the corresponding α and β-values with (2.47).
3. Calculate the PWS with (2.48) on a z-plane $z > z_o$.

2.4 Summary

The SWE and PWE were both derived from the vector Helmholtz equation and their definitions, domains of validity, properties, and use in antenna measurements were discussed. By employing a cartesian xyz-coordinate system and the associated spherical $r\theta\phi$-coordinate system, it was shown that for an antenna with minimum sphere of radius r_o and radiating in free-space, the SWE of the radiated field is valid for $r > r_o$, while the PWE of the same field is valid for $z > z_o$, with z_o being the largest z-coordinate of the antenna and $|z_o| \leq r_o$. For source regions identified by a planar aperture, the PWE allows the computation of the extreme near-field, which can not be directly computed from the SWE.
Though the domains of validity of the SWE and PWE are fundamentally different, the PWE can be obtained from the SWE with a rigorous transformation. The transformation from the SWE to the PWE was then described, providing the mathematical foundation for the proposed antenna diagnostics technique. In particular it was shown that the plane wave spectrum can be calculated from the coefficients of the SWE, in the visible as well as in the invisible regions of the spectral domain, at any z-plane $z > z_o$.

Chapter 3

SWE-to-PWE antenna diagnostics technique

From the analysis conducted in Chapter 2 it was concluded that the SWE-to-PWE transformation is a promising way to develop an antenna diagnostics technique for spherical near-field measurements. The transformation allows the computation of the extreme near-field of the antenna under test, which can not be directly computed from the SWE, see Fig. 3.1. Moreover, the transformation is of general validity and can be applied to every antenna of which we know, or can measure, the SWE of the radiated field.
Though the SWE-to-PWE transformation constitutes the theoretical foundation for the proposed diagnostics technique, several additional steps and observations are necessary to obtain the antenna aperture field from a spherical near-field measurement. Section 3.1 describes the fundamental properties of the SWE-to-PWE transformation, underlying their theoretical as well as practical implications for the diagnostics technique. All considerations are exposed in detail in Paper I, and some numerical aspects are given in Appendix C. Section 3.2 deals with the computation of the aperture field from the PWS: here only a brief summary is provided, but a complete analysis can be found in Paper II. Section 3.3 discusses the concept of resolution and the information contained in a near-field plot. Section 3.4 applies the SWE-to-PWE diagnostics technique to a simple antenna test case, which is presented in Paper III. Section 3.5 summarizes the effects of finite measurement accuracy, on the basis of the results contained in Paper IV.

3.1 Properties of the SWE-to-PWE transformation

Though several works on the SWE-to-PWE transformation have been presented over the years, see for example Stratton [30], Morse and Feshbach [45] and Devaney and Wolf [28], such concepts as convergence mechanism, truncation of the series and integrals involved as well as numerical implementation have been dealt with

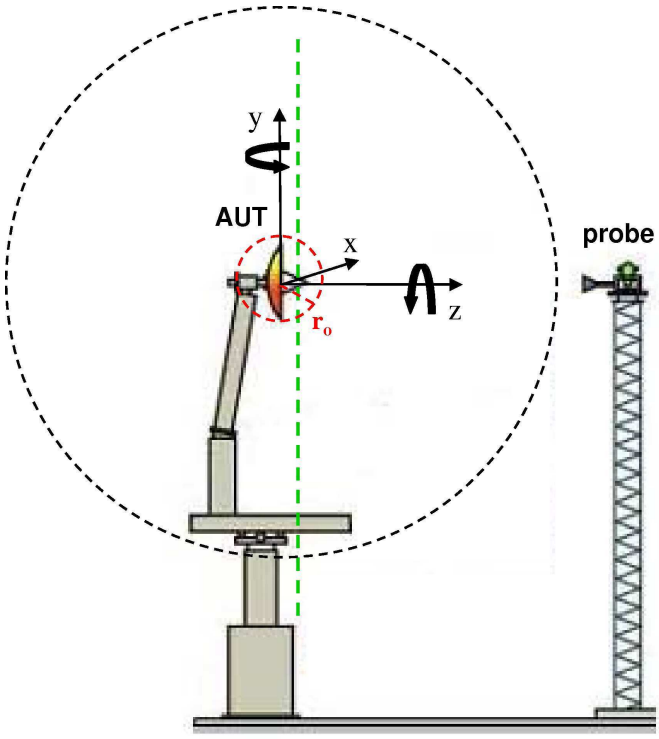

Figure 3.1: Scheme of a spherical near-field facility: the AUT to be measured on the tower, the probe, the measurement sphere of radius R, the antenna minimum sphere of radius r_o, the z-plane in the source-free region where the PWE is valid.

to a lesser degree. It is thus the purpose of the present section to investigate these aspects.
We start by recalling that the PWS $\vec{T}(k_x, k_y, z)$ can be computed on every z-plane $z > z_o$ from the Q coefficients of the SWE by use of (2.48). The computation provides values of the PWS in the visible as well as in the invisible region of the spectral domain, however, values in the invisible region might not give a converged/accurate result, as it will be shown below. The spatial resolution δ_x δ_y, see Section 3.3, of the aperture field obtained from (2.36) is given by

$$\delta_x = \pi/k_{xmax} \qquad \delta_y = \pi/k_{ymax}, \tag{3.1}$$

with $k_{xmax}k_{ymax}$ being the maximum values of the spectral k_xk_y-domain where the PWS is different from zero and has reached convergence. Eq. (3.1) indicates that the value of $\lambda/2$, which is the resolution obtained from the knowledge of the only visible region of the PWS, can be exceeded if a part of the invisible region is taken into account, since either k_x, k_y or both are larger than the wavenumber $k = 2\pi/\lambda$.

We can then observe that

$$\vec{Y}_n^m(\alpha,\beta) \propto \vec{K}_{1mn}(\alpha,\beta) \qquad \hat{k} \times \vec{Y}_n^m(\alpha,\beta) \propto \vec{K}_{2mn}(\alpha,\beta) \tag{3.2}$$

with $\vec{K}_{1mn}$ and $\vec{K}_{2mn}$ being the asymptotic approximations with respect to r of the spherical vector wave functions $F_{1mn}^{(3)}$ and $F_{2mn}^{(3)}$ respectively. By comparing (3.2) with the spectrum complex amplitude $\tilde{E}(\hat{k})$ given in (2.45), it is concluded that $\tilde{E}(\hat{k})$ is equivalent to the SWE of the far-field. This indicates that all information about the visible and invisible spectral regions of the PWS is in principle contained in the far-field and not only in the extreme near-field as it is usually believed.

However, while the traditional truncation value $N = kr_o + 10$, or $N = \lfloor kr_o \rfloor + 3.6\sqrt[3]{kr_o}$, provides an accurate evaluation of the SWE of the electric far-field [26] and thus of the PWS $\vec{T}(k_x, k_y, z)$ computed by (2.48) in the visible region, the same truncation value is in general not sufficient in the invisible region.

There are two reasons why convergence rates are different in the two regions. The first lies in the fact that each spherical wave, for a given n and m mode, contributes to the visible as well as to the invisible region, and thus provides at the same time information on the propagating as well as evanescent waves of the PWE, see Paper I. The second one is given by an inherent mathematical property. While the trigonometric functions necessary for the computation of the spherical harmonics used in (2.49) and (2.50) are finite in the visible region, where the $\alpha\beta$-angles are real and given by $\alpha \in [0, \pi/2]$ and $\beta \in [0, 2\pi]$, they become in theory unbounded in the invisible region, where α is pure imaginary according to Fig. 2.7. In practice, due to the finite extents of the spectral $k_x k_y$-domain, the amplitude reached by the spherical harmonics is limited there, though very large.

Therefore, while the infinite series of (2.48) reaches convergence with $N = kr_o + 10$ terms in the visible region, a larger value of N is necessary in the invisible region, where only extremely low values of Q_{1mn} and Q_{2mn}, corresponding to high n and m modes, can compensate the exponential growth of the spherical harmonics and make the series of (2.48) reach convergence. The truncation number N required to reach convergence in the entire $[-2k, 2k]$ $k_x k_y$-domain depends on r_o and it was found that $N = kr_o + 4kr_o$ was necessary for an array of Hertzian dipoles, see Section 3.4 and Paper I, for which the Q coefficients were computed analytically, and for a rectangular aperture in free-space, see Paper III. Though such a relation may not be generally valid, it was used as a rule-of-thumb also for more complicated antenna cases, to get an idea of the spectral region where the PWS could reach convergence when the Q coefficients were obtained from a spherical near-field measurement. It was noted that the intermediate values encountered in the points of the invisible region in reaching convergence can be very large, in some cases of the order of several hundreds of dB on the z-plane of interest for the diagnostics, while the value to which they converge is normally much lower.

It is underlined that particular attention has to be given in computing the trigonometric functions in the invisible region, already for moderate values of n and m. For this purpose, the embedding of the factor $e^{ik_z z}$ can help controlling the exponential growth. Details about that are given in Paper I and in Appendix C.

It is finally noted that the coordinate system of the SWE coincides with the co-

ordinate system in which the extreme near-field is computed. In some cases the coordinate system used in a spherical near-field measurement is not the most natural for the antenna, but only the most practical, determined by geometrical and mechanical considerations. However, since antenna errors manifest themselves differently in different coordinate systems, a clever choice of the coordinate system in which the extreme near-field is computed can significantly help the errors' identification. For this purpose it is recalled that it is possible to rotate the measured SWE to a new coordinate system [26], and that this operation is implemented at the DTU-ESA Facility and can easily be performed by ROSCOE, a package of SNIFTD [32]. Once the measured SWE is rotated to a new coordinate system, (2.48) allows the immediate computation of the corresponding extreme near-field. This is of fundamental importance for the purpose of antenna diagnostics. For an application of rotation of coordinate systems, see Paper V for the case of an offset reflector antenna measured at the DTU-ESA Facility.

3.2 Aperture field computation

After having computed the plane wave spectrum $\vec{T}(k_x, k_y, z)$ on the z-plane of interest through (2.48), we can calculate the aperture field with (2.36). Since the PWS and the aperture field constitute an inverse Fourier transform pair, the inverse Fast Fourier Transform (IFFT) is the most natural choice of computation. We have pointed out, however, that the PWS normally contains a singularity at $k_z = 0$. Though such a singularity is integrable, a straightforward use of the IFFT provides inaccurate results, unless the singularity is sampled very densely. While on one hand a very dense sampling can in principle be possible, on the other hand it can not be located only in the vicinity of $k_z = 0$ but is necessary over the entire $k_x k_y$-domain, in order to provide the uniform sampling required by the IFFT algorithm. This becomes difficult when the PWS is obtained through measurements, since a very dense spatial sampling in $\theta\phi$ or xy, is then requested. In the present case, i.e., by calculating the PWS through (2.48), a dense spectral sampling is in principle possible, but at the expense of a long computation time. In order to take properly into account the singularity at $k_z = 0$, and ensure the accuracy of the aperture field, we propose to defactorize the spectrum $\vec{T}(k_x, k_y, z)$ into a product of two functions, the finite $\vec{T}_1(k_x, k_y, z)$ and the singular $1/k_z$. Since the inverse Fourier transform (IFT) of a product of two spectral functions is equal to the convolution in the spatial domain of the IFT's of the two separated functions [46], the integral of (2.36) can effectively be solved. The IFT of the finite $\vec{T}_1$ is computed numerically by the IFFT and the IFT of the singular $1/k_z$ is computed analytically using the Weyl identity [36]

$$\frac{e^{ikr}}{i2\pi r} = \frac{1}{2\pi}\int_{-\infty}^{+\infty}\int_{-\infty}^{+\infty}\frac{1}{k_z}e^{ik_z z}e^{i(k_x x + k_y y)}dk_x dk_y \qquad z > 0 \tag{3.3}$$

This allows us to write

$$\vec{E}(x, y, z) = \frac{1}{2\pi}\int_{-\infty}^{+\infty}\int_{-\infty}^{+\infty}\vec{T}(k_x, k_y)e^{ik_z z}e^{i(k_x x + k_y y)}dk_x dk_y$$

$$= \frac{1}{2\pi}\int_{-\infty}^{+\infty}\int_{-\infty}^{+\infty}\vec{T}_1(k_x,k_y)\frac{1}{k_z}e^{ik_z z}e^{i(k_x x+k_y y)}dk_x dk_y$$

$$= \frac{1}{2\pi}\int_{-\infty}^{+\infty}\int_{-\infty}^{+\infty}\vec{T}_1(k_x,k_y)e^{ik_z(z-z_1)}e^{i(k_x x+k_y y)}dk_x dk_y$$

$$\otimes\frac{1}{2\pi}\int_{-\infty}^{+\infty}\int_{-\infty}^{+\infty}\frac{1}{k_z}e^{ik_z z_1}e^{i(k_x x+k_y y)}dk_x dk_y$$

which finally becomes

$$\vec{E}(x,y,z) = \vec{E}_1(x,y,z-z_1)\otimes\frac{e^{ikr_1}}{i2\pi r_1} \tag{3.4}$$

with r_1 being $r_1 = \sqrt{x^2+y^2+z_1^2}$. As it seen in (3.4), the quantity z has to be split in two, i.e., $z = (z-z_1)+z_1$, in order to have an exponential factor of the type of $e^{ik_z z}$ on both terms, which is necessary for the validity of the Weyl identity of (3.3) and for a correct implementation of the convolution.
A deeper analysis of the technique with some numerical examples can be found in Paper II. Here we only recall that the use of the singularity extraction technique of (3.4) to compute the inverse Fourier transform of the PWS of (2.36) ensures accurate values for the aperture field, and allows the recovery of very weak sources, which are otherwise not detectable when the IFFT is applied to a singular PWS. The implementation of the convolution can be optimized by reducing the xy-domain on which the two functions are calculated, see Paper II, because of some physical and mathematical considerations. It is finally recalled that (3.4) can also be used to inverse Fourier transform spectral components which do not present the singularity. The singularity extraction technique of (3.4) will be used in the following sections and chapters to compute the aperture field from the plane wave spectrum.

3.3 Aperture field analysis and resolution

Up to this point, we have seen how to compute the PWS from the SWE and how from the spectrum to arrive at the requested aperture field. We still have not clarified what an aperture field plot is able to reveal.
We can start by saying that generally an antenna diagnostics technique provides information about the extreme near-field radiated by the antenna under test. In most cases, as it is also for the SWE-to-PWE technique so far described, such information is constituted by amplitude and phase plots for every cartesian component of the field on the selected z-plane of observation. In some other cases, other quantities can be computed, like for example the surface distortion of a reflector [7]. No matter which technique is used, the identification of the electrical and mechanical errors which affect the antenna under test is normally possible only if the expected field, i.e., the field that would exist if no errors were present, is known. While the expected field is in practice not known by a measurement, unless for didactic purposes, its distribution can sometimes be provided by the

software used for the antenna design. Most of the times, however, experience and knowledge of the electromagnetic phenomena are the only available tools to interpret the near-field plots.

Of fundamental importance for the quality and accuracy of a near-field plot is the concept of resolution. The word resolution is used in many different fields, from optics to imaging techniques, and its definition can vary depending on the particular application. Though the following discussion is not attempting to be complete, an overview and some general conclusions can be drawn.
A traditional field where resolution is a fundamental concept is optics. At optical frequencies resolution is defined as the ability to distinguish the images of objects in close proximity. Since the images are obtained by a system, we normally talk about resolution, or equivalently resolving power, of the optical system. Optical systems are generally defined by an aperture, a lens for example, through which light is transmitted and focused on a given screen to provide the final image that we observe. Since such an aperture is always of dimensions which are finite and

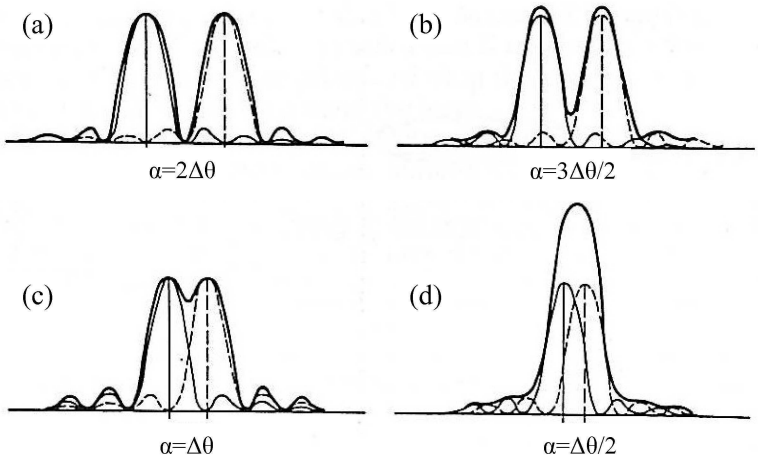

Figure 3.2: Diffraction images of two point sources through an aperture of finite dimensions: (a) and (b) well resolved, (c) just resolved, (d) not resolved.

comparable with the wavelength of the coming ray, the resolution of the system is limited by the diffraction of the light trough the aperture. This means that the image of an ideal point source at infinite distance from the aperture is always a point spread function (PSF) on the screen [47], which in case of a rectangular aperture is given by a sinc function. If the images of two point sources at infinite distance from the aperture overlap such that the peaks of the PSFs are closer than the distance $\Delta\theta$ between the peak and the first minimum of the single PSF, the images are considered unresolved, see Fig. 3.2. For geometrical construction, the

distance α of the images on the screen coincides with the angular separation of the two point sources. For a rectangular aperture of width D, the minimum angular distance two point sources can have in order to be resolved is given by $\Delta\theta \approx \frac{\lambda}{D}$, while for a circular aperture of diameter D it becomes $\Delta\theta \approx 1.22\frac{\lambda}{D}$.

In the field of holography and antenna diagnostics, resolution is defined in a slightly different way. Since the object of interest is the radiation from sources, the concept of plane wave expansion is used. Resolution is defined as the distance between the zeros of the fastest oscillating wave contained in the PWE. If for example the fastest oscillating wave is given by $e^{ikx} = \cos kx + i \sin kx$ with k being the wave number, see Fig. 3.3(a) for a plot of the imaginary part, the obtainable resolution is equal to half a wavelength. This is also the distance that allows one to distinguish a positive amplitude from a negative amplitude. The definition can easily be extended to the two-dimensional case obtaining a resolution in the x- and one in the y- dimension.

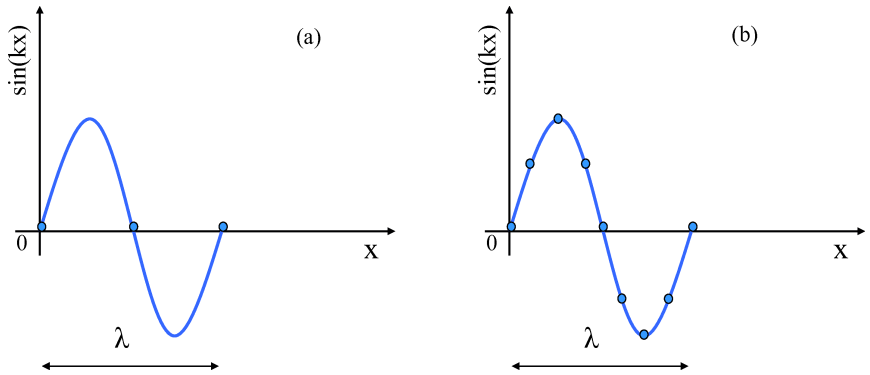

Figure 3.3: Imaginary part of the wave e^{ikx}: (a) Resolution (b) Reconstruction interval from a zero-padded spectrum.

Equivalently, resolution can be defined with the help of a concept always related to the PWE but more close to signal processing theory. Knowing that the spectral extent of a certain signal determines the spatial sampling necessary to reconstruct the original signal from its samples, according to $\Delta x = \pi/k_{max}$ for a one-dimensional signal with spectrum different from zero over $[-k_{max}, k_{max}]$, resolution is then defined as the sampling interval Δx. If $k_{max} = k$, we thus obtain a resolution of $\Delta x = \lambda/2$, like in the previous case. The interval Δx is also called reconstruction interval. It is pointed out that the sampling, or reconstruction, interval can be increased by zero-padding the available spectrum to a larger spectral domain, for example over the entire $[-4k, 4k]$ domain. However, zeropadding does not increase at the same time resolution, since the spatial function obtained from the zero-padded spectrum is the same function of before, only oversampled, see Fig. 3.3(b). As long as the spectrum is different from zero over the only $[-k, k]$ domain, resolution remains equal to half a wavelength. Resolution is thus only determined

by the part of the plane wave spectrum which is different from zero.

Though the definitions and observations given above are correct, we still do not know what the human eye can see in practice in a near-field plot with the aim of making an antenna diagnostics. Is the spectral region where the spectrum is different from zero the only factor that determines when two close sources can be distinguished?
To investigate this issue, we consider an array of three y-oriented electric Hertzian dipoles displaced on the xy-plane and separated by a distance d from each other, according to Fig. 3.4. By exciting each dipole with a dipole moment P, the PWS of the array is computed through (2.39) on the entire $[-5k, 5k]$ $k_x k_y$-domain. The

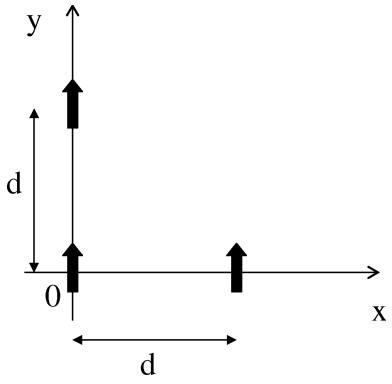

Figure 3.4: Three y-oriented Hertzian dipoles at a distance d from each other.

PWS is then gradually reduced in spectral extent until reaching the visible region, while maintaining the $[-5k, 5k]$ domain, thus zero-padding the remaining domain. The radiated field is finally computed on different z-planes analytically and by inverse Fourier transforming the spectrum with (3.4). While the sampling interval in the near-field plots is always given by $\Delta x = \Delta y = \lambda/10$, resolution varies according to the part of the PWS which is different from zero, i.e., from the value of $\lambda/10$ when the PWS is non-zero on $[-5k, 5k]$ to the value of $\lambda/2$ when the PWS is non-zero only on the visible region. By varying the distance d according to $d = 2\lambda, \lambda, 3/4\lambda, \lambda/2$, we can understand if what resolution in theory ensures is what in practice happens. To make the investigation as accurate as possible, no interpolation in the plots is performed.
First, by looking at the cartesian components of the analytical field in dB on different z-planes, we note that for $d = \lambda, 3/4\lambda, \lambda/2$ the single dipoles can be distinguished only on $z = 0.1\lambda$, since for larger z's the radiation from the dipoles becomes broader preventing the reconstruction of the three sources, see Figs. 3.5-3.6. For $d = 2\lambda$ the dipoles are distinguishable until $z = 0.4\lambda$.
Second, pictures can be more clear, i.e., the contrast is higher and the single dipoles are better identified, when the linear scale is used, or when the color scale is properly adjusted, see Fig. 3.6, in particular Fig. 3.6(a).

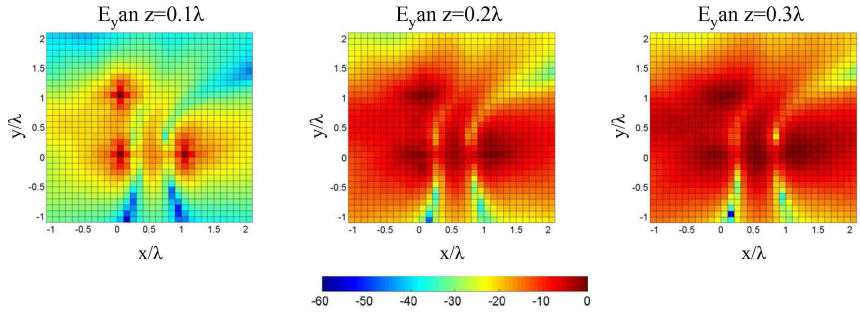

Figure 3.5: Amplitude of E_y analytical in dB scale on different z-planes for the dipole configuration of Fig. 3.4, with $d = \lambda$, and a spatial interval of $\Delta x = \Delta y = \lambda/10$.

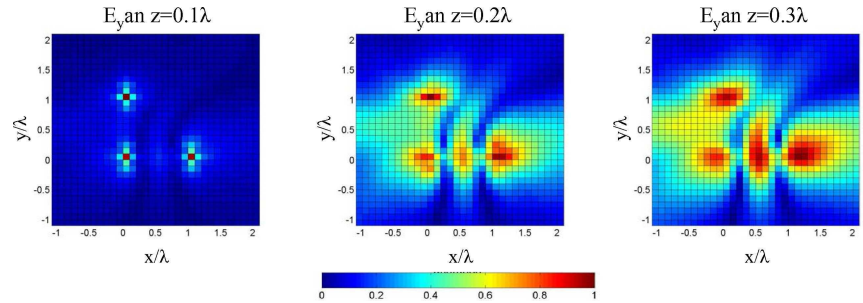

Figure 3.6: Amplitude of E_y analytical in linear scale on different z-planes for the dipole configuration of Fig. 3.4, with $d = \lambda$, and a spatial interval of $\Delta x = \Delta y = \lambda/10$.

On the $z = 0.1\lambda$ plane and for every d, the analytical field is thus compared with the field obtained through (3.4) by varying the region where the PWS is different from zero, see Figs. 3.7-3.9. We note that while the use of non-zero values of the PWS on the entire $[-5k, 5k]$ domain provides field results in very good agreement with the analytical for every value of d, the accuracy clearly diminishes when a smaller region of the PWS is considered. In particular, when the PWS is non-zero only on the visible region, though the resolution is in principle equal to $\lambda/2$, the three dipoles are clearly distinguished only for $d = 2\lambda$, see Fig. 3.7. Though the field provided by the visible region of the PWS gives the correct position of the dipoles on the xy-plane, the field distribution is generally wider than the analytical, and the radiation from the single dipoles overlaps earlier than expected. For $d = \lambda$ the sources are distinguished on the horizontal axis, but not on the vertical axis, Fig. 3.8, while for $d = \lambda/2$ the dipoles can not be resolved, see Fig. 3.9. It is noted that the three dipoles are however better distinguished in the y-component than in the x-component.
This leads us to the conclusion that resolution perceived by the human eye in observing a near-field plot can not be defined by a specific formula and it might be

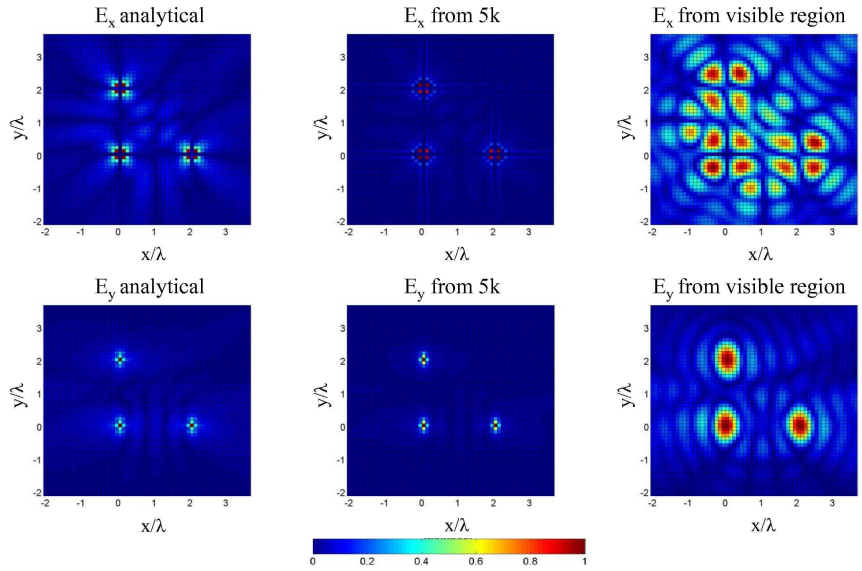

Figure 3.7: Amplitude of E_x and E_y in linear scale on the $z = 0.1\lambda$ plane for the dipole configuration of Fig. 3.4, with $d = 2\lambda$, and a spatial interval of $\Delta x = \Delta y = \lambda/10$.

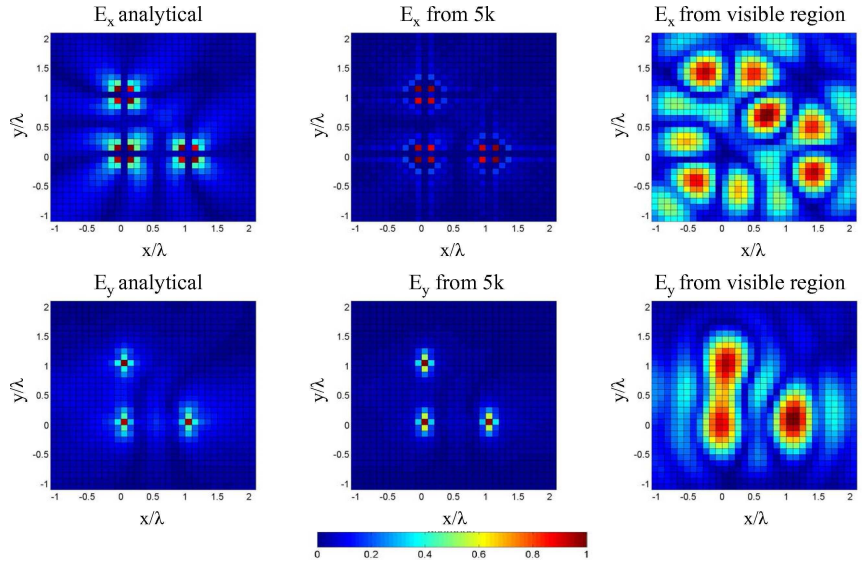

Figure 3.8: Amplitude of E_x and E_y in linear scale on the $z = 0.1\lambda$ plane for the dipole configuration of Fig. 3.4, with $d = \lambda$, and a spatial interval of $\Delta x = \Delta y = \lambda/10$.

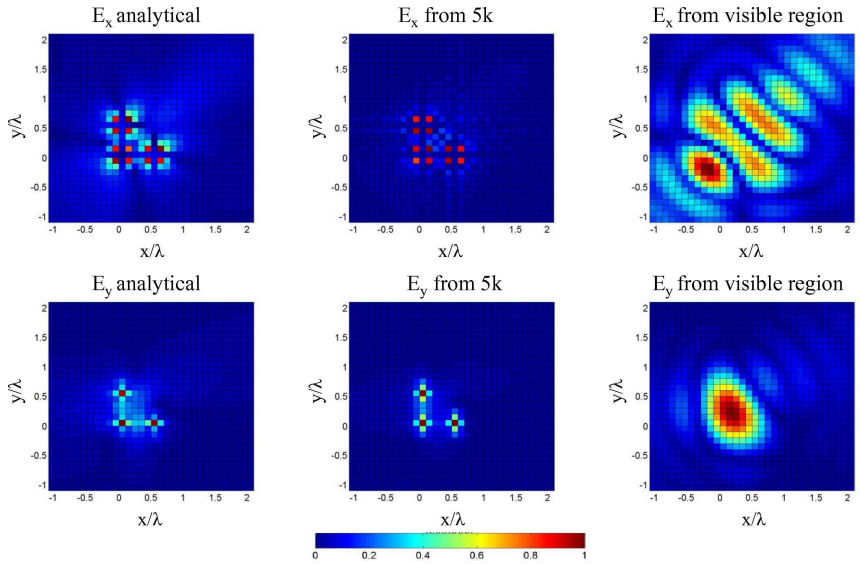

Figure 3.9: Amplitude of E_x and E_y in linear scale on the $z = 0.1\lambda$ plane for the dipole configuration of Fig. 3.4, with $d = \lambda/2$, and a spatial interval of $\Delta x = \Delta y = \lambda/10$.

lower than the expected one, since even at very short distances from the aperture the electromagnetic field is not a point function but has a spatial extent. While the perception of the eye can be improved by choosing between a dB scale or a linear scale, and by properly setting the color scale in order to highlight certain differences and increase the contrast, the nature of the electromagnetic field radiated by the sources influences what the eye perceives. In particular it was noted that what the eye distinguishes generally depends on the polarization of the source, the z-plane of interest, and the component of the field.

3.4 Numerical test case

To validate the SWE-to-PWE transformation and the above theoretical considerations, we now consider a test case constituted by an array of five x-oriented electric Hertzian dipoles on the xy-plane, four equally displaced from the origin with a distance $d = r_o = 2\lambda$ and one at the center, see Fig. 3.10. There are several factors that motivate the choice of such a configuration. First, since any source distribution can in principle be constructed from a combination of properly positioned, oriented, and excited Hertzian dipoles, the present case can be considered a general example of an electrically small antenna. Second, as it will be seen in (3.8)-(3.9), the array of electric Hertzian dipoles possesses an infinite SWE, which thus allows us to study the truncation of (2.48) to finite N-values. Third, an exact PWS which provides the necessary reference to investigate such a truncation can be derived from the dipole excitations, see (2.39). Fourth, the

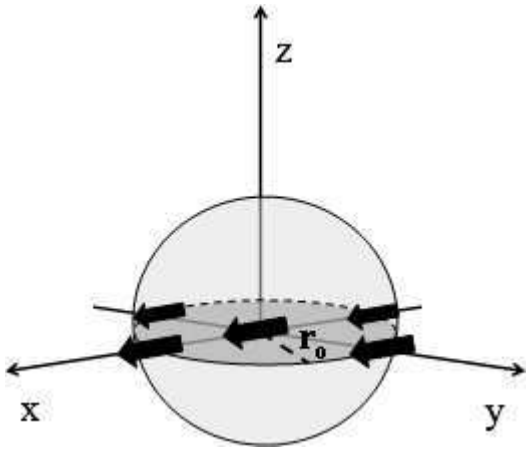

Figure 3.10: Five x-oriented electric Hertzian dipoles displaced on the xy-plane with minimum sphere of radius r_o.

analytical expression of the radiated field is known and can be used as a reference. It is finally noted that since the array is located on the xy-plane, its PWE is valid for $z > 0$, while its SWE is valid for $r > r_o$. Though the present section is mostly based on the first test case of Paper III, other source configurations can be found in the second part of Paper III and in Paper I, showing all the same qualitative properties.
We can thus start by writing the reference PWS in cartesian components as given by (2.39)

$$T_{refx} = \frac{P}{2\pi k}\sqrt{\frac{1}{\eta}}\Big(\cos(k_x r_o) + \cos(k_y r_o) + \frac{1}{2}\Big)\frac{k_x^2 - k^2}{k_z} \tag{3.5}$$

$$T_{refy} = \frac{P}{2\pi k}\sqrt{\frac{1}{\eta}}\Big(\cos(k_x r_o) + \cos(k_y r_o) + \frac{1}{2}\Big)\frac{k_x k_y}{k_z} \tag{3.6}$$

$$T_{refz} = \frac{P}{2\pi k}\sqrt{\frac{1}{\eta}}\Big(\cos(k_x r_o) + \cos(k_y r_o) + \frac{1}{2}\Big)k_x \tag{3.7}$$

with P being the dipole moment and η the admittance of the free-space. It can be seen that T_{refx} and T_{refy} show the singularity $1/k_z$.
The Q coefficients are then calculated analytically from the results contained in Appendix A1 of [26], for the case of a sampled x-polarized planar current ring on the xy-plane, obtaining

$$Q_{1mn} = \frac{ikP4}{\sqrt{8\pi n(n+1)\eta}}\Big(-\frac{m}{|m|}\Big)^m j_n(kr_o)\frac{d\bar{P}_n^{|m|}(\cos\theta)}{d\theta}\Big|_{\theta=\pi/2}(\delta_{m1}^4 - \delta_{m-1}^4) \tag{3.8}$$

$$Q_{2mn} = -\frac{kP4}{\sqrt{8\pi n(n+1)\eta}}\Big(-\frac{m}{|m|}\Big)^m\Big[\frac{n(n+1)}{kr_o}j_n(kr_o)\bar{P}_n^{|m|}(\cos\theta)\Big|_{\theta=\pi/2} \tag{3.9}$$

$$(\delta^4_{m1}+\delta^4_{m-1})+\frac{1}{kr}\frac{d}{d(kr)}(krj_n(kr))\Big|_{kr=kr_o}\frac{m\bar{P}_n^{|m|}(\cos\theta)}{\sin\theta}\Big|_{\theta=\pi/2}(\delta^4_{m1}-\delta^4_{m-1})\Big]$$

where

$$\delta^4_{m\mu}=\begin{cases}1 & \text{if} \quad \bmod(m-\mu,4)=0\\ 0 & \text{otherwise}\end{cases} \tag{3.10}$$

and thus containing arbitrarily high-order modes in n and m.
The spectral components are then computed with (2.48) for different truncation values N and compared to the reference spectrum of (3.5)-(3.7) on the $[-2k,2k]$ k_xk_y-domain. The results for $N=kr_o=12$, $N=kr_o+10=22$ and $N=kr_o+40=52$ are shown in dB in Fig. 3.11 for the x-component on the $z=0.2\lambda$ plane, normalized to the value of T_{refx} at the origin. We notice that the region where the spectrum reaches convergence in the k_xk_y-domain increases gradually with increasing N. For $N=kr_o$ the visible region is still not completely reconstructed but the convergence is reached with $N=kr_o+10$. For $N>kr_o+10$ only changes in the invisible region are noted until the complete picture is obtained by $N=kr_o+40=52$. The singularity for $k_z=0$ is perfectly identified already by $N=kr_o+10$. The convergence mechanism can also be understood by considering the n-mode power spectrum of Fig. 3.12. Extremely low values of power, and thus of Q coefficients, are contained in the high order n-modes, but, due to these low values, the product with the diverging spherical vector wave functions is kept finite, providing the necessary terms for the series of (2.48) to reach convergence. A plot of the x-component of the spectrum in function of N for different points of the spectral domain is given in Fig. 3.13. Points belonging to the visible region reach convergence with $N=kr_o+10$ (blue and red lines), while additional N terms are needed for points in the invisible region ($N=38$ for the green line and $N=50$ for the black line). It is interesting to note that though the amplitude of T_x reaches, in points belonging to the invisible region, very high values for intermediate values of N, in some cases even larger than 80 dB, it finally converges to much lower values, close to -18 dB.
We can then inverse Fourier transform the PWS by use of singularity extraction technique of (3.4) and compare the result with the analytical field. To understand the influence of the invisible region, we consider the spectrum computed with $N=kr_o$, $N=kr_o+10$ and $N=kr_o+40$. Only the part of the spectrum where convergence has been reached is used in these cases, while the remaining part is replaced by zeros. Since the spectral domain has an extent of $[-2k,2k]$, the sampling interval in the xy-domain is equal to $\lambda/4$, while resolution depends on the extent of the PWS where convergence has been reached. Results are shown in Fig. 3.14 for the x-component on $z=0.2\lambda$. Figures are normalized to the value on axis of the analytical field and plotted in linear scale: we can distinguish the five dipoles on the xy-plane in all pictures. However the result provided by $N=kr_o$ is not quantitatively satisfactory in determining the dipoles contribution. On the other hand, already with $N=kr_o+10$ an accurate aperture field is computed. This probably indicates that the most important part of the spectrum to be recovered is constituted by the visible region, the border at $k_z=0$, and a little part of the invisible region.

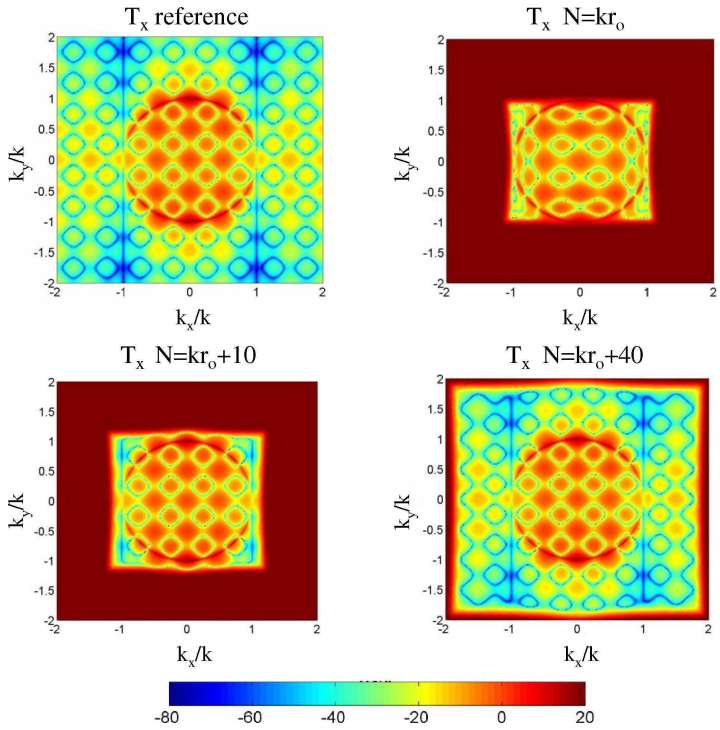

Figure 3.11: Amplitude of the x-component of the PWS of the five dipoles with $r_o = 2\lambda$, on $z = 0.2\lambda$ in dB: the reference T_{refx} and the ones from (2.48) with $N = kr_o$, $N = kr_o + 10$ and $N = kr_o + 40$.

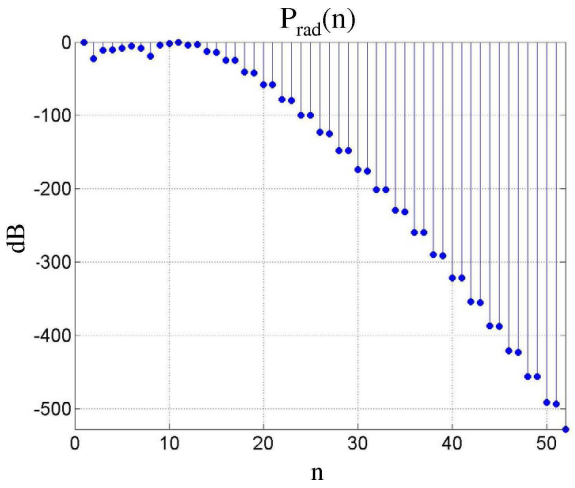

Figure 3.12: Power spectrum for the five dipoles configuration.

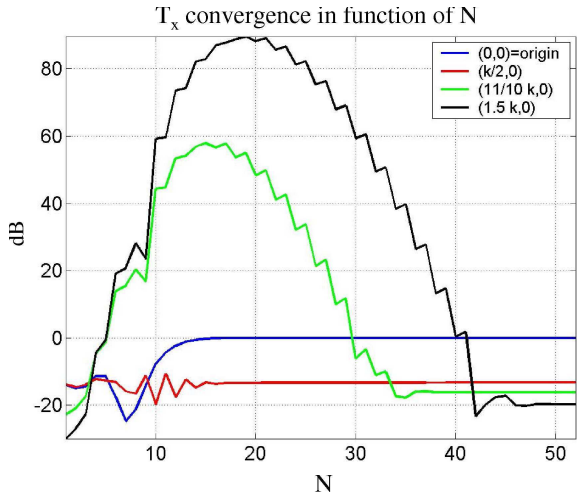

Figure 3.13: Amplitude of the x-component of the PWS of the five dipoles with $r_o = 2\lambda$, on $z = 0.2\lambda$ in dB, in function of N, for different points of the spectral domain.

3.5 Influence of finite measurement accuracy

While so far we have described the fundamental properties of the SWE-to-PWE transformation and the necessary steps to calculate the extreme near-field from the PWS, we now need to investigate how non-ideal measurements aspects influence the SWE-to-PWE diagnostics technique. In order to isolate and control different measurement inaccuracies, the investigation is based on simulations. A model of a Standard Gain Horn (SGH) is first developed by use of electric and magnetic Hertzian dipoles. The near-field radiated by the SGH is computed analytically on a sphere of radius 10 λ, and different measurement electrical inaccuracies are then added to it. From the field distribution on the sphere, the Q coefficients of the SWE are obtained. This allows one to calculate the plane spectrum with (2.48). The extreme near-field is finally computed from the PWS with the singularity extraction technique of (3.4). The present discussion is based on Paper IV, where additional results can also be found.

The antenna model represents a pyramidal horn working at $f = 3$ GHz with an aperture of $a = 4\lambda$ and $b = 3\lambda$ located on the xy-plane, and with the lengths of the flared section in the xz- and yz-planes being $R_2 = R_1 = 5\lambda$ respectively, see Fig. 3.15. The horn is excited by a rectangular waveguide in which the y-polarized TE10 mode is dominant and has amplitude 1. In addition, the x-polarized TE01 mode is present and excited by $C = 10^{-2}e^{-i\pi/4}$, to provide a typical cross-polar component in the radiated far-field. From the equivalence theorem, the equivalent magnetic co-polar currents are computed from the electric field given by the mode

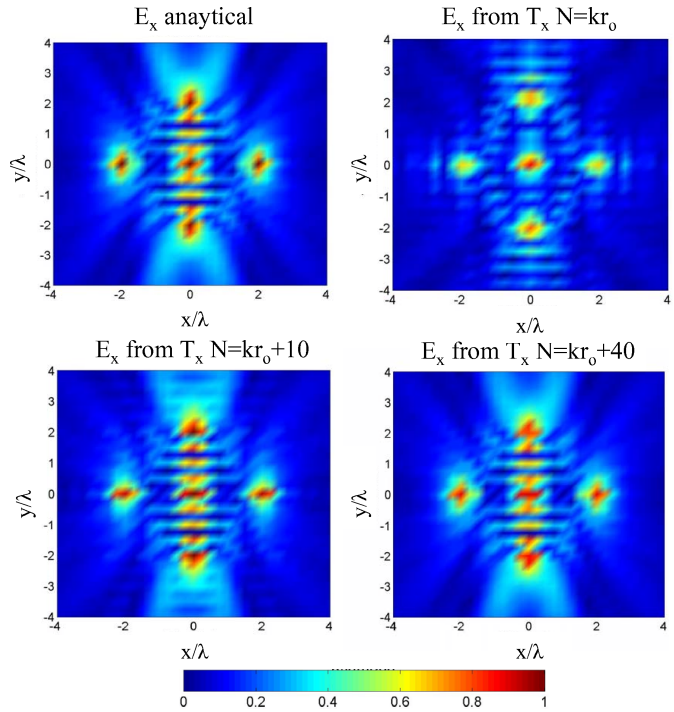

Figure 3.14: Amplitude of the x-component of the field of the five dipoles for $r_o = 2\lambda$, on $z = 0.2\lambda$ in linear scale: the analytical and the ones obtained from (3.4) with $N = kr_o$, $N = kr_o + 10$ and $N = kr_o + 40$.

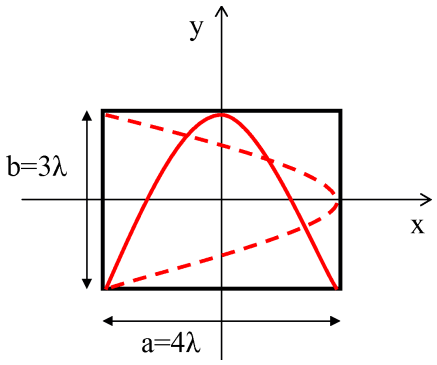

Figure 3.15: Aperture of the SGH model excited by the TE10 and TE01 modes, and the reference coordinate system.

TE10 on the aperture of the horn,

$$\vec{M}_{co} = \cos\left(\frac{\pi x}{a}\right) e^{i\frac{k}{2}(x^2/R_1 + y^2/R_2)}\hat{x} \tag{3.11}$$

where a quadratic phase variation is assumed over the aperture, while the electric are computed from the magnetic imposing a Huygens source dependence

$$\vec{J}_{co} = -\eta \cos\left(\frac{\pi x}{a}\right) e^{i\frac{k}{2}(x^2/R_1 + y^2/R_2)} \hat{y} \tag{3.12}$$

with $x \in [-a/2, a/2]$ and $y \in [-b/2, b/2]$. The cross-polar equivalent currents are computed from the electric field given by the mode TE01 and are equal to

$$\vec{M}_{cro} = -C \cos\left(\frac{\pi y}{b}\right) e^{i\frac{k}{2}(x^2/R_1 + y^2/R_2)} \hat{y} \tag{3.13}$$

$$\vec{J}_{cro} = -C\eta \cos\left(\frac{\pi y}{b}\right) e^{i\frac{k}{2}(x^2/R_1 + y^2/R_2)} \hat{x} \tag{3.14}$$

The current distributions of (3.11)-(3.14) are then sampled every $\lambda/4$ on the SGH aperture providing the excitations of a set of electric and magnetic Hertzian dipoles located on the sampling points. The field radiated by this set of dipoles is then calculated and the directivity is found, see Fig. 3.16, providing a typical SGH

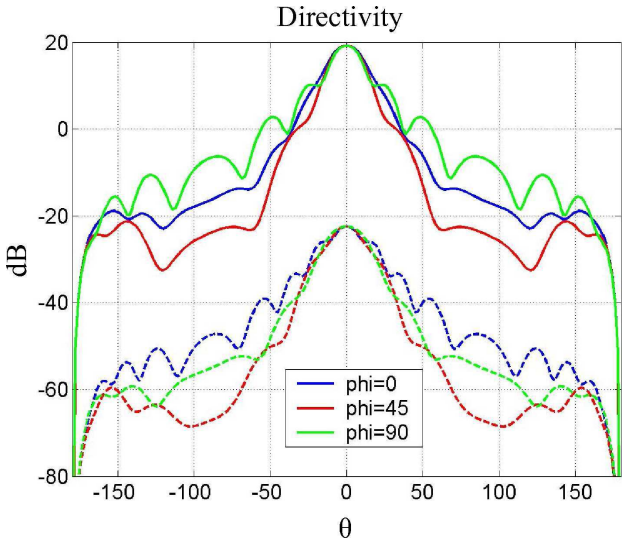

Figure 3.16: Directivity of the SGH model, co-polar (continuous lines), cross-polar (dashed lines).

pattern both in the co-polar as well as in the cross-polar components, according to Ludwig's 3rd definition [26],

$$\hat{i}_{co} = \hat{\theta}\cos(\phi - \phi_o) - \hat{\phi}\sin(\phi - \phi_o) \qquad 0 \le \theta < \pi \tag{3.15}$$

$$\hat{i}_{cro} = \hat{\theta}\sin(\phi - \phi_o) + \hat{\phi}\cos(\phi - \phi_o)$$

with $\phi_o = \pi/2$.

Several sources of errors affect a spherical near-field measurement. These are generally divided into the two general categories of mechanical inaccuracies and electrical inaccuracies, see for an extensive discussion [26]. Examples of the first category are errors in the axes intersection, antenna tower pointing and measurement distance. They are closely related to the precision of the mechanical alignment performed before a measurement. If present, they introduce errors in the measured field, and thus in the obtained SWE. The second category is normally considered as arising in the receiver only. Their effect is of introducing errors in the SWE and, most importantly, of limiting the dynamic range of the measured field. It was decided to study only the effect of electrical inaccuracies on the SWE-to-PWE diagnostics technique, assuming that a good mechanical alignment was performed in the first place.
Drift and noise, in amplitude and in phase, have been chosen to represent the most frequent and important measurement electrical inaccuracies. Drift during a spherical scan was modeled as a linear function of the time t given by $drift_{error} = d \cdot t/T$, with d being the value of the drift, see Tab. 3.1 in amplitude or in phase, and T the duration of a scan, set equal to 3 hours. Noise was considered random and uniformly distributed. By indicating with $X = |X|e^{i\angle X}$ the θ- and ϕ-components of the field radiated by the SGH on the sphere with radius $r = 10\lambda$ with respect to the origin of the measurement coordinate system, we thus obtain

$$X_{tot} = (|X|(1 + drift_{error}))e^{i\angle X} \tag{3.16}$$

when the field is affected by amplitude drift,

$$X_{tot} = |X|e^{i\angle X(1+drift_{error})} \tag{3.17}$$

when the field is affected by phase drift,

$$X_{tot} = (|X| + noise_{error})e^{i\angle X} \tag{3.18}$$

when the field is affected by amplitude noise,

$$X_{tot} = |X|e^{i(\angle X+noise_{error})} \tag{3.19}$$

when the field is affected by phase noise, with $noise_{error}$ being the value of the noise, in amplitude or phase, of Tab. 3.1. The Q coefficients were then computed from the field of the SGH on the sphere with radius $r = 10\lambda$, with and without

Amplitude drift	-0.015 dB
Amplitude noise	-60 dB
Phase drift	0.25 deg
Phase noise	0.15 deg

Table 3.1: Values of measurement electrical inaccuracies for a frequency of 3 GHz and a scan speed of 3 deg/sec.

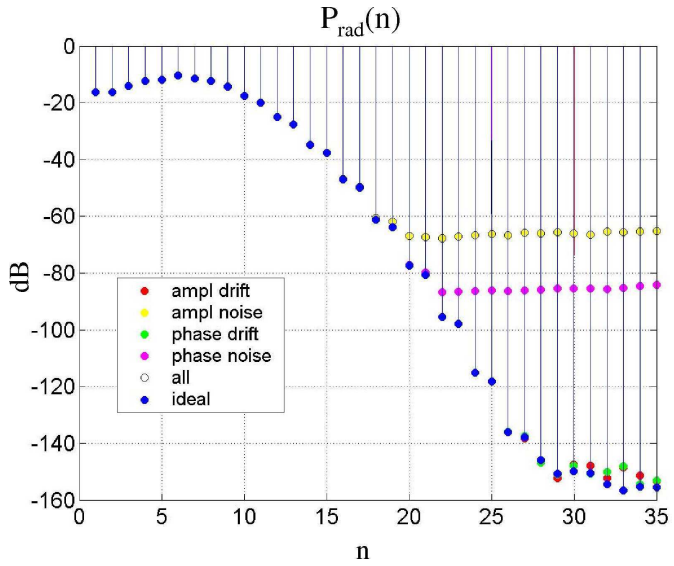

Figure 3.17: SGH power spectrum for different electrical inaccuracies and for the ideal case.

electrical inaccuracies, by the software SNIFTD [32], and the power spectrum was found, according to (2.14), see Fig. 3.17. The plot shows that the major and most evident effect given by the considered electrical inaccuracies is a truncation of the available n-modes. Among all truncations, the most limiting, $N = 18 = kr_o + 3$, is given by the presence of amplitude noise, see the yellow dots, where its value of -60 dB also coincides with the noise floor observed in the power spectrum. It can be noted that numerical noise anyway affects the computation, limiting the n-modes to $N = 28 = kr_o + 13$, as it is seen for the ideal case. Since all types of measurement errors manifest themselves as a constant level of the power spectrum after a certain mode number, it was decided to continue the investigation with the amplitude noise alone, and then investigate different values of this.

The PWS is then computed through (2.48) by using the Q coefficients obtained from the case with amplitude noise equal to -60 dB. The truncation in n is set equal to $N = 18$, and a plane equal to $z = 0.2\lambda$ is selected. The y- and z- components are shown in Fig. 3.18 in dB scale with the values normalized to T_y at the origin, and compared to the ones calculated through the ideal case with a truncation value of $N = 28$. In both cases the visible region is recovered, and the singularity for $k_z = 0$ is identified. The spectral region where convergence was not reached yet is clearly indicated by the dark red zone, corresponding to values equal to or larger than 20 dB. The extra ten n-modes, which are given by an improvement of 80 dB in the dynamic range for the ideal case, allow the reconstruction of a small part of the invisible region with radius $1.1k$, which is reduced for the noisy case to a radius of $1.03k$. The invisible region of the spectrum where convergence was

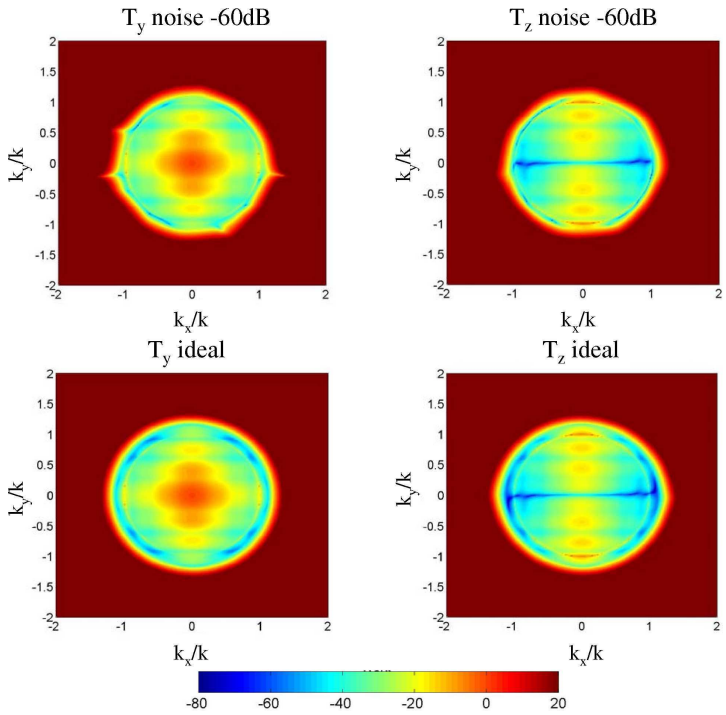

Figure 3.18: Amplitude of T_y and T_z on $z = 0.2\lambda$, for the SGH with a noise amplitude of -60dB (upper) and for the ideal case (lower).

not reached is then replaced by zeros and the entire spectrum is finally inverse Fourier transformed with the singularity extraction technique of (3.4), see Fig. 3.19. Fields are in dB scale and normalized to the value of E_y at the origin when affected by amplitude noise. They are compared to the components given by the

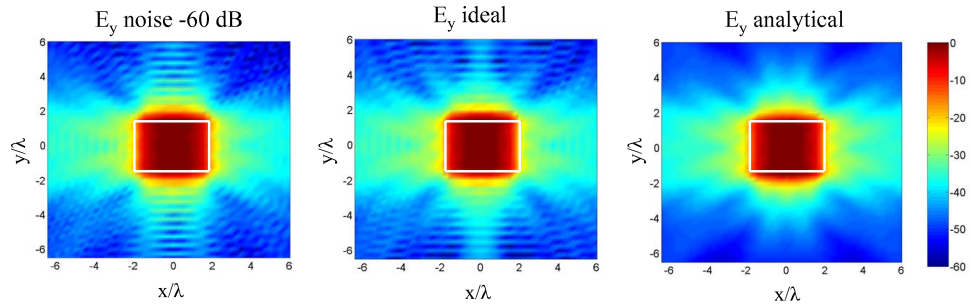

Figure 3.19: Amplitude of E_y on $z = 0.2\lambda$, for the SGH with a noise amplitude of -60dB (left), for the ideal case (middle) and for the analytical case (right).

ideal case, and to the ones provided by the superposition of the analytical dipole contribution. In white the aperture dimension of the SGH is indicated. The results

affected by amplitude noise are satisfactory and in good agreement with the ideal and the analytical ones, both for the y- as well as for the z-component. Very accurate results are provided by the ideal case, where the convergent region has a radius of $1.1k$. We can again conclude that the recovery of the border for $k_z = 0$ and of small part of the invisible region are important and essential to accurately reconstruct the aperture field.

3.6 Summary

The additional steps necessary to obtain the antenna extreme near-field once the PWS is computed from a spherical near-field measurement were addressed. First, the fundamental properties of the SWE-to-PWE transformation were studied, underlying their theoretical as well as practical implications for the antenna diagnostics technique. In particular, it was shown that the infinite series of (2.48) can be truncated at a finite value N, but, while the traditional $N = kr_o + 10$ is sufficient to reach convergence in the visible region, a larger N is necessary in the invisible region. Second, the computation of the aperture field from a singular PWS was discussed, presenting a singularity extraction technique that takes advantage of the IFFT algorithm and the Weyl identity. Third, the concept of resolution and sampling interval were defined. It was noted that resolution perceived by the human eye can be lower than the expected one, and generally depends on the polarization of the source, the z-plane of interest, and the component of the field.
The developed SWE-to-PWE antenna diagnostics technique was then applied to an array of electric Hertzian dipoles in ideal conditions, and to the model of a SGH where the presence of electrical measurement inaccuracies was simulated. It was found that measurement inaccuracy, and in particular amplitude noise, truncate the available n-modes and thus the measured Q coefficients. The truncation of the available n-modes limits the spectral region where the PWS reaches convergence. However, it was shown that, for a SGH under typical measurement conditions, the available Q coefficients were sufficient to reconstruct the visible region of the PWS, the border for $k_z = 0$, and a small part of the invisible region, providing accurate results in the computed aperture field.

We can thus summarize the steps of the SWE-to-PWE antenna diagnostics technique as follows:

1. Obtain the Q coefficients of the SWE from a spherical near-field measurement.

2. Find, from a plot of the power spectrum or an analysis of the values of the Q coefficients, the available n- and m-modes and thus the truncation values N and M.

3. Choose a certain $k_x k_y$-spectral domain according to the desired sampling interval, see Section 3.3.

4. Calculate the plane wave spectrum $\vec{T}(k_x, k_y, z)$ with (2.47) and (2.48) in the

visible and invisible regions, on the z-plane of interest or on a larger z-plane as determined by the guidelines of Appendix C.3.

5. Back-propagate, if necessary, the PWS on the desired z-plane suitable for diagnostics, see Appendix C.3.

6. Replace with zero the region where the spectrum has not reached convergence, and if necessary zeropad the spectrum to a larger $k_x k_y$-domain.

7. Compute the extreme-near field with the singularity extraction technique of (3.4) where $\vec{T}_1 = \vec{T} \cdot k_z$, see Section 3.2.

8. Analyze the extreme-near field in cartesian components, or a combination of these, in amplitude and phase. If necessary, rotate the coordinate system, calculate the corresponding new set of Q coefficients, and repeat steps 1-8.

Chapter 4

Experimental validation

The SWE-to-PWE antenna diagnostics technique presented in the previous chapters is now verified by two experimental test cases employing real measurements data. Section 4.1 deals with an offset reflector antenna while Section 4.2 presents a real diagnostics case. In particular, Section 4.1.1 summarizes the results of a preliminary investigation on the effects of typical mechanical errors on the far-field of a general offset reflector antenna. The three most interesting errors studied in Section 4.1.1 are then used in Section 4.1.2, where a commercially available TRIAX TD64 offset reflector antenna is considered. The selected mechanical errors are intentionally introduced in the TRIAX antenna and the ability and accuracy of the diagnostics technique to identify them are tested. Section 4.2 deals with the antenna system of the Microwave Imaging Radiometer using Aperture Synthesis (MIRAS) for ESA's Soil Moisture and Ocean Salinity (SMOS) mission. The diagnostics technique is used to identify the sources of the anomalies detected in 2 of 138 MIRAS antenna far-field patterns, that were measured during the on-ground calibration at the DTU-ESA Spherical Near-Field Antenna Test Facility in 2006. Finally, in Section 4.2.1 a brief review of the most used windowing techniques is provided and their application to the MIRAS units is described, to limit the truncation error observed in the extreme near-field. Some of the results presented in this chapter are contained in Paper V and VI. Additional information and plots can be found in Appendix A and B.

4.1 Offset reflector test case

4.1.1 Effects of mechanical errors on the far-field

Before the measurements of the TRIAX antenna could take place, a preliminary parametric investigation was conducted to analyze the effects of typical mechanical errors on the far-field of a reflector antenna, and identify the three most significant and interesting to be used in the TRIAX experimental test case. Tilts and defocusing of the feed, and several surface distortions were taken into account. From that, three errors were selected and used in the TRIAX experimental test case de-

scribed in Section 4.1.2. Though some interesting observations can be found in the literature, Rusch [48] and Olver and Syed [49], about the effect of a feed defocusing and a surface distortion, it was decided to base the study on simulations, to isolate the various errors and consider different values of them. The software GRASP9 was used to build the model of a generic reflector, simulate the mechanical errors and compute the radiated far-field.
The antenna model consists of a 15 GHz ($\lambda = 2$ cm) offset parabolic reflector, defined in the xyz-coordinate system (CS) of Fig. 4.1 by a circular projected aperture of diameter $D = 24$ cm, a focal length $f = 19.2$ cm and a clearance $d' = 7.2$ cm. The feed is modeled by a Gaussian beam with -12dB taper and $\pm 28°$ taper angle, and it is linearly polarized along x_f, where $x_f y_f z_f$ is the feed CS, with its origin at the focus and with z_f pointing towards the center point of the reflector. The radiated far-field is computed in the cut CS, $x_{cut} y_{cut} z_{cut}$, with origin at the center of the reflector surface, and axis parallel to the ones of the xyz CS. It is noted that z_{cut} coincides with the direction of the main beam of the reflector and that the feed is perfectly linearly polarized along x_f. Since in principle an offset

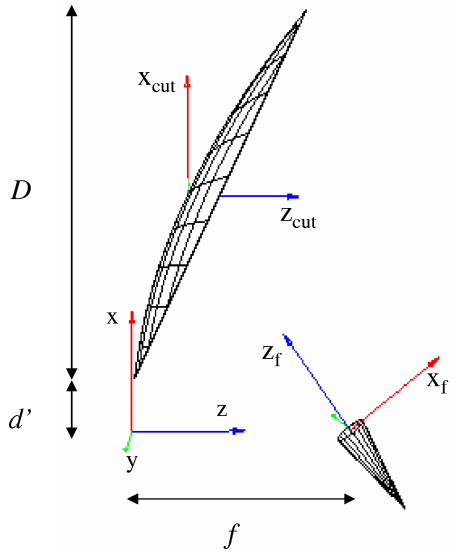

Figure 4.1: Model of the offset reflector, geometry and coordinate systems.

reflector avoids blockage, it was decided to neglect in the simulations the arm supporting the feed. In the analysis, Physical Optics (PO) and Physical Theory of Diffraction (PTD) were used.
First, three different tilts of the feed were taken into account: the feed was tilted around each of the three axis which identify the feed CS. Each tilt had the value of $\pm 1°$, $\pm 3°$, $\pm 5°$ and $\pm 10°$. While under ideal conditions the polarization of the electric field radiated by the feed, and impinging on the reflector, is parallel to the xz plane, which coincides with the plane of incidence, the insertion of a feed tilt modifies the configuration. In particular, a tilt of the feed around x_f introduces

spillover, since the feed does not point towards the center of the reflector, and changes the plane of incidence, while the polarization of the feed remains parallel to the xz-plane. A tilt around y_f provides only spillover, while a tilt around z_f changes the direction of polarization of the feed, keeps the plane of incidence coinciding with xz and does not introduce spillover. It was noted that the effect of the spillover could be noticed in the θ-component of the radiated field in the $\phi = 0°$ cut by a slightly lower main lobe and higher side-lobes than in the ideal case, while a non parallel incidence of the electric field radiated from the feed could be seen in the ϕ-component in the $\phi = 0°$ cut, already for small values of feed tilt, see Fig. 4.2.

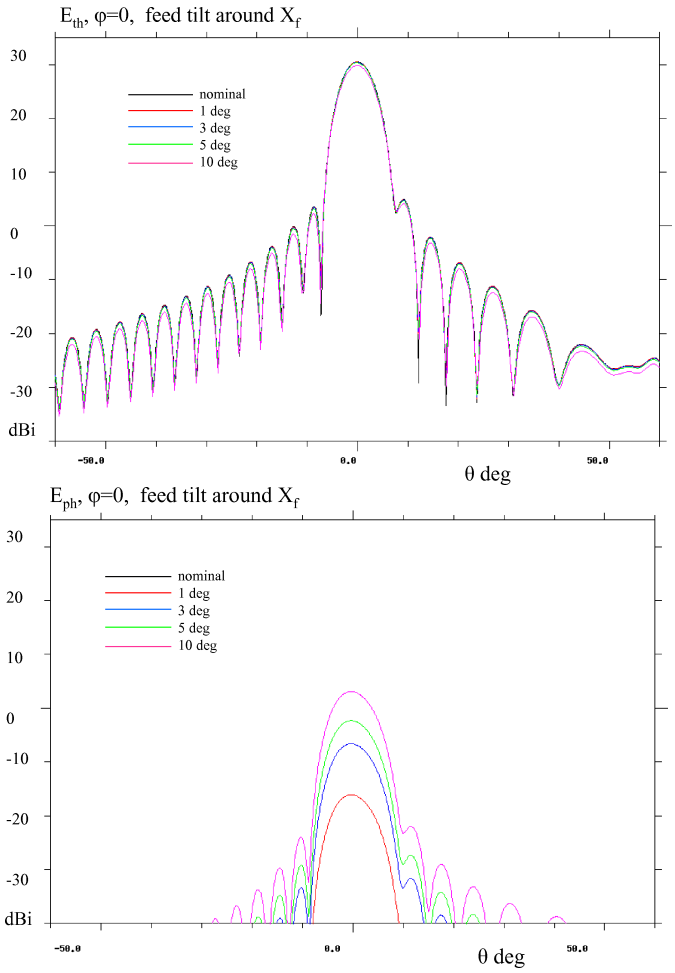

Figure 4.2: Amplitude of the θ- and ϕ-components, upper and lower respectively, in the cut $\phi = 0°$, of the reflector far-field for a tilt of the feed around x_f.

Next, a defocusing of the feed was considered. The feed was moved along the three

axis of the feed CS, by a distance of ±1 mm, ±3 mm and ±5 mm. A squint of the main beam was observed at $\phi = 0°$ for the θ-component and at $\phi = 90°$ for the θ- and ϕ-components, for a defocusing along x_f and y_f respectively, see Fig. 4.3. While these were effects easily recognizable, a defocusing along z_f did not show substantial variations in the far-field, when compared to the ideal case. It was however reported by [49] that a defocused distance along z_f of the order of λ causes a broadening of the main beam, with corresponding reduction of the gain, and modifications in the nulls of the radiation pattern.

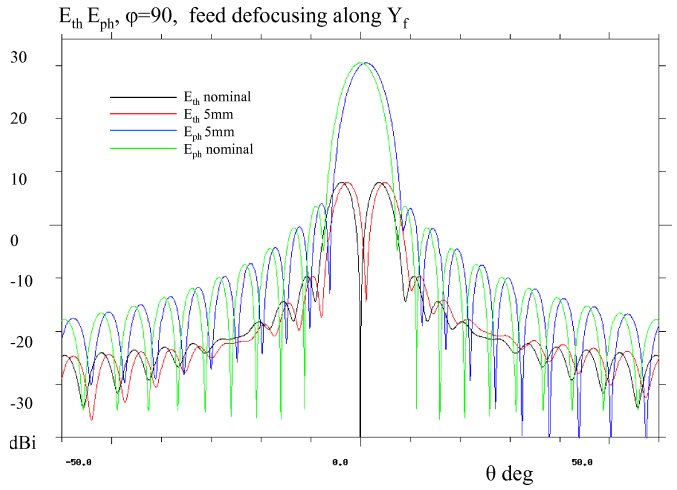

Figure 4.3: Amplitude of the θ- and ϕ-components, in the cut $\phi = 90°$, of the reflector far-field for a feed defocusing along y_f.

Later, different surface distortions were studied. A single and localized bump attached on the reflector was modeled like a Gaussian function, with peak of 1 cm and standard deviation σ equal to 0.5 cm and 1 cm. It was seen that in the two planes $\phi = 0°$ and $\phi = 90°$ the main beam almost coincided with the ideal case, except for a slightly lower peak, while sidelobes were definitely higher, see Fig. 4.4. The effects were more evident when the bump was located along, or close to, the axis of symmetry of the reflector. The ϕ-component which arises at $\phi = 0°$ is now broad and very different from the one noticed for the feed tilt case of Fig. 4.2. For a fixed peak and position of the bump on the reflector surface, a larger sigma provides higher sidelobes, but almost does not affect the main lobe, see Fig. 4.4 (lower).
Finally, a slow and a fast surface distortion were modeled by adding to the z-coordinates of the reflector surface a random error uniformly distributed between the values of $\pm 0.05\lambda = 1$ mm and $\pm 0.1\lambda = 2$ mm, see Fig. 4.5. The random error was defined on the nodes of a rectangular grid equi-spaced located on the xy-plane and including the entire circular reflector rim. Between the nodes, a cubic interpolation was used. A slow surface distortion is supposed to represent distortions given by thermal variations, a fast surface distortion is thought to model man-

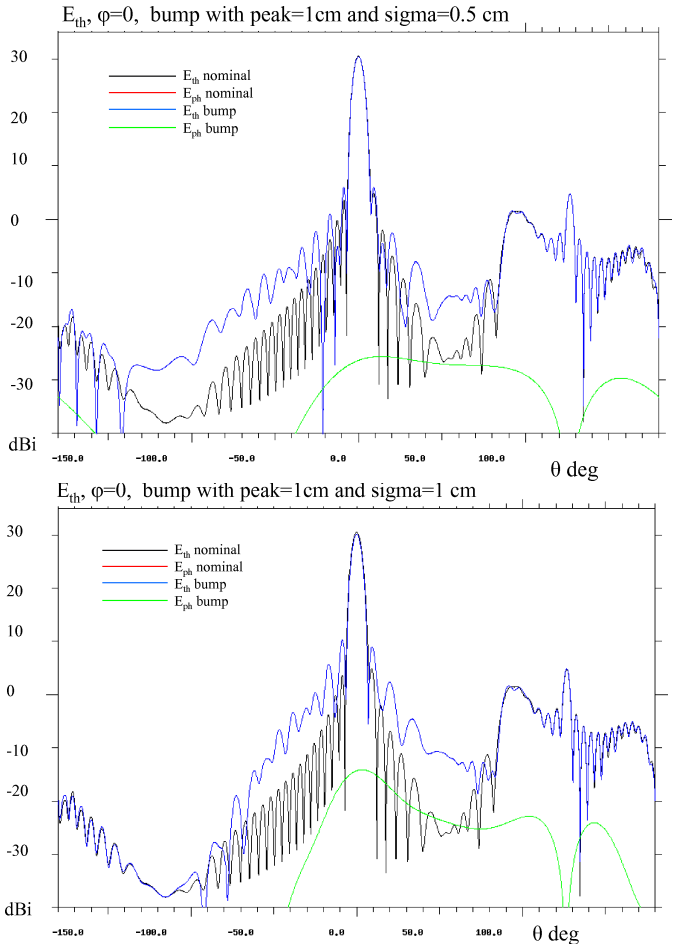

Figure 4.4: Amplitude of the θ-component, in the cut $\phi = 0°$, of the reflector far-field with a localized bump at $x = 19$ cm and $y =$ -5 cm with peak $= 1$ cm and $\sigma = 0.5$ cm (upper), and peak $= 1$ cm and $\sigma = 1$ cm (lower).

ufacturing tolerances. A total number of nodes, equal to 25 and 625, was used to model the slow and fast distortion, respectively. It was observed that a slow surface distortion does not change the width of the main lobe considerably, but it reduces its peak. It also provides values of the first two sidelobes considerably higher than the ideal ones, but it does not affect the remaining ones, see Fig. 4.6 (upper). A fast surface distortion generally modifies in a similar way the main beam, but affects considerably all sidelobes, see Fig. 4.6 (lower). The effects of a distributed surface distortion are thus similar to the ones given by a localized bump.

It can be concluded that, while a defocusing of the feed can be immediately identified by a beamsquint of the far-field pattern, the other mechanical errors are

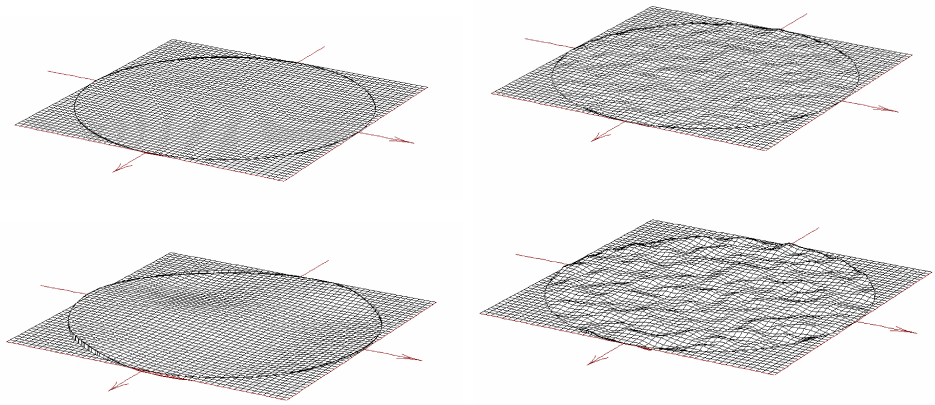

Figure 4.5: Model of the spatial error distribution on the xy-plane for a slow surface distortion (left) and a fast surface distortion (right): above $\pm 0.05\lambda$, below $\pm 0.1\lambda$.

more difficult to be diagnosed by an analysis of the far-field. Sidelobes higher than expected but a main lobe that meets the beamwidth antenna specifications can be considered a good test case for antenna diagnostics, and at the same time an interesting error to be corrected in a link-to-link communication.
It was thus decided to study in the TRIAX experimental test case, summarized in Section 4.1.2, a tilt of the feed around x_f, a localized bump, and a slow surface distortion. It is reminded that what is observed in a real test case is however more complicated than what the present simulations have shown, since several non-ideal factors need to be considered. In practice, the feed is never perfectly linearly polarized and it can be tilted and/or displaced from the focus. There exists a strut supporting the feed; the reflector surface can differ from a perfect paraboloid and the entire antenna sits on the tower of the measurement facility.

4.1.2 TRIAX offset reflector case

The present section reports the diagnostics results obtained for a TRIAX TD64 parabolic offset reflector. The antenna is first measured in its nominal configuration and, from the Q coefficients of the measured SWE, the reference near-field is computed by using the 8 steps of Section 3.6. Later, a tilt of the feed, a localized bump and a global surface distortion are introduced. After observing their effects in the corresponding measured far-fields, the near-fields are computed in two coordinate systems, for each error case, in order to better highlight and identify the errors. While the discussion is mostly based on Paper V, additional material is contained in Appendix A, where the equation of the TRIAX TD64 reflector is experimentally derived, a collection of all measurements results is provided, and an investigation of the non-ideal characteristics of the antenna is performed, through

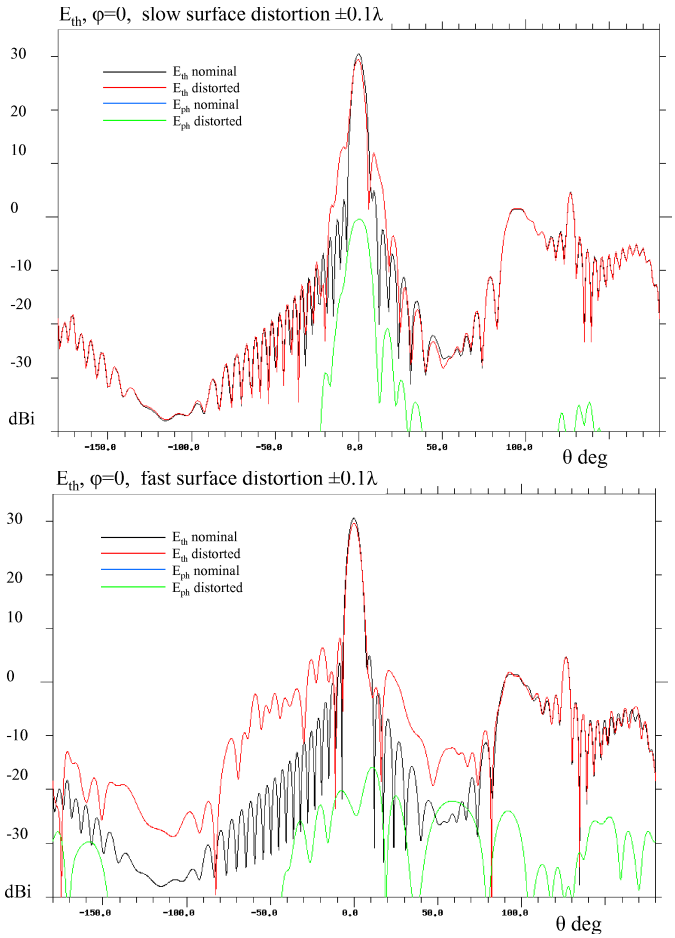

Figure 4.6: Amplitude of the θ-component, in the cut $\phi = 0°$, of the reflector far-field with slow surface distortion between $\pm 0.1\lambda$ (upper) and fast surface distortion between $\pm 0.1\lambda$ (lower).

numerical simulations realized with the commercial software GRASP9 [50].
The TRIAX TD64 antenna is a 12 GHz offset parabolic reflector, defined in the xyz-coordinate system by a circular projected aperture of diameter $D_{proj} = 60$ cm, a focal length $f = 39$ cm and a clearance $d' = 9$ cm, see Fig. 4.7 and Appendix A.1. The feed is linearly polarized along x_f, where $x_f y_f z_f$ is the feed coordinate system, with its origin at the focus and with z_f pointing towards the center point of the reflector. Two coordinate systems (CS) are introduced: the measurement CS, $x_{meas}y_{meas}z_{meas}$, with its origin on the reflector aperture plane and the z_{meas}-axis normal to that and coinciding with the horizontal rotation axis of the measurement system, and the cut CS, $x_{cut}y_{cut}z_{cut}$, obtained by rotating $x_{meas}y_{meas}z_{meas}$ 26.5° around y_{meas}, and with z_{cut} thus aligned to the main beam direction. The

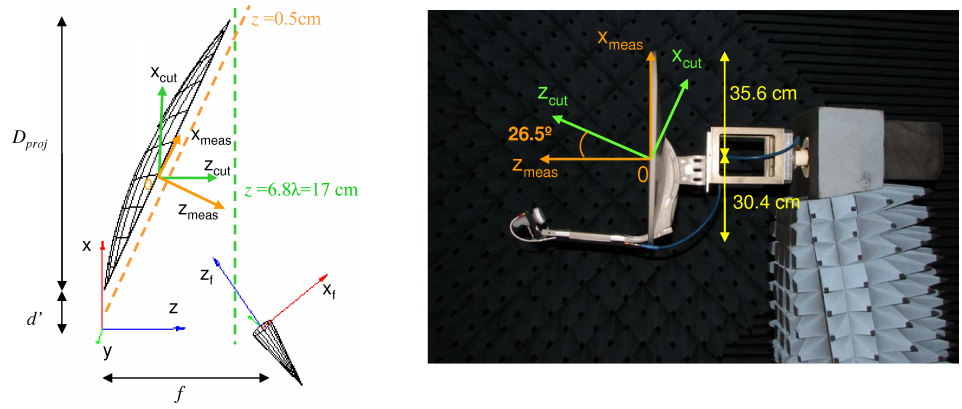

Figure 4.7: TRIAX offset reflector, geometry and coordinate systems: on the left the model, on the right the real antenna on the measurement tower.

measurement set-up of the antenna in its nominal configuration is shown in Fig. 4.7 on the right. By simply rotating the Q coefficients of the SWE of the electric field measured in the measurement CS, the Q coefficients of the SWE in the cut CS are obtained [26].
The amplitude of the measured far-field pattern in the cut CS, of the antenna in its nominal configuration, is plotted in dB in Fig. 4.8, showing co- and cross-polar components according to Ludwig's 3rd definition (3.15) with $\phi_o = 0°$, in the uv-space, normalized to the maximum value of the co-polar component. The behavior is as expected: the main beam is aligned to the z-axis of the cut CS, and the cross-polar component is symmetric with respect to $v = 0$. From the Q

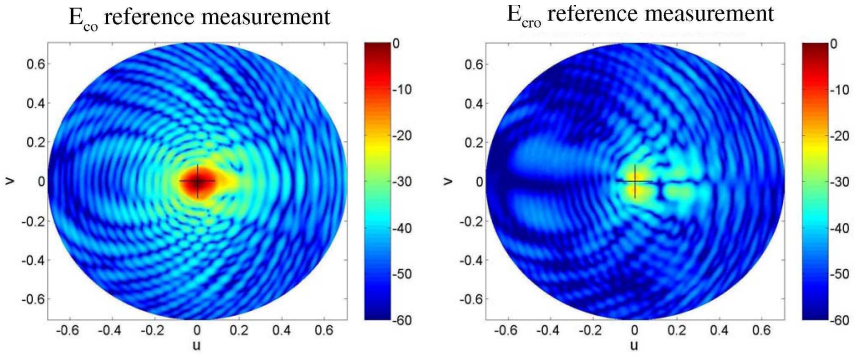

Figure 4.8: Amplitude of co- and cross-polar components in dB of the antenna far-field in its nominal configuration in the cut CS.

coefficients the power spectrum is found, see Fig. 4.9, and the truncation values $N = 135 = kr_o + 22$ and $M = 120$, which will be used in all the analyzed cases, are obtained. These n- and m-truncations in the series of (2.48) allow one to reach

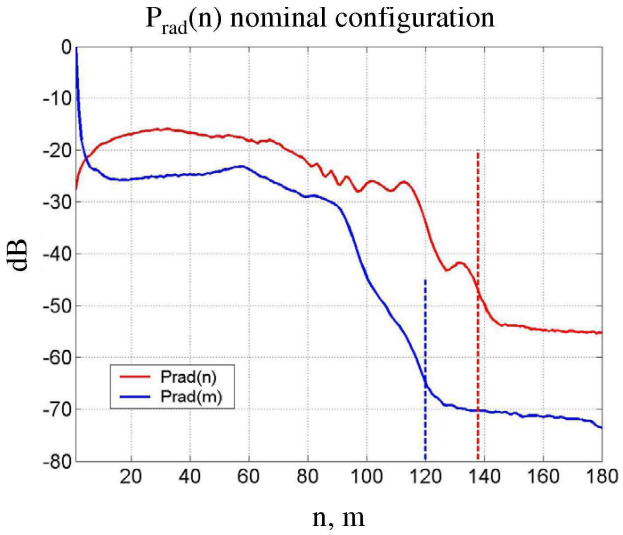

Figure 4.9: Power spectrum in the cut CS of the antenna in the nominal configuration and the truncation numbers $N = 135$ and $M = 120$.

convergence only in the visible part of the PWS and on the border for $k_z = 0$, providing a resolution in the computed near-field equal to $\lambda/2$. After computing the PWS from the measured Q coefficients with (2.48) on the $[-3k, 3k]$ spectral domain in the cut CS on the $z = 17$ cm $= 6.8\lambda$ plane, the aperture field on the same z-plane is obtained with the singularity extraction technique of (3.4), with a sampling interval equal to $\Delta x = \Delta y = \lambda/6$. It is noted that the selected z-plane is not located in the extreme near-field region of the reflector, but it simply is the smallest allowed by the cut CS in order to remain in the source-free region and do not touch the reflector. Plots of the amplitude of the x- and y-components of the

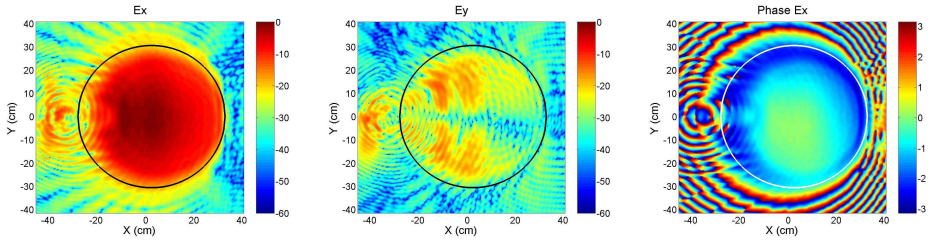

Figure 4.10: Amplitude of E_x and E_y and phase of E_x on $z = 17$ cm, in the cut CS for the nominal configuration.

electric field in dB scale and normalized to the maximum of E_x, are shown in Fig. 4.10 together with the phase of the x-component in radians, and the projected circular rim of the reflector. While the amplitude field distributions of E_x and E_y are almost symmetric around the $y = 0$ axis, as expected, the phase distribution

is not constant, as would be the case for an ideal parabolic reflector antenna, but shows a variation from the center of the aperture to the edge that reaches the maximum value of 2.4 rad. The reflector antenna - even in its nominal configuration - is thus far from ideal, see Appendix A.4. By looking at the left side of the projected circular rim, we clearly distinguish the effect of the diffraction from the strut.

Three mechanical errors are then introduced: a feed tilt of 5° and 10° around the x_f-axis, a localized bump and a global surface distortion, see Fig. 4.11. The tilt

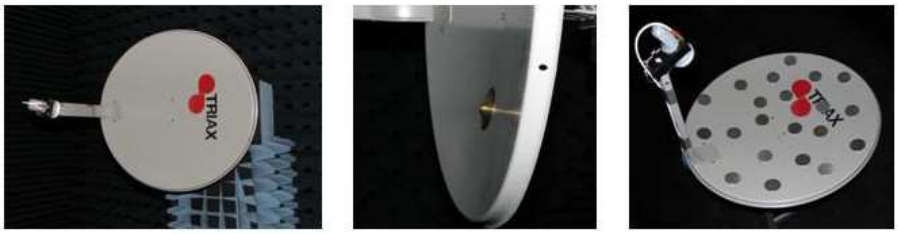

Figure 4.11: Offset reflector with a feed tilt (left), a Gaussian bump (middle) and surface distortion (right).

of the feed causes an asymmetry of the cross-polar far-field which is detectable already for the 5° case but becomes more evident for the 10° case. Following the same procedure of the nominal case, the aperture field is computed on the plane $z = 17$ cm, see Fig. 4.12, for the amplitudes of the x- and y-components. Both, as expected, show a tilt of the feed illumination towards the negative y-axis, when compared to Fig. 4.10.

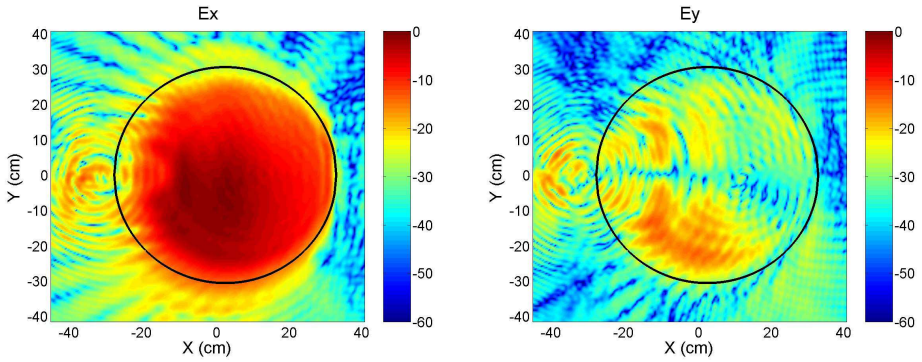

Figure 4.12: Amplitude of E_x and E_y on $z = 17$ cm, in the cut CS for the 10° feed tilt case.

The metallic bump has the shape of a two-dimensional Gaussian function with peak and sigma both of 1 cm. The co- and cross-polar components of the far-field pattern in the cut CS for this configuration maintain the shape of the main beam

of the nominal case, while the structure of the side-lobes changes significantly. The aperture field is then calculated on the $z = 17$ cm plane in the cut CS, see Fig. 4.13 (left). Though the aperture illumination is now almost symmetric, a circular structure of different amplitude is noticed for $x \approx 0$ cm and $y \approx -20$ cm. The picture becomes more clear when the aperture field is computed in the measurement CS on $z = 0.5$ cm, see Fig. 4.13 (right), where the projected elliptical rim of the reflector is also indicated.

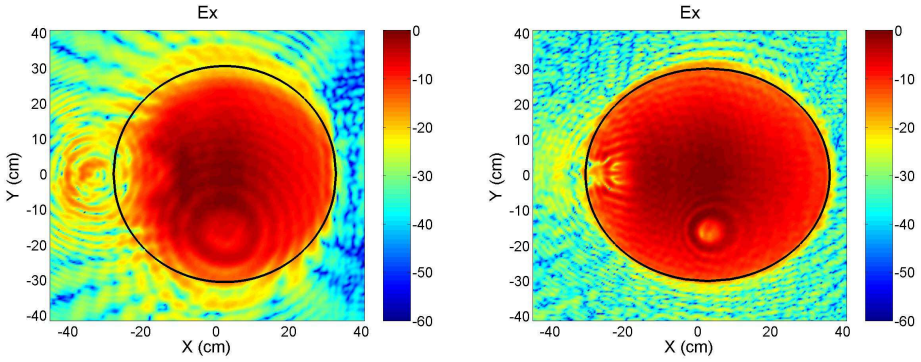

Figure 4.13: Amplitude of E_x on $z = 17$ cm in the cut CS (left), and on $z = 0.5$ cm in the measurement CS (right) for the Gaussian bump case.

The surface distortion is finally modeled by randomly placing 21 dishes of aluminum each with a diameter of 5 cm and thicknesses of 2.5 mm, 1.5 mm and 1 mm ($\lambda = 2.5$ cm) on the entire reflector surface. While the main beam region of the co-polar component remains almost the same as for the nominal configuration, side-lobes of high amplitude appear. The x-component of the aperture field is shown in Fig. 4.14, on the left at $z = 17$ cm in the cut CS, and on the right at $z = 0.5$ cm in the measurement CS. As for the Gaussian bump case, the distortion

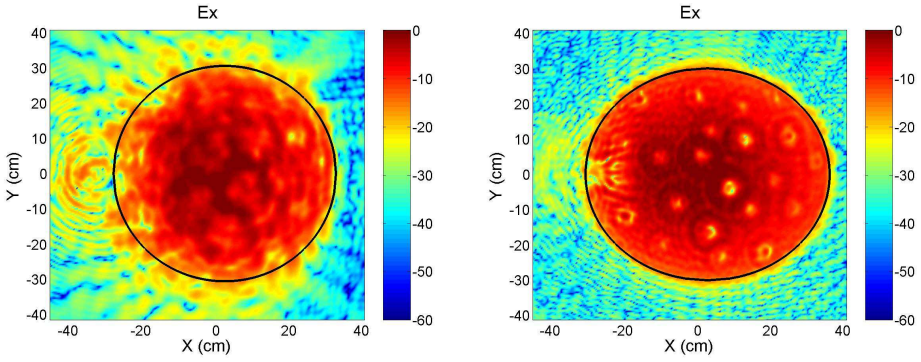

Figure 4.14: Amplitude of E_x on $z = 17$ cm in the cut CS (left), and on $z = 0.5$ cm in the measurement CS (right) for the surface distortion case.

becomes more distinguishable on a plane closer to the reflector surface, in particular all 21 dishes, the thicker clearly, the thinner less strongly, are identified.
To conclude, the SWE-to-PWE antenna diagnostics technique was applied to a simple commercially available offset reflector antenna for satellite TV reception. The diagnostics showed the non-ideal characteristics of the antenna in its nominal configuration, and, even in the presence of these, a correct and accurate identification of a feed tilt and two types of surface distortions. The investigation highlighted the importance of applying different coordinate systems and projected aperture planes.

4.2 SMOS radiometer antenna system test case

The antenna system of the Microwave Imaging Radiometer using Aperture Synthesis (MIRAS) for ESA's Soil Moisture and Ocean Salinity (SMOS) mission is here considered. The present section is based on Paper VI, while a summary of all results can be found in Appendix B. The MIRAS radiometer consists of 69 independent dual-polarized receivers working in the frequency band from 1.404 GHz to 1.423 GHz (L-band) and positioned on an 8 meter diameter Y-shaped support structure, that is folded during launch and un-folded once the satellite is in orbit, see Fig. 4.15. Each receiver includes a dual linearly polarized circular patch antenna. The entire structure is then covered by a Kapton-Germanium thermal protection layer. To accurately determine the soil moisture and ocean salinity, the radiometric signal processing requires an accurate measurement of the far-field patterns of each of the 69 antennas for each of the two polarizations. Thus, 138 independent measurements were performed, exciting one port and one element at a time.
During the measurements of the MIRAS hub, anomalies were discovered in the far-field patterns of two receivers:
1) Port 1 of the receiver unit BC03 showed a high cross-polarization in the $\phi = 90°$ plane.
2) Port 1 of the receiver unit A05 exhibited a noticeable frequency variation in the co- and/or cross-polar components in all ϕ planes.
In order to identify the sources of those anomalies, the SWE-to-PWE diagnostics technique was applied and the aperture fields for these two receivers were computed on the z-plane placed on the surface of the Kapton-Germanium layer, located at z = -5mm in the measurement coordinate system. To have a reference aperture field, the diagnostics was also applied to port 1 of the unit A01 which did not present any anomalies. The co- and cross-polar far-field patterns, according to Ludwig's 3rd definition (3.15) with $\phi_o = 0°$, are shown in Fig. 4.16 for port 1 in the $\phi = 90°$ plane.
From the Q coefficients of the SWE of the field radiated by each element the power spectra were found. Though each unit had its own power spectrum distribution, the finite dynamic range of the measurement system provided a truncation value in n and m which was the same for every unit, $N = 58 = kr_o + 2 = M$, see Fig. 4.17 for the power spectrum of the unit BC03. With this n-truncation in the series of (2.48), it was expected, and it was later confirmed, to recover only the visible part

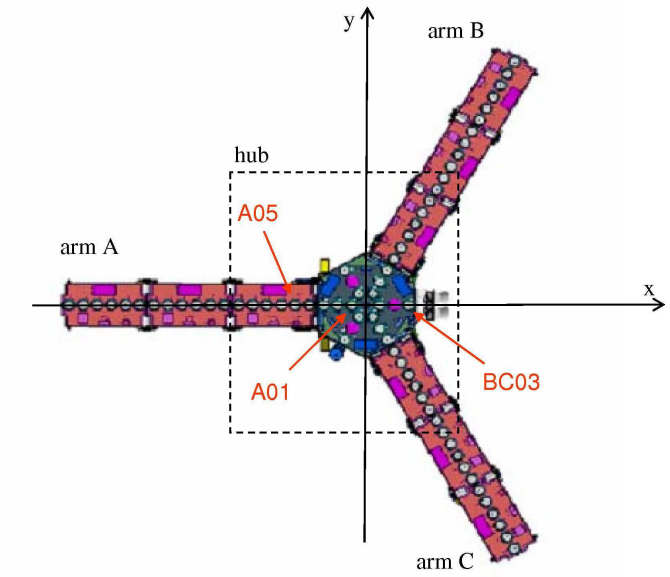

Figure 4.15: The MIRAS antenna system in the measurement coordinate system with the faulty units A05 and BC03 and the correct unit A01 indicated.

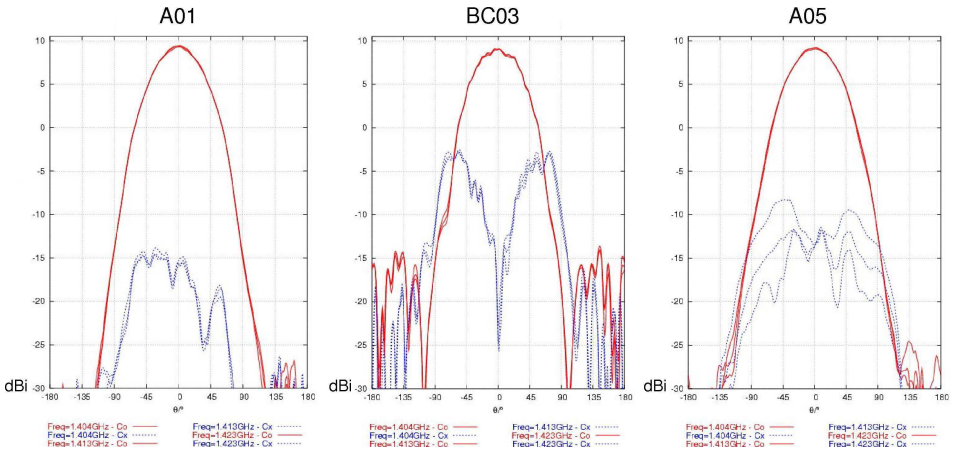

Figure 4.16: Far-field patterns of the unit A01 (left), BC03 (middle), A05 (right), for port 1 in the $\phi = 90°$ plane.

of the PWS and the border at $k_z = 0$. The convergence in points belonging to the invisible region could not be reached. The PWS was thus calculated with (2.48) on the $[-4k, 4k]$ spectral domain, zeropadding the invisible region. The aperture fields were then computed with the singularity extraction technique of (3.4).

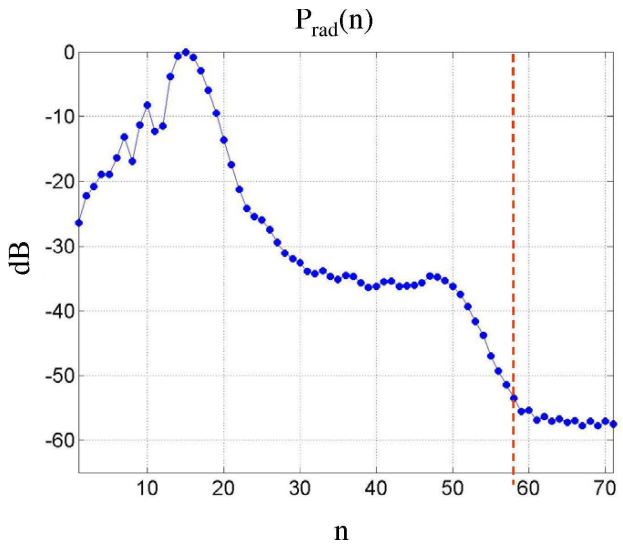

Figure 4.17: Power spectrum of the unit BC03 at $f = 1.423$ GHz and the truncation value $N = 58$.

In Fig. 4.18 the amplitudes of the cross-polar components E_y and E_z of the reference unit A01 are plotted in dB, normalized to the maximum of the x-component. It is possible to distinguish the radiation from the circular patch as well as the diffraction from the edges of the hub. The y-component shows four symmetric lobes, while the z-component is symmetric with respect to the axis parallel to the y-axis and passing through the center of the patch. The same was observed in the corresponding phase plots. The field distribution is however larger than expected, when compared to the extent of the white circle indicating the average dimensions of the circular patch, since only the visible part of the PWS is known, as it was also observed in Section 3.3.
In Fig. 4.19 the amplitudes of the E_y and E_z components of the unit BC03 are shown in dB. Though the diffraction from the edges of the hub is evident, the radiation from the patch presents asymmetries in both components. It was concluded that the anomalies of the pattern in Fig. 4.16 were due to an error in the patch excitation, i.e., in the patch feed network. The unit BC03 was subsequently replaced by a new one and, after a new spherical near-field measurement, the aperture fields were calculated, see Fig. 4.20. The patch excitation is now totally symmetric and the diffraction from the edges has decreased slightly with respect to the faulty element case shown in Fig. 4.19.
The cartesian components of the aperture field of the faulty unit A05 were then compared to the corresponding components of the correct unit A01 for the three frequencies of interest, $f = 1.404$ GHz, 1.413 GHz and 1.423 GHz. While the behavior of the unit A01 remains constant with frequency, the unit A05 shows some changes. In particular, it was noticed that the y- and z-components of the field were asymmetric and changed slightly with frequency, while the diffraction

from the hub edges decreased with increasing frequency, see Fig. 4.21 for a plot of the y-component. The effect was less evident for the co-polar x-component. The same asymmetries were noticed also in the phase plots. Again, it was concluded that the anomalies detected in the far-field pattern were due to errors in the feed network. The presence of such errors was later confirmed by an inspection of the antenna hardware. A summary of the aperture field results for the three units is

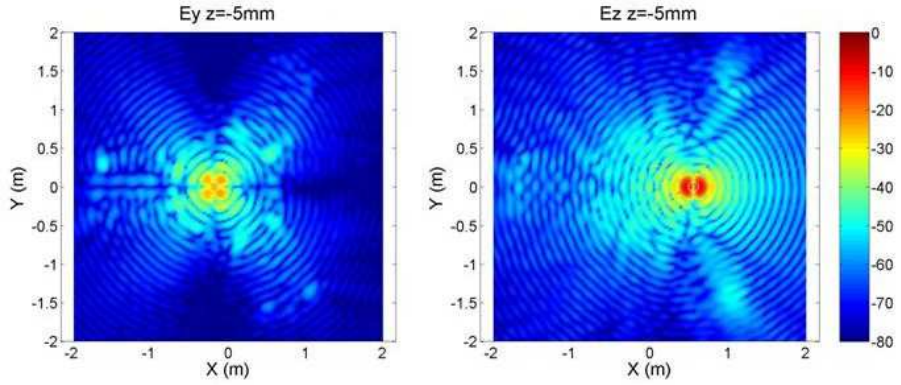

Figure 4.18: Amplitude of E_y and E_z in dB on the z = -5mm plane, for the correct unit A01.

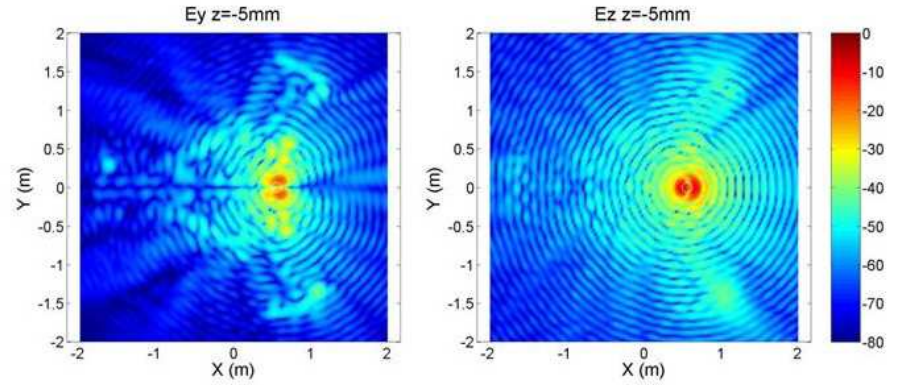

Figure 4.19: Amplitude of E_y and E_z in dB on the z = -5mm plane, for the faulty unit BC03.

given in Appendix B. It is noted that the near-fields plots of Figs. 4.18-4.21 are all affected by significant circular ripples, which modify the radiation from the unit element and the diffraction from the edges of the structure.
To conclude, a diagnostics of two units of the MIRAS antenna system was presented. The diagnostics showed that the anomalies observed in the far-field pattern could be traced back to asymmetries and frequency variations in the extreme

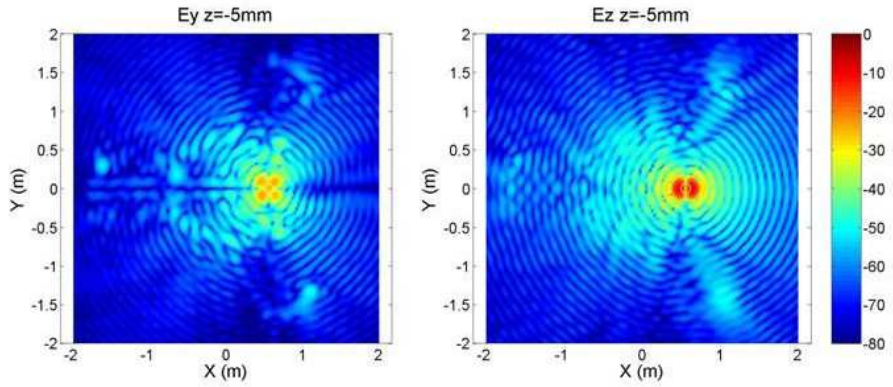

Figure 4.20: Amplitude of E_y and E_z in dB on the z = -5mm plane, for the unit BC03 replaced.

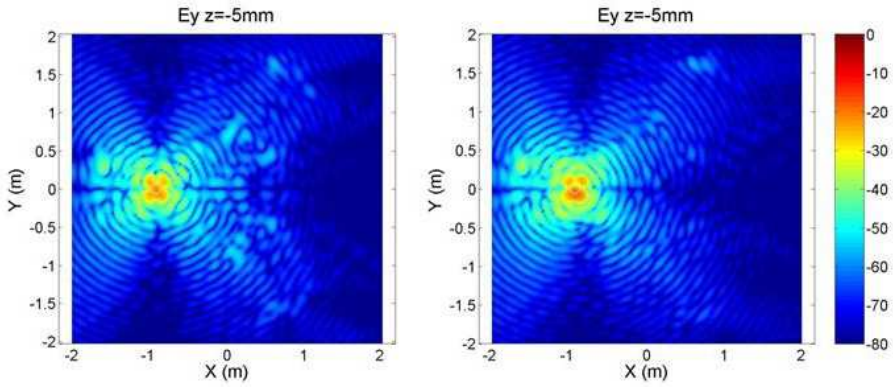

Figure 4.21: Amplitude of E_y in dB on the z = -5mm plane, for the unit A05, at f =1.404 GHz (left) and f = 1.423 GHz (right).

near-field of the antenna elements. In both cases, it was concluded that errors were present in the feed networks of the units. It was noticed that the calculated aperture fields showed not only the field radiated directly by the antenna unit, but also quite clearly the diffraction from the edges and other structural components of the support structure. The investigation underlined the importance of the analysis of the cross-polar components, in amplitude as well as in phase.

4.2.1 Windowing techniques

The present section provides an overview of the possible windowing techniques that can be used to limit the circular ripples in the near-field plots of Section 4.2, but it is not intended to be complete. A brief discussion on linear and non-linear methods is presented, and some of the proposed solutions are applied to the units

of the MIRAS antenna system. A complete collection of plots can be found in Appendix B.
The circular ripples in the near-fields plots of Figs. 4.18-4.21 are artifacts caused by the zero-padding of the PWS in the invisible region. This is equivalent to the product of the PWS on the entire $[-4k, 4k]$ $k_x k_y$-domain with a spectral function defined on the same $k_x k_y$-domain and having amplitude equal to 1 on the circular region of radius k, and amplitude 0 outside, (uniform weighting function). In the transformed spatial domain, this corresponds to a convolution between the IFT of the original PWS and a sinc function with circular symmetry on the xy-plane. From the convolution process, the information contained in the IFT of the original PWS is spread out across the mainlobe and sidelobes of the sinc function. Thus the arising of circular ripples of significant amplitude.
For high directive antennas, i.e., when the PWS is highly concentrated inside the visible region and has low values at the border of the visible region, as for the TRIAX antenna of Section 4.1.2, this ripple effect is negligible. For low directive antennas, i.e., when the PWS is distributed on the entire visible region, as for the units of the MIRAS antenna system, see Paper VI, this ripple effect becomes evident, in particular in regions of the xy-domain far from the source. It is noted that for the Hertzian dipoles of Chapter 3 the effect was in principle present, but it was in practice negligible on the finite extent of the selected xy-plane.
To reduce the ringing effect, and thus the amplitude of the sidelobes, the spectral function of interest can be multiplied by a non-uniform weighting function, prior to inverse Fourier transform. This is a well known method in signal processing and in particular in SAR imaging to avoid that sidelobes of a strong target interfere and/or obscure weaker targets in the neighborhood. A good review of all possible weighting functions is given by Harris [51] and a plot of the most used is in Fig. 4.22 for the one-dimensional case. It is seen that while the first sidelobe of the sinc function lies at -13.5 dB from the peak, the one of the non-uniform functions, like Hanning and Hamming for example, lies at around -30 dB from the peak. Moreover, their sidelobes envelopes decrease faster than the 6 dB per octave of the sinc. However, lower sidelobes are achieved at the expense of an enlargement of the mainlobe. Thus, the result of the IFT of the PWS, once weighted by a non-uniform function, shows much lower ringing effect, but at the same time a field distribution on the patch larger than the one showed in Figs. 4.18-4.21. As an example, see Fig. 4.23 where the Hanning window, chosen as compromise between low sidelobes and large mainlobe, was applied to the PWS of the faulty element BC03 before inverse Fourier transforming with the singularity extraction technique of (3.4). When compared to Fig. 4.19, the advantages of the Hanning window are evident. Though the radiation from the antenna element is broader, and thus artificial, the ringing effect has almost disappeared, and the details of the structure and the diffraction from it are more clear. The anomalies of the field components are still recognizable. If the Hanning window is applied to the unit A05, the variation in frequency remains detectable, see Appendix B. When the windowing function is used on the entire domain of the spectral function of interest, we normally talk about linear windowing.
However, there exists a second class of techniques where a different weighting func-

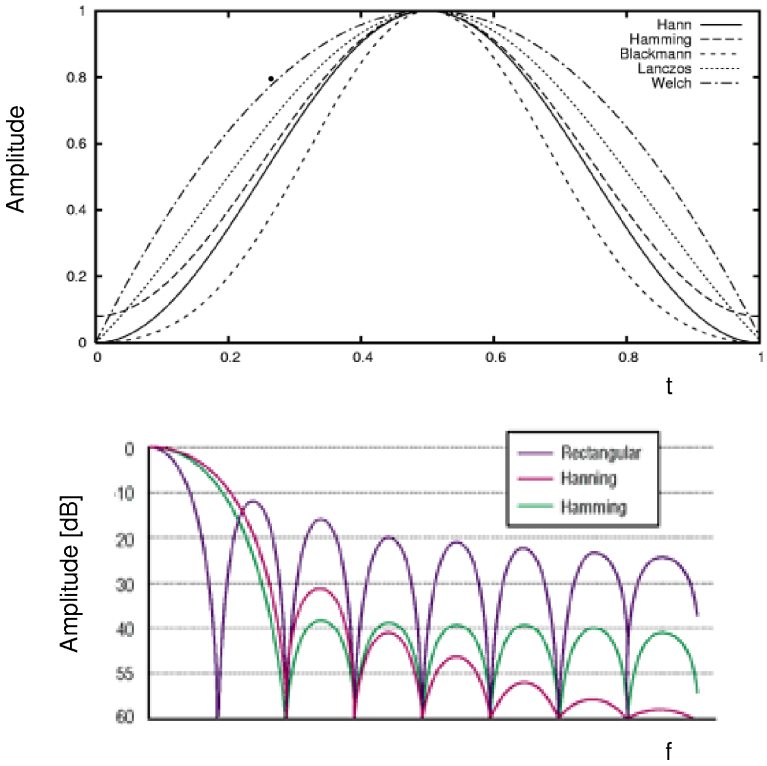

Figure 4.22: Traditional weighting functions (upper) and their Fourier transforms (lower).

tion is used for each pixel of the spectral function. The methods which follow this approach are called non-linear windowing techniques, since the use of non-linear operators is necessary to weight each pixel differently, and are identified by the adjective "spatially variant". They have the big advantage of reducing the sidelobe levels without, or anyway negligibly, enlarging the main lobe. A very good review of all possible variations and implementations can be found in Stankwitz et al. [52].
The easiest non-linear spatially varying procedure to obtain an image with low sidelobes and narrow mainlobe is called Dual Apodization (DA), borrowing a term from optics, apodization, which refers to the suppression of diffraction sidelobes. DA requires the computation of two versions of the image, one with uniform weighting and one with a non-uniform weighting, Hanning for example. The two images are then compared pixel-by-pixel and the minimum between the values of the pixel pair is selected, forming the final image. While DA is normally used for real functions, it can be extended to complex functions by selecting pixel-by-pixel the complex value whose magnitude is minimum, [52].
For complex functions the comparison of the two images, obtained with a uniform and non-uniform weighting function, can otherwise be performed on the real and

imaginary part separately, obtaining what is called Complex Dual Apodization (CDA). For each pixel, the real parts are compared and, depending on their sign, the value zero (opposite sign) or the one with smallest absolute value (same sign) is chosen. The same is done for the imaginary part [52]. From the way the algorithm is constructed, the phase of the resulting image is not correct, while good results can be obtained for the amplitude. In Fig. 4.24 CDA is applied to the faulty unit BC03, choosing Hanning as non uniform weight. The level of the circular ripples is low like when the Hanning window is used, Fig. 4.23, but the spatial extent of the radiation from the patch is now narrower. The anomalies in the field components are anyway maintained, see Appendix B for more results.

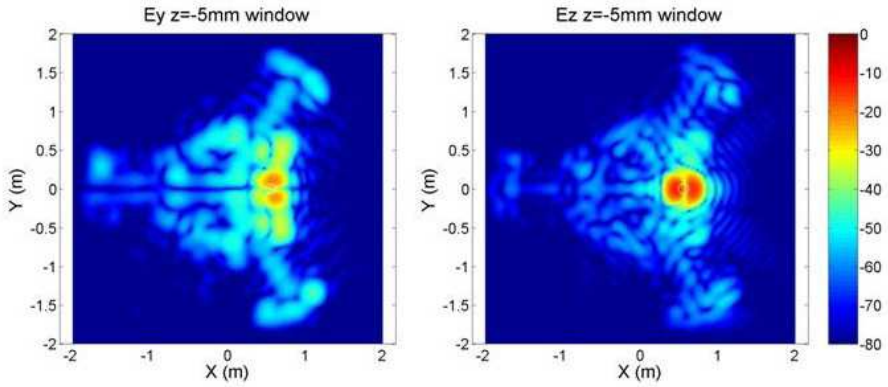

Figure 4.23: Amplitude of E_y and E_z in dB on the z = -5mm plane, for the faulty unit BC03 with Hanning window.

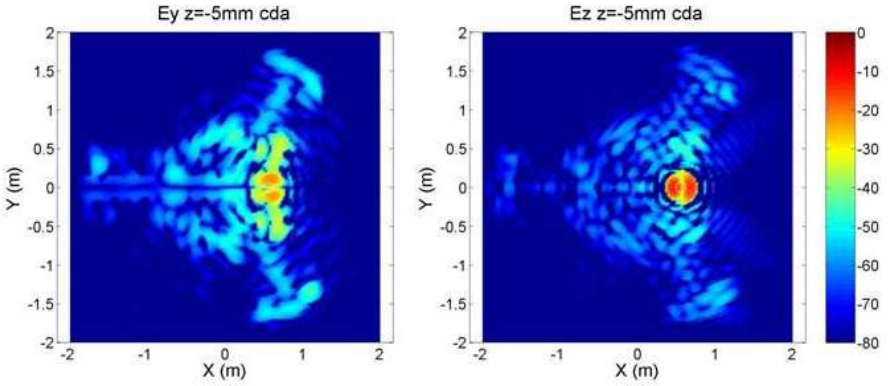

Figure 4.24: Amplitude of E_y and E_z in dB on the z = -5mm plane, for the faulty unit BC03 with CDA.

DA and CDA can be seen as variations of the most general technique called Spatially Variant Apodization (SVA) [52], which allows each pixel of the image to

receive its own spectral weighting function from a continuum of possible weighting functions, where the uniform window, Hanning and Hamming are an example. The SVA technique is based on the fact that all cosine-on-pedestal weighting functions can be computed from the same generating function

$$A(n) = 1 - 2w\cos(2\pi n/N) \tag{4.1}$$

by simply varying the parameter w between 0 (uniform weighting) and 0.5 (Hanning weighting). Eq. (4.1) refers to the discrete one-dimensional case of length N. By employing (4.1), every pixel in the image receives the spectral weighting function given by the value of w that minimizes the magnitude of the output pixel value. It is possible to minimize the real and imaginary parts jointly or separately. The last option provides better performance, as reported by Colone et al. [53]. An alternative minimization scheme has been recently proposed by Smith [54], maintaining the computational efficiency of the general SVA technique.

4.3 Summary

The SWE-to-PWE antenna diagnostics technique was applied to two experimental test cases using real measurements data, in the presence of typical measurement inaccuracies and non-ideal AUTs.
First, a diagnostics of a simple commercially available offset reflector antenna for satellite TV reception was performed. The diagnostics showed the non-ideal characteristics of the antenna in its nominal configuration, and, even in the presence of these, a correct and accurate identification of a feed tilt and two types of surface distortions. The investigation highlighted the importance of applying different coordinate systems and projected aperture planes.
Second, a diagnostics of two units of the MIRAS antenna system was presented. The diagnostics showed that the anomalies observed in the far-field pattern could be traced back to asymmetries and frequency variations in the extreme near-field of the two antenna elements. In both cases, it was concluded that errors were present in the feed networks of the units. Their existence was later confirmed by an inspection of the antenna hardware. It was noticed that the calculated aperture fields showed not only the field radiated directly by the antenna unit, but also quite clearly the diffraction from the edges and other structural components of the support structure. The investigation underlined the importance of the analysis of the cross-polar components, in amplitude as well as in phase.
Finally, a brief review of the most used windowing techniques to diminish the truncation effect in the aperture field of low directive antennas was provided. Linear and non-linear methods were presented, describing their advantages and disadvantages. It was concluded that their use can significantly improve the near-field plots highlighting the effect of the weak sources.

Chapter 5

Conclusions

A new antenna diagnostics technique for spherical near-field antenna measurements was presented. The technique applies to general types of antennas and is based on the transformation of the Spherical Wave Expansion (SWE) to the Plane Wave Expansion (PWE). The plane wave spectrum (PWS) is computed from the coefficients of the SWE and subsequently inverse Fourier transformed, providing the extreme near-field of the antenna under test. A spatial resolution higher than the traditional half a wavelength can be obtained for electrically small antennas. The computation of the extreme near-field is accurate for electrically small as well as large antennas, since the singularity at the border between the visible and invisible spectral region is properly taken into account. The SWE can be obtained from a spherical near-field measurement or be computed by a software. The plane where the extreme near-field is calculated can be arbitrarily oriented with respect to the measurement coordinate system in order to facilitate the identification of the antenna errors.

Chapter 2 provided the necessary theoretical background and the mathematical foundation for the diagnostics technique. The Spherical Wave Expansion and the Plane Wave Expansion were both derived from the vector Helmholtz equation [30][37] and their definitions, domains of validity, properties, and use in antenna measurements were discussed. By employing a cartesian xyz-coordinate system and the associated spherical $r\theta\phi$-coordinate system, it was shown that, for an antenna with minimum sphere of radius r_o and radiating in free-space, the SWE of the radiated field is valid for $r > r_o$, while the PWE of the same field is valid for $z > z_o$, with z_o being the largest z-coordinate of the antenna and $z_o \leq r_o$. The relation between the SWE and PWE was then investigated. Though the domains of validity of the SWE and PWE are fundamentally different, it was shown that the plane wave spectrum can be computed from the coefficients of the SWE through a rigorous transformation [28], in the visible as well as in the invisible region of the spectral domain, at any z-plane $z > z_o$. It was emphasized that the use of the SWE-to-PWE transformation is particularly useful in antenna diagnostics for spherical near-field antenna measurements to calculate the extreme

near-field, which can not be directly computed from the SWE. For this use, it was noted that the recovery of the invisible region of the PWS from the Q coefficients of the SWE can provide a spatial resolution in the extreme near-field higher than the traditional half a wavelength obtained from the visible region of the PWS.

Chapter 3 presented the development of the antenna diagnostics technique on the basis of the SWE-to-PWE transformation. The necessary additional steps to obtain the extreme near-field from a spherical near-field measurement were addressed. First the fundamental properties of the transformation were discussed, with emphasis on their theoretical as well as practical implications. The transformation of individual spherical waves was studied in order to determine how these contribute to different regions of the spectral domain. It was noted that each spherical wave contributes to the visible as well as the invisible region, and thus provides information on the propagating as well as evanescent waves of the PWE. The convergence mechanism of the series expressing the PWS was investigated. It was found that the infinite series can be truncated at a finite value N. While the traditional $N = kr_o + 10$ is sufficient to reach convergence in the visible region, a larger N, which depends on the size of the antenna, the origin of the measurement coordinate system and the part of spectral domain where the PWS is computed, is necessary in the invisible region. It was also shown that the path to convergence in the invisible region involves very large intermediate values. The exponential growth and the resulting numerical difficulties in the computation of the PWS in the invisible region were also addressed and a suggestion was given for a more efficient calculation. The computation of the aperture field from the PWS was then analyzed. It was recalled that the PWS generally possesses a singularity at the border between the visible and invisible regions and, though the singularity is integrable, a straightforward application of the inverse Fast Fourier Transform does not normally provide accurate results. A singularity extraction technique for computation of extreme near-fields of antennas from singular plane wave spectra was thus developed and presented. The algorithm is based on the Weyl identity and the inverse Fast Fourier Transform, and allows the accurate computation of the aperture field when a dense sampling in the spectral domain is not possible. Next, the concept of resolution was studied and its fundamental difference from the concept of sampling interval was underlined. It was found that resolution perceived by the human eye in observing a near-field plot can not be defined by a specific formula and it might be lower than the one defined as the distance between the zeros of the fastest oscillating wave contained in the PWE. It was noted that what the eye distinguishes generally depends on the polarization of the source, the z-plane of interest, and the component of the field. Finally, the effects of finite measurement accuracy on the proposed antenna diagnostics technique were studied through numerical simulations. It was concluded that electrical inaccuracies, and in particular amplitude noise, limit in practice the available Q coefficients and thus the spectral region where the PWS reaches convergence. Under typical measurements conditions, the recovery of the PWS is generally obtained in the visible region and at the border where the singularity exists. For electrically small antennas a part of the invisible region of the PWS can also be reconstructed, but for

electrically large antennas the entire invisible region must be normally discarded.

Chapter 4 dealt with the experimental verification of the SWE-to-PWE antenna diagnostics technique. Real measurements were performed at the DTU-ESA Spherical Near-Field Antenna Test Facility [27], in presence of typical measurement inaccuracies and complex AUTs. First, a diagnostics of a simple commercially available offset reflector antenna for satellite TV reception was performed. The diagnostics showed the non-ideal characteristics of the antenna in its nominal configuration, and, even in the presence of these, a correct and accurate identification of a feed tilt and two types of surface distortions. The investigation highlighted the importance of applying different coordinate systems and projected aperture planes. Second, the antenna system of the satellite-based Soil Moisture and Ocean Salinity (SMOS) radiometer was investigated, in particular the diagnostics technique was used to successfully identify the sources of the anomalies detected in 2 of the 138 measured antenna far-field patterns. The diagnostics showed that the anomalies observed in the far-field pattern could be traced back to asymmetries and frequency variations in the extreme near-field of the two antenna elements. In both cases, it was concluded that errors were present in the feed networks of these units. These errors were later confirmed by an inspection of the antenna hardware. It was noted that the calculated aperture fields showed not only the field radiated directly by the antenna unit, but also quite clearly the diffraction from the edges and other components of the support structure. The investigation underlined the importance of the analysis of the cross-polar components, in amplitude as well as in phase. Finally a brief review of some windowing techniques, to diminish the truncation effect in the aperture field of low directive antennas, was provided. Linear and non-linear methods were presented, describing their advantages and disadvantages, and successfully applied to the units of the SMOS radiometer antenna system.

The work presented in this thesis can be extended in many ways. First of all, the computation of the PWS from the Q coefficients should be implemented in a more efficient way in order to speed up the calculation. Given a certain set of Q coefficients, either obtained from a spherical near-field measurement or computed by a software like GRASP9 [50] and SNIFTD [32], the truncation value N should be immediately determined avoiding the visual inspection of the power spectrum. Similarly, the number of points in the spectral domain, the z-plane of observation, and the z_1-plane required by the singularity extraction technique, should be automatically chosen. At the moment, the antenna diagnostics software is written in two languages, FORTRAN90 to compute the PWS, and MATLAB to calculate the extreme near-field from the PWS and plot the obtained results. A combination of these two programs should be made to speed up the computation. A deeper study on linear and non-linear windowing techniques should be conducted, both to find a proper method that can reconstruct the phase, since this is not the case when the CDA [52] is used, and to get a better insight into the advantages and disadvantages of the different techniques. The analysis of the magnetic extreme near-field could also be taken into consideration, since this could be more advan-

tageous for some types of antennas. The Poynting vector could also be analyzed. Since it was shown that finite measurement accuracy and numerical noise limit the region where the PWS reaches convergence to normally the visible region and the border where the singularity exists, the possibility of extending the spectrum into the invisible region could be investigated. This would increase the resolution in the extreme near-field and would take full advantage of the SWE-to-PWE transformation. An idea could be a variation of the iterative technique based on the Gerchberg-Papoulis algorithm recently developed by Martini et al. [18]. The possibility of extrapolating the value of the Q coefficients for higher n- and m-modes could also be studied.

Finally, a few recommendations for a diagnostics tool. Such a software should be able to:
- Rotate the Q coefficients from the measurement coordinate system to a new coordinate system more advantageous to perform the diagnostics.
- Automatically determine the truncation value N, the number of points in the spectral domain, the z-plane where the extreme near-field is computed, its extent in the xy-coordinate, and the z_1-plane for such a computation.
- Compute the electric and magnetic extreme near-field and maybe also the Poynting vector.
- Plot the extreme near-field in cartesian components, or a combination of these, in amplitude and phase. The choice between the dB scale or the linear scale should be possible when plotting the amplitude, and the possibility of adjusting the color scale to increase the contrast should be implemented too.
- Choose among a list of possible windowing techniques to limit the truncation effect for low directive antennas.
- Allow the use and combination of alternative antenna diagnostics techniques, for example the source reconstruction suggested by [24] and [25].

Appendix A

TRIAX offset reflector

A.1 Equation of the TRIAX paraboloid

When the TRIAX TD64 reflector antenna was bought, we knew from the technical specifications that the antenna worked in the frequency range 10.7-12.75 GHz, its overall dimensions were 60 cm x 65 cm and the paraboloid was characterized by a $f/D = 0.6$. The SWE-to-PWE antenna diagnostics technique only requires the Q coefficients of the SWE in a given coordinate system to compute the PWS and subsequently the aperture field distribution. However, in order to identify the direction of the main beam with respect to the z-axis of the measurement coordinate system (CS) and perform the diagnostics on the most convenient aperture plane, it was decided to derive the equation of the TRIAX paraboloid.
The derivation was not straightforward since we did not know in which coordinate system f and D were defined, and what the quantity D represented.
We started by considering the TRIAX antenna as a general offset parabolic reflector defined with respect to a certain xyz-coordinate system according to [55], see Fig. A.1. On the basis of the geometrical construction of the paraboloid and the distances we could measure, we looked for D_{proj}, d' and f. We knew that for a point $P(x, y, z)$ on a rotationally symmetric paraboloid with focal length f the following equations hold

$$\rho^2 = x^2 + y^2 \tag{A.1}$$

$$\rho^2 = 4fz \tag{A.2}$$

$$r = f + z. \tag{A.3}$$

We also knew that the edge of a paraboloid is contained in a plane which makes the angle θ_c with the z-axis,

$$\theta_c = \tan^{-1}\Big(\frac{2f}{d' + D_{proj}/2}\Big), \tag{A.4}$$

and that the edge curve is an ellipse with the major and minor axis being

$$a = (D_{proj}/2)/\sin\theta_c \qquad b = D_{proj}/2 \tag{A.5}$$

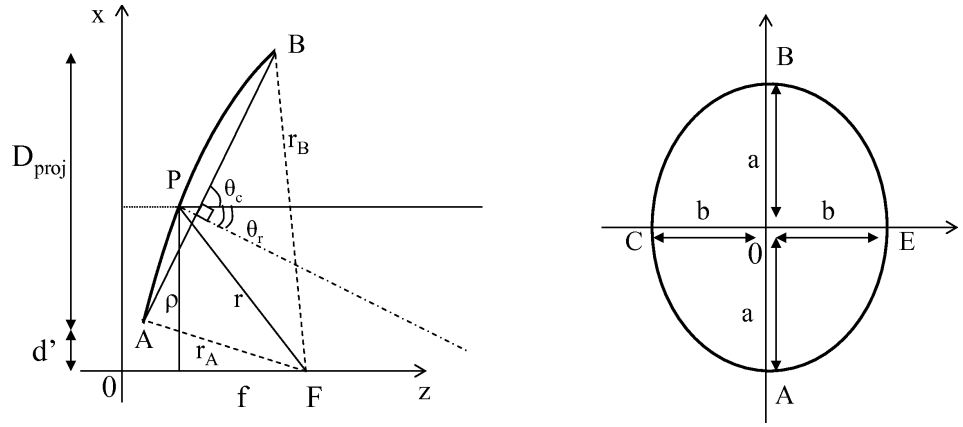

Figure A.1: TRIAX reflector paraboloid in the xyz-coordinate system (left) and ellipse with axis a and b representing the edge of the paraboloid (right).

respectively, [55], see Fig. A.1.
We first assumed that the feed was located in the focal point F of the paraboloid, see Fig. A.1. We then measured the axis of the ellipse described by the edge of the TRIAX. It is noted that every measurement of distance that we performed was affected by non negligible measurement errors given by the non sharp reflector edge and the difficulty of defining the phase center of the feed, where the focal point was supposed to lie. It is estimated that the accuracy of the measured values was approximately ± 0.5 cm. For the axis of the ellipse we measured $a = 33$ cm and $b = 30$ cm. From (A.5), $D_{proj} = 60$ cm and $\theta_c = 65.3°$ were thus obtained. To verify their values and find the clearance d' and the focal length f we did the following.
We considered the two edges A and B of the reflector in the xz-plane, and measured their distances from the focal point, FA $= r_A = 39.5$ cm and FB $= r_B = 69.5$ cm, see Fig. A.1. We then used the specification $f = 0.6D = 39$ cm, assuming D equal to the largest dimension of the reflector, as reported in the datasheet, $D = 65$ cm. For the point A, from (A.3) and (A.2), we wrote

$$z_A = r_A - f = 0.5 \text{ cm} \tag{A.6}$$

$$\rho_A = \sqrt{4fz_A} = x_A = d' = 9 \text{ cm} \tag{A.7}$$

and for the point B

$$z_B = r_B - f = 30.5 \text{ cm} \tag{A.8}$$

$$\rho_B = \sqrt{4fz_B} = d' + D_{proj} = 69 \text{ cm} \tag{A.9}$$

obtaining

$$D_{proj} = \rho_B - \rho_A = 60 \text{ cm}. \tag{A.10}$$

The value of D_{proj} in (A.10) agreed with the measured distance $2b = 60$ cm obtained from (A.5). The angle θ_c was then calculated with (A.4) obtaining

$\theta_c = 63.5°$, which, once inserted in (A.5), provided $a = 33.5$ cm. Considering an accuracy of ± 0.5 cm, the value agreed with the measured distance $a = 33$ cm. By assuming $\theta_c = 63.5°$, the angle θ_r between the direction of the antenna main beam, which for geometrical construction is parallel to the z-axis, and the normal to the plane containing the edge of the reflector is equal to $\theta_r = 90° - \theta_c = 26.5°$, see Fig. A.1. This is also the angle between the antenna main beam direction and the z-axis of the measurement CS used in Section 4.1.2.
The TRIAX TD64 offset reflector antenna is thus constituted by a 12 GHz parabolic offset reflector, described in the xyz-coordinate system of Fig. A.1 by

1. a circular projected rim of diameter $D_{proj} = 60$ cm
2. a focal length $f = 39$ cm
3. a clearance $d' = 9$ cm
4. an angle $\theta_c = 63.5°$ between the edge of the reflector and the z-axis
5. an angle $\theta_r = 26.5°$ between the antenna main beam direction and the normal to the plane containing the edge of the reflector
6. an elliptical edge curve with major axis $a = 33$ cm and minor axis $b = 30$ cm

A.2 Cut coordinate system

This section contains the far-field and aperture field results of the TRIAX antenna in the cut CS, see Fig. 4.7 for a picture of the geometrical configuration. It is recalled that the z-axis of the cut CS is aligned with the direction of the antenna's main beam. Far-field distributions are plotted in amplitude in the co- and cross-polar components according to Ludwig's 3rd definition (3.15) with $\phi_o = 0°$ in the uv-plane. Results are in dB and normalized to the maximum of the co-polar component in the nominal configuration. Aperture fields are plotted in amplitude and phase for each of the cartesian components on the $z = 17$ cm plane, together with the projected rim of the reflector (circle of radius $r = 30$ cm centered at $x_o = 2.8$ cm and $y_o = 0$ cm in the cut CS). Amplitude results are in dB and normalized to the maximum value of the x-component of the field in the nominal configuration, phase results are in radians and normalized to the phase of the corresponding cartesian component of the nominal configuration at the origin $x = y = 0$. For details about the introduced mechanical errors, see Paper V or Section 4.1.2.

A.2.1 Far-fields

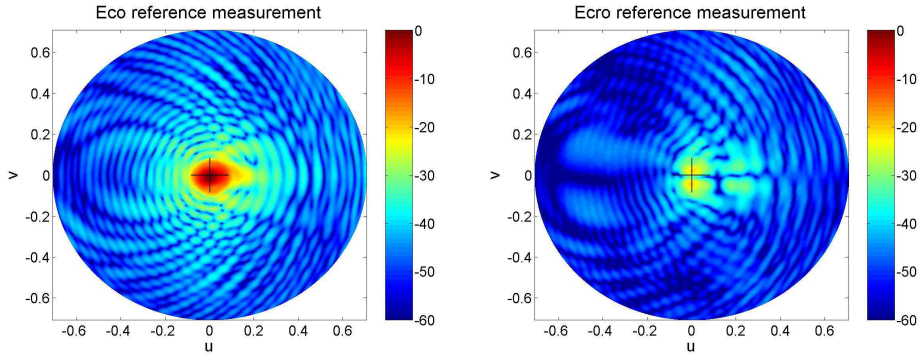

Figure A.2: Amplitude of the co- and cross-polar components in dB of the antenna far-field, nominal configuration.

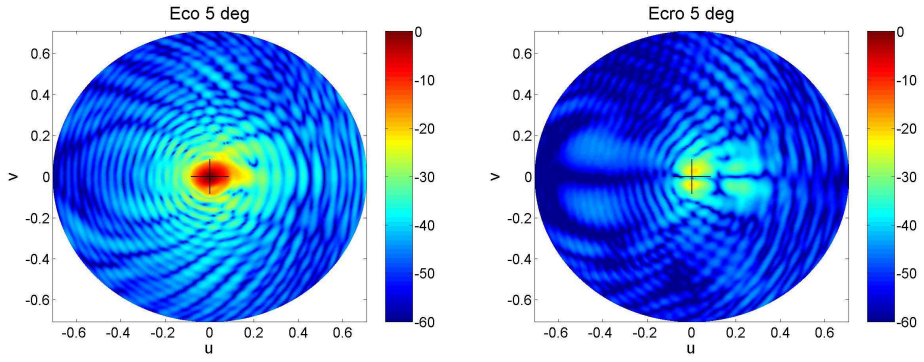

Figure A.3: Amplitude of the co- and cross-polar components in dB of the antenna far-field, 5° feed tilt.

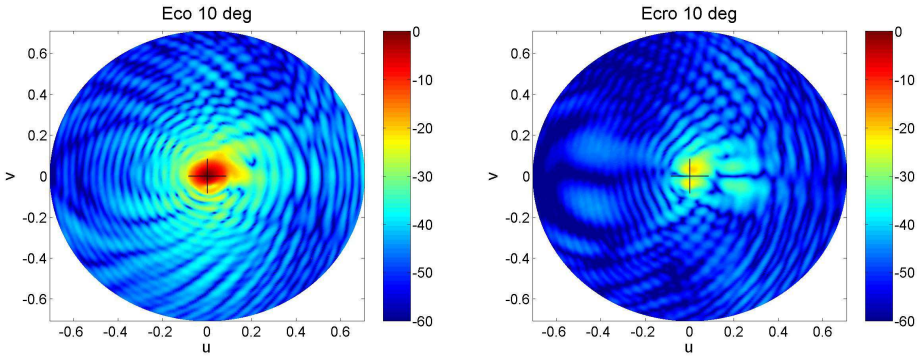

Figure A.4: Amplitude of the co- and cross-polar components in dB of the antenna far-field, 10° feed tilt.

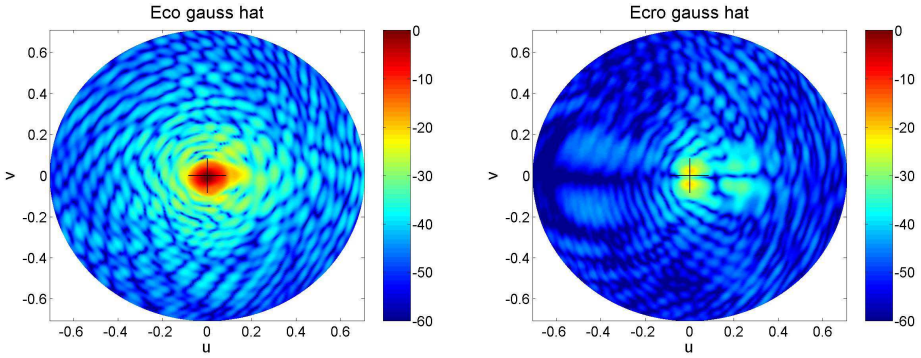

Figure A.5: Amplitude of the co- and cross-polar components in dB of the antenna far-field, Gaussian bump.

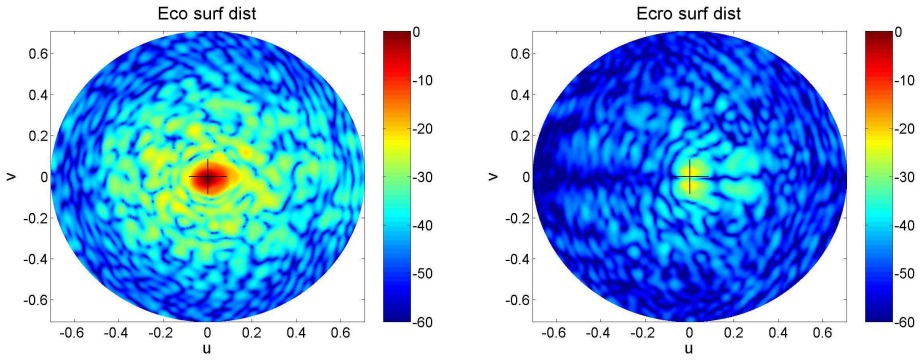

Figure A.6: Amplitude of the co- and cross-polar components in dB of the antenna far-field, surface distortion.

A.2.2 Aperture fields

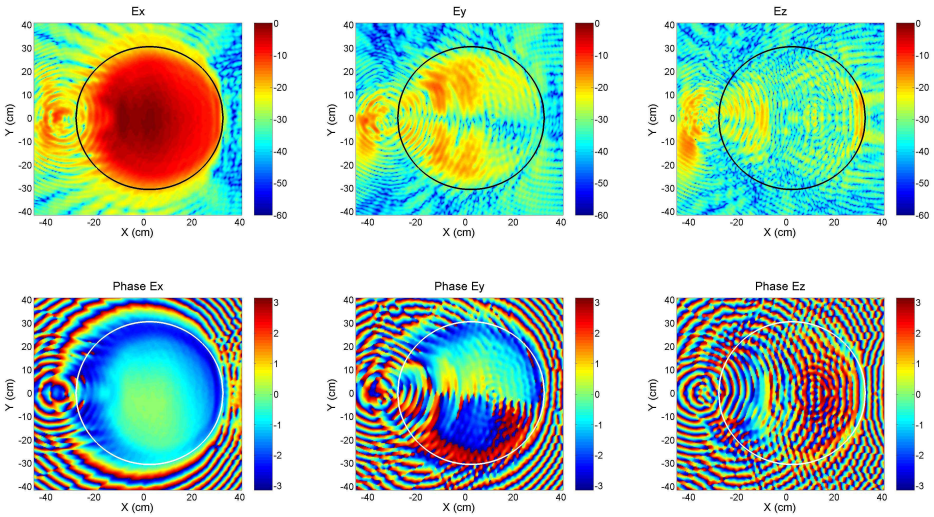

Figure A.7: Amplitude in dB (upper) and phase in radians (lower) of the cartesian components of the electric field on $z = 17$ cm, nominal configuration.

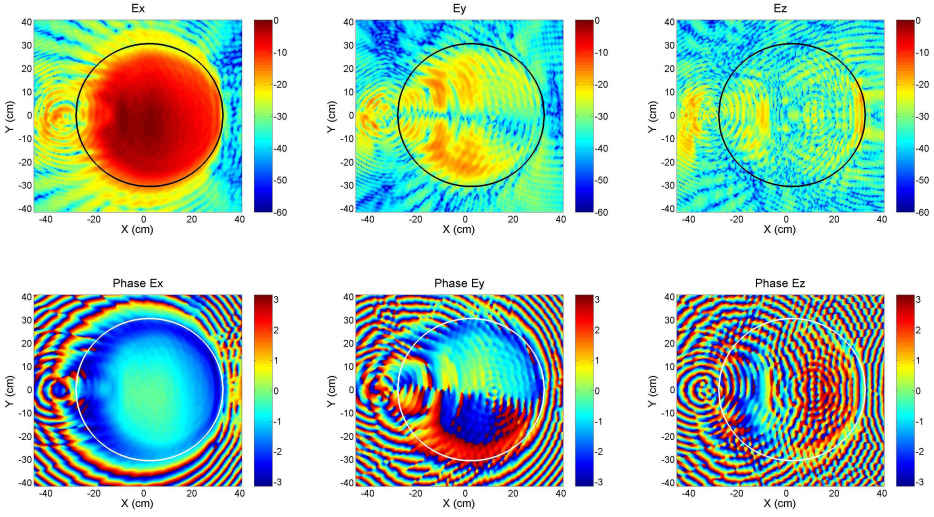

Figure A.8: Amplitude in dB (upper) and phase in radians (lower) of the cartesian components of the electric field on $z = 17$ cm, 5° feed tilt.

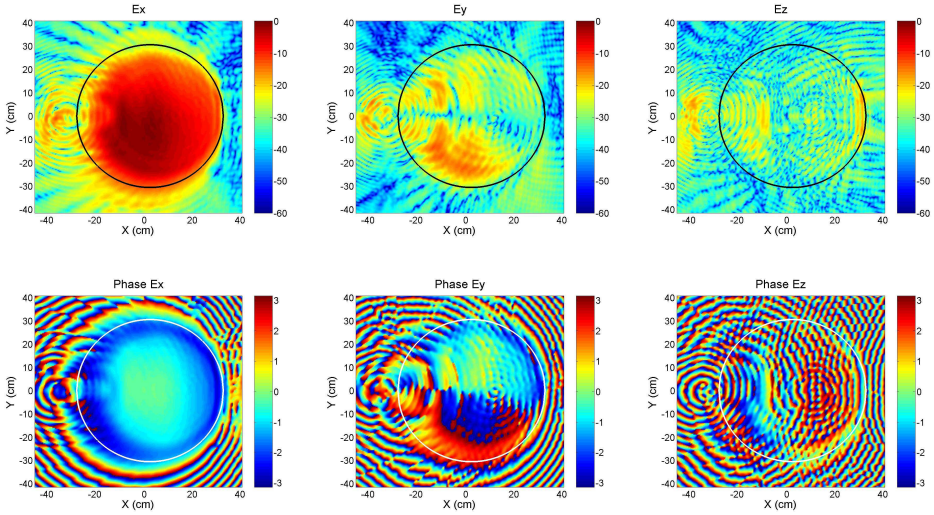

Figure A.9: Amplitude in dB (upper) and phase in radians (lower) of the cartesian components of the electric field on $z = 17$ cm, 10° feed tilt.

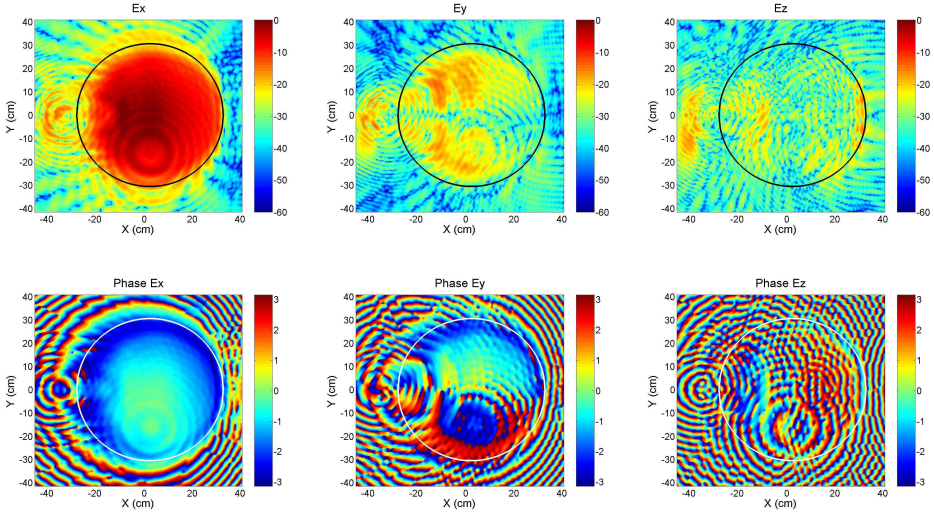

Figure A.10: Amplitude in dB (upper) and phase in radians (lower) of the cartesian components of the electric field on $z = 17$ cm, Gaussian hat.

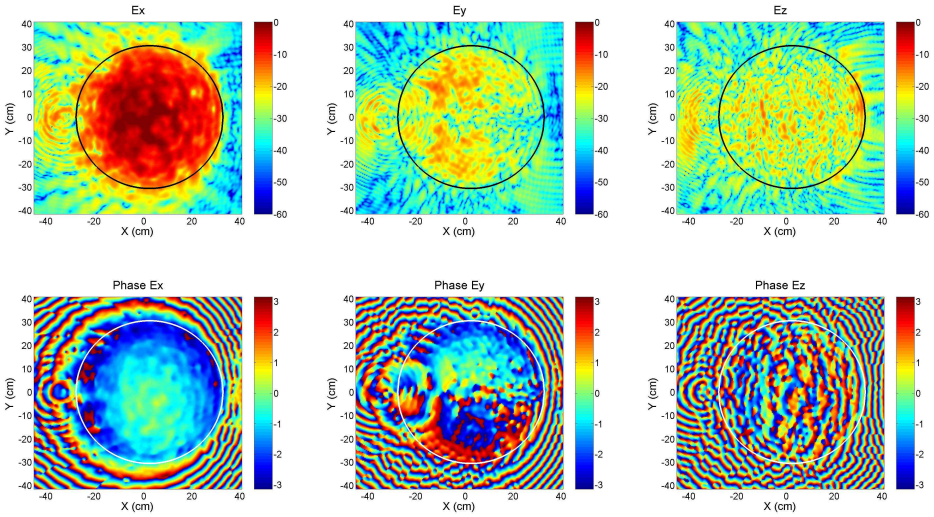

Figure A.11: Amplitude in dB (upper) and phase in radians (lower) of the cartesian components of the electric field on $z = 17$ cm, surface distortion.

A.3 Measurement coordinate system

This section contains the aperture field results of the TRIAX antenna in the measurement CS, see Fig. 4.7 for a picture of the geometrical configuration. It is recalled that the z-axis of the measurement CS is not aligned with the direction of the antenna main beam. Aperture fields are plotted in amplitude and phase for each of the cartesian components on the $z = 0.5$ cm plane, together with the projected rim of the reflector (ellipse of axis $a = 33$ cm and $b = 30$ cm centered at $x_o = 2.6$ cm and $y_o = 0$ cm in the measurement CS). Amplitude results are in dB and normalized to the maximum value of the x-component of the field in the nominal configuration, phase results are in radians and normalized to the phase of the corresponding cartesian component of the nominal configuration at the origin $x = y = 0$. For details about the introduced mechanical errors, see Paper V or Section 4.1.2.

A.3.1 Aperture fields

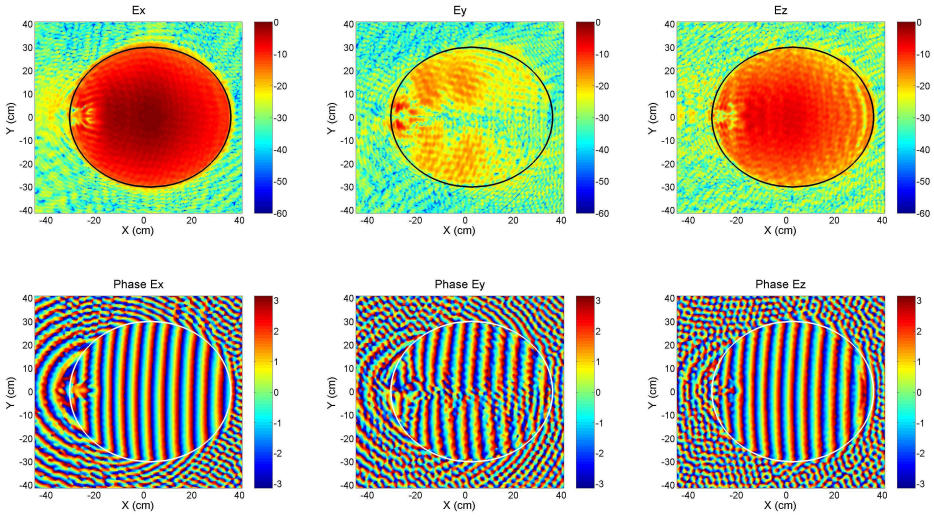

Figure A.12: Amplitude in dB (upper) and phase in radians (lower) of the cartesian components of the electric field on $z = 0.5$ cm, nominal configuration.

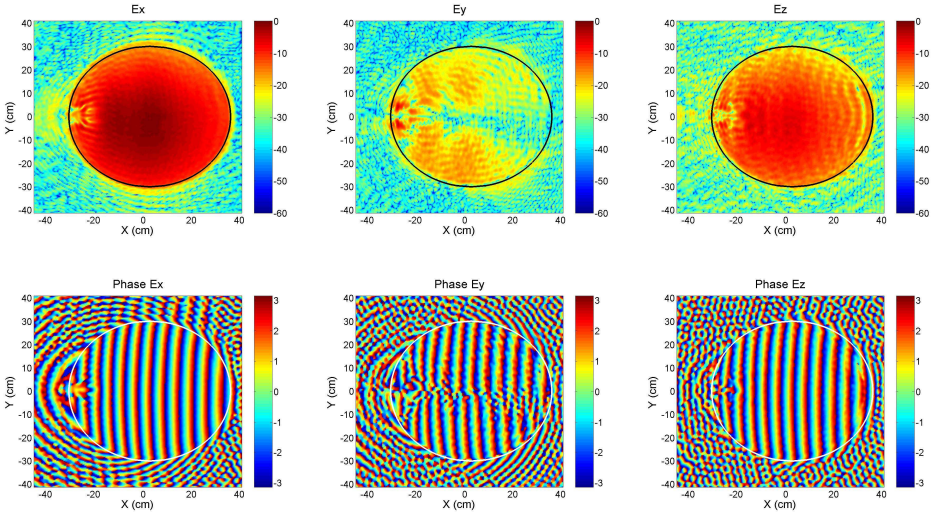

Figure A.13: Amplitude in dB (upper) and phase in radians (lower) of the cartesian components of the electric field on $z = 0.5$ cm, 5° feed tilt.

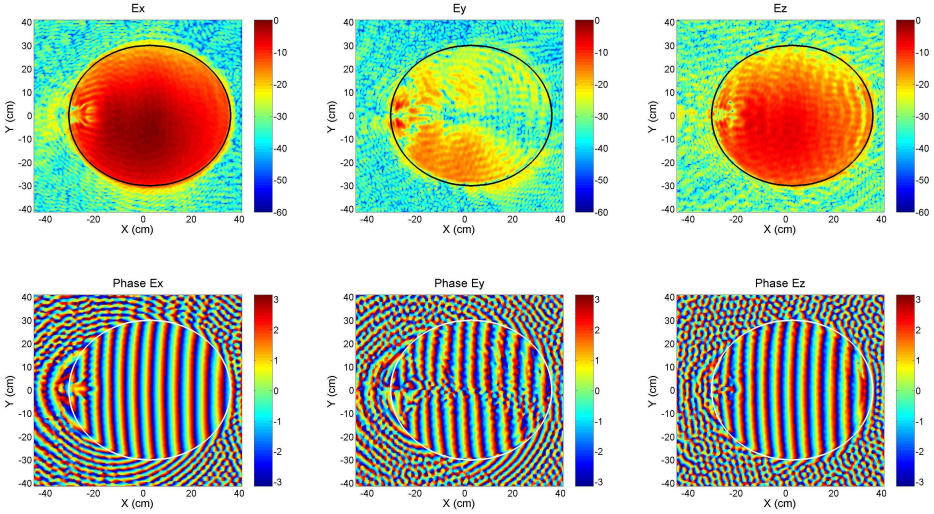

Figure A.14: Amplitude in dB (upper) and phase in radians (lower) of the cartesian components of the electric field on $z = 0.5$ cm, 10° feed tilt.

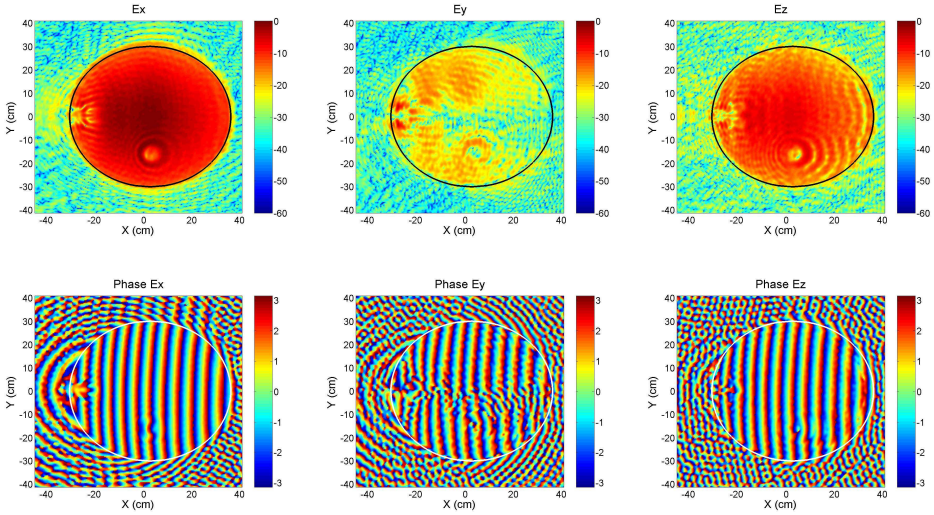

Figure A.15: Amplitude in dB (upper) and phase in radians (lower) of the cartesian components of the electric field on $z = 0.5$ cm, Gaussian hat.

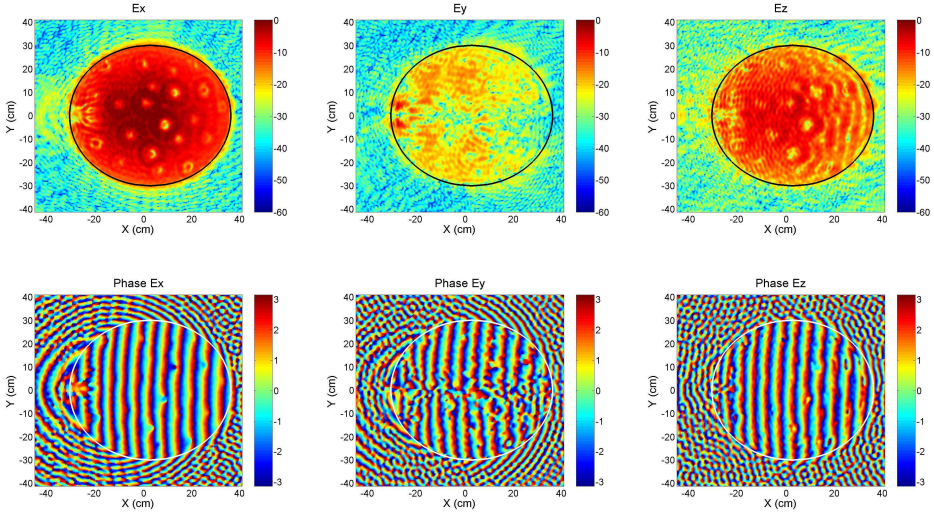

Figure A.16: Amplitude in dB (upper) and phase in radians (lower) of the cartesian components of the electric field on $z = 0.5$ cm, surface distortion.

A.4 GRASP9 simulations for the TRIAX reflector

In Section A.1 we derived the equation of the TRIAX paraboloid and determined the angle θ_r between the antenna main beam direction and the z-axis of the measurement coordinate system. This allowed us to rotate the SWE defined in the measurement CS and perform a diagnostics also in the cut CS, to better identify the mechanical errors. After the computation of the field of the reflector in the nominal configuration at the z=17 cm plane, see Fig. A.7, it was clear that the antenna was not an ideal paraboloid. The non-ideal characteristics were particularly evident in the phase of the x-component of the field. It was thus decided to build a model of the TRIAX reflector with the software GRASP9, and study the antenna more in detail.
The reflector model was designed according to the parameters derived in Section A.1: a 12 GHz parabolic offset reflector described in the xyz-coordinate system by a circular projected rim of diameter $D_{proj} = 60$ cm, a focal length $f = 39$ cm and a clearance $d' = 9$ cm, see Fig. A.17. The feed, located at the focal point, was linearly polarized along x_f, where $x_f y_f z_f$ was the feed coordinate system, with origin at the focus and with z_f pointing towards the center point of the reflector.

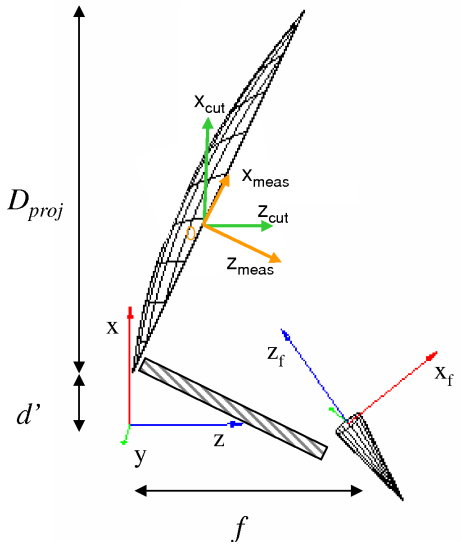

Figure A.17: Model of the TRIAX reflector.

The real feed of the TRIAX reflector was a conical horn with aperture of diameter 4.5 cm. A full sphere measurement of the feed was performed at the DTU-ESA Facility and the SWE of the radiated field was obtained, see Fig. A.18 for a plot of the co- and cross-polar components of the feed far-field pattern in dB in the $\phi = 0°$ and $\phi = 90°$ cuts. It is seen that the co-polar component is similar in the two plots, and that the cross-polar component is low though not negligible. The measured SWE was used in the GRASP9 model to describe the radiation

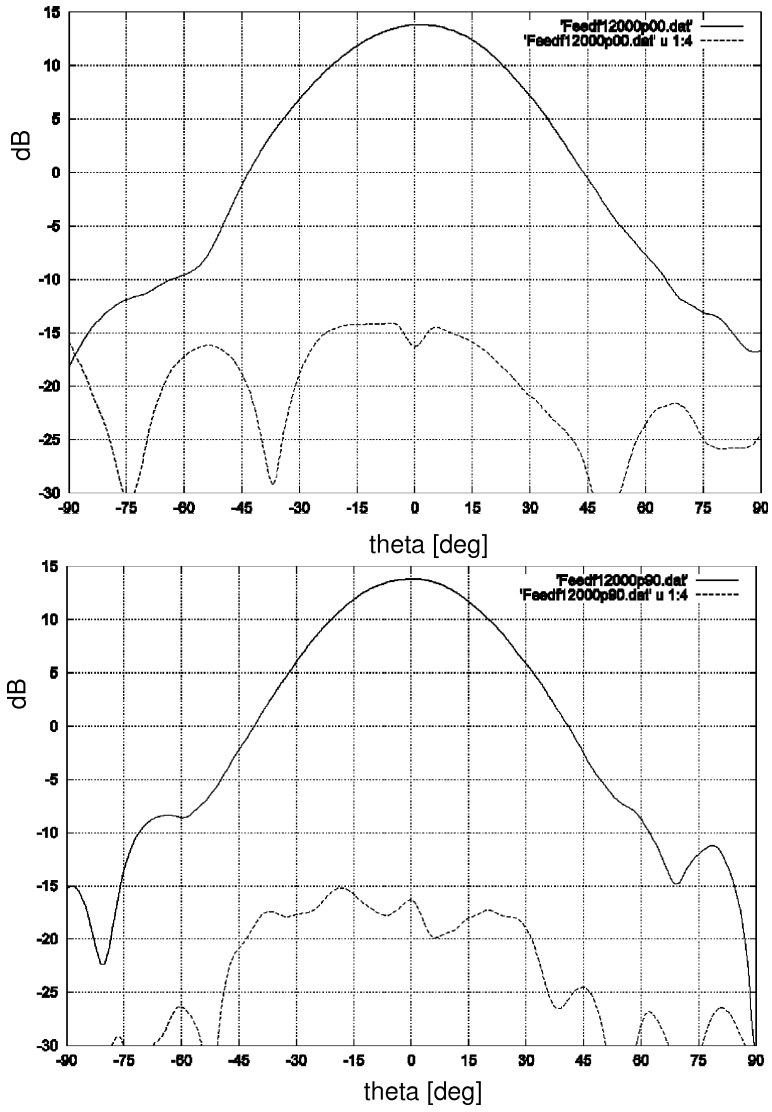

Figure A.18: Co- and cross-polar components of the far-field pattern in dB of the feed of the TRIAX reflector in the principle planes: $\phi = 0°$ (upper), $\phi = 90°$ (lower).

from the feed and thus the field illuminating the reflector. A strut of rectangular cross-section 5 cm x 2 cm and length of 38 cm, according to the dimensions of the arm supporting the feed, was finally added to the model.
The pattern given by the TRIAX model was compared with the measured pattern for the antenna in the nominal configuration, see Figs. A.19 and A.20 (above the entire theta range, below a zoom) in the cut coordinate system. The computa-

tion with GRASP9 was performed by Physical Optics (PO) and Physical Theory of Diffraction (PTD). As it is seen, patterns are quite different. In particular, at $\phi = 0°$ the peak of the measured main beam is 2 dB lower than the one obtained by the GRASP9 simulation. Also, its width is definitely broader with the consequence that the first sidelobe disappears. On the other hand the remaining sidelobes agree quite well with the designed ones. The measured ϕ-component is quite in agreement, in shape and peak, with the designed one. PO and PTD are however not accurate in describing the radiation for $130° < \theta < 180°$. For $\phi = 90°$ the peak of the measured pattern is again 2 dB lower than the one computed by GRASP9, and also slightly shifted. A similar behavior is seen in the θ-component. In this cut PO and PTD provide quite accurate results.
From the analysis conducted in Section 4.1.1 the far-field shift in Fig. A.20 was interpreted as given by a feed defocusing. The differences in the peak and width of the main lobe, together with the good agreement of the majority of the sidelobes, were instead thought as given by a slow distortion of the reflector surface. The model was thus modified according to these observations and the method of analysis was changed, using Method of Moments (MOM) for the entire scatterer given by the reflector and the strut, to more accurately compute the diffraction from the strut. After several experiments, it was found that the model that best fitted the measurements results assumed the existence of several mechanical inaccuracies. The final model of the TRIAX antenna was constituted by:

1. a 12 GHz parabolic offset reflector described in the xyz-coordinate system by a circular projected rim of diameter $D_{proj} = 60$ cm, a focal length $f = 39$ cm and a clearance $d' = 9$ cm, see Fig. A.17

2. a feed, located at the focal point and linearly polarized along x_f, where $x_f y_f z_f$ was the feed coordinate system

3. a strut of rectangular cross-section 5 cm x 2 cm and length of 38 cm

4. a slow surface distortion of amplitude $\pm$ 0.3 cm, randomly distributed, described by 4 nodes in the x-direction and 3 nodes in the y-direction, for details see Section 4.1.1 or GRASP9 technical description [55]

5. a feed tilt of 7° around x_f and of 3° around y_f

6. a feed defocusing of -5 mm along x_f and of -9 mm along y_f

Results are in Figs. A.21 and A.22. It is noted that MOM better describes the radiation at large θ values. Looking at a smaller angular region, it is evident how the shape of the main lobe is now correctly reconstructed in peak, width and position, though results are slightly better at $\phi = 0°$ than at $\phi = 90°$. The envelope of the first sidelobes is also very well represented. There are however some differences, mostly in the ϕ-component at $\phi = 0°$ and in the θ-component at $\phi = 90°$, were results get worse with respect to the ones obtained by the ideal model of Figs. A.19 and A.20. This is probably because the surface distortion of the TRIAX antenna is in practice not random, like in the GRASP9 model, but

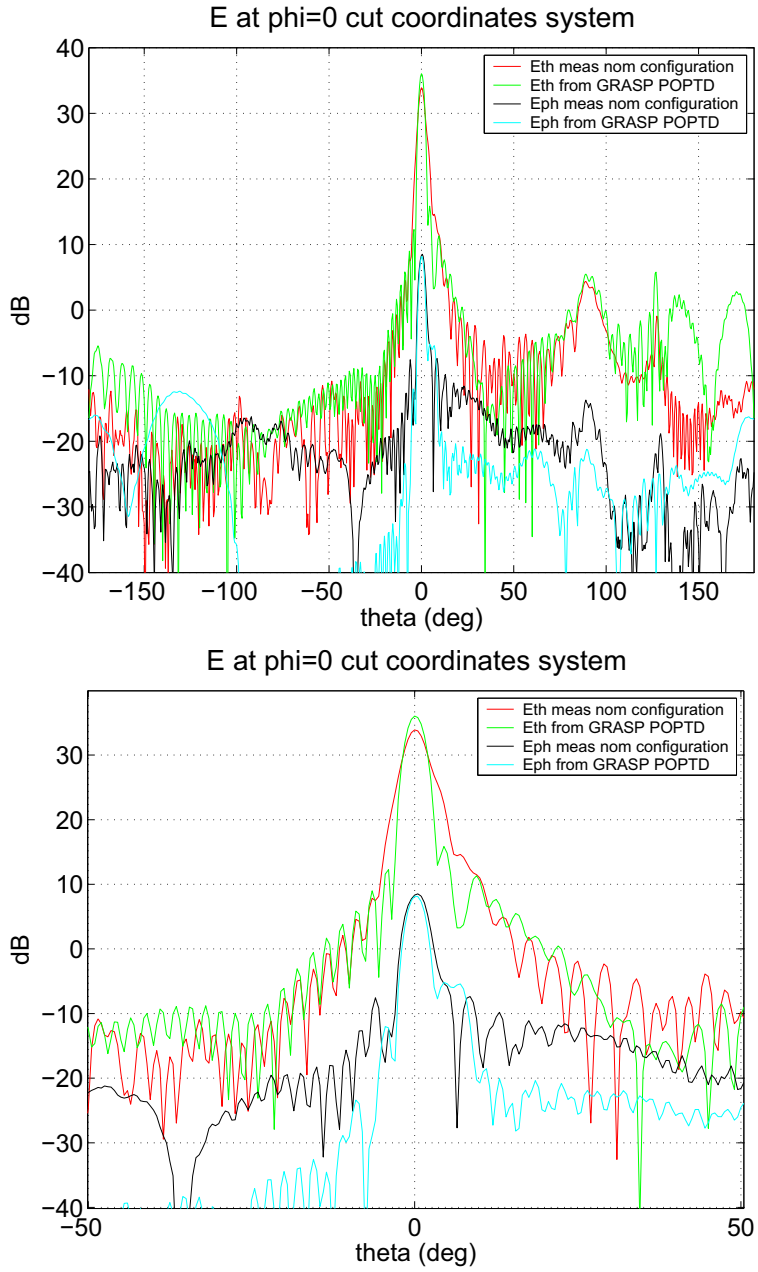

Figure A.19: Theta- and phi-components of the far-field pattern in dB of the TRIAX reflector at $\phi = 0°$: measurements results and GRASP9 simulations for the nominal configuration.

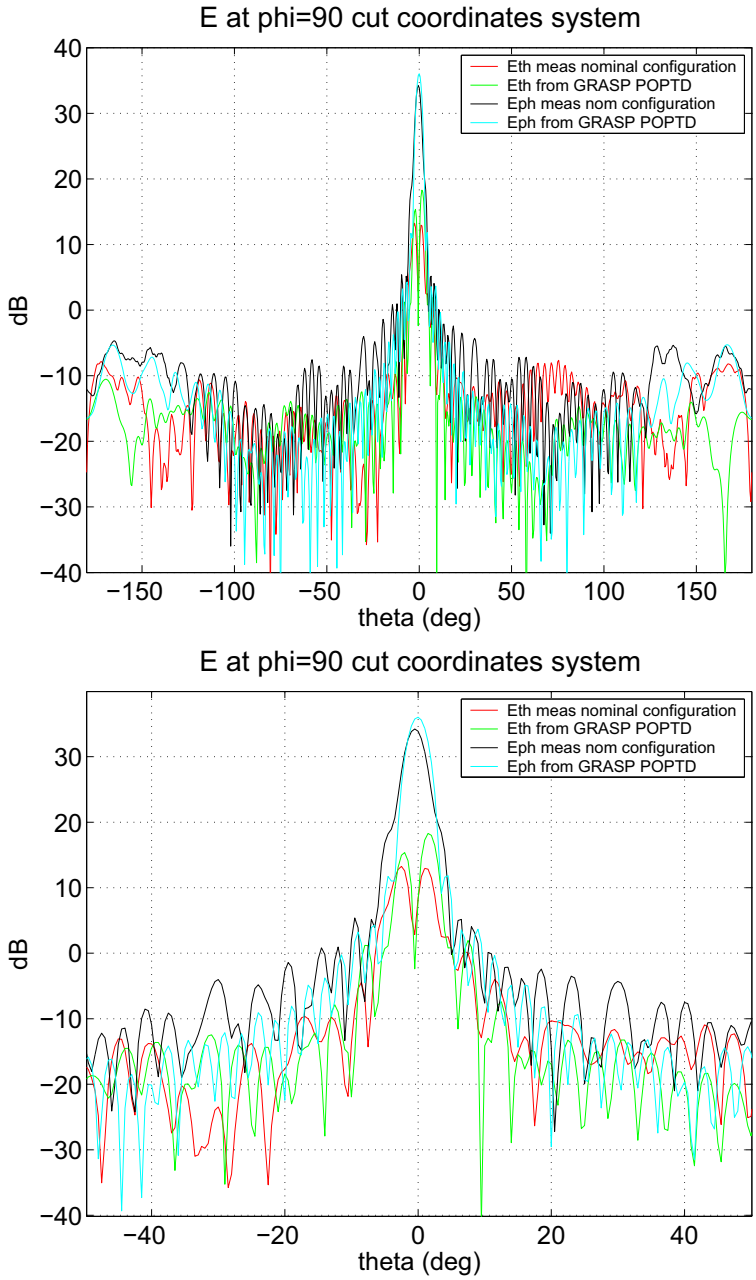

Figure A.20: Theta- and phi-components of the far-field pattern in dB of the TRIAX reflector at $\phi = 90°$: measurements results and GRASP9 simulations for the nominal configuration.

described by a smoother and slower varying surface which less influences the cross-polar components. The parameters used in the final model were however the ones that best reconstructed the radiation of the θ-component at $\phi = 0^\circ$ in the angular region $-30^\circ < \theta < 30^\circ$.

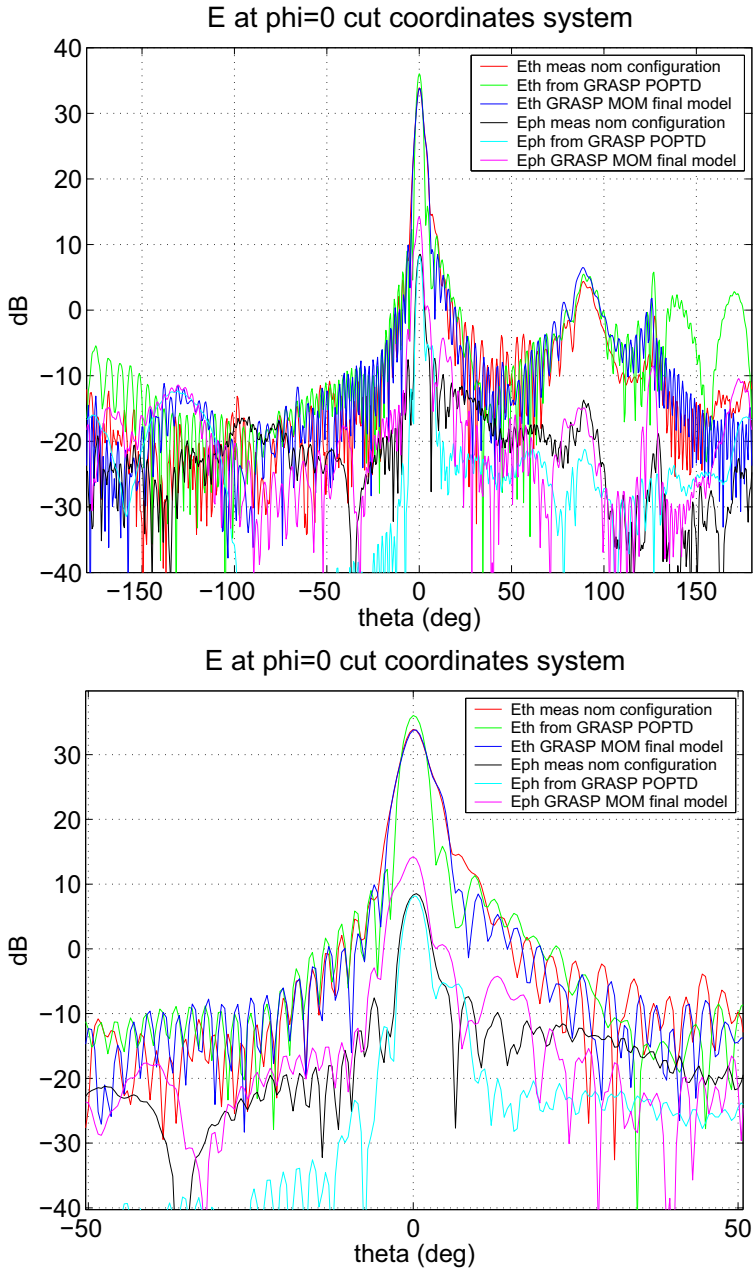

Figure A.21: Theta- and phi-components of the far-field pattern in dB of the TRIAX reflector at $\phi = 0°$: measurements results and GRASP simulations for the nominal configuration.

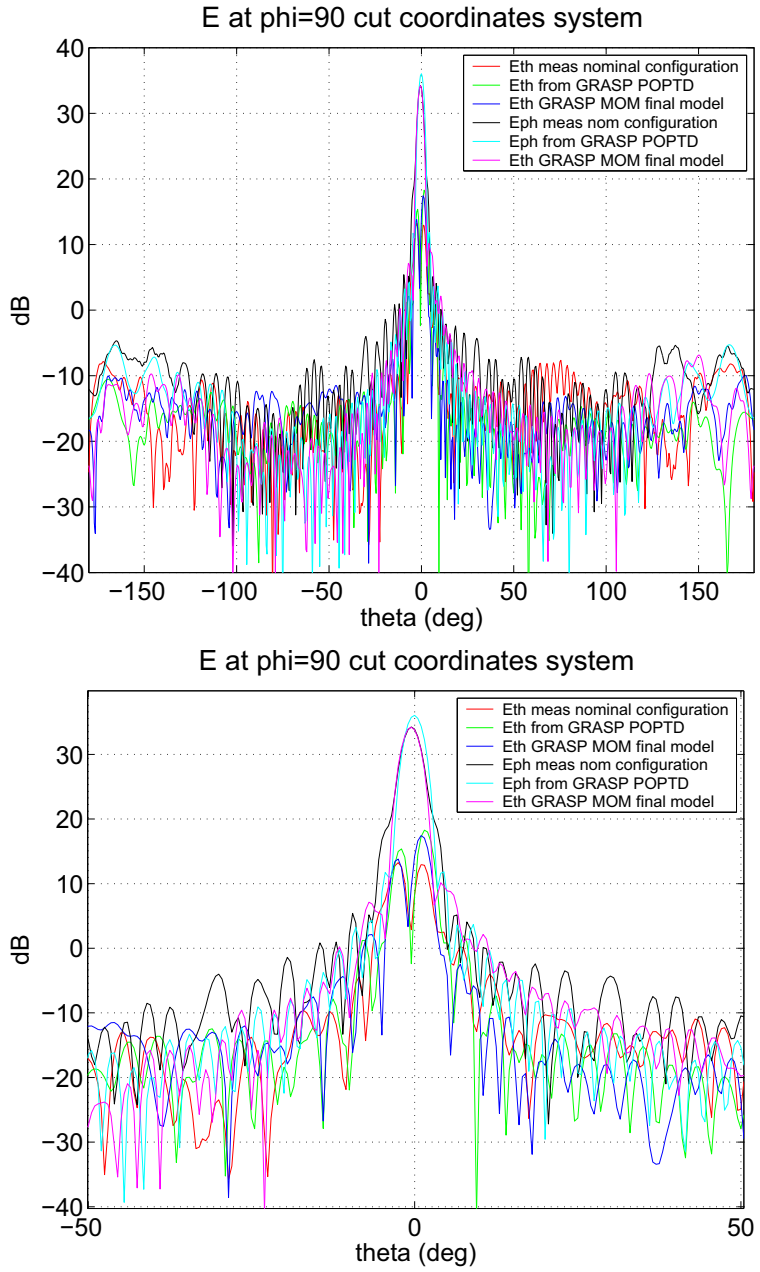

Figure A.22: Theta- and phi-components of the far-field pattern in dB of the TRIAX reflector at $\phi = 90°$: measurements results and GRASP simulations for the nominal configuration.

Appendix B

SMOS radiometer antenna units

The diagnostics results obtained for the SMOS radiometer antenna units are reported. Aperture fields are computed in cartesian components in amplitude and phase on the z-plane placed on the surface of the Kapton-Germanium layer, located at z = -5 mm in the measurement coordinate system. Amplitude results are in dB and normalized to the maximum of the x-component, phase results are in radians and are not normalized. The circle corresponding to the average dimension of the circular patch is also drawn. Three sets of results are provided for every unit: first the aperture field, presented also in Paper VI and showing an evident truncation effect, second the aperture field with use of the Hanning window, third the aperture field with use of the CDA algorithm. While amplitude and phase are shown for the first two sets, phase results computed with CDA are shown only for the unit BC03, to prove that the quantity can not be correctly reconstructed by the algorithm. Only one frequency, f = 1.423 GHz, is considered for the units BC03 and A01, since same results were obtained for the other two frequencies of interest. All frequencies are taken into account for the unit A05.

B.1 BC03 unit, $f = 1.423$ GHz

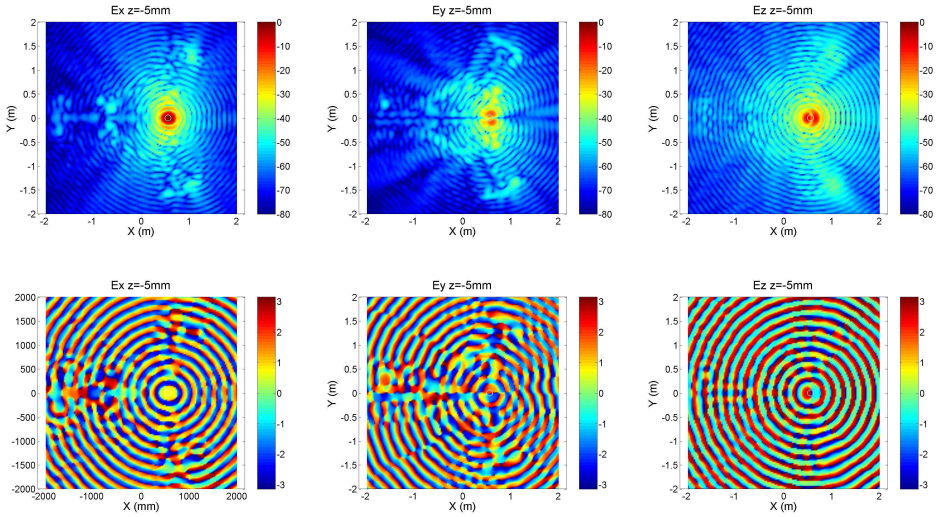

Figure B.1: Amplitude in dB (upper) and phase in radians (lower) of the cartesian components of the electric field on z = -5 mm, unit BC03.

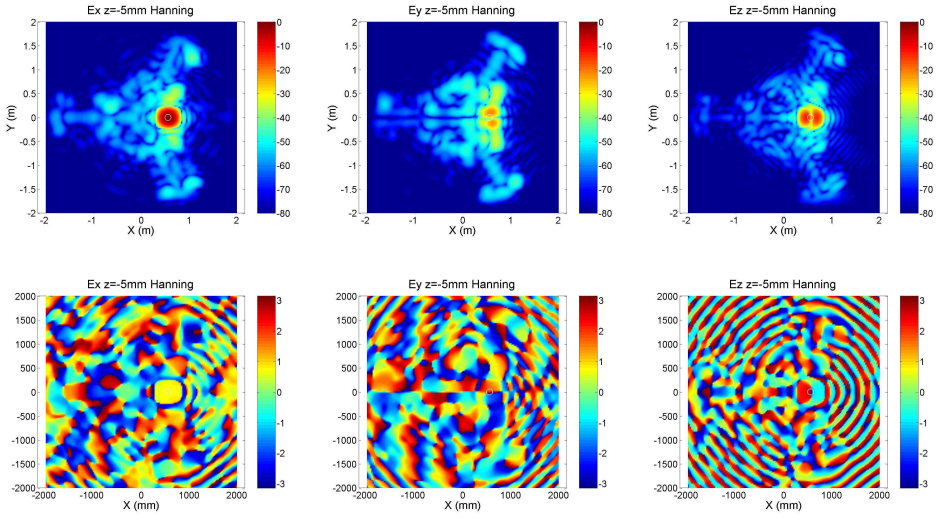

Figure B.2: Amplitude in dB (upper) and phase in radians (lower) of the cartesian components of the electric field on z = -5 mm, unit BC03 with Hanning window.

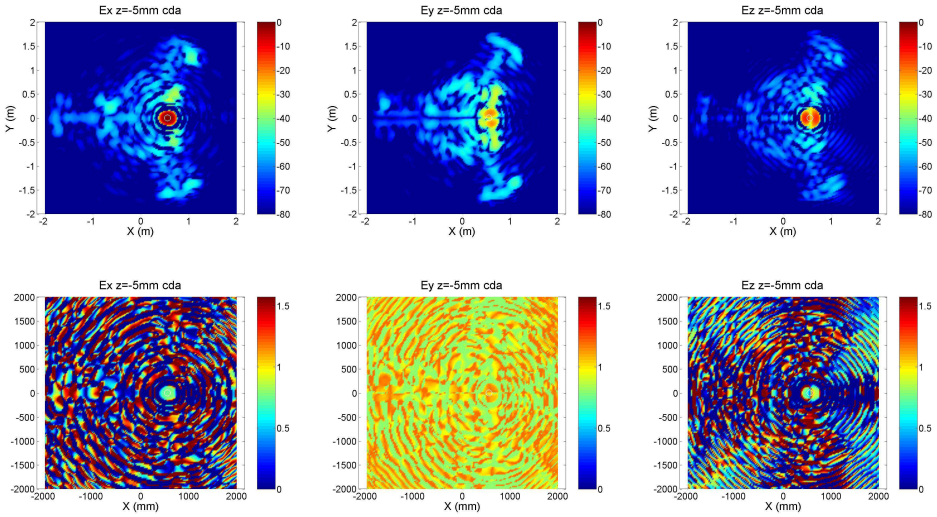

Figure B.3: Amplitude in dB (upper) and phase in radians (lower) of the cartesian components of the electric field on z = -5 mm, unit BC03 with CDA.

B.2 A05 unit, f = 1.404 GHz

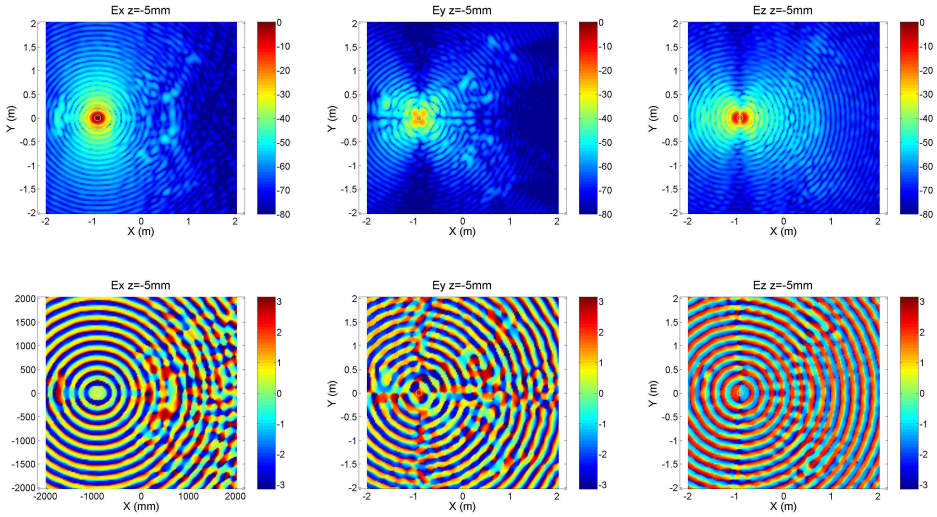

Figure B.4: Amplitude in dB (upper) and phase in radians (lower) of the cartesian components of the electric field on z = -5 mm, unit A05.

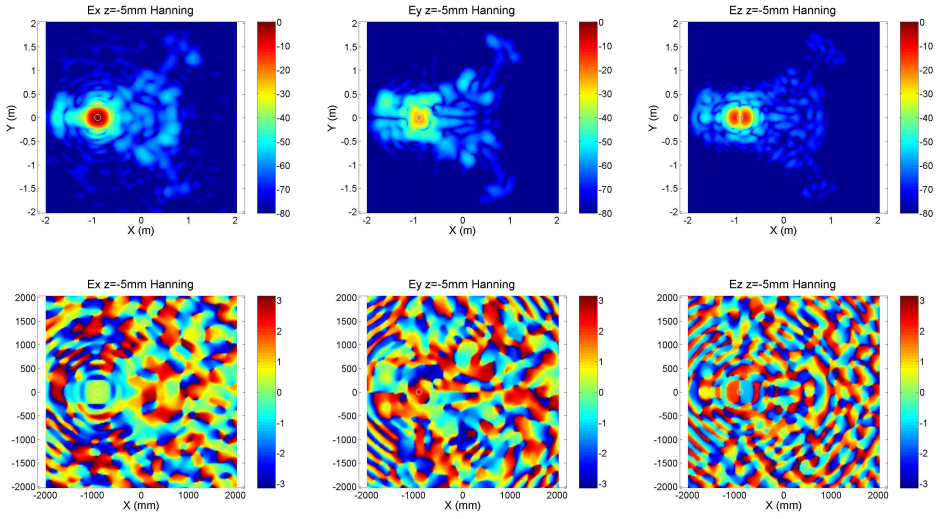

Figure B.5: Amplitude in dB (upper) and phase in radians (lower) of the cartesian components of the electric field on z = -5 mm, unit A05 with Hanning window.

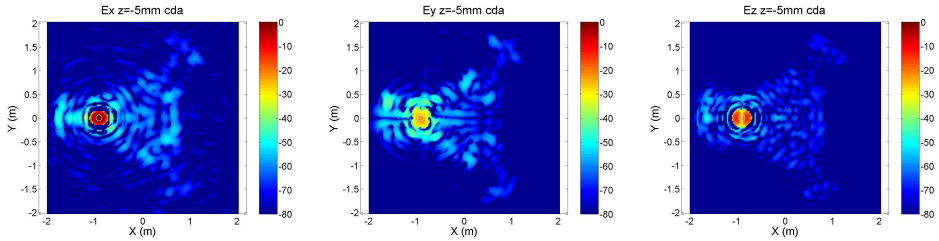

Figure B.6: Amplitude in dB (upper) and phase in radians (lower) of the cartesian components of the electric field on z = -5 mm, unit A05 with CDA.

B.3 A05 unit, f = 1.413 GHz

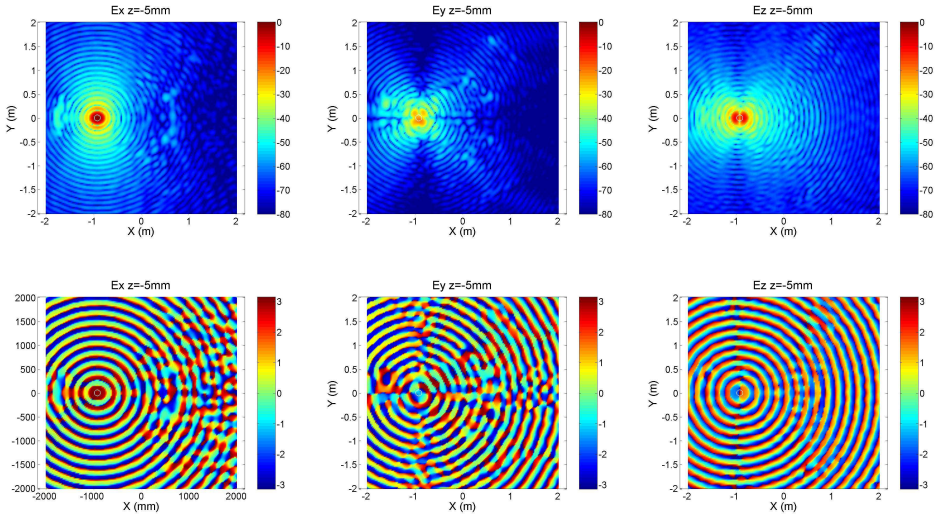

Figure B.7: Amplitude in dB (upper) and phase in radians (lower) of the cartesian components of the electric field on z = -5 mm, unit A05.

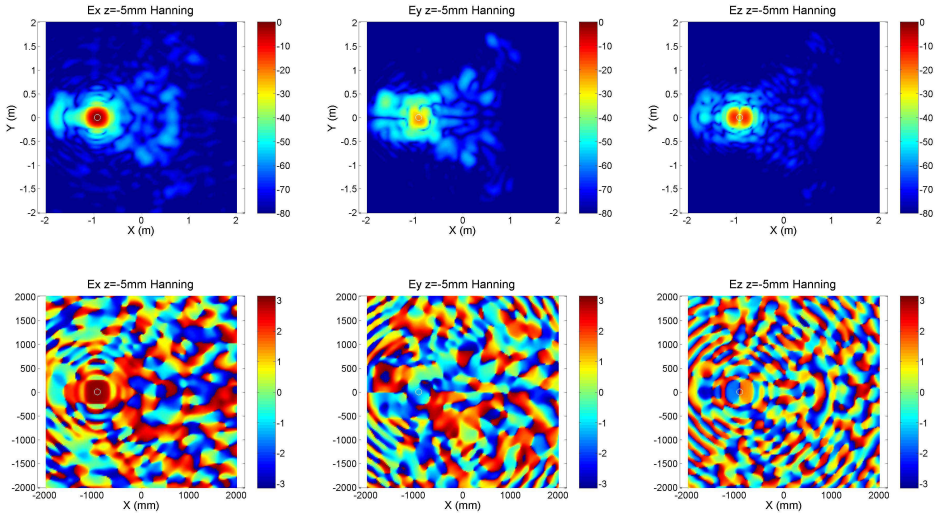

Figure B.8: Amplitude in dB (upper) and phase in radians (lower) of the cartesian components of the electric field on z = -5 mm, unit A05 with Hanning window.

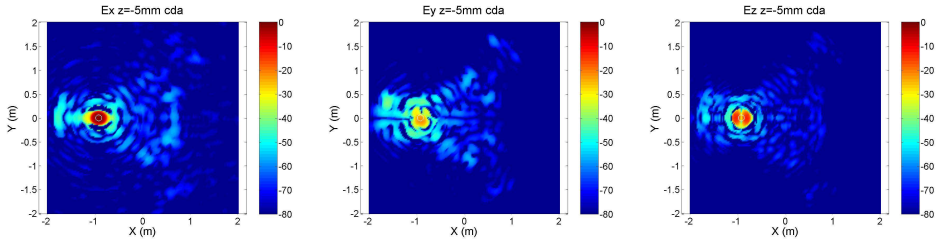

Figure B.9: Amplitude in dB (upper) and phase in radians (lower) of the cartesian components of the electric field on z = -5 mm, unit A05 with CDA.

B.4 A05 unit, f = 1.423 GHz

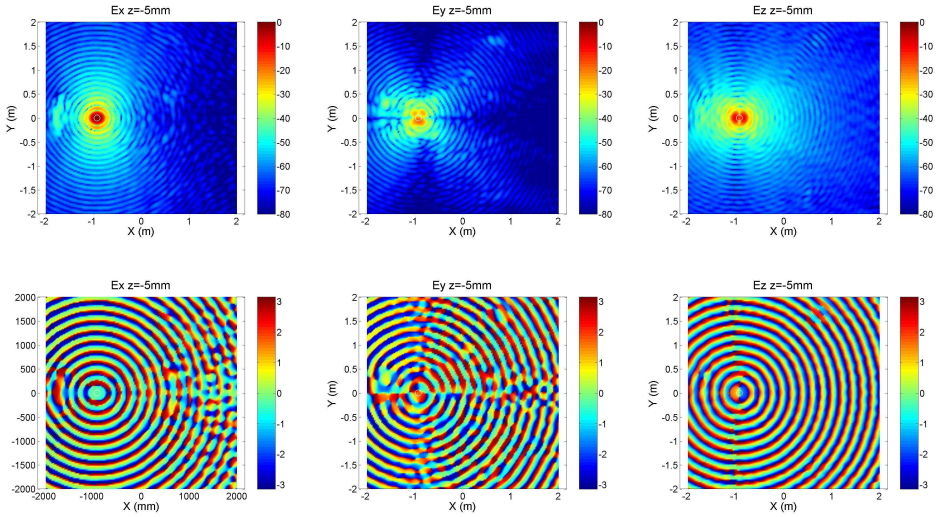

Figure B.10: Amplitude in dB (upper) and phase in radians (lower) of the cartesian components of the electric field on z = -5 mm, unit A05.

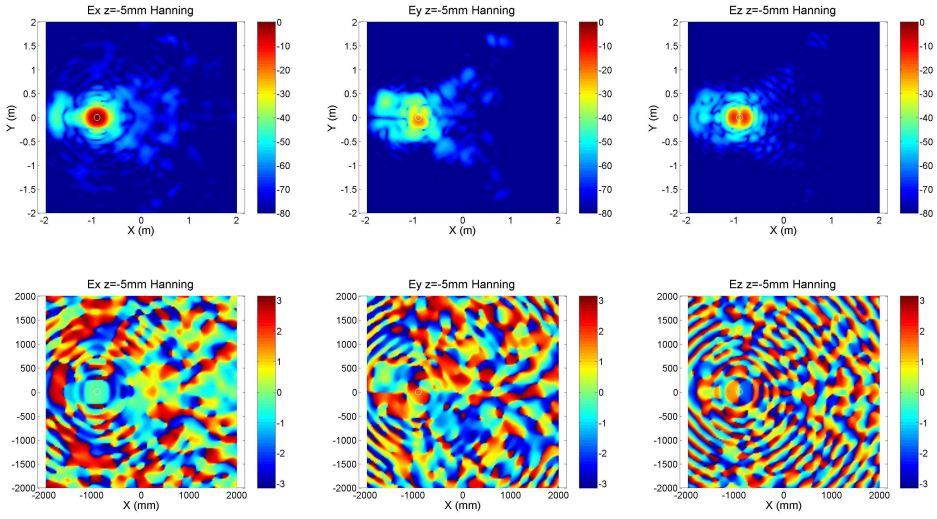

Figure B.11: Amplitude in dB (upper) and phase in radians (lower) of the cartesian components of the electric field on z = -5 mm, unit A05 with Hanning window.

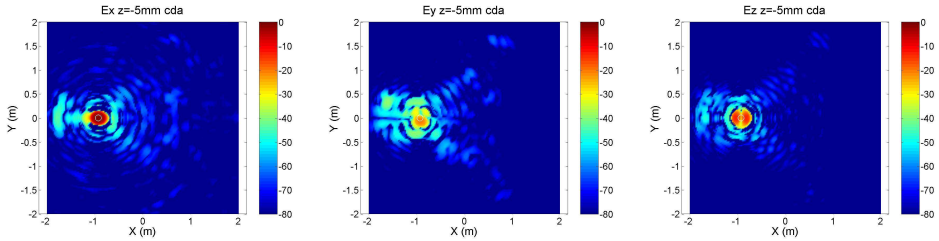

Figure B.12: Amplitude in dB (upper) and phase in radians (lower) of the cartesian components of the electric field on z = -5 mm, unit A05 with CDA.

B.5 A01 unit, f = 1.423 GHz

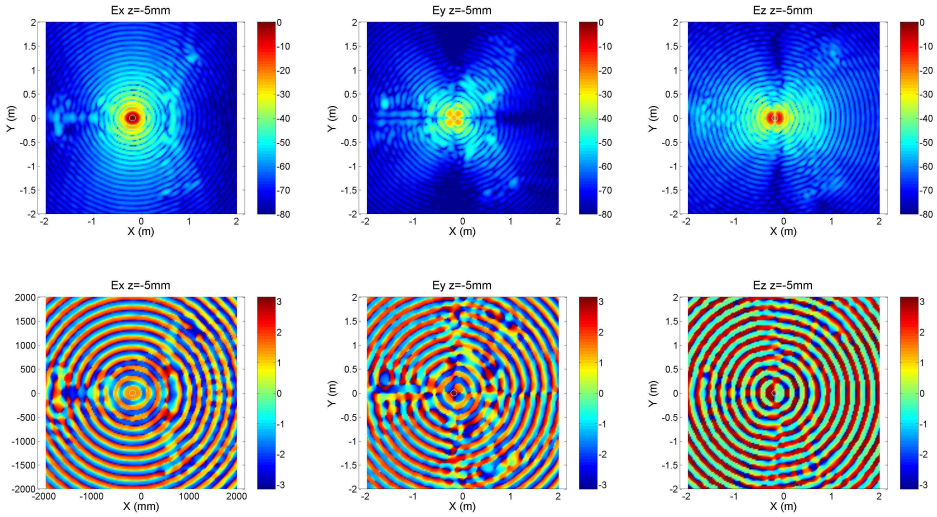

Figure B.13: Amplitude in dB (upper) and phase in radians (lower) of the cartesian components of the electric field on z = -5 mm, unit A01.

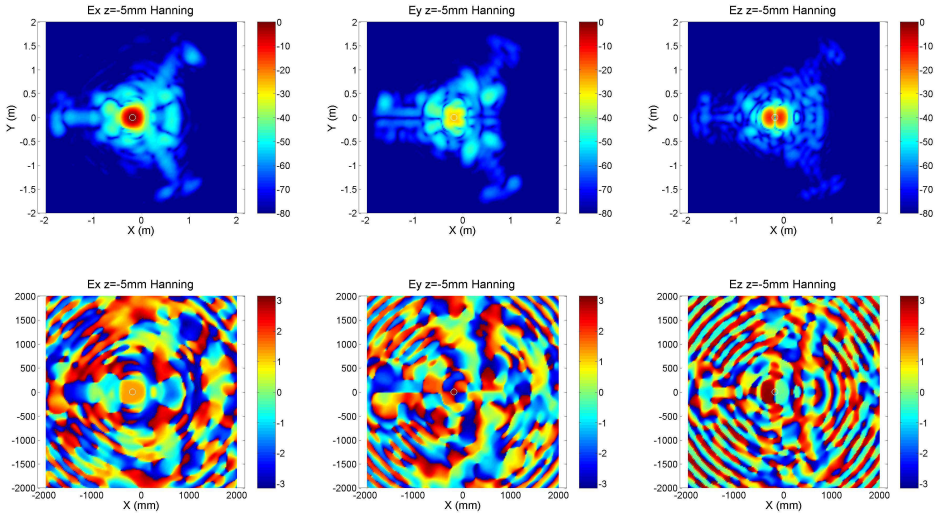

Figure B.14: Amplitude in dB (upper) and phase in radians (lower) of the cartesian components of the electric field on z = -5 mm, unit A01 with Hanning window.

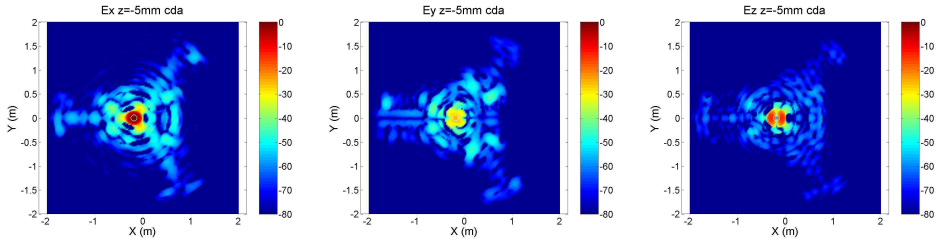

Figure B.15: Amplitude in dB (upper) and phase in radians (lower) of the cartesian components of the electric field on z = -5 mm, unit A01 with CDA.

Appendix C

SWE-to-PWE computation

The SWE-to-PWE transformation is here analyzed from a computational point of view. In particular, the computation of the plane wave spectrum in the invisible region of the spectral domain as given by (2.48) is considered. In section C.1 the series of (2.48) is rewritten in a simplified form. In section C.2 the computation of the normalized associated Legendre functions is described. In section C.3 the embedding of the exponential term is discussed, in order to control the exponential growth of the Legendre functions in the invisible region, and guidelines for the selection of an appropriate z-plane are provided.

C.1 Plane wave spectrum computation

We start by considering the expression of the plane wave spectrum written in function of the Q coefficients of the SWE, as presented in (2.48)

$$\vec{T}(k_x, k_y, z) = \sum_{n=1}^{\infty} \sum_{m=-n}^{n} Q_{1mn}^{(3)} \vec{T}_{1mn}(k_x, k_y, z) + Q_{2mn}^{(3)} \vec{T}_{2mn}(k_x, k_y, z) \tag{C.1}$$

with

$$\vec{T}_{1mn}(k_x, k_y, z) = \frac{e^{ik_z z}}{k_z} \frac{(-i)^{n+1}}{\sqrt{\eta}\sqrt{n(n+1)}} \vec{Y}_n^m(\alpha, \beta) \tag{C.2}$$

$$\vec{T}_{2mn}(k_x, k_y, z) = \frac{e^{ik_z z}}{k_z} \frac{(-i)^{n}}{\sqrt{\eta}\sqrt{n(n+1)}} \hat{k} \times \vec{Y}_n^m(\alpha, \beta). \tag{C.3}$$

Except for the factor $\frac{e^{ik_z z}}{k_z}$, equation (C.1) coincides with (2.45)

$$\tilde{E}(\alpha, \beta) = \sum_{n=1}^{\infty} \sum_{m=-n}^{n} \frac{(-i)^n}{\sqrt{\eta}\sqrt{n(n+1)}} \Big[-iQ_{1mn}^{(3)} \vec{Y}_n^m(\alpha, \beta) + Q_{2mn}^{(3)} \hat{k} \times \vec{Y}_n^m(\alpha, \beta) \Big]. \tag{C.4}$$

By writing the vector spherical harmonics $\vec{Y}_n^m(\alpha,\beta)$ in the α- and β-components,

$$\vec{Y}_n^m(\alpha,\beta) = \frac{-i}{\sqrt{2\pi}}\Big(-\frac{m}{|m|}\Big)^m\Big(-\frac{im}{\sin\alpha}\bar{P}_n^{|m|}(\cos\alpha)e^{im\beta}\hat{\alpha} + \frac{d}{d\alpha}\bar{P}_n^{|m|}(\cos\alpha)e^{im\beta}\hat{\beta}\Big) \tag{C.5}$$
$$= Y_{n\alpha}^m(\alpha,\beta)\hat{\alpha} + Y_{n\beta}^m(\alpha,\beta)\hat{\beta}$$

with $\hat{\alpha} = \cos\alpha\cos\beta\hat{x} + \cos\alpha\sin\beta\hat{y} - \sin\alpha\hat{z}$ and $\hat{\beta} = -\sin\beta\hat{x} + \cos\beta\hat{y}$, and by inserting it into (C.4), we obtain

$$\tilde{E}(\alpha,\beta) = \sum_{n=1}^{N}\sum_{m=-M}^{M}\frac{(-i)^n}{\sqrt{\eta}\sqrt{n(n+1)}}\Big[\Big(-iQ_{1mn}^{(3)}Y_{n\alpha}^m(\alpha,\beta) - Q_{2mn}^{(3)}Y_{n\beta}^m(\alpha,\beta)\Big)\hat{\alpha} \tag{C.6}$$
$$+\Big(-iQ_{1mn}^{(3)}Y_{n\beta}^m(\alpha,\beta) + Q_{2mn}^{(3)}Y_{n\alpha}^m(\alpha,\beta)\Big)\hat{\beta}\Big]$$
$$= \tilde{E}_\alpha(\alpha,\beta)\hat{\alpha} + \tilde{E}_\beta(\alpha,\beta)\hat{\beta},$$

where the truncation numbers N and M with $M \leq N$, for the n- and m-modes respectively, have been used.
Since the associated Legendre functions depend on $|m|$, the summation over the indices n and m in (C.6) can be computed in a more efficient way, see Fig. C.1, according to

$$\tilde{E}(\alpha,\beta) = \sum_{m=1}^{M}\sum_{n=m}^{N}.... + \sum_{m=-1}^{-M}\sum_{n=|m|}^{N}.... + \sum_{n=1}^{N}\Big|_{m=0} \tag{C.7}$$

and obtaining, after a few mathematical steps,

$$\tilde{E}_\alpha(\alpha,\beta) = \sum_{m=1}^{M}\sum_{n=m}^{N}\frac{i(-i)^n}{\sqrt{\eta}\sqrt{n(n+1)2\pi}}\Big[\frac{m}{\sin\alpha}\bar{P}_n^{|m|}(\cos\alpha)\Big(Q_{1mn}^{(3)}(-1)^m e^{im\beta} \tag{C.8}$$
$$-Q_{1-mn}^{(3)}e^{-im\beta}\Big) + \frac{d}{d\alpha}\bar{P}_n^{|m|}(\cos\alpha)\Big(Q_{2mn}^{(3)}(-1)^m e^{im\beta} + Q_{2-mn}^{(3)}e^{-im\beta}\Big)\Big] + term_a$$

and

$$\tilde{E}_\beta(\alpha,\beta) = \sum_{m=1}^{M}\sum_{n=m}^{N}\frac{(-i)^n}{\sqrt{\eta}\sqrt{n(n+1)2\pi}}\Big[\frac{m}{\sin\alpha}\bar{P}_n^{|m|}(\cos\alpha)\Big(-Q_{2mn}^{(3)}(-1)^m e^{im\beta} \tag{C.9}$$
$$+Q_{2-mn}^{(3)}e^{-im\beta}\Big) - \frac{d}{d\alpha}\bar{P}_n^{|m|}(\cos\alpha)\Big(Q_{1mn}^{(3)}(-1)^m e^{im\beta} + Q_{1-mn}^{(3)}e^{-im\beta}\Big)\Big] + term_b.$$

The quantities $term_a$ and $term_b$ correspond to the contribution for $m = 0$ and are given by

$$term_a = \sum_{n=1}^{N}\frac{i(-i)^n}{\sqrt{\eta}\sqrt{2\pi n(n+1)}}Q_{20n}^{(3)}\frac{d}{d\alpha}\bar{P}_n^0(\cos\alpha) \tag{C.10}$$

$$term_b = \sum_{n=1}^{N} -\frac{(-i)^n}{\sqrt{\eta}\sqrt{2\pi n(n+1)}}Q_{10n}^{(3)}\frac{d}{d\alpha}\bar{P}_n^0(\cos\alpha). \tag{C.11}$$

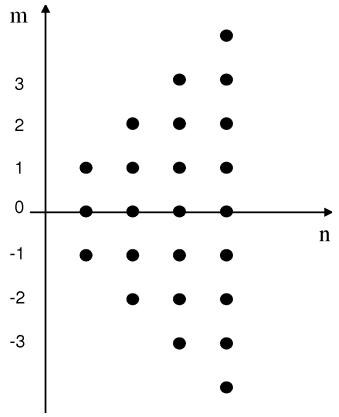

Figure C.1: nm-modes in the SWE.

C.2 Normalized associated Legendre functions computation

In computing the series of (C.4) by use of (C.8) and (C.9), we notice that, once the Q coefficients are known, only $\frac{m\bar{P}_n^{|m|}(\cos\alpha)}{\sin\alpha}$ and $\frac{d\bar{P}_n^{|m|}(\cos\alpha)}{d\alpha}$ are needed.
There are several computation schemes to do that, and here the approach that makes use of the so called rotation coefficients $d^n_{\mu m}(\theta)$ is chosen. The function $d^n_{\mu m}(\theta)$ is normally used in the SWE rotation theory, see Appendix A.2.3 of [26].
For the purpose of computing the quantities $\frac{m\bar{P}_n^{|m|}(\cos\alpha)}{\sin\alpha}$ and $\frac{d\bar{P}_n^{|m|}(\cos\alpha)}{d\alpha}$, the use of the rotations coefficients turns out to be particularly useful since it can be shown that [26]

$$\frac{m\bar{P}_n^{|m|}(\cos\alpha)}{\sin\alpha} = -(d^n_{1m}(\alpha) + d^n_{-1m}(\alpha))\sqrt{\frac{n(n+1)(2n+1)}{2}}\frac{1}{2(-\mathrm{sgn}(m))^m} \quad \text{(C.12)}$$

$$\frac{d\bar{P}_n^{|m|}(\cos\alpha)}{d\alpha} = -(d^n_{1m}(\alpha) - d^n_{-1m}(\alpha))\sqrt{\frac{n(n+1)(2n+1)}{2}}\frac{1}{2(-\mathrm{sgn}(m))^m} \quad \text{(C.13)}$$

where

$$d^n_{\mu m}(\alpha) = \sqrt{(n+\mu)!(n-\mu)!(n+m)!(n-m)!} \quad \cdot \quad \text{(C.14)}$$
$$\sum_{\sigma=\max(0,-m-\mu)}^{\min(n-m,n-\mu)} \frac{(-1)^{n-\mu-\sigma}}{\sigma!(n-m-\sigma)!(m+\mu+\sigma)!(n-\mu-\sigma)!}\Big(\cos\frac{\alpha}{2}\Big)^{2\sigma+\mu+m}$$
$$\cdot\Big(\sin\frac{\alpha}{2}\Big)^{2n-2\sigma-\mu-m}$$

It is noted that the relations hold for α real as well as for α complex and belonging to the contour B depicted in Fig. C.2, describing the invisible region of the spectral

$k_x k_y$-domain. It is reminded that only values $m > 0$ are considered in computing the series in (C.8) and (C.9).

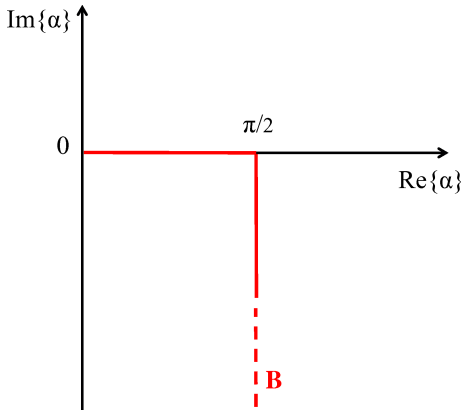

Figure C.2: Domain of the variable α on the contour B.

C.3 Embedding of the exponential term $e^{ik_z z}$

It is observed that the computation of the normalized associated Legendre functions with (C.12) and (C.13) confines the α-dependence to the terms $(\cos(\alpha/2))^{2\sigma+\mu+m}$ and $(\sin(\alpha/2))^{2n-2\sigma-\mu-m}$.
While for real values of $\alpha = x + iy$, corresponding to $x \in [0, \pi/2]$ and $y = 0$ on the contour B, the functions are equivalent to $(\cos(x/2))^{2\sigma+\mu+m}$ and $(\sin(x/2))^{2n-2\sigma-\mu-m}$ respectively, for complex values of α, i.e., for $x = \pi/2$ and $y \in (-\epsilon, -\infty)$, the computation is not straightforward but requires the use of

$$\cos(\alpha) = \cos(x + iy) = \cos x \cosh y - i \sin x \sinh y \tag{C.15}$$

$$\sin(\alpha) = \sin(x + iy) = \sin x \cosh y + i \cos x \sinh y. \tag{C.16}$$

From (C.15) and (C.16) we obtain

$$\left(\cos\frac{\alpha}{2}\right)^{2\sigma+\mu+m} = \left[\frac{\sqrt{2}}{2}\left(\cosh\frac{y}{2} - i\sinh\frac{y}{2}\right)\right]^{2\sigma+\mu+m} \tag{C.17}$$

$$\left(\sin\frac{\alpha}{2}\right)^{2n-2\sigma-\mu-m} = \left[\frac{\sqrt{2}}{2}\left(\cosh\frac{y}{2} + i\sinh\frac{y}{2}\right)\right]^{2n-2\sigma-\mu-m} \tag{C.18}$$

It is thus evident from (C.17) and (C.18) that trigonometric functions are not limited once defined on a complex domain, due to the presence of the hyperbolic sine and cosine.
We notice however that, in order to determine the plane wave spectrum at the given z-plane according to (C.1) and (C.4), we do not need the calculation of $\tilde{E}(\alpha, \beta)$

itself, but rather its product with the function $e^{ik_z z}$, which is exponentially decaying in the invisible region. The exponential growth of the complex trigonometric functions can thus be limited by embedding the term $e^{ik_z z}$ into the computation of $\tilde{E}(\alpha,\beta)$, i.e., into (C.12) and (C.13), for complex values of α and choosing the z-plane appropriately. This also reduces the computation time of (C.1).
We thus come back to the expression of $d^n_{\mu m}(\alpha)$ given in (C.14) and concentrate on the product $(\cos(\alpha/2))^{2\sigma+\mu+m}(\sin(\alpha/2))^{2n-2\sigma-\mu-m}$ when α is complex and given by $x=\pi/2$ and $y\in(-\epsilon,-\infty)$. By using (C.17) and (C.18) after a few manipulations we obtain

$$\Big(\cos\frac{\alpha}{2}\Big)^{2\sigma+\mu+m}\Big(\sin\frac{\alpha}{2}\Big)^{2n-2\sigma-\mu-m}=\Big(\frac{\sqrt{2}}{2}\Big)^{2n}e^{-i2\mathrm{atan}\left(\frac{\sinh\frac{y}{2}}{\cosh\frac{y}{2}}\right)(2\sigma+\mu+m)}\cdot\Big(\cosh\frac{y}{2}+i\sinh\frac{y}{2}\Big)^{2n} \tag{C.19}$$

We conclude that the exponential growth in the invisible region is thus governed by the last term, which, written in amplitude and phase, becomes

$$\Big(\cosh\frac{y}{2}+i\sinh\frac{y}{2}\Big)^{2n}=\Big(\Big(\cosh\frac{y}{2}\Big)^2+\Big(\sinh\frac{y}{2}\Big)^2\Big)^n e^{i\mathrm{atan}\left(\frac{\sinh\frac{y}{2}}{\cosh\frac{y}{2}}\right)2n} \tag{C.20}$$

We now multiply the amplitude of (C.20) with the exponential $e^{ik_z z}$, noticing that $e^{ik_z z}=e^{kz\sinh(y)}$, since $k_z=k\cos\alpha$.
From (C.20) we then get

$$\Big(\Big(\cosh\frac{y}{2}\Big)^2+\Big(\sinh\frac{y}{2}\Big)^2\Big)^n e^{kz\sinh(y)}=\Big(\frac{e^y+e^{-y}}{2}\Big)^n e^{kz\sinh(y)}. \tag{C.21}$$

If we now recall that a general binomial of the form $(a+b)^n$ can be expressed as

$$(a+b)^n=a^n+\binom{n}{1}a^{n-1}b+\binom{n}{2}a^{n-2}b^2+...+b^n \tag{C.22}$$

where $\binom{n}{k}=\frac{n!}{k!(n-k)!}$ are the binomial coefficients, then, by calling $a=e^y$ and $b=e^{-y}$ we obtain

$$(e^y+e^{-y})^n=e^{ny}+\binom{n}{1}e^{y(n-1)}e^{-y}+\binom{n}{2}e^{y(n-2)}e^{-2y}+...+e^{-ny}. \tag{C.23}$$

In this way we can embed the exponential $e^{ik_z z}=e^{kz\sinh(y)}$ into every term involved in (C.23).
The final expression of $d^n_{\mu m}(\alpha)e^{ik_z z}$ in the invisible region thus becomes, from (C.14) and (C.19),

$$d^n_{\mu m}(\alpha)e^{ik_z z}=\sqrt{(n+\mu)!(n-\mu)!(n+m)!(n-m)!}\ \cdot\sum_{\sigma=\max(0,-m-\mu)}^{\min(n-m,n-\mu)}\frac{(-1)^{n-\mu-\sigma}}{\sigma!(n-m-\sigma)!(m+\mu+\sigma)!(n-\mu-\sigma)!} \tag{C.24}$$

$$\frac{1}{2^{2n}} e^{-i2\mathrm{atan}\left(\frac{\sinh\frac{y}{2}}{\cosh\frac{y}{2}}\right)(2\sigma+\mu+m-n)} (e^{y}+e^{-y})^{n} e^{kz\sinh(y)}$$

where the last two terms can be computed through (C.23). Attention is obviously paid while computing the factorials.
It can be seen, from (C.23)and (C.24), that the embedding of the factor $e^{ik_z z}$ into the normalized associated Legendre functions results in a sum of exponential terms where the largest contribution is given by

$$f(n, y, z) = e^{-ny+kz\sinh(y)}. \tag{C.25}$$

Eq. (C.25) shows that, for a given point in the invisible region of the plane wave spectrum characterized by a negative value of y, and a given term in the SWE characterized by the index n, the exponent can be kept bounded and less than a certain value S provided that the z-coordinate is chosen according to

$$z > \frac{S+ny}{k\sinh(y)}. \tag{C.26}$$

Eq. (C.26) can thus be used as a guideline to select the appropriate z-plane for a given point in the invisible region and the maximum $n = N$ in the series of (C.1). It is finally noted that the z-plane given by (C.26) is normally too large for the purpose of diagnostics, where only the extreme near-field is of interest. However, because of the simple z-dependence of the plane wave spectrum, we are allowed to choose with (C.26) a certain z-plane to make the computation (C.1) more efficient, and then back-propagate the final result of (C.1) to a new z_2-plane, $z_2 < z$, which is the one of interest for the diagnostics. This can be accomplished by multiplying the final result by $e^{-ik_z \Delta z}$, with $\Delta z = z - z_2$.

Bibliography

[1] H. G. Booker, P. C. Clemmow. The concept of an angular spectrum of plane waves and its relation to that of polar diagram and aperture distribution. *Proc. Inst. Elec. Eng.*, vol. 97(1): pages 11–16, January 1950.

[2] O. M. Bucci, M. D. Migliore, G. Panariello, M. Sgambato. Accurate diagnosis of conformal arrays from near-field data using the matrix method. *IEEE Trans. Antennas Propagat.*, vol. 53(3): pages 1114–1120, March 2005.

[3] J. J. Lee, E. M. Ferren, D. P. Woollen, K. M. Lee. Near-field probe used as a diagnostics tool to locate defective elements in an array antenna. *IEEE Trans. Antennas Propagat.*, vol. 36(6): pages 884–889, June 1988.

[4] P. A. Langsford, M. J. C. Hayes, R. I. Henderson. Holographic diagnostics of a phased array antenna from near field measurements. *Proceedings of Antenna Measurements Technique Association Symposium, AMTA 1989*, pages 32–36, 1989.

[5] D. J. Rochblatt. A methodology for diagnostics and performance improvement for large reflector antennas using microwave holography. *Proceedings of Antenna Measurements Technique Association Symposium, AMTA 1992*, pages 7–12, 1992.

[6] D. J. Rochblatt, B. L. Seidel. Microwave antenna holography. *IEEE Trans. on Microw. Theory and Tech.*, vol. 40(6): pages 1294–1300, June 1992.

[7] Y. Rahmat-Samii. Surface diagnosis of large reflector antennas using microwave holographic metrology: an iterative approach. *Radio Science*, vol. 19(5): pages 1205–1217, 1984.

[8] Y. Rahmat-Samii, J. Lemanczyk. Application of spherical near-field measurements to microwave holographic diagnosis of antennas. *IEEE Trans. Antennas and Propagation*, vol. 36(6): pages 869–878, June 1988.

[9] L. S. Taylor. The phase retrieval problem. *IEEE Trans. Antennas and Propagation*, vol. 29(3): pages 386–391, March 1981.

[10] R. G. Yaccarino, Y. Rahmat-Samii. Phaseless bi-polar planar near-field measurements and diagnostics of array antennas. *IEEE Trans. Antennas and Propagation*, vol. 47(3): pages 574–583, March 1999.

[11] D. Smith, M. Leach, M. Elsdon, S. J. Foti. Indirect holographic techniques for determining antenna radiation characteristics and imaging aperture fields. *IEEE Antennas Propagat. Magazine*, vol. 49(61): pages 54–67, February 2007.

[12] J. D. Hanfling, G. V. Borgiotti, L. Kaplan. The backward transform of the near field for reconstruction of aperture fields. *IEEE Trans. Antennas Propagat. Soc. Symp. Dig.*, pages 764–767, 1979.

[13] A. D. Yaghjian. Upper-bound errors in far-field antenna parameters determined from planar near-field measurements, part i: Analysis. *Nat. Bur. Stand. and Tech.*, Note 667, 1975.

[14] R. W. Gerchberg. Super-resolution through error energy reduction. *Optica Acta*, vol. 21(9): pages 709–720, May 1974.

[15] A. Papoulis. A new algorithm in spectral analysis and bandlilmited extrapolation. *IEEE Trans. Circuits Syst.*, vol. 22(9): pages 735–742, September 1975.

[16] M. S. Narasimhan, B. Preetham Kumar. A technique of synthesizing the excitation currents of planar arrays or apertures. *IEEE Trans. Antennas Propagat.*, vol. 38(9): pages 1326–1332, September 1990.

[17] M. Johansson, B. Svensson. Array antenna diagnosis and calibration. *Proceedings of Antenna Measurements Technique Association Symposium, AMTA 1990*, pages 27–32, 1990.

[18] E. Martini, O. Breinbjerg, S. Maci. Reduction of truncation errors in planar near-field antenna measurements using the method of alternating projections. *Proceedings of European Conference on Antennas and Propagation, EuCAP*, 2006.

[19] D. Sanchez-Escuderos, M. Baquero-Escudero, E. Alfonso-Alos, F. Vico-Bondia. Currents reconstruction with high resolution using the FFT iterative method and spectrum replies. *Proceedings of European Conference on Antennas and Propagation, EuCAP*, 2006.

[20] J. J. H. Wang. An examination of the theory and practices of planar near-field measurement. *IEEE Trans. Antennas and Propagation*, vol. 36(6): pages 746–753, June 1988.

[21] E. B. Joy, M. G. Guler. Microwave holography for antenna and radome diagnostics. *Proceedings of the IEEE 2001 Internat. Symposium on Antennas and Propagat.*, vol. 4: pages 440–443, July 2001.

[22] M. G. Guler, E. B. Joy. High resolution spherical microwave holography. *IEEE Trans. Antennas Propagat.*, vol. 43(5): pages 464–472, May 1995.

[23] T. K. Sarkar, A. Taaghol. Near-field to near/far-field transformation for arbitrary near-field geometry utilizing an equivalent electric current and MOM. *IEEE Trans. Antennas Propagat.*, vol. 47(3): pages 566–573, March 1999.

[24] F. Las-Heras, T. K. Sarkar. Radial field retrieval in spherical scanning for current reconstruction and NF-FF transformation. *IEEE Trans. Antennas Propagat.*, vol. 50(6): pages 866–874, June 2002.

[25] K. Persson, M. Gustafsson. Near field to equivalent currents transformation with radome applications. *Proceedings of 2004 URSI EMTS, International Symposium on Electromagnetic Theory*, vol. 2(5): pages 1122–1124, May 2004.

[26] J. E. Hansen. *Spherical near-field antenna measurements.* Peter Peregrinus Ltd., London, UK, 1988.

[27] Homepage of the DTU-ESA Facility. http://www.emi.dtu.dk/research/afg/snf/snf.html.

[28] A. J. Devaney, E. Wolf. Multipole expansions and plane wave representations of the electromagnetic field. *Journal of Mathematical and Physics*, vol. 15: pages 234–244, February 1974.

[29] W. W. Hansen. A new type of expansion in radiation problems. *Phys. Rev.*, vol. 47: pages 139–143, January 1935.

[30] J. A. Stratton. *Electromagnetic theory.* McGraw-Hill, 1941.

[31] J. E. Hansen, F. Jensen. Spherical near-field scanning at the Technical University of Denmark. *IEEE Trans. Antennas Propagat.*, vol. 36(6): pages 734–739, June 1988.

[32] Homepage of SNIFTD. http://www.ticra.com/script/site/page.asp?artid=27.

[33] F. Jensen, A. Frandsen. On the number of modes in spherical wave expansions. *Proceedings of Antenna Measurements Technique Association Symposium, AMTA 2004*, pages 489–494, 2004.

[34] G. T. Whittaker, G. N. Watson. *Modern analysis*, chapter 18. Cambrige U.P., 1927.

[35] D. M. Kerns. Plane wave scattering-matrix theory of antennas and antenna-antenna interactions: formulation and applications. *Journ. of Research of the National Bureau of Standards*, vol. 80B: pages 5–51, March 1976.

[36] T. B. Hansen, A. D. Yaghjian. *Plane wave theory of time-domain fields, near-field scanning applications*, chapter 3. IEEE PRESS, 1999.

[37] R. E. Collin. *Antennas and radiowave propagation*, chapter 4. McGraw-Hill, New York, 1985.

[38] A. D. Yaghjian. An overview of near-field antenna measurements. *IEEE Trans. Antennas and Propagation*, vol. 34(1): pages 30–45, January 1986.

[39] H. P. Baltes, H. G. Schmidt-Weinmar. Bandlimiting at variance with the strong radiation condition. *Phys. Lett.*, vol. 60: pages 275–277, 1977.

[40] M. Xiao. A study of resolution limit in optical microscopy: near and far field. *Optics Comm.*, vol. 132: pages 403–409, 1996.

[41] M. Xiao. Short communication. Evanescent fields do contribute to the far field. *Journ. of Modern Optics.*, vol. 46(4): pages 729–733, May 1999.

[42] J. T. Foley, E. Wolf. Note on the far field of a Gaussian beam. *Journ. Opt. Soc. Am.*, vol. 69(5): pages 761–764, 1979.

[43] E. Wolf, J. T. Foley. Do evanescent waves contribute to the far field? *Optics Letters*, vol. 23(1): pages 16–18, January 1998.

[44] G. C. Sherman, J. J. Stamnes, E. Lalor. Asymptotic approximations to angular-spectrum representations. *Journ. of Math. Phys.*, vol. 17(5), May 1976.

[45] P. Morse, H. Feshbach. *Methods of theoretical physics.* International Series in Pure and Applied Physics, McGraw-Hill, 1953.

[46] A. Papoulis. *Signal analysis.* McGraw-Hill, 1977.

[47] F. A. Jenkins, H. E. White. *Fundamental of optics.* McGraw-Hill, 1976.

[48] W. V. T. Rusch. The current state of the reflector antenna art. *IEEE Trans. Antennas Propagat.*, vol. 32(4): pages 313–329, April 1984.

[49] A. D. Olver, J. I. I. Syed. Variable beamwidth reflector antenna by feed defocusing. *IEE Proc.-Microw. Antennas Propagat.*, vol. 142(5): pages 394–398, October 1995.

[50] Homepage of GRASP9. http://www.ticra.com/script/site/page.asp?artid=33.

[51] F. J. Harris. On the use of windows for harmonic analysis with the discrete Fourier transform. *Proc. IEEE*, vol. 66(1): pages 51–83, January 1978.

[52] H. C. Stankwitz, R. J. Dallaire, J. R. Fienup. Nonlinear apodization for sidelobe control in SAR imagery. *IEEE Trans. Aerosp. Elect. Syst.*, vol. 31(1): pages 267–279, January 1995.

[53] F. Colone, M. G. Viscito, D. Pastina, P. Lombardo. Effects of spatially variant apodization on SAR image classification. *Proceedings of the IEEE International Geoscience and Remote Sensing Symposium, IGARSS*, pages 3903–3906, 2006.

[54] B. H. Smith. An analytic nonlinear approach to sidelobe reduction. *IEEE Trans. Imag. Proces.*, vol. 10(8): pages 1162–1168, August 2001.

[55] K. Pontoppidan. *GRASP9 Technical Description.* TICRA, 2005.

Paper I

Properties of the Transformation from the Spherical Wave Expansion to the Plane Wave Expansion

Cecilia Cappellin [1-2], Olav Breinbjerg [1], Aksel Frandsen [2]

[1] Ørsted•DTU, Technical University of Denmark, DK-2800 Kgs. Lyngby, Denmark
E-mail: cca@oersted.dtu.dk, ob@oersted.dtu.dk

[2] TICRA, Læderstræde 34, DK-1201 Copenhagen K, Denmark
E-mail: af@ticra.com

Keywords: spherical wave expansion, plane wave expansion, antenna diagnostics, antenna measurements

Abstract

The transformation between the Spherical Wave Expansion (SWE) and the Plane Wave Expansion (PWE) is investigated with respect to a range of its fundamental properties. First, the transformation of individual spherical waves is studied in order to understand how these contribute to the different regions of the plane wave spectrum. Second, the number of spherical waves necessary to accurately determine the PWE over different regions of the spectral domain is investigated. Third, numerical aspects of the transformation are addressed.

1. Introduction

The Spherical Wave Expansion (SWE) and the Plane Wave Expansion (PWE) are two well-known techniques to express time-harmonic electromagnetic fields in source-free regions of space. While the SWE expresses the field as an infinite series of discrete spherical waves, the PWE expresses the field as an infinite continuous spectrum of plane waves. Each of these expansions exists in slightly different forms, e.g., with different expansion functions and different spectral domains, but these forms are all equivalent. The original form of the SWE was introduced by W. W. Hansen [1935], while the theory was popularized a few years later by Stratton [1941]. A more recent treatment was given by J. E. Hansen [1988] in relation to spherical near-field antenna measurements. The original PWE was introduced by Whittaker and Watson [1927], reformulated by Stratton [1941], employed by Kerns [1976] for planar near-field antenna measurements, and recently treated by T. B. Hansen and Yaghjian [1999]. One form of the PWE employs as spectral variables the Cartesian components of the wave propagation vector [*Hansen and Yaghjian*, 1999], while another form employs instead its spherical components [*Stratton*, 1941]. The SWE and PWE have been extensively employed in both the optical and microwave frequency bands in areas like propagation and diffraction theory, imaging techniques, and antenna measurements, [*Devaney*, 1982], [*Hansen and Johansen*, 2000], [*Mehler*, 1988] and [*Yaghjian*, 1986]. The choice of employing the SWE or the PWE is determined by the geometry of the source configuration, the spatial region of interest, and the available information about the radiated fields.

Though the SWE and the PWE can both be derived from the homogeneous vector Helmholtz equation, their regions of validity are fundamentally different. Employing a Cartesian (x, y, z)-coordinate system and the associated spherical (r, θ, φ)-coordinate system, the SWE is valid for all $r > r_o$, where r_o is the largest r-coordinate of the source and hence the radius of the so-called *minimum sphere*, while the PWE is valid for all $z > z_o$ where z_o is the largest z-coordinate of the source, see Fig. 1. It is noted, for later use, that r_o is obviously always larger than or equal to z_o, i.e., $r_o \geq |z_o|$. For source regions with a planar aperture, the PWE will, by a proper orientation of the coordinate system, be valid in the extreme near-field of the aperture while this will not be the case for the SWE, see Fig. 1.

While the mathematical formulations of the PWE and SWE are very different, as are their respective regions of validity, it can be shown that it is possible to derive one expansion from the other through a rigorous transformation. The necessary equations to perform the transformation, i.e. the PWE of the spherical vector wave functions of the SWE, were first presented by [*Stratton*, 1941, pp. 417] and later by [*Morse and Feshbach*, 1953, pp. 1865]. A complete treatment of the transformation was given by [*Devaney and Wolf*, 1974] and recently by [*Varadan, Lakhtakia and Varadan*, 1991]. These works on the SWE-to-PWE transformation concentrate on its mathematical derivation, while such aspects as convergence mechanism and

truncation of the series and integrals involved in the transformation, as well as its numerical implementation, have been dealt with to a lesser degree.

It is thus the primary purpose of the present work to investigate the fundamental properties of the SWE-to-PWE transformation. The transformation of individual spherical waves will be studied in order to understand how these contribute to the different regions of the plane wave spectrum. Also, the number of spherical waves necessary to accurately determine the PWE over different regions of the plane wave spectrum will be investigated. Furthermore, numerical aspects of the transformation will be addressed.

The SWE-to-PWE transformation is particularly useful in antenna diagnostics for spherical near-field antenna measurements [*Cappellin, Frandsen and Breinbjerg*, 2006][*Cappellin, Breinbjerg and Frandsen*, 2006]. Electrical and mechanical errors in an antenna may seriously affect the antenna performance, and while their presence is normally detected by anomalies in the measured far-field pattern, often only an analysis of the extreme near-field can allow their identification. However, the computation of the extreme near-field is generally not possible when the field is expressed as a SWE obtained from a spherical near-field measurement, since the SWE is valid only outside the antenna minimum sphere of radius r_o. One way to overcome this limitation is to transform the SWE into the PWE, which is valid on any z-plane $z > z_o$, with $|z_o| \leq r_o$. Once the PWE is known, the extreme near-field can be computed and subjected to the diagnostics. For this use, it is particularly interesting to note that the SWE-to-PWE transformation provides the contributions of the spherical waves in the visible as well as invisible regions of the spectral domain. The contribution of the invisible region of the PWE to the extreme near-field can be significant at distances less than one wavelength from the antenna, [*Yaghjian*, 1986] and [*Wang*, 1988], and it gives a spatial resolution better than the half wavelength provided by the visible region of the PWE [*Booker and Clemmow*, 1950].

The present manuscript focuses on fundamental properties of the SWE-to-PWE transformation that constitutes an essential step in this antenna diagnostics technique but does not document the diagnostics technique as such. The fundamental properties of the SWE-to-PWE transformation do have practical implications for the antenna diagnostics technique but this relies also on other essential steps, see e.g. [*Cappellin, Frandsen and Breinbjerg*, 2006][*Cappellin, Breinbjerg and Frandsen*, 2006], and it is documented in more practically oriented works [*Cappellin, Frandsen and Breinbjerg*, 2007][*Cappellin et al.*, 2007].

The present manuscript is organized as follows: In Section 2 the SWE and PWE are briefly summarized with attention to their definitions and regions of validity. In Section 3 the derivation of the SWE-to-PWE transformation is described and its fundamental properties are discussed in detail. In Section 4 a test case is presented for numerical investigation. All expressions are given in the S.I. rationalized system with a suppressed $e^{-i\omega t}$ time convention.

2. The Spherical Wave Expansion (SWE) and Plane Wave Expansion (PWE)

We begin by introducing the SWE of the electric field $\bar{E}$ radiated by an antenna enclosed in a minimum sphere of radius r_o [*Hansen*, 1988],

$$\bar{E}(\bar{r}) = \frac{k}{\sqrt{\eta}} \sum_{n=1}^{\infty} \sum_{m=-n}^{n} Q_{1mn}^{(3)} \bar{F}_{1mn}^{(3)}(\bar{r}) + Q_{2mn}^{(3)} \bar{F}_{2mn}^{(3)}(\bar{r}), \quad r > r_o \tag{1}$$

with η being the medium intrinsic admittance, k the wave number, and $\bar{r}$ the position vector expressed in spherical coordinates (r, θ, φ). The expansion coefficients are denoted by $Q_{1mn}^{(3)}$

and $Q_{2mn}^{(3)}$, while $\bar{F}_{1mn}^{(3)}(\bar{r})$ and $\bar{F}_{2mn}^{(3)}(\bar{r})$ are the power-normalized spherical vector wave functions given by

$$\bar{F}_{1mn}^{(3)}(\bar{r}) = \frac{1}{\sqrt{2\pi}} \frac{1}{\sqrt{n(n+1)}} \left(-\frac{m}{|m|} \right)^m \left\{ h_n^{(1)}(kr) \frac{im}{\sin\theta} \bar{P}_n^{|m|}(\cos\theta) e^{im\varphi} \hat{\theta} - h_n^{(1)}(kr) \frac{d}{d\theta} \bar{P}_n^{|m|}(\cos\theta) e^{im\varphi} \hat{\varphi} \right\} \tag{2}$$

$$\bar{F}_{2mn}^{(3)}(\bar{r}) = \frac{1}{\sqrt{2\pi}} \frac{1}{\sqrt{n(n+1)}} \left(-\frac{m}{|m|} \right)^m \left\{ \frac{n(n+1)}{kr} h_n^{(1)}(kr) \bar{P}_n^{|m|}(\cos\theta) e^{im\varphi} \hat{r} + \frac{1}{kr} \frac{d}{d(kr)} (kr h_n^{(1)}(kr)) \frac{d}{d\theta} \bar{P}_n^{|m|}(\cos\theta) e^{im\varphi} \hat{\theta} + \frac{1}{kr} \frac{d}{d(kr)} (kr h_n^{(1)}(kr)) \frac{im}{\sin\theta} \bar{P}_n^{|m|}(\cos\theta) e^{im\varphi} \hat{\varphi} \right\} \tag{3}$$

In these expressions $h_n^{(1)}(kr)$ is the spherical Hankel function of the first kind, $\bar{P}_n^{|m|}(\cos\theta)$ the normalized associated Legendre function of degree *n* and order *m* [*Hansen*, 1988, eq. A1.25], and $\hat{r}, \hat{\theta}, \hat{\varphi}$ are the spherical unit vectors. It can be seen from Eqs. 2-3 that the *r*-dependence of the spherical vector wave functions is given by $h_n^{(1)}(kr)$. For each spherical mode with index *n* a transition region exists around $r_n = n/k$, since the mode decays rapidly with increasing *r* for $r << r_n$, corresponding to an evanescent wave, while it decays as r^{-1} for $r >> r_n$, corresponding to a propagating wave. Though all modes are thus propagating in the far-field, this transition property implies that, for an antenna with a minimum sphere radius r_o, the high-order modes with $n > kr_o$ are highly suppressed outside the minimum sphere and only modes with $n < kr_o$ contribute to the far-field. Hence, the *n*-series in Eq. 1 can be truncated at $N \cong kr_o + 10$ while maintaining a high accuracy of the far-field [*Hansen*, 1988].

The PWE of the same electric field $\bar{E}$ in the spectral $k_x k_y$-domain valid for $z > z_o$, with z_o being the largest *z*-coordinate of the antenna, is given by [*Hansen and Yaghjian*, 1999]

$$\bar{E}(\bar{r}) = \frac{1}{2\pi} \int_{-\infty}^{\infty} \int_{-\infty}^{\infty} \bar{T}(k_x, k_y) e^{ik_z z} e^{i(k_x x + k_y y)} dk_x dk_y, \quad z > z_o \tag{4}$$

where $\bar{r}$ is the position vector with Cartesian coordinates (x, y, z) and k_x, k_y are the spectral variables, which, together with $k_z = \sqrt{k^2 - k_x^2 - k_y^2}$, constitute the Cartesian components of the wave propagation vector $\bar{k}$, $\bar{k} = k_x \hat{x} + k_y \hat{y} + k_z \hat{z}$. $\bar{T}(k_x, k_y)$ is the plane wave spectrum at $z = 0$, while $\bar{T}(k_x, k_y) e^{ik_z z}$ is the spectrum for a given *z*-coordinate. The spectral domain is divided in two regions, the visible region for $k_x^2 + k_y^2 \le k^2$, and the invisible region for $k_x^2 + k_y^2 > k^2$, see Fig. 2a. While the spectral variables k_x and k_y are real everywhere, k_z is real in the visible region and purely imaginary with a positive imaginary part in the invisible region. Real values of k_z correspond to propagating plane waves, while imaginary values of k_z correspond to evanescent plane waves that are exponentially attenuated with *z*. Their contribution is usually negligible at distances larger than one wavelength from the antenna [*Yaghjian*, 1986][*Wang*,

1988]. In practice, the k_x- and k_y-integrals in Eq. 4 are truncated at finite values $\pm k_{xmax}$ and $\pm k_{ymax}$, respectively. At the border between the visible and invisible regions $k_z = 0$ and a singularity of the type $1/k_z$ is generally present in at least one component of the plane wave spectrum $\bar{T}$ [*Hansen and Yaghjian*, 1999]. A necessary but not sufficient condition to avoid such a singularity is that the antenna far-field pattern exhibits a null for $\theta = \pi/2$. It is finally recalled that a simple relation exists between the far-field and the visible region of the plane wave spectrum, according to [*Hansen and Yaghjian*, 1999, eq. 3.133] and [*Booker and Clemmow*, 1950],

$$\begin{aligned}\bar{E}_{far}(r,\theta,\varphi) &= \lim_{kr\to\infty} \bar{E}(r,\theta,\varphi) \\ &= -\frac{e^{ikr}}{r} ik\cos\theta\, \bar{T}(k\sin\theta\cos\varphi, k\sin\theta\sin\varphi) \quad \theta\in[0,\pi/2], \quad \varphi\in[0,2\pi]\end{aligned} \tag{5}$$

3. The SWE-to-PWE transformation and its properties

3.1 Theory

It will now be shown how the SWE of Eq. 1 can be transformed into the PWE of Eq. 4. The following derivation is based on [*Devaney and Wolf*, 1974], however it has been extended [*Cappellin, Frandsen and Breinbjerg*, 2006] in order to use the power-normalized spherical vector wave functions, the k_xk_y-PWE, and the S.I. system of units. The use of the power-normalized spherical vector wave functions turns out to be particular advantageous since these are employed in the textbook [*Hansen*, 1988] and in the software SNIFTD [homepage of SNIFTD], which have become widely used standards for spherical near-field antenna measurements. There are alternative derivations of the SWE-to-PWE transformation, and one such approach is given in Appendix A. The transformation will be derived in 3 steps.

The first step consists of introducing the PWE of the spherical vector wave functions, and since [*Devaney and Wolf*, 1974] employs the spectral $\alpha\beta$-domain we thus take outset in

$$\bar{F}^{(3)}_{1mn}(\bar{r}) = \frac{(-i)^{n+1}}{2\pi\sqrt{n(n+1)}} \int_{-\pi}^{\pi}\int_{B} \bar{Y}^m_n(\alpha,\beta) e^{ik\hat{k}\cdot\bar{r}} \sin\alpha\, d\alpha\, d\beta \tag{6}$$

$$\bar{F}^{(3)}_{2mn}(\bar{r}) = \frac{(-i)^{n}}{2\pi\sqrt{n(n+1)}} \int_{-\pi}^{\pi}\int_{B} \hat{k}\times\bar{Y}^m_n(\alpha,\beta) e^{ik\hat{k}\cdot\bar{r}} \sin\alpha\, d\alpha\, d\beta \tag{7}$$

with $\hat{k} = \bar{k}/k = \sin\alpha\cos\beta\,\hat{x} + \sin\alpha\sin\beta\,\hat{y} + \cos\alpha\,\hat{z}$ being the unit wave propagation vector, the spectral variable β belonging to the interval $[-\pi, \pi]$ and the spectral variable α belonging to the complex contour B, see Fig. 3. Real values of α correspond to propagating waves, while complex values of α correspond to evanescent waves. The function $\bar{Y}^m_n(\alpha,\beta)$ is the vector spherical harmonics which can be expressed as

$$\bar{Y}^m_n(\alpha,\beta) = -\frac{i}{\sqrt{2\pi}}\left(-\frac{m}{|m|}\right)^m \left(\frac{d}{d\alpha}\bar{P}^{|m|}_n(\cos\alpha)e^{im\beta}\hat{\beta} - \frac{im}{\sin\alpha}\bar{P}^{|m|}_n(\cos\alpha)e^{im\beta}\hat{\alpha}\right) \tag{8}$$

with $\hat{\alpha} = \cos\alpha\cos\beta\hat{x} + \cos\alpha\sin\beta\,\hat{y} - \sin\alpha\,\hat{z}$ and $\hat{\beta} = -\sin\beta\hat{x} + \cos\beta\,\hat{y}$.

Second, the PWEs of Eqs. 6-7 are substituted into the SWE of Eq. 1 and the order of integration and summation is interchanged, obtaining the PWE of the electric field in the spectral $\alpha\beta$-domain

$$\bar{E}(\bar{r}) = \frac{k}{2\pi} \int_{-\pi}^{\pi} \int_{B} \tilde{E}(\hat{k}) e^{ik\hat{k}\cdot\bar{r}} \sin\alpha \, d\alpha \, d\beta \tag{9}$$

where the *spectrum complex amplitude* $\tilde{E}(\hat{k})$ is given by

$$\tilde{E}(\hat{k}) = \sum_{n=1}^{\infty} \sum_{m=-n}^{n} \frac{(-i)^n}{\sqrt{\eta}\sqrt{n(n+1)}} \left[-iQ_{1mn}^{(3)} \bar{Y}_n^m(\alpha,\beta) + Q_{2mn}^{(3)} \hat{k} \times \bar{Y}_n^m(\alpha,\beta) \right]. \tag{10}$$

Thus, the spectrum complex amplitude can be calculated from the knowledge of the SWE coefficients $Q_{1mn}^{(3)}$ and $Q_{2mn}^{(3)}$.

Third, the spectrum in the spectral $\alpha\beta$-domain, $\tilde{E}(\hat{k}) e^{ik\cos\alpha z}$, is translated into the $k_x k_y$-domain obtaining $\bar{T}(k_x, k_y) e^{ik_z z}$, since it can be shown that

$$\bar{T}(k_x, k_y) e^{ik_z z} = \frac{1}{k_z} \tilde{E}(\hat{k}) e^{ik\cos\alpha z} \tag{11}$$

where α and β on the right hand side are expressed as functions of the spectral variables k_x and k_y according to

$$\alpha = \arcsin\left(\sqrt{\frac{k_x^2 + k_y^2}{k^2}} \right) \text{ and } \beta = \arctan\left(\frac{k_y}{k_x} \right) \tag{12}$$

Obviously the arcsin and arctan functions must be implemented to ensure the correct contour B for the angle α and the interval $[-\pi, \pi]$ for the angle β.

Eq. 11 is derived by applying to Eq. 9 a change in the integration variables using $k_x = k\sin\alpha\cos\beta$, $k_y = k\sin\alpha\sin\beta$, $k_z = k\cos\alpha$, and by identifying the obtained result with Eq. 4. With Eq. 12, the α- and β-values corresponding to chosen k_x- and k_y-values can be calculated exactly without interpolation. By combining Eqs. 10-11-12, the plane wave spectrum $\bar{T}(k_x, k_y) e^{ik_z z} = \bar{T}(k_x, k_y, z)$ can finally be written as

$$\bar{T}(k_x, k_y, z) = \sum_{n=1}^{\infty} \sum_{m=-n}^{n} Q_{1mn}^{(3)} \bar{T}_{1mn}(k_x, k_y, z) + Q_{2mn}^{(3)} \bar{T}_{2mn}(k_x, k_y, z) \tag{13}$$

where

$$\bar{T}_{1mn}(k_x, k_y, z) = \frac{e^{ik_z z}}{k_z} \frac{(-i)^{n+1}}{\sqrt{\eta}\sqrt{n(n+1)}} \bar{Y}_n^m(\alpha,\beta) \tag{14}$$

$$\bar{T}_{2mn}(k_x, k_y, z) = \frac{e^{ik_z z}}{k_z} \frac{(-i)^{n}}{\sqrt{\eta}\sqrt{n(n+1)}} \hat{k} \times \bar{Y}_n^m(\alpha,\beta) \tag{15}$$

In order to calculate the PWE of Eq. 4 from the known SWE of Eq. 1 we can summarize the required steps as follows:

1. Choose a certain $k_x k_y$-spectral domain according to the desired spatial resolution (see later).
2. For every point in the $k_x k_y$-spectral domain determine the corresponding α- and β-values from Eq. 12.

3. Calculate the plane wave spectrum at the chosen *z*-plane with Eq. 13.

It is emphasized that Eqs. 6-7-10 are of fundamental importance in the theory of modal expansions and provide the theoretical justification for the SWE-to-PWE transformation. In particular it is noted that the spectrum complex amplitude $\tilde{E}(\hat{k})$ is an analytic function in its complex domain of definition, since it can be expressed by the spatial Fourier transform of the finite source distributions, [*Devaney and Wolf*, 1974] and [*Gerchberg*, 1974]. Second, $\tilde{E}(\hat{k})$ is a vector function normal to the unit vector $\hat{k}$, i.e., $\hat{k}\cdot\tilde{E}(\hat{k})=0$. Third, the vector spherical harmonics $\bar{Y}_n^m(\alpha,\beta)$ and $\hat{k}\times\bar{Y}_n^m(\alpha,\beta)$ constitute a complete orthogonal basis for all analytical vector functions normal to the unit vector $\hat{k}$, [*Devaney and Wolf*, 1974]. Thus Eq. 10 becomes the necessary intermediate step for the transformation from the SWE to the PWE, or vice- versa. It is finally noted that though we begin with a SWE that is only valid outside the minimum sphere, $r > r_o$, the obtained PWE is valid also inside the minimum sphere for all points with $z > z_o$ since $\tilde{E}(\hat{k})$ is independent of *z*.

3.2 Fundamental properties

We will now discuss some fundamental properties of the SWE-to-PWE transformation related to resolution, exponential growth of the spherical vector wave functions, and transformation of individual spherical modes.

First, once the plane wave spectrum $\bar{T}(k_x,k_y,z)$ is computed through Eq. 13, the spatial resolution along the *x*- and *y*-directions, δ_x and δ_y, of the electric field obtained from Eq. 4 is given by $\delta_x=\pi/k_{x\max}$ $\delta_y=\pi/k_{y\max}$. A spatial resolution better than half a wavelength, $\lambda/2$, is thus provided when part of the invisible region is taken into account, since either k_x, k_y or both are larger than the wavenumber $k = 2\pi/\lambda$. Here, the resolution is defined as the spatial distance between the nulls of the fastest oscillating spectral component. On the other hand, for a given desired spatial resolution, δ_x and δ_y, the required range of the PWE is obtained from $k_{x\max}=\pi/\delta_x$ and $k_{y\max}=\pi/\delta_y$, and this range will then determine the number of modes in the SWE and thus the truncation number *N* (see later).

Second, from Eqs. 2-3-8 we observe that

$$\begin{aligned}&\bar{Y}_n^m(\alpha,\beta)\propto\bar{K}_{1mn}(\alpha,\beta)\\&\hat{k}\times\bar{Y}_n^m(\alpha,\beta)\propto\bar{K}_{2mn}(\alpha,\beta)\end{aligned}\qquad(16)$$

where $\bar{K}_{smn}(\theta,\varphi)=\lim_{kr\to\infty}\frac{kr}{e^{ikr}}\bar{F}_{smn}^{(3)}(r,\theta,\varphi)$, with $s = 1, 2,$ is the far-field pattern function of the spherical vector waves [*Hansen*, 1988]. Thus, the computation of $\tilde{E}(\hat{k})$ by Eq. 10 corresponds to the SWE of the far-field. This implies that all information about the visible and invisible spectral regions of the plane wave spectrum is in principle contained in the far-field. However, while the traditional truncation in the *n*-index at $N = kr_o+10$ provides accurate values of the SWE of the electric far-field [*Hansen*, 1988] and thus of the spectrum $\bar{T}(k_x,k_y)$ in the visible region, the same truncation value will in general not be sufficient in the invisible region as it

will be shown below. The reason for different convergence rates in the two regions lies in the fact that the invisible region is described by complex values of the spectral variable α, see Fig. 3. The trigonometric functions in α appearing in the associated Legendre functions contained in $\bar{Y}_n^m(\alpha,\beta)$, see Eqs. 8-14-15, are not limited in the complex domain described by the contour *B*. This has two consequences: The first one is that computational problems appear in the evaluation of the associated Legendre functions in the invisible region already for moderate values of *n*. The second one is that the exponential growth of these functions requires *Q* coefficients of extremely low values, normally provided by high *n*- and *m*-modes, in order for the series of Eq. 13 to reach convergence. While the exponential growth of the trigonometric functions in the invisible region is an inherent mathematical property, we notice however that the transformation of Eqs. 13-15 does not require the calculation of the vector spherical harmonics $\bar{Y}_n^m(\alpha,\beta)$ themselves but rather their product with the function $\exp(ik_z z)$, which is exponentially decaying in the invisible region. The exponential growth of the vector spherical harmonics can thus be limited by embedding the term $\exp(ik_z z)$ into the computation of $\bar{Y}_n^m(\alpha,\beta)$ for complex values of α and choosing the *z*-plane appropriately. The intermediate computation of the extremely large values contained in the vector spherical harmonics is thus avoided since the product with $\exp(ik_z z)$ is automatically considered. This procedure also reduces the computation time of Eq. 13. If the associated Legendre functions are computed through the rotation coefficients defined in [*Hansen*, 1988, eqs. A2.17-18-19], it is found that the embedding of the factor $\exp(ik_z z)$ results in a sum of exponential terms where the largest contribution is $f(n, \alpha, z)$ given by

$$f(n,\alpha,z) = \exp(-n\,\mathrm{Im}\{\alpha\} + k\,z\sinh(\mathrm{Im}\{\alpha\})) \tag{17}$$

with α belonging to the domain *B* depicted in Fig. 3, and *n* being the degree of the associated Legendre function $\bar{P}_n^{|m|}(\cos\alpha)$ in Eq. 8. Hence, for a given point in the invisible region of the plane wave spectrum characterized by a negative value of $\mathrm{Im}\{\alpha\}$, and a given term in the SWE characterized by the index *n*, Eq. 17 shows that the exponent can be kept bounded and less than a certain value *S* provided that the *z*-coordinate is chosen according to

$$z > \frac{S + n\,\mathrm{Im}\{\alpha\}}{k\sinh(\mathrm{Im}\{\alpha\})} \tag{18}$$

Eq. 18 can thus be used as a guideline to select the appropriate *z*-plane for a given point in the invisible region and the maximum $n = N$ in the series of Eq. 13. In Fig. 4 the relation of Eq. 18 is illustrated for different values of *n*, *z* and $\mathrm{Im}\{\alpha\}$ in the case of $S = 0$. For example, if $\mathrm{Im}\{\alpha\} = -1.317$, corresponding to $k_x = 2k$ (light blue line), and if $n = 50$, the *z*-plane should be selected larger than 6λ. It is noted that the *z*-plane given by Eq. 18 is normally too large for the purpose of diagnostics where only the extreme near-field is of interest. However, since the *z*-dependence of the plane wave spectrum $\bar{T}$ is given by $\exp(ik_z z)$, we are allowed to choose with Eq. 18 a certain *z*-plane to make the computation of the single terms of Eq. 13 more efficient, and then back-propagate the result of the double summation of Eq. 13 to a new z_2-plane, $z_2 < z$, which is the one of interest for the diagnostics. This can be accomplished by simply multiplying by $\exp(-ik_z \Delta z)$, with $\Delta z = z - z_2$.

In order to provide an insight into how the plane wave spectrum depends on the *n*- and *m*-spherical modes and to better understand how a given spherical wave transforms and contributes to the visible and invisible regions of the spectral $k_x k_y$-domain, we now concentrate on Eqs. 14-15 and study the behaviour of $\bar{T}_{1mn}$ and $\bar{T}_{2mn}$ on the *z*-plane $z = 0$ with varying *n*

and *m*. We first note that the magnitudes $|\bar{T}_{1mn}| = |\bar{T}_{1-mn}| = |\bar{T}_{2mn}| = |\bar{T}_{2-mn}|$ and that these are azimuthally constant since the β dependence is given by $e^{im\beta}$. We can then choose either a fixed *n*-mode and vary the *m*-modes, $|m|$ = 0, 1, ..., *n*, or a fixed *m*-mode and vary the *n*-modes, *n* = max(1, $|m|$), …, *N*, see Fig. 2b. For a fixed *n*-mode, see Fig. 5 for the case of *n* = 3, we observe that every *m*-mode with $|m| \neq 1$ provides a null at $k_x = k_y = 0$, and this null is surrounded by a circular region of low magnitude with a radius that increases for increasing *m*, in accordance with the well-know property that only modes with $|m| = 1$ are nonzero on the *z*-axis. We also notice that the smaller the $|m|$, the larger the value of $|\bar{T}_{1mn}|$ in the invisible region, again see Fig. 5. For a fixed *m*-mode, see Fig. 6 for the case *m* = 0, there is an annular null inside the visible region, with a radius that decreases for increasing *n*. We finally observe that for larger *n*, the period of oscillation of $|\bar{T}_{1mn}|$ inside the visible region becomes smaller, and the magnitude in the invisible region becomes larger, again see Fig. 6.

All these observations are useful in understanding the mapping of a given spherical wave into the spectral $k_x k_y$-domain. It should be kept in mind however that what happens in the general case of a series of spherical waves is more complicated, since the spherical waves are weighted by the coefficients $Q_{1mn}^{(3)}$ and $Q_{2mn}^{(3)}$. The influence of the expansion coefficients on Eq. 13 will be analyzed through an extensive numerical investigation in Section 4, where the possibility of truncating the infinite *n*-modes to a finite *N* will be also taken into account.

It is finally noticed that the number of terms contained in Eq. 13 for a given truncation in the *n*-modes equal to *N*, is given by $2N\cdot(N+2)$. If the extents of the spectral $k_x k_y$-domain are given by $2k_{xmax}$ and $2k_{ymax}$ along the k_x- and k_y-axis respectively, then, for chosen sampling densities δk_x and δk_y, $R = (2k_{x\max}/\delta k_x)+1$ points will be present in k_x and $V = (2k_{y\max}/\delta k_y)+1$ points in k_y. Thus, the total number of terms that must be calculated in Eq. 13 is $R\cdot V\cdot 2N\cdot(N+2)$, where each term is of the form of Eq. 14 or 15.

3.3 A simple test case: the electric Hertzian dipole at the origin

In order to illustrate the SWE-to-PWE transformation and the computation of the visible as well as invisible regions of the plane wave spectrum from the *Q* coefficients of the SWE, we consider a *z*-oriented electric Hertzian dipole with dipole moment *p* located at the origin of the coordinate system.

For this antenna configuration we know from [*Hansen*, 1988, Eq. 2.117] that the SWE of the radiated field contains only the single mode *s* = 2, *m* = 0, *n* = 1, where

$$Q_{201}^{(3)} = -\frac{kp}{\sqrt{\eta 6\pi}} \tag{19}$$

$$\bar{F}_{201}^{(3)}(\bar{r}) = \frac{\sqrt{6}}{2\sqrt{\pi}}\left(\frac{h_1^{(1)}(kr)}{kr}\cos\theta\,\hat{r} - \frac{1}{2}\frac{1}{kr}\frac{d}{d(kr)}(krh_1^{(1)}(kr))\sin\theta\,\hat{\theta}\right) \tag{20}$$

When Eq. 19 is substituted into Eq. 13 and Eq. 12 is used, the plane wave spectrum becomes

$$\bar{T}(k_x,k_y,z)=\frac{p}{4\pi k\eta}\left(k_x\hat{x}+k_y\hat{y}+\frac{k_z^2-k^2}{k_z}\hat{z}\right)e^{ik_z z}\ , \tag{21}$$

which agrees with the plane wave spectrum obtained directly from the dipole current [*Hansen and Yaghjian*, 1999, eq. 3.109]. Though this configuration is particularly simple, it illustrates the general property that each spherical vector wave contributes to the entire spectral domain of the PWE – the visible region as well as the invisible region – and that the complete PWE can be obtained from the complete SWE. For a general antenna more *Q* coefficients will be present in the SWE of the radiated field, and thus more terms will be required in the computation of Eq. 13 as illustrated in the following section.

4. Numerical investigation on the SWE-to-PWE transformation

In this section we investigate the properties of the SWE-to-PWE transformation of Eq. 13, in particular the convergence mechanism, in the general case where the coefficients $Q_{1mn}^{(3)}$ and $Q_{2mn}^{(3)}$ are included. The purpose is to study the possibility of truncating the infinite *n*-series to a finite value *N* that might be different from the truncation number used in far-field calculations. In order to do that, we investigate the case of an *x*-oriented electric Hertzian dipole displaced on the *x*-axis, see Fig. 7. In spite of its apparent simplicity, this test case possesses characteristics that are representative for more complex antennas, and its use here is motivated by several factors. First, since any source distribution can in principle be constructed from a combination of properly positioned, oriented and excited Hertzian dipoles, the case of a single dipole is representative for more realistic sources. Second, as it will be seen in Eqs. 22-23, a single electric Hertzian dipole displaced from the origin of the coordinate system possesses an infinite SWE like any complex antenna, which allows us to study the truncation of Eq. 13 to finite *N*-values. Third, the Hertzian dipole allows the analytical calculation of the exact plane wave spectrum which provides the necessary reference to investigate such a truncation, see Eqs. 24-26. We have investigated other source configurations, see for example [*Cappellin, Frandsen and Breinbjerg*, 2006][*Cappellin, Breinbjerg and Frandsen*, 2006] for an array of Hertzian dipoles and a rectangular aperture in free-space, but the present one with a single dipole shows qualitatively – though not quantitatively – the same properties.

For the *x*-oriented dipole with dipole moment *p* located at the position $x = r_o$ the *Q* coefficients can be calculated analytically [*Hansen*, 1988, eq. A1.78]

$$Q_{1mn}^{(3)}=0 \qquad n=1,2,..\infty \quad m=-n,..,n \tag{22}$$

$$Q_{2mn}^{(3)}=\frac{-kp}{\sqrt{\eta}}\left(-\frac{m}{|m|}\right)^m\frac{\sqrt{n(n+1)}}{\sqrt{2\pi}}\frac{j_n(kr_o)}{kr_o}\bar{P}_n^{|m|}(0) \qquad n=1,2,..\infty \quad m=-n,..,n \tag{23}$$

with $j_n(kr)$ being the spherical Bessel function of the first kind. Different values of r_o have been studied and here the results for $r_o = 2\lambda$, corresponding to $kr_o = 12$, are presented. The *n*-mode power spectrum, $P_{rad}(n)=\frac{1}{2}\sum_{s=1}^{2}\sum_{m=-n}^{n}\left|Q_{smn}^{(3)}\right|^2$ [*Hansen*, 1988, eq. 2.55], normalized to the value of $P_{rad}(1)$, is shown in Fig. 8. It is seen that the peak occurs at $n\approx kr_o=12$, as expected, and that the major amount of power is contained in the first $N=kr_o+10$ modes. By use of Eqs. 12-13-22-23 the plane wave spectrum is calculated for different truncation numbers *N* and resolved in its Cartesian components T_x, T_y, and T_z. These are then compared to the exact plane

wave spectrum, calculated analytically from the dipole current distribution as [*Hansen and Yaghjian*, 1999, eq. 3.109]

$$T_{ref\,x} = \frac{p}{4\pi k\eta}\frac{k_x^2 - k^2}{k_z} e^{-ik_x r_o} e^{ik_z z} \tag{24}$$

$$T_{ref\,y} = \frac{p}{4\pi k\eta}\frac{k_x k_y}{k_z} e^{-ik_x r_o} e^{ik_z z} \tag{25}$$

$$T_{ref\,z} = \frac{p}{4\pi k\eta} k_x e^{-ik_x r_o} e^{ik_z z} \tag{26}$$

From Eqs. 24-26 it is seen that $T_{ref\,x}$ and $T_{ref\,y}$ contain the singularity in k_z. Fig. 9 shows the normalized magnitude (in logarithmic scale) of the x-component, $T_{ref\,x}$ and T_x, on the plane $z = 0.2\lambda$, for $N = kr_o$, $N = kr_o+10$, $N = kr_o+20$, $N = kr_o+30$, and $N = kr_o+38$, while the corresponding phase plots in radians are given in Fig. 10. From Fig. 9 it is possible to distinguish the singularity for $k_z = 0$, the nulls occurring at $k_x = \pm k$, and the exponential decay in the invisible region. Eq. 13 is a convergent series and we notice from Fig. 9 that the spectral region in the $k_x k_y$-domain where the convergence is reached gradually increases with increasing N. For $N = kr_o = 12$ the visible region is not completely reconstructed but the convergence is reached with $N = kr_o+10 = 22$, in the visible region and at $k_z = 0$. Values of $N > kr_o + 10$ only influence the invisible region.

The convergence mechanism can also be understood by considering the n-mode power spectrum of Fig. 8. The extremely low values of power contained in the high n-modes are given by corresponding extremely low values of Q-coefficients which keep finite the product with the diverging spherical vector wave functions, and provide the necessary terms in order for the series of Eq. 13 to reach convergence. A plot of the amplitude of T_x as a function of N for specific points in the spectral domain is shown in Fig. 11. We clearly distinguish two different mechanisms: the series of Eq. 13 reaches convergence with $N = kr_o+10 = 22$ for points in the visible region, while additional N terms are needed to reach convergence for points in the invisible region. In particular, for the spectral point $(k_x, k_y) = (1.2k, 0)$ (blue curve in right-hand plot of Fig. 11), convergence is not reached until $N = kr_o+23 = 35$. For the spectral point $(k_x, k_y) = (1.6k, 0)$ (red curve in right-hand plot of Fig. 11) convergence is not reached until $N = kr_o+33 = 45$; and for $(k_x, k_y) = (1.8k, 1.8k)$ (black curve in right-hand plot of Fig. 11) convergence is not within the first 50 terms of the SWE. Furthermore, it is interesting to note that for these spectral points the magnitude of the accumulated series becomes very large, in excess of 100dB, for intermediate values of N before it converges at a level of some -10dB. For all of these spectral points in the invisible region, the first few terms ($N < 5$) are bounded and the accumulated series has values comparable to those for points in the visible region. A plot of the real and imaginary parts of T_x as a function of N, see Fig. 12, shows that the path to convergence for points with $k_y = 0$ and $k_x > k$ forms a rectangular spiral which initially diverges but then converges to the final value. For points within the visible region, the convergence path is more irregular though obviously much faster. It has been observed that these mechanisms of convergence are independent of the spectral component and govern both the amplitude and the phase. The truncation number N required to reach convergence in the $[-2k, 2k]$ domain depends on r_o and it has been found that $N = kr_o + 4kr_o$ constitutes a good rule-of-thumb. This rule holds for the present case of a single dipole and was also observed for other antenna configurations [*Cappellin, Frandsen and Breinbjerg*, 2006] [*Cappellin, Breinbjerg and Frandsen*, 2006], though it may not be generally valid. Moreover, as a consequence of the properties of the expansion of Eq. 10, the convergence mechanism is independent of the z-plane of observation

though the spectrum in the invisible region of course becomes negligible with larger z-coordinates, see Fig. 13 for the case $z = 4\lambda$.

Since the Hertzian dipole investigated here is displaced along the x-axis, the convergence of the SWE-to-PWE transformation depends only on the k_x spectral variable and is thus independent of the k_y spectral variable as seen from Figs. 9-10. For sources distributed along both the x- and y-axes, the convergence will depend on both k_x and k_y in the sense that all points in the visible region reach convergence with $N = kr_o+10$, while all points in the invisible require more terms depending on their location in the spectral domain and the antenna size.

5. Conclusions

Fundamental properties of the SWE-to-PWE transformation have been investigated analytically and numerically. The transformation allows the calculation of the PWE in the visible as well as the invisible spectral regions from the knowledge of the Q-coefficients of the SWE. The transformation of individual spherical waves was studied in order to determine how these contribute to different regions of the spectral domain. It was noted that each spherical wave contributes to the visible as well as the invisible regions and thus provides information on the propagating as well as evanescent waves of the PWE. Also, the convergence properties of the transformation were studied, and it was found that these are vastly different for the visible and invisible regions of the PWE. While a truncation in the n-modes at $N = kr_o+10$, with r_o being the radius of the minimum sphere, is generally sufficient to reach convergence in the visible region, a much higher value is necessary in the invisible region, where the path to convergence was found to involve very large intermediate values. For the configuration investigated here, a truncation number $N = kr_o+4\ kr_o$ was found to be necessary for a $[-2k, 2k]$ region of the spectral domain. Furthermore, it was shown how the numerical problem of calculating the spherical wave functions for a given n- and m- mode in points of the invisible region can be overcome by embedding the $\exp(ik_z z)$ term in the calculation of the associated Legendre functions, and guidelines were provided to find the proper z-plane. Finally, it was pointed out that the determination of the PWE in the invisible region leads to an improved spatial resolution compared to the traditional half a wavelength provided by the visible region alone.

The SWE-to-PWE transformation constitutes an essential step in a new antenna diagnostics technique for spherical near-field antenna measurements, where the extreme near-field must subsequently be computed from the obtained PWE using Eq. 4 by either a direct numerical integration or, more efficiently, an inverse Fourier transform [*Cappellin, Frandsen and Breinbjerg,* 2006]. It is noted that the antenna diagnostics technique based on the SWE-to-PWE transformation will be influenced and limited by the finite dynamic range and accuracy of the measurement system. This will limit the number of terms in the SWE that can be accurately measured and the spectral region where convergence can be reached [*Cappellin, Breinbjerg and Frandsen,* 2006] [*Cappellin, Frandsen and Breinbjerg,* 2007][*Cappellin et al.,* 2007]. Nevertheless, the properties of the SWE-to-PWE transformation investigated above are generally also of practical importance and determine, along with the quality of the measurement system, the accuracy and the efficiency of this antenna diagnostics technique [*Cappellin, Frandsen and Breinbjerg,* 2007][*Cappellin et al.,* 2007].

Appendix A

In this appendix the SWE-to-PWE transformation is derived along the lines of [*Hansen and Yaghjian*, 1999, Section 3]. We begin by introducing the far-field expression for the SWE of Eq. 1 [*Hansen*, 1988, eq. 2.179],

$$\begin{aligned}\bar{E}_{far}(\bar{r}) &= \lim_{kr\to\infty} \bar{E}(\bar{r}) = \frac{e^{ikr}}{r}\frac{1}{\sqrt{\eta}}\frac{1}{\sqrt{4\pi}}\sum_{n=1}^{\infty}\sum_{m=-n}^{n} Q_{1mn}^{(3)}\bar{K}_{1mn}(\theta,\varphi) + Q_{2mn}^{(3)}\bar{K}_{2mn}(\theta,\varphi) \\ &= \frac{e^{ikr}}{r}\bar{F}(\theta,\varphi)\end{aligned} \tag{a}$$

with $\theta \in [0,\pi]$ and $\varphi \in [0,2\pi]$. $\bar{F}(\theta,\varphi)$ is the far-field pattern, and $\bar{K}_{smn}(\theta,\varphi)$ the far-field pattern functions [*Hansen*, 1988, pp. 49]

$$\bar{K}_{smn}(\theta,\varphi) = \lim_{kr\to\infty} \frac{\sqrt{4\pi}kr}{e^{ikr}}\bar{F}_{smn}^{(3)}(r,\theta,\varphi) \qquad s = 1, 2 \tag{b}$$

$$\bar{K}_{1mn}(\theta,\varphi) = \sqrt{\frac{2}{n(n+1)}}\left(-\frac{m}{|m|}\right)^{m} e^{im\varphi}(-i)^{n+1}\left[\frac{im\bar{P}_n^{|m|}(\cos\theta)}{\sin\theta}\hat{\theta} - \frac{d\bar{P}_n^{|m|}(\cos\theta)}{d\theta}\hat{\varphi}\right] \tag{c}$$

$$\bar{K}_{2mn}(\theta,\varphi) = \sqrt{\frac{2}{n(n+1)}}\left(-\frac{m}{|m|}\right)^{m} e^{im\varphi}(-i)^{n}\left[\frac{d\bar{P}_n^{|m|}(\cos\theta)}{d\theta}\hat{\theta} + \frac{im\bar{P}_n^{|m|}(\cos\theta)}{\sin\theta}\hat{\varphi}\right] \tag{d}$$

Next, we consider the PWE of Eq. 4 and in particular its far-field expression in Eq. 5 [*Hansen and Yaghjian*, 1999, eq. 3.133]

$$\begin{aligned}\bar{E}_{far}(\bar{r}) &= \lim_{kr\to\infty} \bar{E}(\bar{r}) = -\frac{e^{ikr}}{r} ik\cos\theta\,\bar{T}(k\sin\theta\cos\varphi, k\sin\theta\sin\varphi) \quad \theta\in[0,\pi/2], \quad \varphi\in[0,2\pi] \\ &= \frac{e^{ikr}}{r}\bar{F}(\theta,\varphi)\end{aligned} \tag{e}$$

By identifying Eq. (a) and (e) in the spatial domain where both hold, $\theta \in [0,\pi/2]$ $\varphi \in [0,2\pi]$, the plane wave spectrum $\bar{T}$ can be expressed as

$$\begin{aligned}\bar{T}(k\sin\theta\cos\varphi, k\sin\theta\sin\varphi) &= \frac{i}{\sqrt{\eta}}\frac{1}{\sqrt{4\pi}}\frac{1}{k\cos\theta}\sum_{n=1}^{\infty}\sum_{m=-n}^{n} Q_{1mn}^{(3)}\bar{K}_{1mn}(\theta,\varphi) + Q_{2mn}^{(3)}\bar{K}_{2mn}(\theta,\varphi) \\ &= \frac{i}{k\cos\theta}\bar{F}(\theta,\varphi)\end{aligned} \tag{f}$$

where $k\sin\theta\cos\varphi = k_x$ and $k\sin\theta\sin\varphi = k_y$ are the spectral variables. In the first place, this relation holds for real θ-angles and thus the visible region, $k_x^2 + k_y^2 \le k^2$. However, since the far-field pattern of a finite source distribution is an analytic function, [*Hansen and Yaghjian*, 1999] and [*Gerchberg*, 1974], it is possible to analytically continue the far-field pattern to complex θ-angles, obtaining from Eq. (f) the plane wave spectrum also in the invisible region, $k_x^2 + k_y^2 > k^2$. While the relationship between the plane wave spectrum and the far-field pattern can be found from Eq. (e) alone, the use of Eq. (a), and thus of the first equality in Eq. (f),

allows the analytical continuation to complex values of θ, overcoming the difficulty of continuing a measured far-field pattern [*Hansen and Yaghjian*, 1999, pp. 136].
By writing θ and φ as functions of the spectral variables k_x and k_y according to

$$\theta = \arcsin\left(\sqrt{\frac{k_x^2 + k_y^2}{k^2}}\right),\ \varphi = \arctan\left(\frac{k_y}{k_x}\right) \tag{g}$$

allowing values of k_x and k_y larger than k and ensuring $\theta \in B$ and $\varphi \in [0, 2\pi]$, writing $k_z = k\cos\theta$ and by defining $\bar{T}(k_x, k_y)e^{ik_z z} = \bar{T}(k_x, k_y, z)$, from Eq. (f) it follows that

$$\bar{T}(k_x, k_y, z) = \sum_{n=1}^{\infty}\sum_{m=-n}^{n} Q_{1mn}^{(3)}\bar{T}_{1mn}(k_x, k_y, z) + Q_{2mn}^{(3)}\bar{T}_{2mn}(k_x, k_y, z) \tag{h}$$

where

$$\bar{T}_{1mn}(k_x, k_y, z) = \frac{e^{ik_z z}}{k_z}\frac{i}{\sqrt{4\pi}\sqrt{\eta}}\bar{K}_{1mn}(\theta, \varphi) \tag{i}$$

$$\bar{T}_{2mn}(k_x, k_y, z) = \frac{e^{ik_z z}}{k_z}\frac{i}{\sqrt{4\pi}\sqrt{\eta}}\bar{K}_{2mn}(\theta, \varphi) \tag{l}$$

The plane wave spectrum $\bar{T}(k_x, k_y, z)$ can thus be written in its entire $k_x k_y$-domain from the knowledge of the Q coefficients of the SWE of the radiated field.

References

Booker, H. G., and P. C. Clemmow (1950), The concept of an angular spectrum of plane waves, and its relations to that of polar diagram and aperture distribution, *Proc. Inst. Elec. Eng.***,** *97*, 11-17.

Cappellin, C., O. Breinbjerg, and A. Frandsen (2006), The influence of finite measurement accuracy on the SWE-to-PWE antenna diagnostics technique, presented at EuCAP European Conference on Antennas and Propagation, Nice, France.

Cappellin, C., A. Frandsen, and O. Breinbjerg (2007), Application of the SWE-to-PWE antenna diagnostics technique to an offset reflector antenna, submitted to Antenna Measurements Technique Association Symposium, AMTA 2007, St. Louis, USA, November.

Cappellin, C., A. Frandsen, S. Pivnenko, G. Lemanczyk, and O. Breinbjerg (2007), Diagnostics of the SMOS radiometer antenna system at the DTU-ESA spherical near-field antenna test facility, submitted to European Conference on Antennas and Propagation, EuCAP 2007, Edinburgh, UK, November.

Cappellin, C., A. Frandsen, and O. Breinbjerg (2006), On the relationship between the spherical wave expansion and the plane wave expansion for antenna diagnostics, presented at AMTA Europe Symposium, Munich, Germany.

Devaney, A. J. (1982), A filtered backpropagation algorithm for diffraction tomography, *Ultrason. Imag.*, *4*, 336–360.

Devaney, A. J., and E. Wolf (1974), Multipole expansion and plane wave representations of the electromagnetic field, *Journ. of Math. and Phys.*, *15*, 234-244.

Gerchberg, R. W. (1974), Super-resolution through error energy reduction, *Optica Acta*, *21*, 709-720.

Hansen, J. E. (Ed.) (1988), *Spherical Near-Field Antenna Measurements*, Peter Peregrinus Ltd. London.

Hansen, W. W. (1935), A new type of expansion in radiation problems, *Phys. Rev.*, *47*, 139-143.

Hansen, T. B., and P. M. Johansen (2000), Inversion scheme for ground penetrating radar that takes into account the planar air-soil interface, *IEEE Trans. on Geoscience and Remote Sensing*, *38*, 496-506.

Hansen, T. B., and A. D. Yaghjian (Eds.) (1999), *Plane Wave Theory of Time-Domain Fields, Near-Field Scanning Applications*, IEEE PRESS.

Homepage of SNIFTD software: http://www.ticra.dk/script/site/page.asp?artid=27.

Kerns, D. M. (1976), Plane wave scattering-matrix theory of antennas and antenna-antenna interactions: formulation and applications, *Journal of Research of the National Bureau of Standards*, *80B*, 5-51.

Mehler, M. J. (1988), Application of spherical wave expansions to direct GO far field synthesis, *Microwaves Antennas and Propagation, IEE Proceedings H*, *135*, 41-47.

Morse, P., and H. Feshbach (Eds.) (1953), *Methods of theoretical physics*, International Series in Pure and Applied Physics, McGraw-Hill, New York.

Stratton, J. A. (Ed.) (1941), *Electromagnetic Theory***,** McGraw-Hill, New York.

Varadan, V. V., A. Lakhtakia, and V. K. Varadan (Eds.) (1991), *Field representations and introduction to scattering*, Elsevier Science Publishers B. V.

Wang, J. J. H. (1988), An examination of the theory and practices of planar near/field measurement, *IEEE Trans. Antennas Propagat.*, *36*, 746-753.

Whittaker, G. T., and G. N. Watson (Eds.) (1927), *Modern Analysis***,** Cambridge Univ. Press, London.

Yaghjian, A. D. (1986), An overview of near-field antenna measurements, *IEEE Trans. Antennas Propagat.*, *34*, 30–45.

List of figures

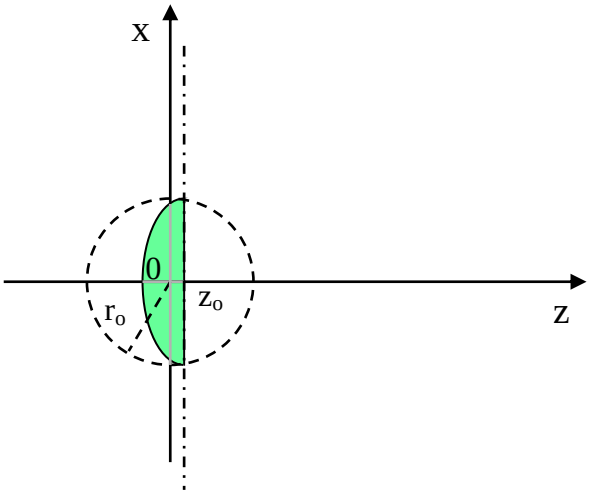

Figure 1

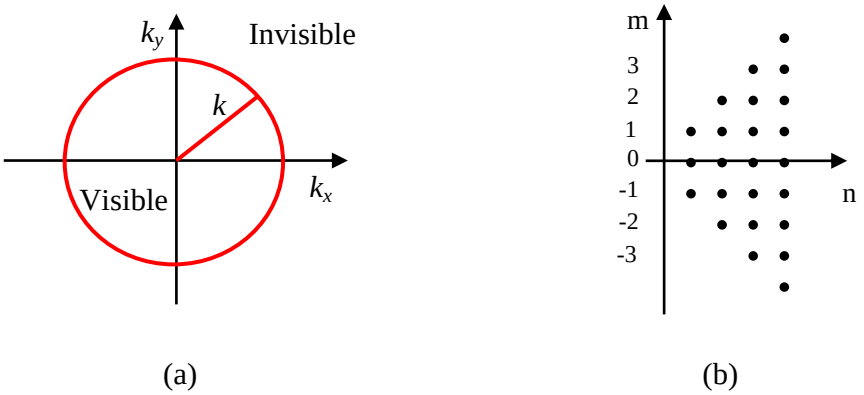

(a) (b)

Figure 2

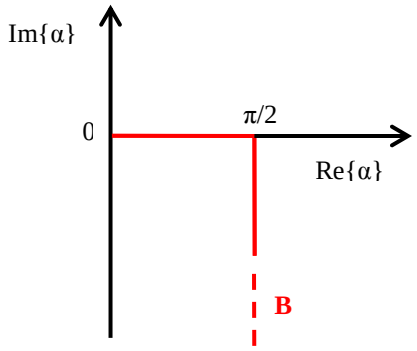

Figure 3

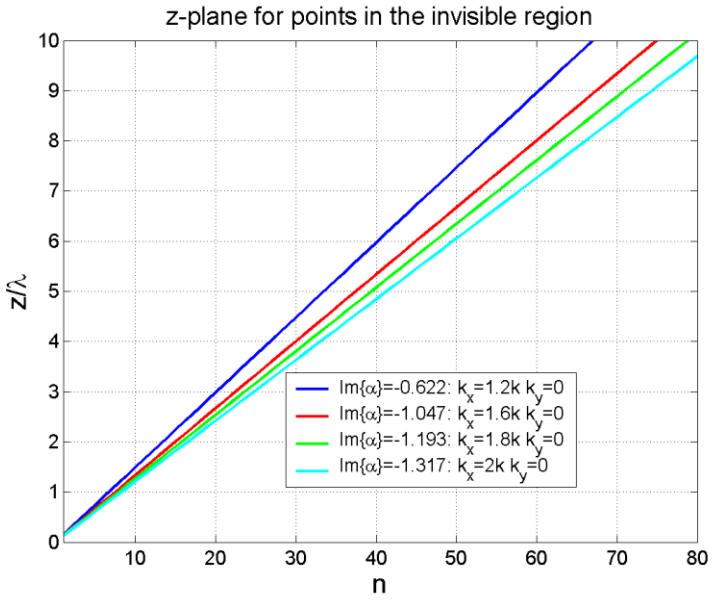

Figure 4

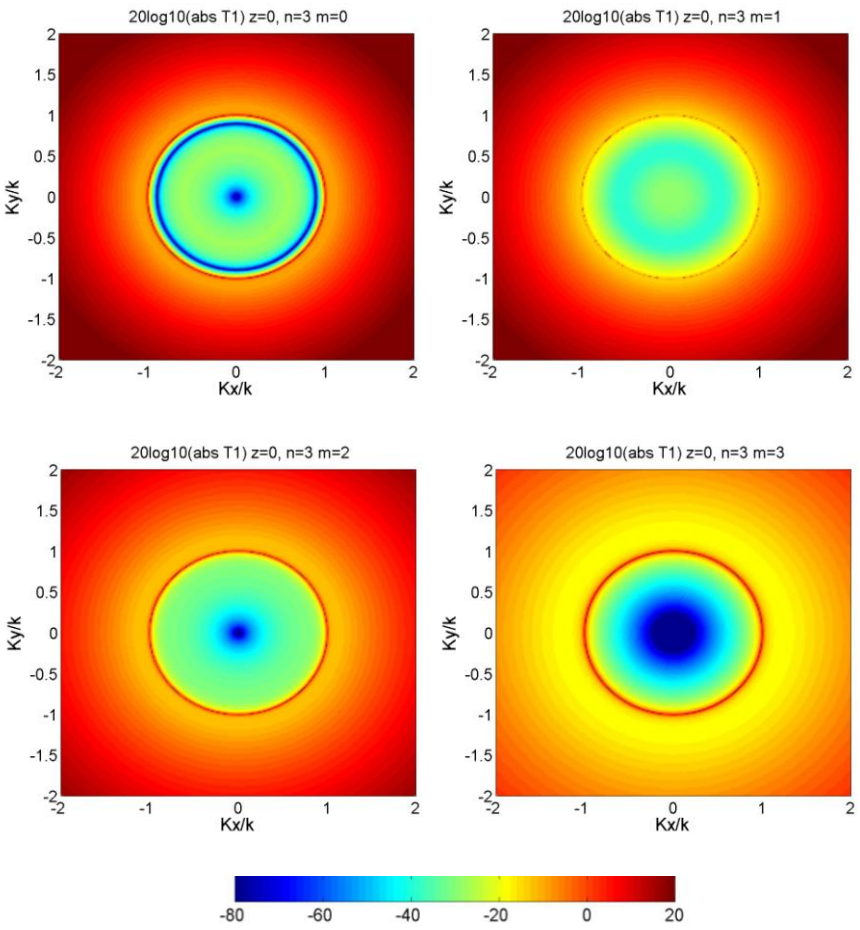
20log10(abs T1) z=0, n=3 m=0
20log10(abs T1) z=0, n=3 m=1
20log10(abs T1) z=0, n=3 m=2
20log10(abs T1) z=0, n=3 m=3
Ky/k
Kx/k
2
1.5
1
0.5
0
-0.5
-1
-1.5
-2
-80
-60
-40
-20
0
20

Figure 5

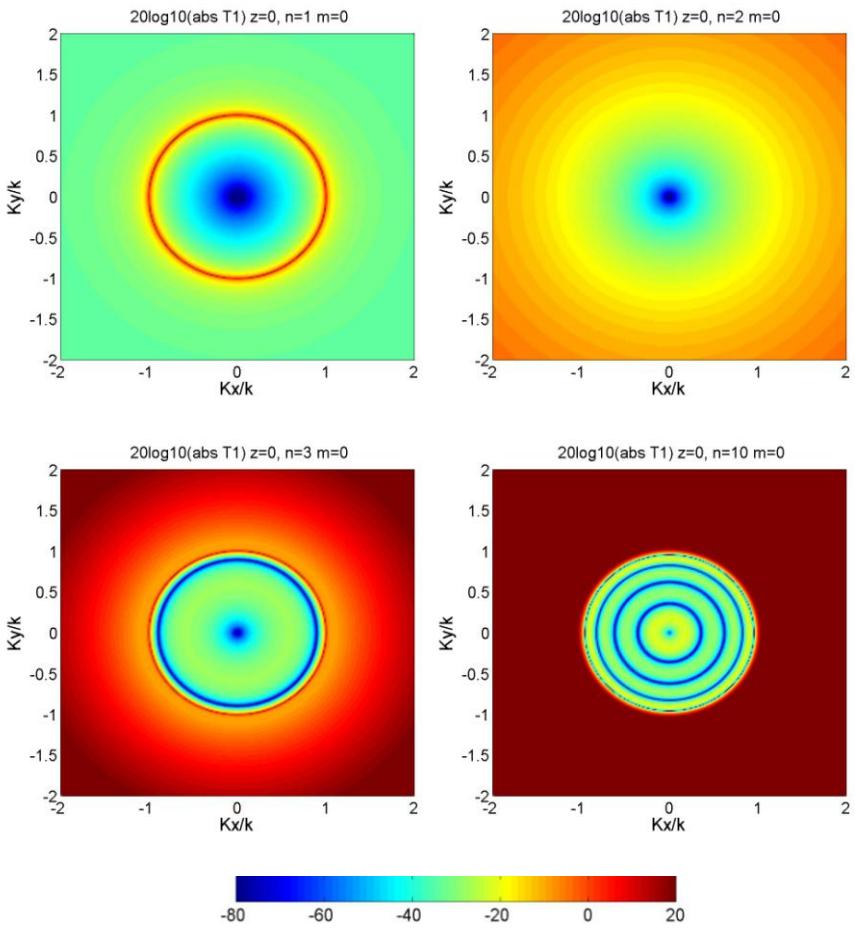
20log10(abs T1) z=0, n=1 m=0
20log10(abs T1) z=0, n=2 m=0
20log10(abs T1) z=0, n=3 m=0
20log10(abs T1) z=0, n=10 m=0
Ky/k
Kx/k
2
1.5
1
0.5
0
-0.5
-1
-1.5
-2
-80
-60
-40
-20
0
20

Figure 6

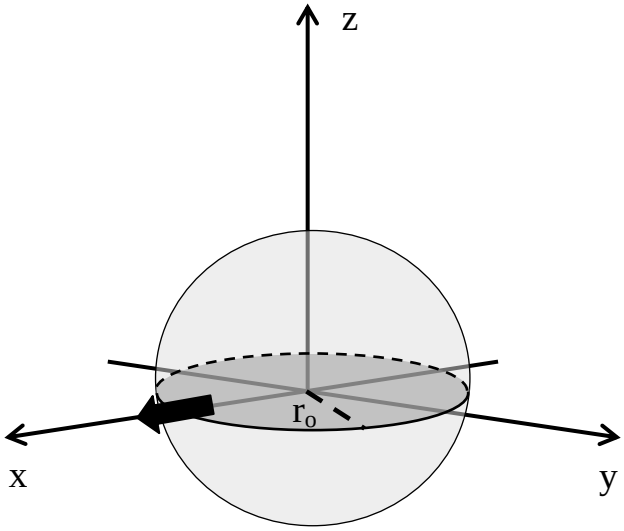

Figure 7

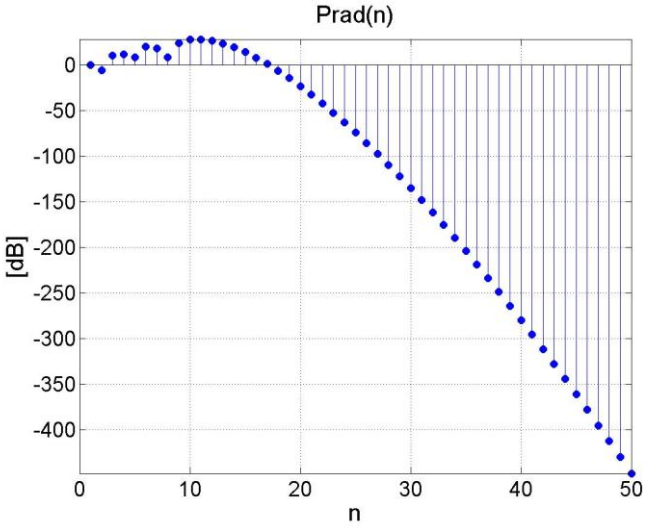

Figure 8

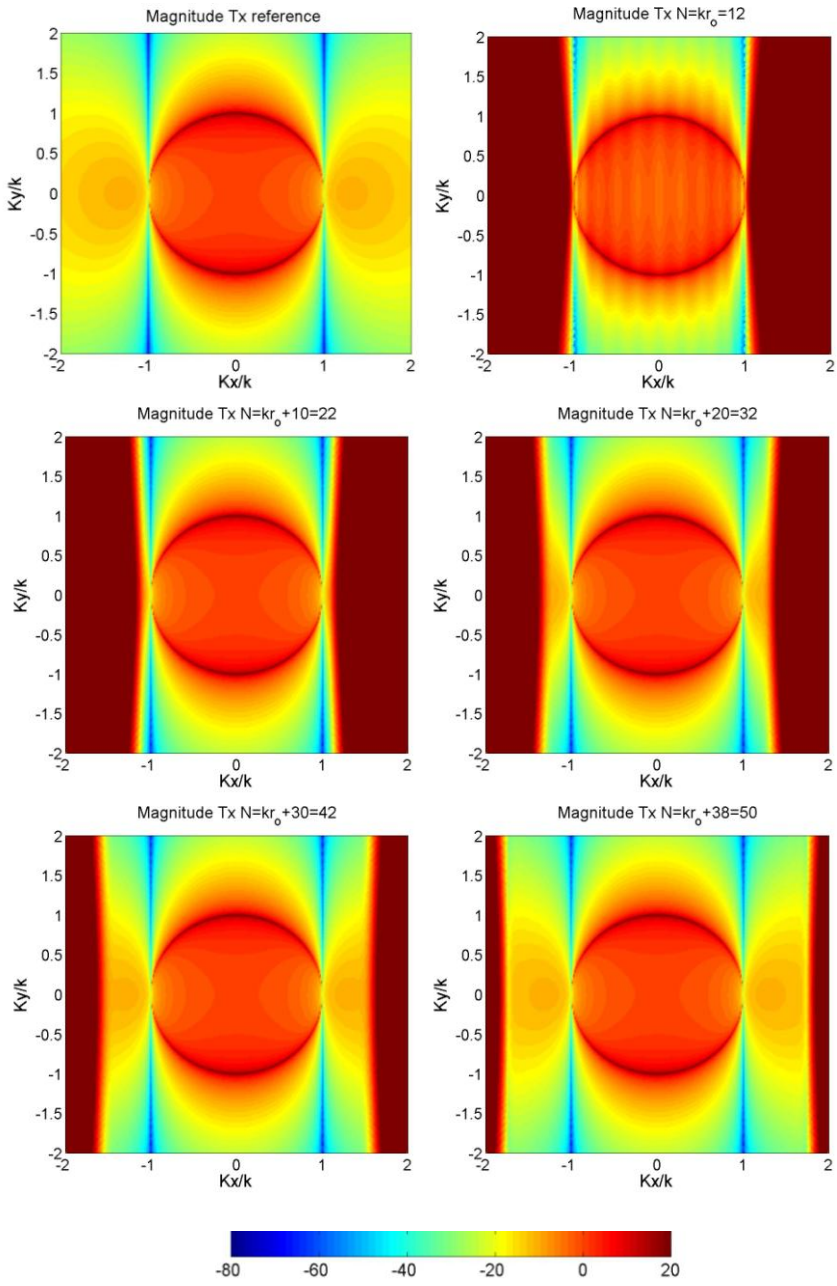
Magnitude Tx reference
Magnitude Tx N=kr$_o$=12
Magnitude Tx N=kr$_o$+10=22
Magnitude Tx N=kr$_o$+20=32
Magnitude Tx N=kr$_o$+30=42
Magnitude Tx N=kr$_o$+38=50
Ky/k
Kx/k
2
1.5
1
0.5
0
-0.5
-1
-1.5
-2
-80
-60
-40
-20
0
20

Figure 9

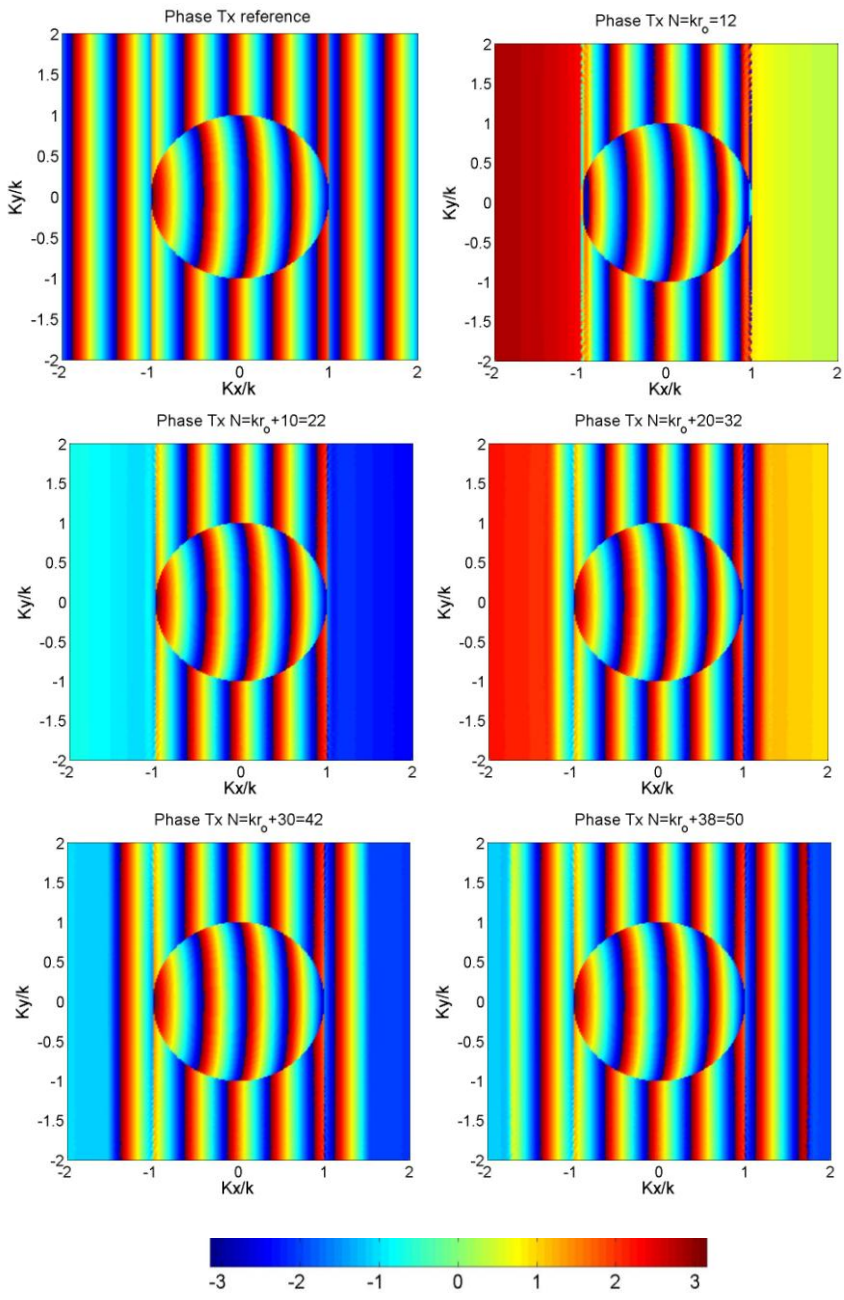
Phase Tx reference
Phase Tx N=kr$_o$=12
Phase Tx N=kr$_o$+10=22
Phase Tx N=kr$_o$+20=32
Phase Tx N=kr$_o$+30=42
Phase Tx N=kr$_o$+38=50
Ky/k
Kx/k
2
1.5
1
0.5
0
-0.5
-1
-1.5
-2
-3

Figure 10

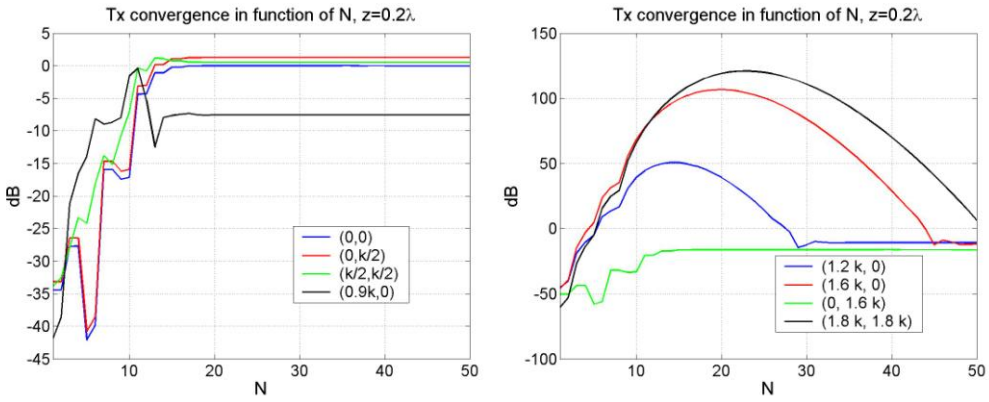

Figure 11

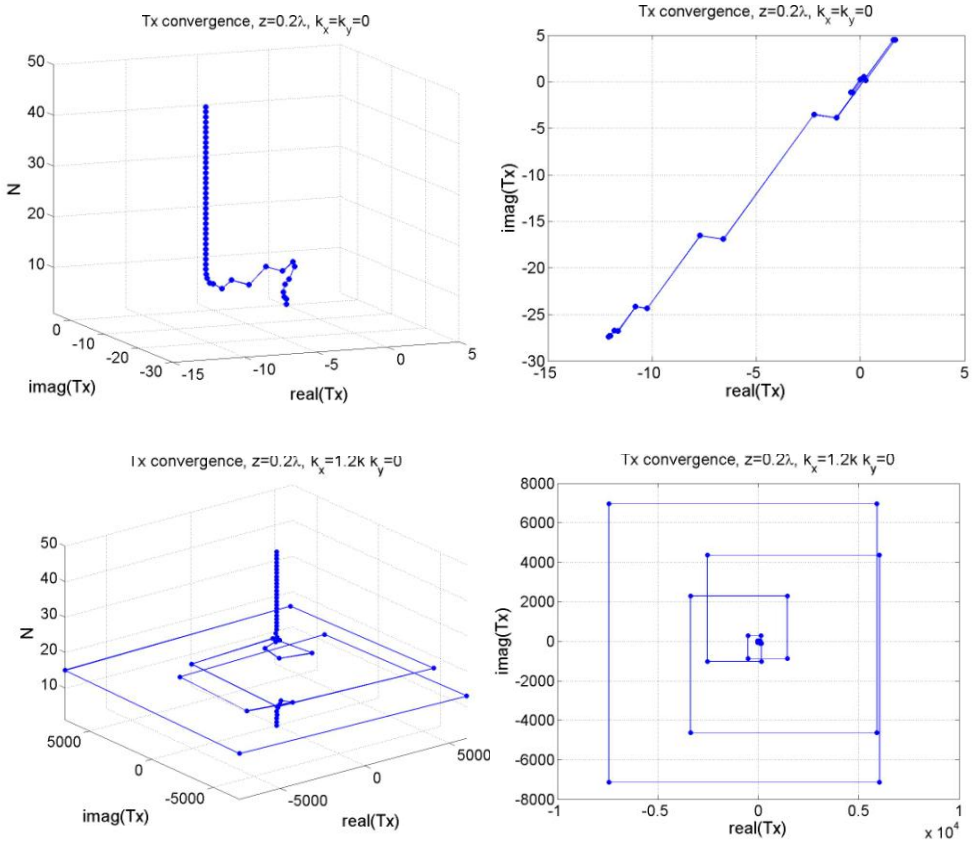

Figure 12

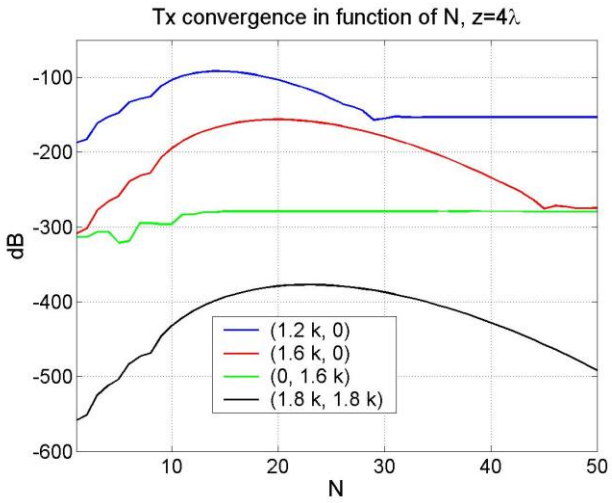
Tx convergence in function of N, z=4λ
-100
-200
-300
-400
-500
-600
dB
10
20
30
40
50
N
(1.2 k, 0)
(1.6 k, 0)
(0, 1.6 k)
(1.8 k, 1.8 k)

Figure 13

Paper II

A Singularity Extraction Technique for Computation of Antenna Aperture Fields from Singular Plane Wave Spectra

Cecilia Cappellin [1-2], Olav Breinbjerg [1], Aksel Frandsen [2]

[1] Ørsted•DTU, Technical University of Denmark, DK-2800 Kgs. Lyngby, Denmark

[2] TICRA, Læderstræde 34, DK-1201 Copenhagen K, Denmark

Corresponding author:

Cecilia Cappellin
TICRA, Læderstræde 34, DK-1201 Copenhagen K, Denmark
Tel: +45 2273 9882
Fax: +45 3312 0880
Email: cc@ticra.com

Keywords: plane wave expansion, singularity extraction, Fast Fourier Transform, Weyl-identity

Abstract

An effective technique for extracting the singularity of plane wave spectra in the computation of antenna aperture fields is proposed. The singular spectrum is first factorized into a product of a finite function and a singular function. The finite function is inverse Fourier transformed numerically using the Inverse Fast Fourier Transform, while the singular function is inverse Fourier transformed analytically, using the Weyl-identity, and the two resulting spatial functions are then convolved to produce the antenna aperture field. This paper formulates the theory of the singularity extraction technique and illustrates the effect of this for an array of electric Hertzian dipoles.

1. Introduction

The plane wave expansion (PWE) is widely used in antenna theory, as well as diffraction, imaging and propagation theory, to represent the electromagnetic field in source-free regions of space as an infinite, continuous spectrum of plane waves [1]-[3]. The plane wave spectrum (PWS) of the PWE is an analytic function on the entire spectral domain, except possibly at the circular border between the visible and invisible spectral regions where a singularity may exist [4]. Since the PWS at, and close to, this circular border corresponds to the far-field radiation pattern at wide angles, a zero of the pattern at those angles is a necessary condition for the PWS to be finite. Otherwise, the PWS possesses a singularity there, and this is thus the case for most antennas.

In applications where the aperture field is calculated from the PWS this singularity must be taken properly into account in order to ensure the accuracy of the aperture field. In some cases, e.g., where the PWS is determined from a planar near-field measurement over a finite scan plan,

the PWS is reliable only over the central part of the visible region of the spectral domain [5], and the part of the domain where the singularity exists must be disregarded. However, in other cases, e.g., where the PWS is determined from a far-field measurement, a compact range measurement or a spherical near-field measurement, the PWS at, or close to, the border between the visible and invisible regions can be determined and the singularity is thus known.

Since the PWS and the aperture field constitute an inverse Fourier transform pair, the Inverse Fast Fourier Transform (IFFT) is normally used for computation of the aperture field from the PWS. However, the singularity of the PWS, though integrable, prevents a straightforward application of the IFFT. Many singularity extraction techniques for numerical integration have been proposed, in particular for integral equation and method of moment techniques [6][7], but here a different approach is used.

The purpose of this work is to formulate and validate a new singularity extraction technique for the computation of antenna aperture fields from singular plane wave spectra. In this technique the singular PWS is first factorized into a product of a finite function and a singular function. The inverse Fourier transforms of these two spectral functions are then calculated. For the finite function this is done numerically using the IFFT, and for the singular function this is done analytically using the Weyl-identity. Finally, the two thus obtained spatial functions are convolved to produce the antenna aperture field. In this work the effect of the singularity extraction technique is applied to a simple test case in order to isolate and identify the singularity and its influence on the aperture field. However, the singularity extraction technique has been applied also to real measurements data for practical and complicated antennas [8]-[9].

The present manuscript is organized as follows: In Section 2 the PWE theory is briefly summarized with particular attention to the singularity. In Section 3 the singularity extraction technique is formulated, while Section 4 illustrates its effect through a numerical test case. All expressions are given in the S.I. rationalized system with a suppressed $e^{-i\omega t}$ time convention.

2. The Plane Wave Expansion

The PWE of the electric field $\bar{E}$, valid for $z > z_o$ with z_o being the largest z-coordinate of the antenna as indicated in Fig. 1a, is given by [4]

$$\bar{E}(x,y,z) = \frac{1}{2\pi}\int_{-\infty}^{\infty}\int_{-\infty}^{\infty} \bar{T}(k_x,k_y)\, e^{ik_z z} e^{i(k_x x + k_y y)} dk_x dk_y = F^{-1}\left\{\bar{T}(k_x,k_y,z)\right\}, \qquad z > z_o \tag{1a}$$

where (x,y,z) are the Cartesian coordinates of the observation point with position vector $\bar{r}$, while k_x and k_y are the spectral variables which together with $k_z = \sqrt{k^2 - k_x^2 - k_y^2}$, with k being the wavenumber, constitute the Cartesian components of the wave propagation vector $\bar{k}$. Eq. 1a shows that the two-dimensional inverse Fourier transform (IFT), F^{-1}, of the PWS for a given z-coordinate $z > z_o$, $\bar{T}(k_x,k_y,z) \equiv \bar{T}(k_x,k_y)e^{ik_z z}$, provides the electric field $\bar{E}$ at that z-plane. The inverse of Eq. 1a is obviously

$$\bar{T}(k_x,k_y,z) = \frac{1}{2\pi}\int_{-\infty}^{\infty}\int_{-\infty}^{\infty} E(x,y,z) e^{-i(k_x x + k_y y)} dx\, dy = F\left\{\bar{E}(x,y,z)\right\}, \qquad z > z_o \tag{1b}$$

The spectral $k_x k_y$-domain is divided into two regions, see Fig. 1b. The visible region, for $k_x^2 + k_y^2 \le k^2$, contains propagating plane waves and the invisible region, for $k_x^2 + k_y^2 > k^2$, contains evanescent plane waves. The two spectral variables k_x and k_y are real, while k_z is real in the visible region but purely imaginary with a positive imaginary part in the invisible region to

satisfy the radiation condition. Since the evanescent plane waves are exponentially attenuated with increasing z-coordinate, their contribution to the field is usually negligible at distances larger than one wavelength from the antenna [3]. In practice, the k_x- and k_y-integrals are truncated at finite values $\pm k_{xmax}$ and $\pm k_{ymax}$, respectively, and in cases where the PWS is obtained from measurements, the PWS is reliable only over the visible region or an even smaller spectral domain [5].

The PWS is an analytic function on the entire spectral domain except possibly at the border between the visible and invisible region where $k_z = 0$ and a singularity of the type $1/k_z$ often exists in one or more of its components [4]. This constitutes the only possible singularity and a necessary but insufficient condition to prevent its exsistence is a null in the xy-plane of the antenna far-field pattern. While the singularity in the PWS does not explicitly appear in Eq. 1b, it is seen when $\bar{T}(k_x, k_y)$ is expressed as a function of the volume current density $\bar{J}$ of the antenna [4]

$$\bar{T}(k_x, k_y) = \frac{1}{k_z} \frac{1}{4\pi k \eta} \bar{k} \times \left(\bar{k} \times \int_V \bar{J}(\bar{r}) e^{-i(k_x x + k_y y + k_z z)} dV \right) \tag{2}$$

with η being the medium intrinsic admittance, or when the visible region of $\bar{T}(k_x, k_y)$ is expressed in terms of the far-field pattern [4],

$$\begin{aligned} \bar{E}_{far}(r, \theta, \varphi) &= \lim_{kr \to \infty} \bar{E}(r, \theta, \varphi) \\ &= -\frac{e^{ikr}}{r} ik \cos\theta \, \bar{T}(k \sin\theta \cos\varphi, k \sin\theta \sin\varphi) \quad \theta \in [0, \pi/2], \quad \varphi \in [0, 2\pi] \end{aligned} \tag{3}$$

since $k \cos\theta = k_z$.

3. The singularity extraction technique

Though the singularity of $\bar{T}(k_x, k_y)$ is integrable, a direct use of the IFFT results in an inaccurate aperture field unless the singularity is sampled very densely. While on one hand this could in principle be possible, on the other hand such a high density would be necessary over the entire $k_x k_y$-domain in order to have the uniform sampling required by the IFFT algorithm. This presents a problem when the plane wave spectrum is obtained from measurements since a very dense angular or spatial sampling, in θ- and φ-coordinates for far-field measurements or in x- and y-coordinates for planar near-field measurements, is then required. Another possible approach is to employ a special numerical integration scheme incorporating a singularity extraction technique like for example is shown in [6][7]. Finally, it is possible to transform the Cartesian spectral variables into spherical spectral variables in which case the singularity disappears. However, in both cases one would loose the advantages of the IFFT.

Here, we propose to defactorize the spectrum $\bar{T}$ into a product of two functions, the finite $\bar{T}_1$ and the singular $1/k_z$ whereby

$$\bar{T}(k_x, k_y) = \bar{T}_1(k_x, k_y) \frac{1}{k_z} \quad . \tag{4}$$

Since the IFT of a product of two spectral functions is equal to the convolution of the two corresponding spatial functions [10] the integral of Eq. 1a is effectively solved since the IFT of

the finite $\bar{T}_1$ can be computed numerically by the IFFT and the IFT of the singular $1/k_z$ is computed analytically using the Weyl-identity [4]

$$\frac{e^{ikr}}{i2\pi r} = \frac{1}{2\pi}\int_{-\infty}^{\infty}\int_{-\infty}^{\infty}\frac{1}{k_z}e^{i(k_x x+k_y y+k_z z)}dk_x dk_y \qquad z>0\ . \tag{5}$$

Thus Eq. 1a is rewritten as follows,

$$\begin{aligned}\bar{E}(x,y,z) &= \frac{1}{2\pi}\int_{-\infty}^{\infty}\int_{-\infty}^{\infty}\bar{T}(k_x,k_y)\,e^{ik_z z}e^{i(k_x x+k_y y)}dk_x dk_y \qquad z>z_o \\ &= \frac{1}{2\pi}\int_{-\infty}^{\infty}\int_{-\infty}^{\infty}\bar{T}_1(k_x,k_y)\frac{1}{k_z}e^{ik_z z}e^{i(k_x x+k_y y)}dk_x dk_y \\ &= \frac{1}{2\pi}\int_{-\infty}^{\infty}\int_{-\infty}^{\infty}\bar{T}_1(k_x,k_y)e^{ik_z (z-z_1)}e^{i(k_x x+k_y y)}dk_x dk_y \otimes \frac{1}{2\pi}\int_{-\infty}^{\infty}\int_{-\infty}^{\infty}\frac{1}{k_z}e^{ik_z z_1}e^{i(k_x x+k_y y)}dk_x dk_y \\ &= \bar{E}_1(x,y,z-z_1)\otimes\frac{e^{ikr_1}}{i2\pi r_1}\end{aligned} \tag{6}$$

As it seen in Eq. 6, the *z*-coordinate is split in two $z = (z\text{-}z_1)+z_1$ and hence $r_1 = \sqrt{x^2+y^2+z_1^2}$. This is done to have an exponential term of the type of $e^{ik_z z}$ in both factors, in order to use the Weyl identity of Eq. 5 and ensure an accurate implementation of the convolution, as explained in the following.

From a computational point of view the following important observations can be made.

First it is noted that, in practical implementations of Eqs. 1a and 6, the PWS is known only at *N* x *N* discrete points on a finite $\pm k_{xmax}$ and $\pm k_{ymax}$ domain and thus with sampling densities $\Delta k_x = 2k_{x\max}/(N-1)$ and $\Delta k_y = 2k_{y\max}/(N-1)$, respectively. In virtue of the Nyquist sampling criterion and the discrete Fourier transform theory, the transformed electric field is also given at *N*x*N* discrete points centered at the origin and with sampling densities $\Delta x = 2\pi/(\Delta k_x N)$ and $\Delta y = 2\pi/(\Delta k_y N)$, respectively [3].

Second we notice that the Green's function, that is usually computed at the same *N* x *N* discrete spatial points[1], is azimuthally symmetric and, once convolved with the function $\bar{E}_1$, it provides the electric field $\bar{E}$ at (2*N*-1) x (2*N*-1) discrete points.

Third, though the result of Eq. 6 is in principle independent of the chosen z_1, the result is accurate only when the truncation errors of the two spatial functions on the chosen *xy*-domain are negligible. For the AUT considered in Section 4 which has a size of 8λ, a *z*-coordinate less than 0.2λ ensures $\bar{E}_1$ values with negligible truncation error on the [-30λ : 30λ] *xy*-domain and a z_1-plane of about 0.01λ provides the Green's function with a sufficient decay on the same spatial region. The effect of the convolution will always be that of a more accurate field;

[1] The Green's function can however be computed on an even larger *xy*-domain, provided that the sampling in *x*- and *y*- is maintained, since we know its expression analytically.

however, for small z_1-values the Green's function is very peaked and it may happen that the effect is quantitatively limited.

Fourth, if we want to compute the electric field $\bar{E}$ only on a certain spatial window of the entire *xy*-domain, whether centered or not, we can easily modify the convolution algorithm by providing as input the function $\bar{E}_1$ on the desired *xy*-window, as long as a sufficient decay of $\bar{E}_1$ is ensured. The Green's function can also be considered on a window smaller than the entire *xy*-domain, provided that such a window is centered at the origin and a decay of at least 60dB from the peak is ensured. By doing that, the computational time for the convolution drastically diminishes.

Fifth, it is noted that the singularity extraction technique provides the correct aperture field also for non-singular spectral components and the technique can thus be applied to all components of the PWS without a priori considerations on the absence or presence of the singularity.

4. Test case

In order to illustrate the effect of the singularity extraction technique presented in Section 3, we investigate here an array of 5 *y*-oriented electric Hertzian dipoles displaced along the *x*-axis at a distance of 2λ from each others, see Fig. 2. The excitations of the 5 dipoles are *P*, *P*/2, *P*/5, *P*/8, and *P*/10, respectively, with *P* being the dipole moment of the dipole at the origin. The exact PWS is first computed from Eq. 2 on the [-2*k*, 2*k*] $k_x k_y$-domain with 91 sampling points in both directions, see Fig. 3. The PWS clearly shows the singularity in both the *x*- and *y*-components. In the computation of the aperture field from this PWS, only the visible region is taken into account since this is most often the case in practice, while the invisible region is zero-padded.

Fig. 4a shows the analytical *x*- and *y*-components of the electric field on the $z = 0.1\lambda$ plane while Fig. 4b shows the result of a straightforward IFFT of the singular PWS without the use of the singularity extraction technique. It is evident that while all 5 dipoles are seen in Fig 4a, only the first 2 are clearly distinguished in Fig 4b. The last 3 dipoles, having a weaker excitation, can not be correctly detected since the singularity is not properly taken into account. Fig 4c then shows the result of applying the singularity extraction technique. In this case all 5 dipoles are clearly detected and the difference in their excitations can also be seen. The slightly wider extensions of these compared to the analytical result is due to the truncation of the PWS to the visible region and the truncation of the two functions involved in the convolution on the finite *xy*-plane.

5. Conclusions

An effective technique to extract the singularity of plane wave spectra in the computation of antenna aperture fields was presented. The algorithm is based on the Inverse Fast Fourier Transform and Weyl-identity and allows the accurate computation of the aperture field when a dense sampling in the spectral domain is not possible. The detection of sources of very weak amplitude has been verified by a numerical example and the evident advantages compared to the Inverse Fast Fourier Transform of the plane wave spectrum without the singularity extraction have been underlined.

References

[1] Devaney A. J., "A filtered backpropagation algorithm for diffraction tomography," *Ultrason. Imag.*, Vol. 4, pp. 336–360, 1982.

[2] Hansen T. B., Johansen P. M., "Inversion scheme for ground penetrating radar that takes into account the planar air-soil interface", *IEEE Trans. on Geoscience and Remote Sensing*, Vol. 38, Issue.1, pp. 496-506, 2000.

[3] Wang J. J. H., "An examination of the theory and practices of planar near/field measurement", *IEEE Trans. Ant. Propag.*, Vol. 36, No. 6, pp. 746-753, June 1988.

[4] Hansen T. B., Yaghjian A. D., *Plane Wave Theory of Time-Domain Fields, Near-Field Scanning Applications*, IEEE PRESS, 1999.

[5] Yaghjian A. D., "Upper-bound errors in far-field antenna parameters determined from planar near-field measurements, Part I: Analysis", Nat. Bur. Stand. and Tech. Note 667, 1975.

[6] Yaghjian A. D., "Electric dyadic Green's functions in the source region", *Proc. of IEEE*, Vol. 68, No. 2, pp. 248-263, February 1980.

[7] Duffy M. G., "Quadrature over a pyramid or cube of integrands with a singularity at a vertex", *SIAM J. Numer. Anal.*, Vol. 19, No. 6, pp. 1260-1262, December 1982.

[8] Cappellin C., Frandsen A., Breinbjerg O., "Application of the SWE-to-PWE antenna diagnostics technique to an offset reflector antenna*", AMTA Antenna Measurements Technique Association,* St. Louis, USA, November 2007.

[9] Cappellin C., Frandsen A., Pivnenko S., Lemanczyk G., Breinbjerg O., "Diagnostics of the SMOS radiometer antenna system at the DTU-ESA spherical near-field antenna test facility", *EuCAP European Conference on Antennas and Propagation,* Edinburgh, UK, November 2007.

[10] Papoulis A., *Signal Analysis*, McGraw-Hill, 1977.

Figure legends

Figure 1. PWE for a general antenna: (a) Spatial domain of validity, $z > z_o$, (b) Visible and invisible regions of the spectral $k_x k_y$-domain.

Figure 2. Array of five *y*-oriented electric Herzian dipoles displaced on the *x*-axis.

Figure 3. Amplitude of the Cartesian components of the PWS $\overline{T}$ for the array of Hertzian dipoles in dB scale and normalized to the center value of T_y, on the $z = 0.1\lambda$ plane.

Figure 4. Amplitude of the *x*- and *y*-component of the electric field in dB scale at $z = 0.1\lambda$ normalized to the maximum of the *y*-component of the analytical field: (a) analytical field, (b) IFFT of the visible region of the PWS without the singularity extraction, (c) IFT of the visible region of the PWS with the singularity extraction.

Figures

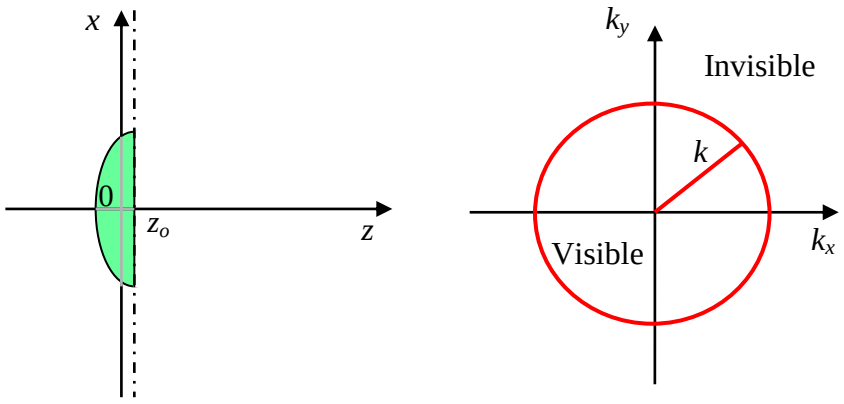

Figure 1

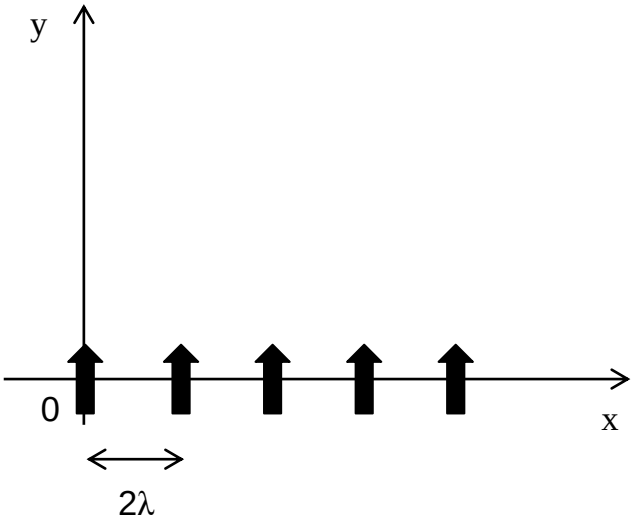

Figure 2

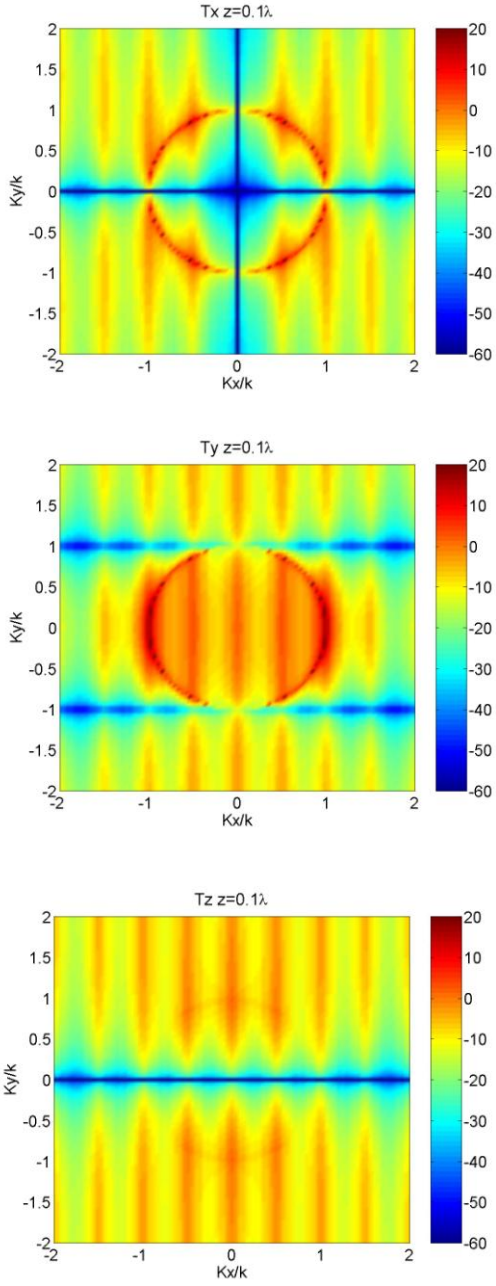
Tx z=0.1λ
Ty z=0.1λ
Tz z=0.1λ
Ky/k
Kx/k
2
1.5
1
0.5
0
-0.5
-1
-1.5
-2
20
10
0
-10
-20
-30
-40
-50
-60

Figure 3

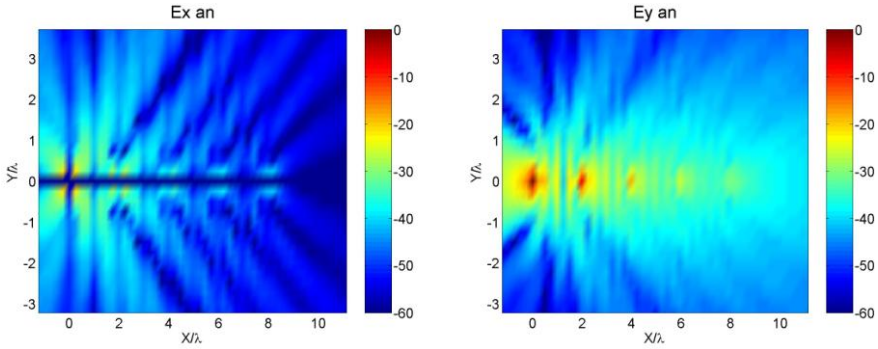

(a)

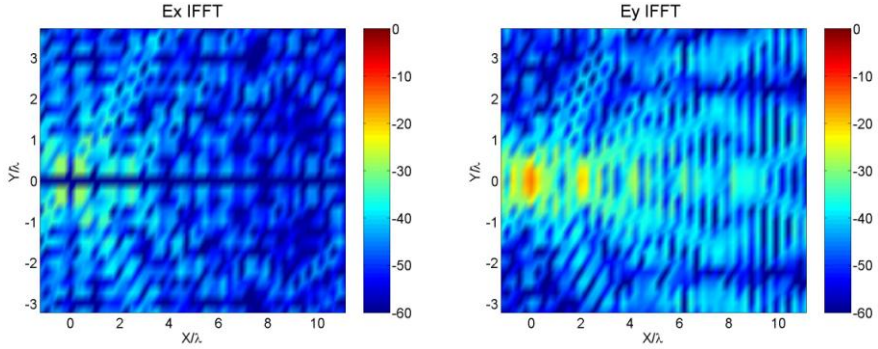

(b)

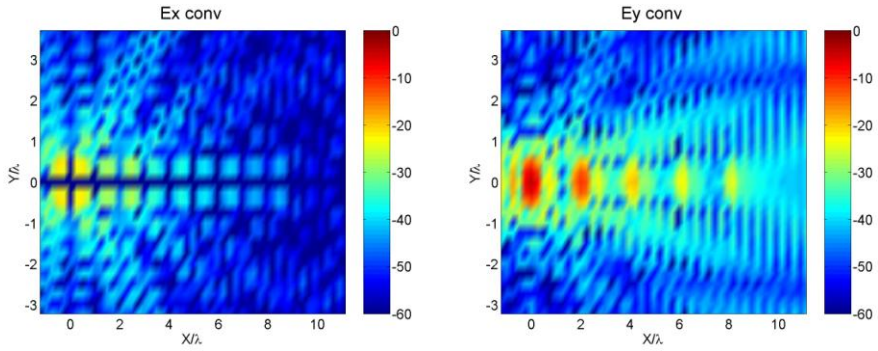

(c)

Figure 4

Paper III

ON THE RELATIONSHIP BETWEEN THE SPHERICAL WAVE EXPANSION AND THE PLANE WAVE EXPANSION FOR ANTENNA DIAGNOSTICS

Cecilia Cappellin [1,2], Aksel Frandsen [1], Olav Breinbjerg [2]

[1] TICRA, Læderstræde 34, DK-1201 Copenhagen K, Denmark
[2] Ørsted•DTU, Technical University of Denmark, DK-2800 Kgs. Lyngby, Denmark

ABSTRACT

The relation between the plane wave expansion (PWE) and the spherical wave expansion (SWE) is investigated. It is shown how the SWE can be transformed into the PWE, from which the aperture field can subsequently be calculated. Through the SWE-to-PWE transformation the visible as well as the invisible regions of the plane wave spectrum can be recovered, providing a high spatial resolution of the aperture field.
The SWE-to-PWE transformation allows an efficient antenna diagnostics for spherical near-field antenna measurements. Different test cases are examined and the limitations implied by the practical truncation of the SWE are investigated and clarified.

Keywords: Spherical wave expansion, plane wave expansion, antenna diagnostics.

1. Introduction

Electrical and mechanical errors in an antenna can be identified by use of an efficient antenna diagnostics technique. The presence of such errors is usually observed in the measured far-field pattern, however their causes can only be explained by analyzing the extreme near-field amplitude and phase. Since a direct measurement of this quantity is not usually implemented in measurement facilities, an alternative procedure has to be used. Several non-invasive diagnostics techniques have been proposed over the years [1] and [4]; however, all methods are limited either in terms of the type of antennas for which they can be used, or in terms of the accuracy that they can provide e.g. methods based on planar and cylindrical near-field or far-field measurements. There is thus a need for an antenna diagnostics technique that applies to general types of antennas and that is intrinsically accurate. We propose a new technique to be applied at the DTU-ESA Spherical Near-Field Antenna Test Facility located at the Technical University of Denmark [2]. The measurement technique employed at the DTU-ESA Facility is based on the SWE of the field radiated by the antenna [3]. This expansion is mathematically valid in any source-free region of space outside the minimum sphere of the antenna, the smallest sphere centered at the origin of the measurement coordinate system which completely encloses the antenna. Thus the aperture field in the extreme near-field of the antenna can not be computed [4]. One way to overcome this is to transform the SWE of the radiated field into a PWE. We will show how the plane wave spectrum can be computed by the coefficients of the SWE, on any aperture plane in the antenna source-free region. This will give two main advantages. The first is that the plane wave spectrum can be evaluated also in part of the spectrally invisible region, the second is that the aperture field can be computed as an inverse Fourier transform (IFT) of this spectrum. Hence, the spatial resolution achieved in the aperture field can in principle exceed the traditional value of half a wavelength, provided by the traditional techniques. In this manuscript analytical calculations as well as numerical simulations will be shown and investigations on the number of spherical modes necessary for the PWE convergence will be presented. All results are expressed in the S.I. rationalized system with $e^{-i\omega t}$ time convention.

2. Theory

2a) Theoretical derivation

We start by introducing the SWE of the electric field $\bar{E}$ radiated by an antenna circumscribed by a minimum sphere of radius r_o. In any source-free region $r > r_o$ the field can be expressed as [3],

$$\bar{E}(\bar{r}) = \frac{k}{\sqrt{\eta}} \sum_{n=1}^{\infty} \sum_{m=-n}^{n} Q_{1mn}^{(3)} \bar{F}_{1mn}^{(3)}(\bar{r}) + Q_{2mn}^{(3)} \bar{F}_{2mn}^{(3)}(\bar{r}) \qquad (1)$$

Where $Q_{1mn}^{(3)}$ and $Q_{2mn}^{(3)}$ are the expansion coefficients, that can be obtained from a spherical near-field measurement, and $\bar{F}_{1mn}^{(3)}(\bar{r})$ and $\bar{F}_{2mn}^{(3)}(\bar{r})$ are the power-normalized spherical vector wave functions. The medium intrinsic admittance is denoted by η, k is the wave number, and $\bar{r}$ is the position vector expressed as a function of the traditional spherical coordinates (r, θ, φ). In practice, the n-summation of the SWE is truncated at $n = N$, with N usually being equal to $N = kr_o+10$. The PWE of the same electric field in the spectral k_xk_y-domain valid for $z > z_o$, with z_o being the largest z-coordinate of the source region, is given by [5]

$$\bar{E}(x,y,z) = \frac{1}{2\pi}\int_{-\infty}^{\infty}\int_{-\infty}^{\infty}\bar{T}(k_x,k_y)\,e^{ik_z z}e^{i(k_x x+k_y y)}dk_x dk_y \quad (2)$$

where k_x, k_y, k_z are the Cartesian components of the wave propagation vector $\bar{k}$ with $k_z = \sqrt{k^2 - k_x^2 - k_y^2}$. The spectral domain, defined by the variables k_x and k_y, can be divided in two regions, the first one called "visible" for $k_x^2 + k_y^2 \le k^2$, responsible of the propagating plane waves, and the second one called "invisible" for $k_x^2 + k_y^2 > k^2$, see Fig. 1, constituted by the evanescent plane waves. The two variables k_x and k_y are always real, while k_z is real in the visible region but purely imaginary in the invisible region. In practice, the k_xk_y-integrals are truncated at finite values $\pm k_{xmax}$ and $\pm k_{ymax}$.

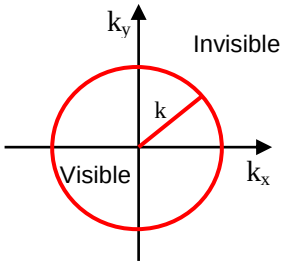

Figure 1. Visible and invisible regions in the spectral k_xk_y-domain.

The plane wave spectrum for a given z-coordinate is equal to $\bar{T}(k_x,k_y)e^{ik_z z}$. It was previously shown [6-7] how the SWE of Eq. 1 can be transformed into the PWE of Eq. 2, arriving at the following relation

$$\bar{T}(k_x,k_y)e^{ik_z z} = \frac{1}{k_z}\hat{E}(\hat{s})e^{ik\cos\alpha\, z} \quad (3)$$

where $\hat{E}(\hat{s})$ is given by

$$\hat{E}(\hat{s}) = \sum_{n=1}^{\infty}\sum_{m=-n}^{n}\frac{(-i)^n}{\sqrt{\eta}\sqrt{n(n+1)}}\Big[Q_{2mn}^{(3)}\,\hat{s}\times\bar{Y}_n^m(\alpha,\beta) + -iQ_{1mn}^{(3)}\bar{Y}_n^m(\alpha,\beta)\Big] \quad (4)$$

with $\hat{s} = \sin\alpha\cos\beta\,\hat{x} + \sin\alpha\sin\beta\,\hat{y} + \cos\alpha\,\hat{z}$, $\beta \in [-\pi, \pi]$ and $\alpha \in$ B, see Fig. 2. The vector spherical harmonics $\bar{Y}_n^m(\alpha,\beta)$ is defined by

$$\bar{Y}_n^m(\alpha,\beta) = -\frac{i}{\sqrt{2\pi}}\left(-\frac{m}{|m|}\right)^m\left(\frac{d}{d\alpha}\bar{P}_n^m(\cos\alpha)e^{im\beta}\hat{\beta} + -\frac{1}{\sin\alpha}\bar{P}_n^m(\cos\alpha)ime^{im\beta}\hat{\alpha}\right) \quad (5)$$

with $\bar{P}_n^m(\cos\alpha)$ being the normalized associated Legendre function as defined by [3], $\hat{\alpha} = \cos\alpha\cos\beta\,\hat{x} + \cos\alpha\sin\beta\,\hat{y} - \sin\alpha\,\hat{z}$ and $\hat{\beta} = -\sin\beta\,\hat{x} + \cos\beta\,\hat{y}$. The variables α and β on the right hand side of Eq. 3 must be expressed as functions of the spectral variables k_x and k_y according to $\hat{s} = \bar{k}/k$. The spatial resolution δ_x and δ_y obtained in the aperture field is given by $\delta_x = \pi/k_{x\max}$, $\delta_y = \pi/k_{y\max}$ and can thus be controlled by selecting k_{xmax} and k_{ymax} appropriately in the SWE-to-PWE transformation.

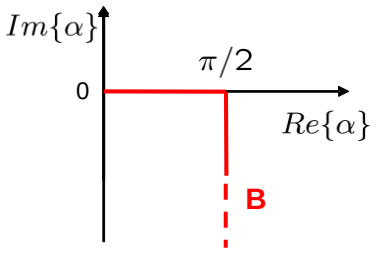

Figure 2. Domain of the angle α on contour B.

We can therefore summarize the required steps of this antenna diagnostics technique as follows:

1. Evaluate the Q coefficients through a spherical near-field measurement of the AUT.

2. Calculate the plane wave spectrum in the k_xk_y-domain on a given z-plane, $z>z_o$, according to Eqs. 3-4.

3. Compute the field on the desired *z*-plane as the IFT of the spectrum through Eq. 2.

2b) Theoretical considerations

We will now focus on three specific aspects of the SWE-to-PWE transformation. First, by looking at the expression of the $\bar{Y}_n^m(\alpha,\beta)$ function, in Eq. 5, we see after a few mathematical manipulations that

$$\hat{s}\times\bar{Y}_n^m(\alpha,\beta)\propto\bar{K}_{2mn}(\alpha,\beta)\quad \bar{Y}_n^m(\alpha,\beta)\propto\bar{K}_{1mn}(\alpha,\beta) \tag{6}$$

where $\bar{K}_{smn}(\theta,\varphi)=\lim_{kr\to\infty}\frac{kr}{e^{ikr}}\bar{F}_{smn}^{(3)}(r,\theta,\varphi)$, with s = 1,2 is the far-field pattern function of the spherical vector waves functions. We conclude that the spectrum in the $\alpha\beta$-domain, $\hat{E}(\hat{s})e^{ikz\cos\alpha}$, is thus given by the SWE of the far-field. All information about the visible and invisible spectral regions of the PWE is therefore in principle contained in the far-field. As an example of this important property, a *z*-oriented Hertzian dipole located at the origin of the coordinate system can be considered. Its SWE contains only the single mode s = 2, m = 0, n = 1. From the knowledge of the corresponding coefficient $Q_{201}^{(3)}$ the plane wave spectrum is completely reconstructed in the visible as well as in the invisible region. For more realistic antennas the SWE of the field is given by a larger number of modes, however, the concept of deriving the complete set of Q's from the far-field remains principally valid and its consequences will be discussed later. Second, since the variable α becomes purely imaginary in the invisible domain, see Fig. 2, the trigonometric functions in α included in $\bar{Y}_n^m(\alpha,\beta)$ are not limited in that region, and this gives rise to computational problems already for moderate values of *n*. An example is shown in Fig. 3, where the amplitude of the spectrum on $z=\lambda$ for s = 1, m = 0 and n = 20 and $Q_{1020}^{(3)}=1$ is presented in logarithmic scale and normalized to the value on-axis. On the other hand, the exponential term $e^{ik_z z}$, which is also included in the spectrum, provides a decay in the invisible region. A way to partly control the computational difficulties is thus to embed the term $e^{ik_z z}$ into the calculation of the vector spherical harmonics.

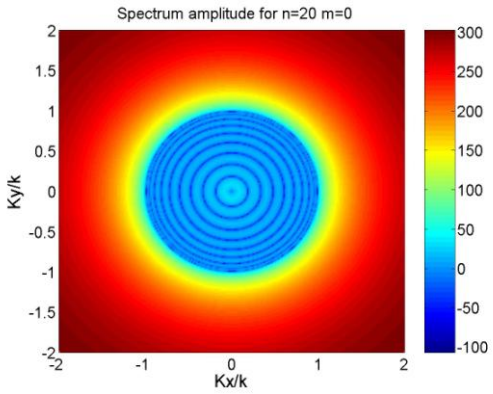

Figure 3. Amplitude of the spectrum for *n* = 20, *m* = 0 on *z* = *λ*, in dB.

Third, we concentrate on Eq. 3. It is noted that a singularity for $k_z = 0$ ($k_x^2 + k_y^2 = k^2$) will always be present at least in one component of any antenna spectrum, and that the necessary, but not sufficient, condition to avoid that is a null for $\theta = \pi/2$ of the antenna far-field pattern [5]. The singularity prevents a direct use of the fast IFT for the calculation of the aperture field, since an infinite number of points would be required to correctly sample the function in the vicinity of $k_z = 0$. But there is a way to overcome the problem and get an accurate value of the field even from components affected by the singularity. For this purpose, we write the spectrum $\bar{T}$ as a product of two functions, the finite $\bar{T}_1$ and the singular $1/k_z$, i.e. $\bar{T}(k_x,k_y)=\bar{T}_1(k_x,k_y)\frac{1}{k_z}$. We know that the IFT of $\bar{T}$ is equal to the convolution in the spatial *xyz*-domain of the IFT's of the two separated functions. We inverse transform, with a fast IFT, $\bar{T}_1$ and we write the inverse Fourier transform of $1/k_z$ by use of the Weyl identity [5] for $z > 0$

$$\frac{e^{ikr}}{i2\pi r}=\frac{1}{2\pi}\int_{-\infty}^{\infty}\int_{-\infty}^{\infty}\frac{1}{k_z}e^{i(k_x x+k_y y+k_z z)}dk_x dk_y \tag{7}$$

To properly convolve $\bar{E}_1(x,y,z)=\mathrm{F}^{-1}\left\{\bar{T}_1(k_x,k_y,z)\right\}$ with the Green's function [8], we need to split the quantity z in two, $z=z-z_1+z_1$, to have an exponential factor of the type of $e^{ik_z z}$ on both terms. We thus get

$$\mathrm{F}^{-1}\{\bar{T}(k_x,k_y,z)\} = \bar{E}(x,y,z) = \bar{E}_1(x,y,z-z_1) \otimes \frac{e^{ikr_1}}{i2\pi r_1} \quad (8)$$

with $r_1 = \sqrt{x^2 + y^2 + z_1^2}$. The results and the accuracy of this method will be shown in the following section, dedicated to the test cases.

3. Test Cases

3a) Array of Hertzian dipoles

A set of five *x*-oriented Hertzian dipoles on the *xy*- plane, four equally displaced from the origin with the distance r_o and one at the center, see Fig. 4, is the first test case.

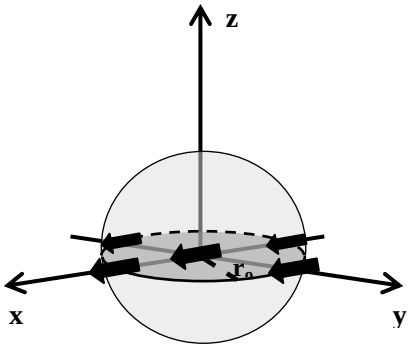

Figure 4. Five Hertzian dipoles displaced on the *xy*- plane, with minimum sphere of radius r_o.

With such a configuration the aperture plane can be moved into the minimum sphere of radius r_o, still remaining in a source-free region. For this antenna the *Q* coefficients can be calculated analytically, by use of the results reported in [3, pp. 339] for a sampled *x*-polarized planar current ring. Since the SWE contains arbitrarily high-order modes in *n* and *m*, the influence of the truncation in *n* in Eq. 4 can be analyzed. We consider as reference spectrum the one calculated through the dipole currents [5]

$$T_x = \frac{P}{2\pi k}\sqrt{\frac{\mu}{\varepsilon}}\left(\cos(k_x r_o)+\cos(k_y r_o)+\frac{1}{2}\right)\frac{k_x^2-k^2}{k_z}$$

$$T_y = \frac{P}{2\pi k}\sqrt{\frac{\mu}{\varepsilon}}\left(\cos(k_x r_o)+\cos(k_y r_o)+\frac{1}{2}\right)\frac{k_x k_y}{k_z} \quad (9)$$

$$T_z = \frac{P}{2\pi k}\sqrt{\frac{\mu}{\varepsilon}}\left(\cos(k_x r_o)+\cos(k_y r_o)+\frac{1}{2}\right)k_x$$

with *P* being the dipole moment. T_x and T_y contain the singularity in k_z. Different values of r_o have been studied, and here the results for $r_o = 2\lambda$ corresponding to kr_o=12, will be considered. The spectral components are then computed with Eq. 4 for different values of *N*. Plots for $N=kr_o$, $N=kr_o$+10 and $N=kr_o$+40 are shown in dB in Fig. 5, for the *x*-component on $z = 0.2\lambda$, normalized to the value of T_x in the origin.

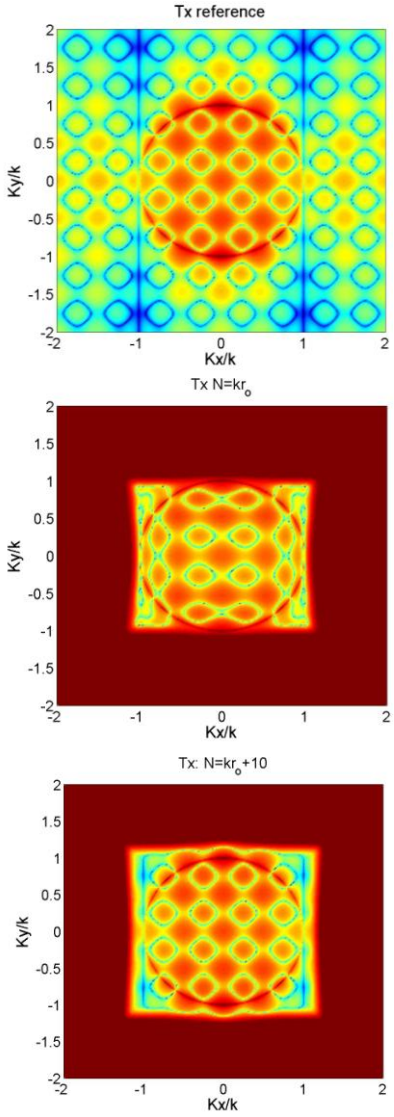

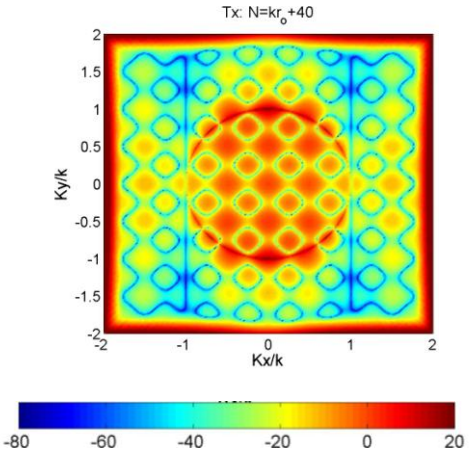

Figure 5. Amplitude of the *x*-component of the spectrum of the five dipoles with $r_o=2\lambda$, on $z=0.2\lambda$ in dB: the reference T_x, $N=kr_o$, $N=kr_o+10$ and $N=kr_o+40$.

We see how the convergence region in the k_xk_y-domain increases gradually with increasing N. For $N=kr_o$ the visible region is still not completely reconstructed but its convergence is reached with $N=kr_o+10$. For $N>kr_o+10$, only changes in the invisible region are noted until the complete picture is obtained by $N=kr_o+40=52$. The singularity for $k_z = 0$ is perfectly identified, already by $N=kr_o+10$.

To better understand the convergence mechanism, we also plot the n-mode power spectrum, $P_{rad}(n)=\frac{1}{2}\sum_{sm}\left|Q_{smn}^{(3)}\right|^2$ in function of n, see Fig. 6.

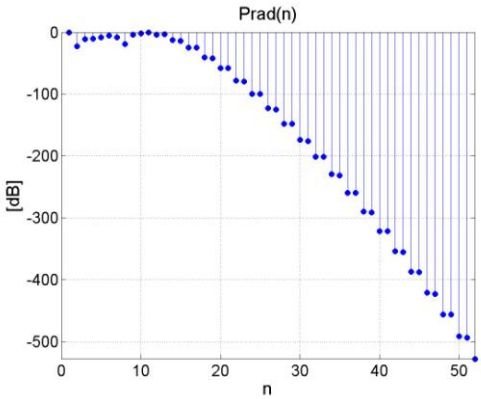

Figure 6. *n*-mode power spectrum for $r_o=2\lambda$.

Extreme low values of power are contained in the high n modes, however, due to the corresponding low values of Q's the product with the diverging vector spherical harmonics is kept finite. A plot of the x-component of the spectrum in function of N, for different points of the spectral domain, can finally clarify the convergence mechanism, see Fig. 7. Points belonging to the visible region reach convergence with $N=kr_o+10$, while points in the invisible region need more modes as they move away from the visible region. The maximum N required for a complete convergence in the $[-2k, 2k]$ domain depends on r_o. It was found that generally $N=kr_o+4kr_o$ is needed for the five dipoles case. From Fig. 7 we see that the series behaves as one with alternating sign. At every step n a new quantity is summed to the previous terms, adding or subtracting a certain amount of spectrumThis is necessary in order to "clean" the spectral invisible region, until the convergence values are reached. We can therefore inverse Fourier transform the spectrum and compare the quantity with the analytical field. The z-component can be directly fast inverse Fourier transformed, while the x- and y-components require the procedure of the convolution. To understand the influence of the invisible region, we consider the spectrum computed with $N=kr_o+40=52$, $N=kr_o+10=22$ and $N=kr_o=12$.

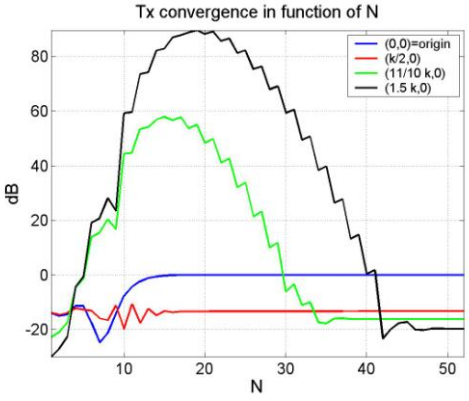

Figure 7. Amplitude of the *x*-component of the spectrum in function of N, $kr_o=12$, for different points of the spectral domain.

Only the convergent part of the spectrum is used in these cases, while the non-convergent part is replaced by zeros. Results are shown in Fig. 8 for the x-component on $z=0.2\lambda$, normalized to the value on axis of the analytical field and plotted in linear scale: we can distinguish the five dipoles on the xy-plane in all pictures. However the result provided by $N=kr_o$ is not quantitatively satisfactory in determining the dipoles contribution. On the other hand, already with

$N=kr_o+10$ terms a very accurate aperture field is computed. This means that the most important part of the spectrum to be recovered is constituted by the visible region, the singularity for $k_z = 0$, and a little part of the invisible region.

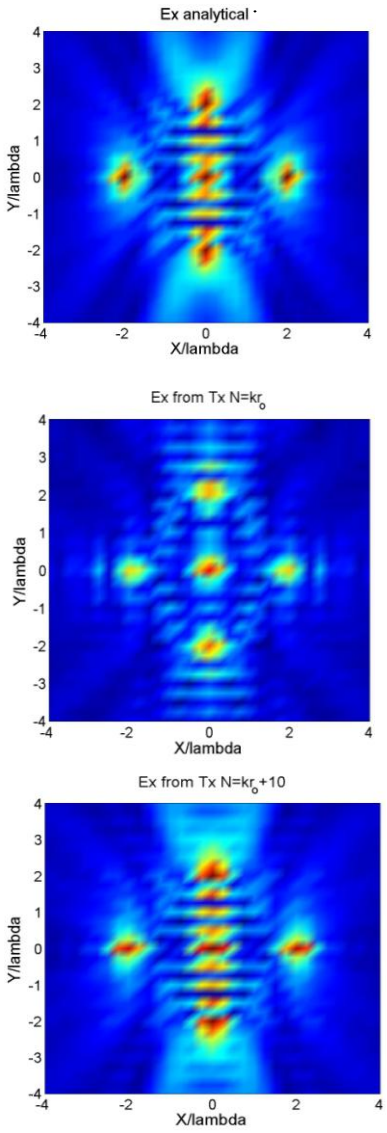

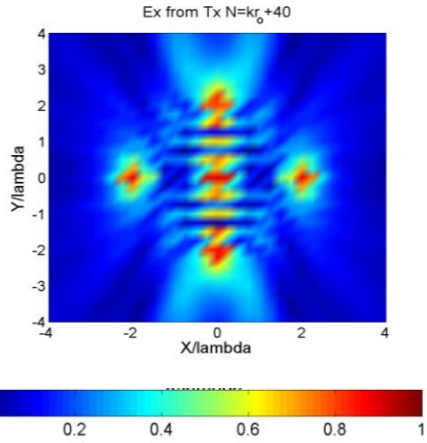

Figure 8. Amplitude of the *x*-component of the field on $z=0.2\lambda$, for $r_o=2\lambda$ in linear scale: the analytical, the one obtained by $N=kr_o$, $N=kr_o+10$ and $N=kr_o+40$.

3b) Rectangular aperture in free-space

The second antenna test case is a rectangular aperture excited by a TE01 mode, located on the *xy*-plane and radiating in free space, see Fig. 9.

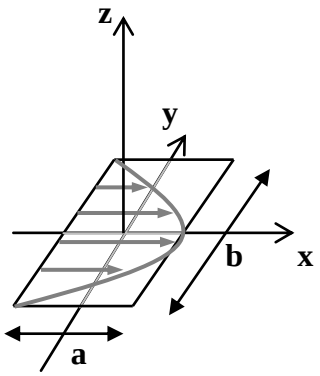

Figure 9. Rectangular aperture, of dimensions *a* and *b*, located on the *xy*-plane, excited by the TE01 mode.

From the analytical far-field pattern $\bar{F}(\theta,\varphi)$, based on electrical and magnetic equivalent currents [9], the reference spectrum $\bar{T}$ is calculated as $\bar{T}(k\sin\theta\cos\varphi, k\sin\theta\sin\varphi) = \dfrac{i\bar{F}(\theta,\varphi)}{k\cos\theta}$ [5], with $\theta \in [0, \pi/2]$ and $\varphi \in [0, 2\pi)$. This immediately provides the expression for $\bar{T}$ in the visible region $k_x^2 + k_y^2 \le k^2$. However, it is possible to

analytically continue the far-field pattern $\overline{F}(\theta,\varphi)$ to complex values of θ [5], so that, by the use of the same expression, the spectrum $\overline{T}$ in the invisible region is also calculated. The angle θ is substituted by α defined on the domain B, and φ by β. The Q coefficients are calculated from the projection of the far-field on the functions $\hat{s}\times\overline{Y}_n^m(\alpha,\beta)$ and $\overline{Y}_n^m(\alpha,\beta)$, and, due to numerical noise, only N=19 terms are available.

Different values of a and b have been analyzed, and here we present the results for $a=\lambda$ and $b=2\lambda$, corresponding to kr_o=6. The expressions of the reference spectral components are:

$$T_x = \frac{abk}{4k_z}\frac{\cos Y}{Y^2-(\pi/2)^2}\frac{\sin X}{X}\left(\frac{k_z k_x^2}{k(k_x^2+k_y^2)}\left(1+\frac{\beta_{01}k_z}{k^2}\right)+\frac{k_z k_y^2}{k(k_x^2+k_y^2)}\left(1+\frac{\beta_{01}}{k_z}\right)\right) \quad (10)$$

with $\beta_{01}/k=\sqrt{1-(\lambda/(2b)^2)}$, $X=k_x a/2$, and $Y=k_y b/2$. $T_y=0$ and $T_z=-k_x T_x/k_z$, from $\overline{k}\cdot\overline{T}=0$. The singularity in k_z=0 is present both in T_x and T_z. Again, we calculate the spectrum through Eq. 4 with different values of N, and we focus on the x-component, see Fig. 10 where the quantities are normalized to the value of T_x in the origin and plotted on z=0.2λ. The convergence mechanism is similar to the one shown by the five dipoles case. As before, the singularity on k_z = 0 is perfectly identified. Slightly more than kr_o terms are needed to reach convergence in the visible region, while modes with $n>kr_o$ have only influence on the invisible region.

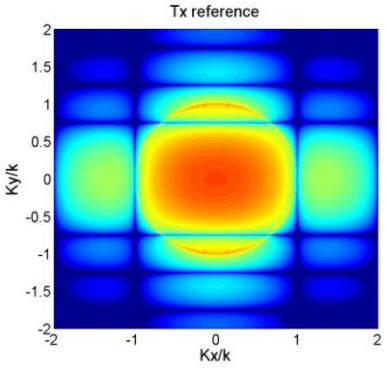

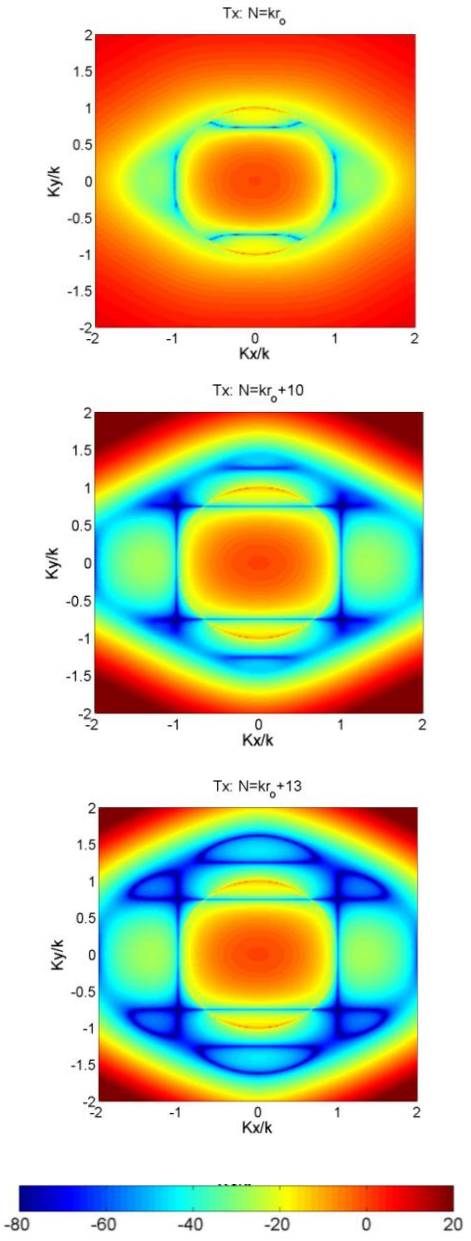

Figure 10. Amplitude of the *x*-component of the spectrum for the rectangular aperture with $a=\lambda$ and $b=2\lambda$, on $z=0.2\lambda$ in dB: the reference T_x, $N=kr_o$, $N=kr_o+10$ and $N=kr_o+13$.

The n-mode power spectrum is reported in Fig. 11, and compared to the one of a set of five dipoles with $r_o=\lambda$ having the same value of kr_o.

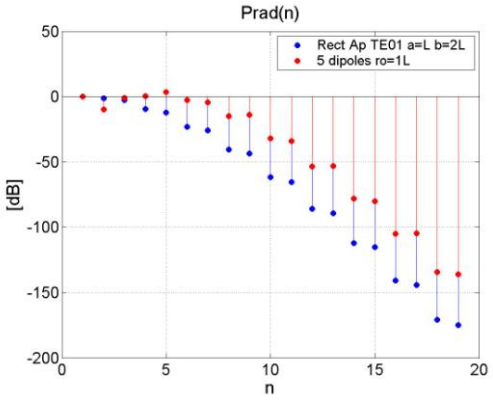

Figure 11. *n*-mode power spectrum for a rectangular aperture with $a=\lambda$ and $b=2\lambda$, compared with the one given by five dipoles with the same r_o.

The power contained in the high n modes is lower than in the five dipoles case: the corresponding Q's can therefore better control the product with the diverging vector spherical harmonics. This could be the reason why a large part of the invisible region is reconstructed already for $N=kr_o+10$. The x-component of the field is finally calculated on $z=0.2\lambda$ as IFT of the x-component of the spectrum with the use of the convolution, see Fig. 12.

No analytical expression of the field is known on that z-plane, so the comparison is done between the IFT of the reference spectrum and the IFT of the spectrum represented by $N=kr_o+10$ terms, with the non-converging region replaced by zeros. Results are in linear scale and normalized in respect of the value on axis of the field obtained by the reference spectrum. The aperture dimensions on the xy-plane are identified, and again, extremely good agreement is found between the two pictures.

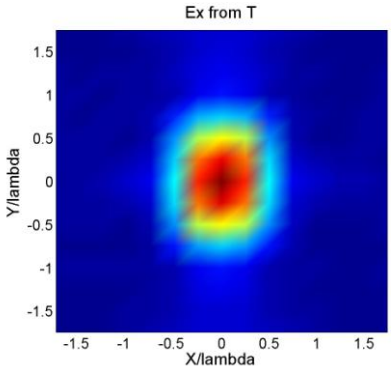

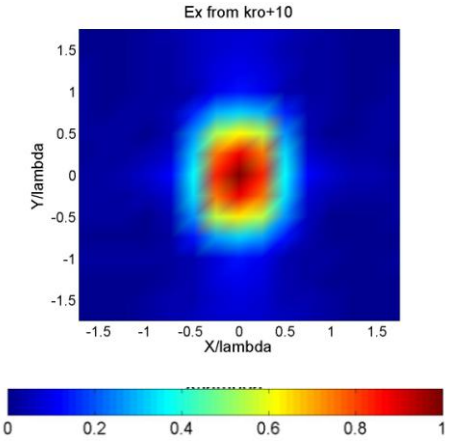

Figure 12. Amplitude of the x-component of the field on $z=0.2\lambda$, for a rectangular aperture with $a=\lambda$ and $b=2\lambda$, in linear scale: above from the reference spectrum, below from $N=kr_o+10$.

4. Conclusions

A new antenna diagnostics technique for spherical near-field antenna measurements has been presented. The theoretical derivations as well as the two test cases have shown an important property: the plane wave spectrum, in the visible as well as in part of the invisible region, can be derived by the knowledge of the Q coefficients of the SWE of the field. This provides a spatial resolution in the aperture field higher than the usual half wavelength provided by the traditional techniques. It is important to point out that, while the reconstruction of the invisible region of the PWE is in principle possible from the SWE, the practical truncation of the SWE in real measurements will of course enforce a limitation on this. However, it has been shown that very accurate aperture fields can be obtained with a realistic truncation number, provided that the spectrum at $k_z=0$ is recovered. Future work will focus on the influence of finite dynamic range on the truncation number, for different types of antennas. Real measured data will then be included in the analysis.

REFERENCES

[1] Kaplan L., Hanfling J. D., Borgiotti G. V., *The Backward Transform of the Near-Field for Reconstruction of Aperture Field*, IEEE Trans. on Ant. and Prop. Soc. Symp. Dig., 764-767, 1979.

[2] Homepage of the DTU-ESA Facility: http://www.oersted.dtu.dk/English/research/emi/afg/dtu_esa_facility.aspx

[3] Hansen J. E., *Spherical Near-Field Antenna Measurements*, Peter Peregrinus Ltd. London, 1988.

[4] Joy E. B., Guler M. G., *High Resolution Spherical Microwave Holography*, IEEE Trans. on Ant. and Prop., vol. 43, 464-472, 1995.

[5] Hansen T. B., Yaghjian A. D., *Plane Wave Theory of Time-Domain Fields, Near-Field Scanning Applications*, IEEE PRESS, 1999.

[6] Devaney A. J., Wolf E., *Multipole Expansion and Plane Wave Representations of the Electromagnetic Field*, Journal of Math. and Physics, Vol. 15, 234-244, February 1974.

[7] Cappellin C., Breinbjerg O., Frandsen A., *A High Resolution Antenna Diagnostics Technique for Spherical Near-Field Measurements*, 28th ESA Antenna Workshop, ESTEC, Noordwijk, The Netherlands, 899-906, 2005.

[8] Oppenheim A. V., Schafer R. W., *Digital Signal Processing*, Prentice-Hall, 1975.

[9] Silver S., *Microwave Antenna Theory and Design*, Peter Peregrinus Ltd. London, 1984.

Paper IV

THE INFLUENCE OF FINITE MEASUREMENT ACCURACY ON THE SWE-TO-PWE ANTENNA DIAGNOSTICS TECHNIQUE

C. Cappellin[1-2], O. Breinbjerg[1], A. Frandsen[2]

[1] Ørsted•DTU, *Technical University of Denmark, DK-2800 Kgs. Lyngby, Denmark*
[2]*TICRA, Læderstræde 34, DK-1201, Copenhagen, Denmark*

ABSTRACT

A new antenna diagnostics technique based on the transformation of the spherical wave expansion (SWE) into the plane wave expansion (PWE) is proposed. The new technique allows the recovery of the plane wave spectrum in the visible region, and in principle also in part of the invisible region, from data acquired during a spherical near-field measurement. From the PWE the aperture field can subsequently be calculated. While the fundamental properties of the SWE-to-PWE transformation have been reported in previous articles, we concentrate here on the influence of non-ideal measurements aspects on this diagnostics technique. In order to isolate different measurement inaccuracies, the investigation is based on simulations

1. INTRODUCTION

While the effect of electrical or mechanical errors in an antenna is observed in its measured far-field pattern, the errors themselves are more easily identified in the extreme near-field of the antenna. Several non-invasive diagnostics techniques have been proposed over the years [1]-[3], but generally these techniques possess limitations with respect to the type of antennas and antenna errors to which they apply, and/or to the accuracy they provide.

We have proposed a new diagnostics technique [4]-[5] to be applied at the DTU-ESA Spherical Near-Field Antenna Test Facility located at the Technical University of Denmark [6]. The measurement technique employed at the DTU-ESA Facility is based on the SWE of the field radiated by the antenna. The SWE is valid outside the antenna minimum sphere and does not readily allow the calculation of the aperture field in the extreme near-field of the antenna. One way to overcome this is to transform the SWE of the radiated field into a PWE. The plane wave spectrum can be computed from the knowledge of the coefficients of the SWE, on any aperture plane in the extreme near-field outside the antenna. This technique gives two main advantages. The first is that the plane wave spectrum can in principle be evaluated also in part of the spectrally invisible region, and the second is that the aperture field can be computed as Inverse Fourier Transform (IFT) of this spectrum. Hence, the spatial resolution achieved in the aperture field can theoretically exceed the traditional limit of half a wavelength. While the fundamental properties of the SWE-to-PWE transformation have been described in previous articles [4]-[5], we will concentrate here on how non-ideal measurements aspects affect the diagnostics technique. To do that, we will consider an antenna model consisting of electric and magnetic Hertzian dipoles. Electrical measurements inaccuracies will be added to the calculated near-field. The effects of such quantities on the obtained Q coefficients, and on the extreme near-field provided by the diagnostics will be then studied. Finally, errors will be introduced in the antenna model and the ability of the diagnostics technique to identify these will be tested. All results are expressed in the S.I. rationalized system with the $e^{-i\omega t}$ time convention.

2. THEORY OF THE SWE-TO-PWE TRANSFORMATION

We begin by introducing the SWE of the electric field $\bar{E}$ radiated by an antenna circumscribed by a minimum sphere of radius r_o [7], with $r > r_o$,

$$\bar{E}(\bar{r}) = \frac{k}{\sqrt{\eta}} \sum_{n=1}^{\infty} \sum_{m=-n}^{n} Q_{1mn}^{(3)} \bar{F}_{1mn}^{(3)}(\bar{r}) + Q_{2mn}^{(3)} \bar{F}_{2mn}^{(3)}(\bar{r}), \quad (1)$$

Where $Q_{1mn}^{(3)}$ and $Q_{2mn}^{(3)}$ are the expansion coefficients, obtained from a spherical near-field measurement, and $\bar{F}_{1mn}^{(3)}(\bar{r})$ and $\bar{F}_{2mn}^{(3)}(\bar{r})$ are the power-normalized spherical vector wave functions. The medium intrinsic admittance is η, k is the wave number, and $\bar{r}$ is the position vector expressed in terms of spherical coordinates (r, θ, φ) or rectangular coordinates (x, y, z). In practice,

the *n*-summation of the SWE is truncated at $N=kr_o+10$ since this is sufficient for an accurate calculation of the far-field. The PWE of the same electric field $\bar{E}$ in the spectral k_xk_y-domain valid for $z > z_o$, with z_o being the largest *z*-coordinate of the antenna, is given by [8]

$$\bar{E}(x,y,z)=\frac{1}{2\pi}\int_{-\infty}^{\infty}\int_{-\infty}^{\infty}\bar{T}(k_x,k_y)\,e^{ik_z z}e^{i(k_x x+k_y y)}dk_x dk_y \quad (2)$$

where k_x and k_y, are the spectral variables and $k_z=\sqrt{k^2-k_x^2-k_y^2}$. The spectral domain can be divided in two regions, the visible, for $k_x^2+k_y^2\le k^2$, containing the propagating plane waves, and the invisible, for $k_x^2+k_y^2>k^2$, containing the evanescent plane waves, see Fig. 1. The two variables k_x and k_y are always real, while k_z is real in the visible region but purely imaginary with a positive imaginary part in the invisible region. In practice, the k_x- and k_y-integrals are truncated at finite values $\pm k_{xmax}$ and $\pm k_{ymax}$ respectively. At the border between the visible and invisible regions k_z = 0 and the PWE generally possesses a singularity there [8].

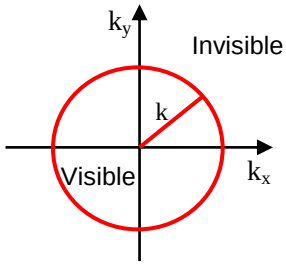

Figure 1. Visible and invisible regions of the spectral k_xk_y-domain.

The plane wave spectrum for a given *z*-coordinate is thus $\bar{T}(k_x,k_y)e^{ik_z z}$. It was previously shown [4]-[5] and [9] how the SWE of Eq. 1 can be transformed into the PWE of Eq. 2, arriving at the following relation

$$\bar{T}(k_x,k_y)e^{ik_z z}=\frac{1}{k_z}\hat{E}(\hat{s})\exp(ik\cos\alpha\, z) \quad (3)$$

where $\hat{E}(\hat{s})$ is given by

$$\hat{E}(\hat{s})=\sum_{n=1}^{\infty}\sum_{m=-n}^{n}\frac{(-i)^n}{\sqrt{\eta}\sqrt{n(n+1)}}\left[Q_{2mn}^{(3)}\,\hat{s}\times\bar{Y}_n^m(\alpha,\beta)+-iQ_{1mn}^{(3)}\bar{Y}_n^m(\alpha,\beta)\right] \quad (4)$$

with $\hat{s}=\sin\alpha\cos\beta\,\hat{x}+\sin\alpha\sin\beta\,\hat{y}+\cos\alpha\,\hat{z}$, $\beta\in[-\pi,\ \pi]$ and equal to $\beta=\operatorname{atan}(k_y/k_x)$, $\alpha\in$ B see Fig. 2 and equal to $\alpha=\operatorname{acos}(k_z/k)$, and $\bar{Y}_n^m(\alpha,\beta)$ being the vector spherical harmonics, see also [4]-[5]. The imaginary values of the angle α correspond to the invisible k_xk_y-domain, and make the spherical harmonics $\bar{Y}_n^m(\alpha,\beta)$ divergent in that region. Eq. 4 shows that the plane wave spectrum can be expressed as a series of spherical harmonics weighted by the *Q* coefficients of the SWE of the radiated field.

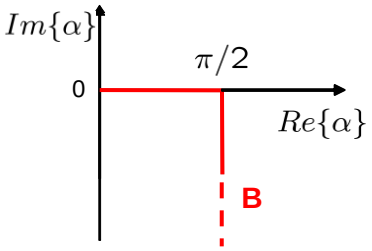

Figure 2. Domain of the variable α on contour B.

But, while the visible region of the spectrum reaches convergence around $N=kr_o$, the invisible requires many more modes [5]. In practice the high order modes can not be measured due to the finite dynamic range. However, it has been shown [5] that the recovery with $N \approx kr_o$ terms of the visible region and the singularity for k_z = 0 provides accurate aperture fields. The spatial resolution (δ_x,δ_y) obtained in the aperture field is given by $\delta_x=\pi/k_{xmax}$, $\delta_y=\pi/k_{ymax}$ and can in principle be controlled by selecting k_{xmax} and k_{ymax} appropriately in the SWE-to-PWE transformation. While in previous works [4]-[5] the investigations were based on ideal noise-free test cases, we will concentrate in the following on more realistic cases.

3. SIMULATION MODEL FOR FINITE MEASUREMENT ACCURACY

It is the purpose of this section to consider some of the most typical measurement electrical inaccuracies in order to clarify their influence on the proposed diagnostics technique. To do that, a Standard Gain Horn (SGH) model consisting of electric and magnetic Hertzian dipoles will be considered. Different measurement electrical errors will be added to its radiated near-field, and from that field distribution the *Q* coefficients will

be computed. The aperture field will be then calculated by using Eqs. 2-3-4.

3.1 Antenna Model

The SGH model works at the frequency of 3GHz. It represents a pyramidal horn with an aperture of $a=4\lambda$ and $b=3\lambda$ located on the *xy*-plane, see Fig. 3, and with the lengths of the flared section in the *xz*- and *yz*-planes being $R_2=R_1=5\lambda$. v The dominant TE10 mode constitutes the co-polar component, it is *y*-polarized and excited with amplitude 1, while the TE01 mode provides a typical cross-polar component, it is *x*-polarized and has an amplitude of 10^{-2} and a phase of $-i\pi/4$, see Fig. 3.
From the equivalence theorem, the equivalent magnetic co-polar currents are

$$\bar{M}_{co} = \cos\left(\frac{\pi x}{a}\right)\exp(i\frac{k}{2}(x^2/R_2 + y^2/R_1))\hat{x} \qquad (5)$$

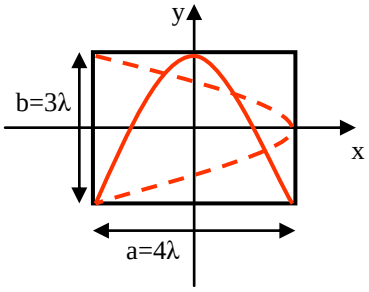

Figure 3. Aperture of the SGH model with the TE10 and TE01 modes, and the reference coordinate system.

while the electrical are computed from the magnetic imposing a Huygens source dependence

$$\bar{J}_{co} = -\eta\cos\left(\frac{\pi x}{a}\right)\exp(i\frac{k}{2}(x^2/R_2 + y^2/R_1))\hat{y} \qquad (6)$$

with $x \in [-a/2, a/2]$ and $y \in [-b/2, b/2]$. The cross-polar equivalent currents are computed in the same way and are equal to, with $C = 10^{-2}\exp(-i\pi/4)$,

$$\bar{J}_{cro} = -\eta C\cos\left(\frac{\pi y}{b}\right)\exp(i\frac{k}{2}(x^2/R_2 + y^2/R_1))\hat{x} \qquad (7)$$

$$\bar{M}_{cro} = -C\cos\left(\frac{\pi y}{b}\right)\exp(i\frac{k}{2}(x^2/R_2 + y^2/R_1))\hat{y} \qquad (8)$$

The current distributions of Eqs. 5-8, are sampled every $\lambda/4$ on the *xy*-plane to provide on the sampling points the excitation of a set of electric and magnetic Hertzian dipoles distributed on the aperture. From this dipole distribution the radiated field is computed and the directivity is plotted, see Fig. 4. It can be seen that the model represents a typical SGH pattern both in the co-polar as well as in the cross-polar components, computed according to Ludwig's 3rd definition [7].

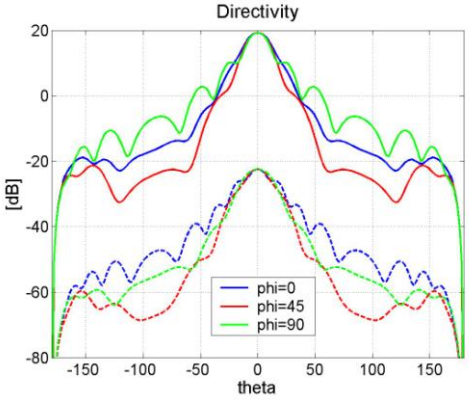

Figure 4. Directivity of the SGH model, co-polar (continuous lines), cross-polar (dashed lines).

3.2 Measurement Electrical Inaccuracies Model

Drift and noise, in amplitude and in phase, have been chosen to represent the most frequent and important measurement electrical inaccuracies. Their values are reported in Tab. 1, for a frequency of 3GHz and a scan speed of 3 deg/sec. Drift during a spherical scan has been modelled as a linear function of the time *t*, $drift_{error} = d \cdot t / T$, with *d* being the value of the drift, see Tab. 1 in amplitude or in phase, and *T* the duration of a scan.

Amplitude drift	-0.015 dB
Amplitude noise	-60 dB
Phase drift	0.25°
Phase noise	0.15°

Table 1. Values of measurement electrical inaccuracies.

If $X = |X|e^{i\angle X}$ is the θ- or φ-component of the electric field $\bar{E}$ on a sphere of radius of 10λ from the origin, then the field is equal to $X_{tot} = (|X| \cdot (1 + drift_{error}))e^{i\angle X}$ when affected by amplitude drift and to $X_{tot} = (|X|)e^{i\angle X(1+drift_{error})}$ when affected by phase drift. Noise has been considered random

and uniformly distributed providing $X_{tot} = (|X| + noise_{error})e^{i\angle X}$ for the amplitude noise and $X_{tot} = |X|e^{i(\angle X + noise_{error})}$ for the phase noise. The Q coefficients have then been computed from the near-field distribution with electrical inaccuracies by the software SNIFTD [10], and the power spectrum $P_{rad}(n) = \frac{1}{2}\sum_{sm}\left|Q^{(3)}_{smn}\right|^2$ has been found, see Fig. 5.

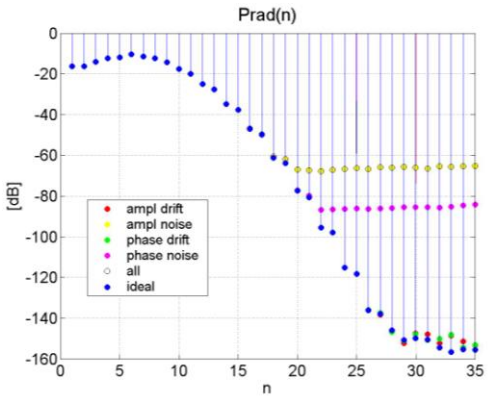

Figure 5. SGH power spectrum for different electrical inaccuracies and for the ideal case.

Fig. 5 shows that the major and most evident effect of the considered electrical inaccuracies is to truncate the available n-modes. It can be noted that numerical noise will anyway affect the computation, limiting the n-modes to $N=28=kr_o+13$ for the ideal case. Since all types of measurement errors manifest themselves as a constant level of the spectrum after a certain mode number, it was decided to continue the investigation with the amplitude noise alone, and then investigate different values of this.

3.3 Spectra and Near-Fields Results

The plane wave spectrum is then computed by using Eqs. 3-4 with the Q coefficients obtained from the field distribution affected by an amplitude noise of -60 dB. The truncation in n is set equal to 18 and an aperture plane equal to $z = 0.2\lambda$ is selected. A plot of the y- and z-components is reported in Fig. 6 in dB scale with the values normalized to $T_y(0,0)$, and compared to the ones calculated through the ideal case with a truncation in n equal to 28. In both cases the visible region is recovered, and the singularity at $k_z = 0$ is identified. The extra ten n-modes, provided by an improvement of 80 dB in the dynamic range of the ideal case, allow the reconstruction of a small part of the invisible region, which is reduced for the noisy case. The spectrum in the invisible region is then replaced by zeros in the non-converging region and inverse Fourier transformed, see Fig. 7. For the data affected by amplitude noise the convergent region has a radius of $1.03k$, while for the ideal case it is $1.1k$. Fields are in dB scale and normalized to the value of $E_y(0,0)$ when affected by amplitude noise.

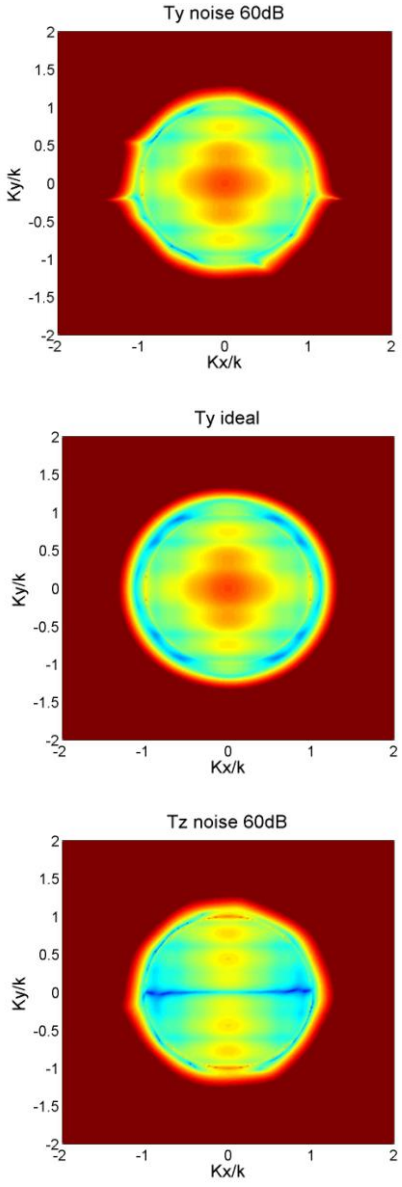

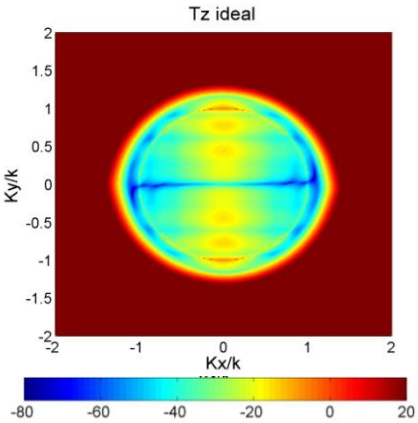

Figure 6. Amplitude of T_y and T_z on $z=0.2\lambda$, for a noise amplitude of -60dB and for the ideal case.

They are compared to the components given by the ideal case, and to the ones provided by the superposition of the analytical dipole contribution. The results affected by amplitude noise are satisfactory and in good agreement with the ideal and the analytical ones, both for the *y*- as well as for the *z*-component. Very accurate results are provided by the ideal case, where the convergent region has a radius of $1.1k$. We can again conclude that the recovery of the singularity for $k_z = 0$ and of small part of the invisible region are important to reconstruct the aperture field.

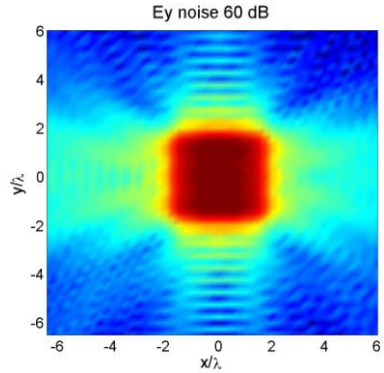

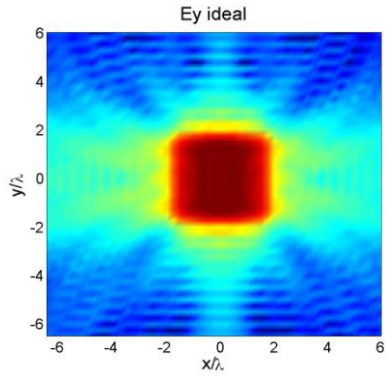

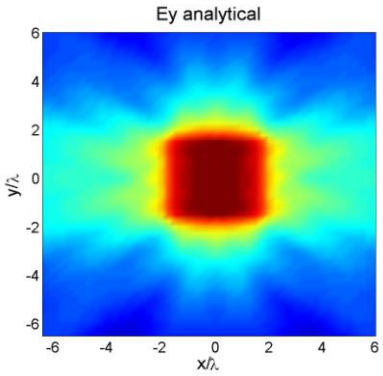

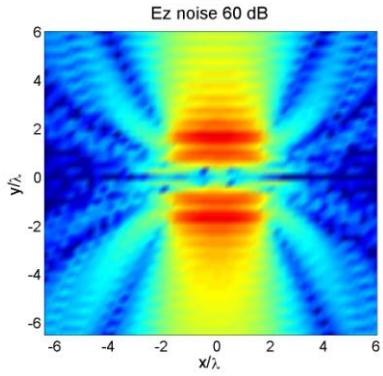

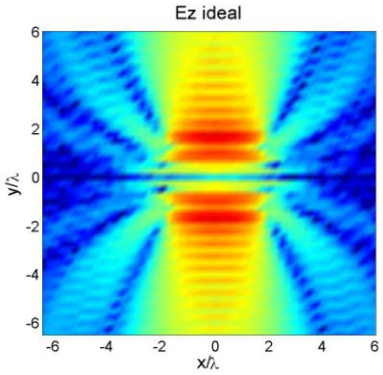

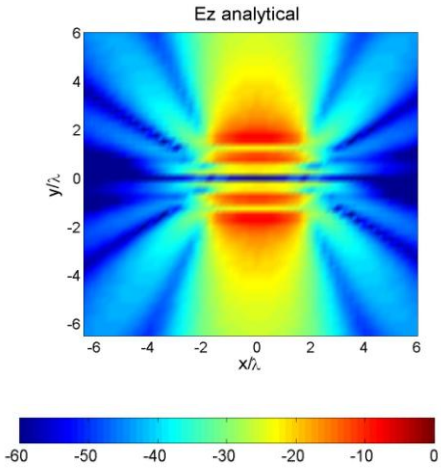

Figure 7. Amplitude of E_y and E_z on $z=0.2\lambda$, for a noise amplitude of -60dB, for the ideal case and for the analytical case.

4. DIAGNOSTICS EXPERIMENT

The TE20 mode is now introduced in the SGH aperture, to simulate an overmoding error, with an amplitude equal to 0.1 or 0.2. The presence of this error gives rise to an asymmetry both in the main lobe and the side–lobes of the directivity pattern, see Fig. 8. For every TE20 amplitude case an amplitude noise varying between -70 dB and -50 dB is later added to the SGH near-field distribution on the spherical surface with radius 10λ from the origin. The Q coefficients are computed by SNIFTD [10] and the power spectrum is calculated, see Fig. 9.

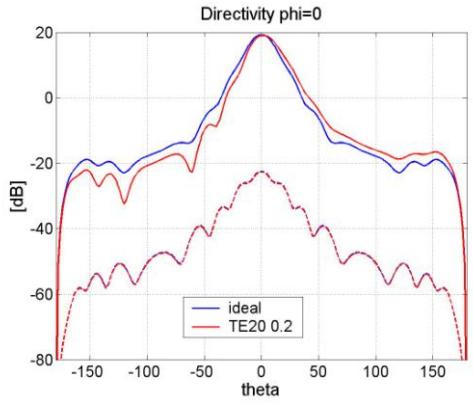

Figure 8. Directivity on $\varphi=0$ for the SGH with TE20 amplitude equal to 0.2: co-polar (continuous line), cross-polar (dashed line), in blue the ideal case with no overmoding.

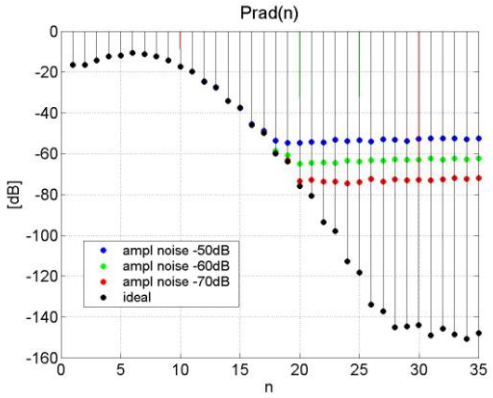

Figure 9. Power spectrum for different values of noise amplitude: SGH with TE20 amplitude equal to 0.2.

It can be seen that for a noise amplitude of -50 dB we have N=17 modes, and that a new mode is obtained every time the noise is decreased by -10 dB. The effect is the same whether the amplitude of the TE20 mode is 0.1 or 0.2. The spectral components are then computed on the plane $z = 0.2\lambda$, with the N truncation values of Tab. 2.

-50dB amplitude noise	N=17
-60 dB amplitude noise	N=18
-70 dB amplitude noise	N=19

Table 2. Truncation value N for different values of noise amplitude.

For both amplitudes of the TE20 mode and for all noise amplitudes, the visible region of the plane wave spectrum reaches convergence and the singularity is identified. For all cases, the effect in Eq. 4 of an extra mode in n reflects into an enlargement of the convergent region of the invisible spectrum. For -50dB noise the reconstructed region has a radius of $1.02k$ which becomes $1.04k$ for -60dB and -70dB noise and $1.14k$ for the ideal case. The invisible region where convergence has not been reached is replaced by zeros and the spectral components are inverse Fourier transformed. Plots for the x- and y-components of the aperture field are shown in Fig. 10 for the TE20 amplitude equal to 0.2, in dB scale and normalized to $E_y(0,0)$ when -50 dB noise is present. The aperture distribution is compared to the one provided by the ideal case with no noise and N=27, and to the analytical dipole distribution. Different colour scales are used for the x- and y-components to better visualize the amplitude variations. The asymmetry in the aperture distribution is clearly

detected in both components, providing accurate results in comparison with the analytical ones. The importance of the detection of the singularity for $k_z = 0$ is again noticed.

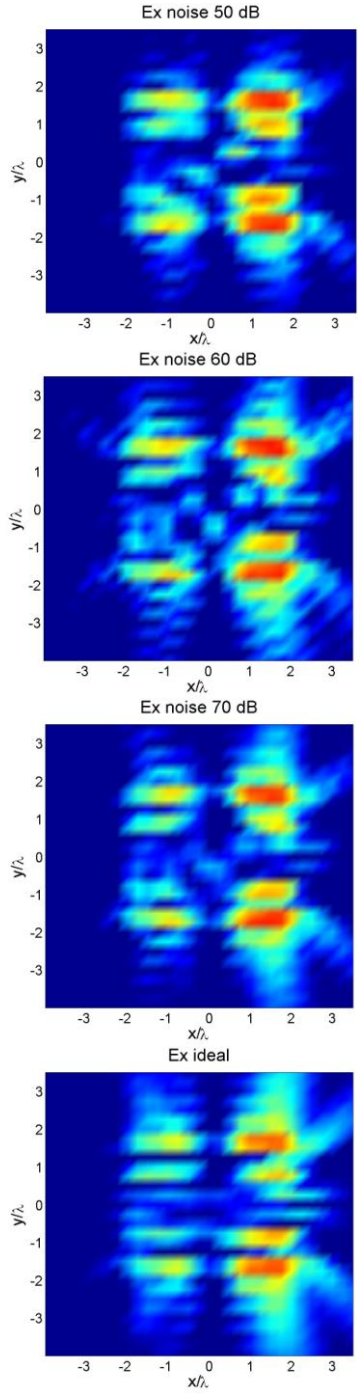

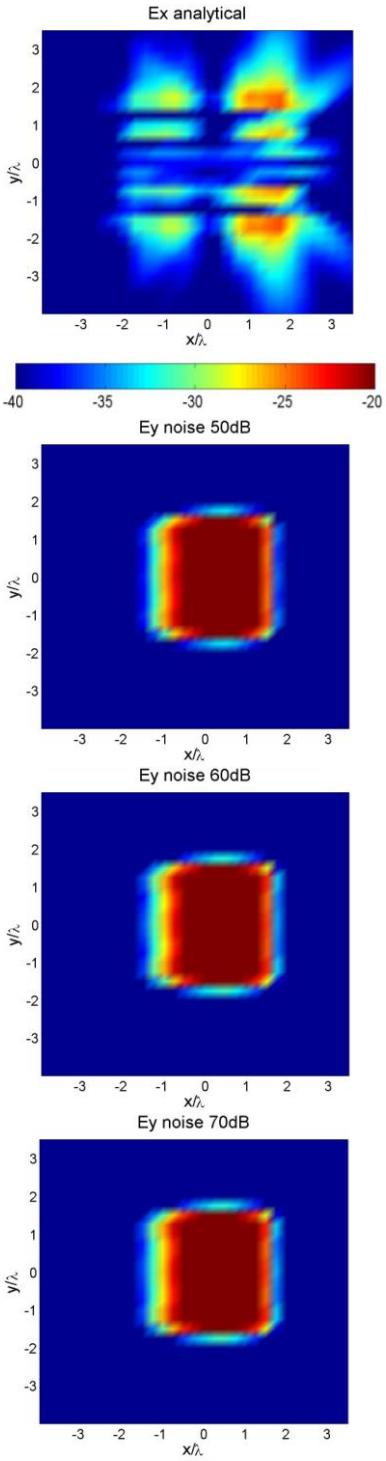

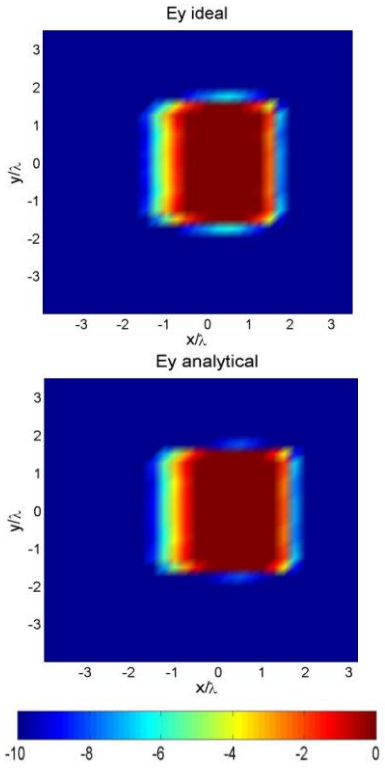

Figure 10. Amplitude of E_x and E_y on $z=0.2\lambda$ for a TE20 amplitude of 0.2. From the top: noise amplitude -50dB, -60dB and -70dB, ideal case, and analytical case.

To underline its importance for a diagnostics point of view, the radius of the converging region for -60dB noise is now selected first equal to 0.8*k* and then 0.95*k*, while the remaining spectrum is replaced by zeros. The spectra are inverse Fourier transformed on $z = 0.2\lambda$, and the results are shown in Fig. 11, for the *x*-component. Even though an asymmetry is detected, the accuracy in respect of the ideal or the analytical case is very poor and not satisfactory. We can conclude that the singularity, well reconstructed by 17 modes, and a small part of the invisible region are important for an accurate diagnostics technique.

To support that the aperture field obtained in Fig. 10 is the consequence of an overmoding error and not of a mechanical tilt of the SGH aperture, the phase of the *y*-component is plotted, see Fig. 12. The symmetry of this on the *xy*-plane indicates that a tilt is not present.

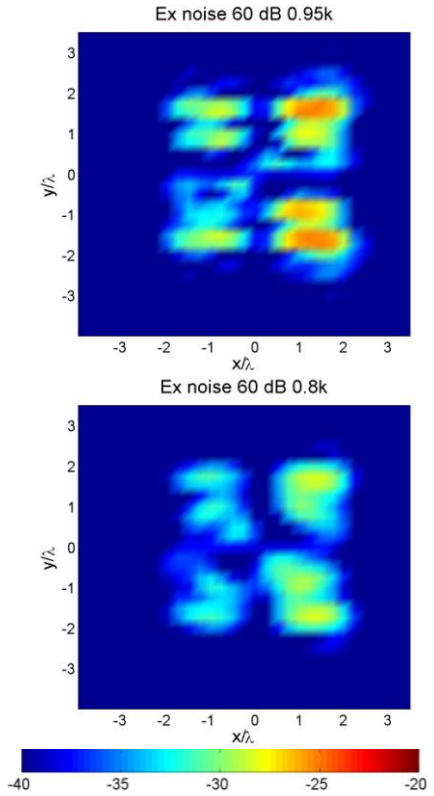

Figure 11. Amplitude of E_x on $z=0.2\lambda$ for a TE20 amplitude of 0.2 and -60dB amplitude noise: region of radius 0.95k (above), region of radius 0.8k (below).

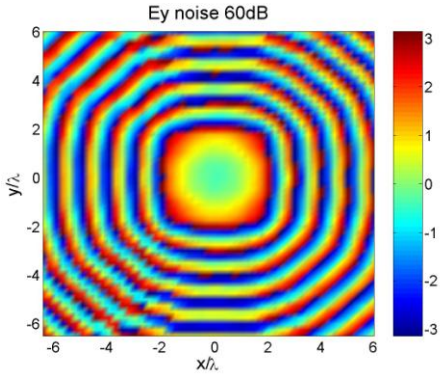

Figure 12. Phase of E_y on $z=0.2\lambda$ for a TE20 amplitude of 0.2, -60dB amplitude noise and 1.04k convergent region.

5. CONCLUSIONS

The effects of finite measurement accuracy on the SWE-to-PWE diagnostics technique have been presented. It was found that among the numerous

kinds of measurement electrical errors, the amplitude noise was the strongest and the most important. The effect of such a noise distribution generally reflects into a truncation of the available Q coefficients of the SWE of the field. It has been found that for a SGH the measured Q's are anyway sufficient to reconstruct the visible region of the plane wave spectrum, the singularity for $k_z = 0$, and a small circular region in the invisible region. This spectral distribution provides very accurate results in the computed aperture field. The effect of an overmoding error has also been studied. It has been found that an overmode of amplitude 0.1 and 0.2 can be detected and identified, in amplitude as well as in the phase, in the presence of typical measurement noise. Future investigations will concentrate on different antenna types with the purpose of identifying other antenna errors.

References

[1] Kaplan L., Hanfling J. D., Borgiotti G. V., *The Backward Transform of the Near Field for Reconstruction of Aperture Field*, IEEE Trans. on Ant. and Prop. Soc. Symp. Dig., 764-767, 1979.

[2] Rahmat-Samii Y., Lemanczyk J., *Application of Spherical Near-Field Measurements to Microwave Holographic Diagnosis of Antennas*, IEEE Trans. on Ant. and Prop., vol. 36, no. 6, 869-878, June 1988.

[3] Joy E. B., Guler M. G., *High Resolution Spherical Microwave Holography*, IEEE Trans. on Ant. and Prop., vol. 43, 464-472, 1995.

[4] Cappellin C., Breinbjerg O., Frandsen A., *A High Resolution Antenna Diagnostics Technique for Spherical Near-Field Measurements*, 28th ESA Antenna Workshop, ESTEC, Noordwijk, The Netherlands, 899-906, 2005.

[5] Cappellin C., Frandsen A., Breinbjerg O., *On the Relationship between the Spherical Wave Expansion and the Plane Wave Expansion for Antenna Diagnostics*, AMTA Europe Symposium, Munich, Germany, 2006.

[6] Homepage of the DTU-ESA Facility: http://www.oersted.dtu.dk/English/research/emi/afg/dtu_esa_facility.aspx.

[7] Hansen J. E., *Spherical Near-Field Antenna Measurements*, Peter Peregrinus Ltd. London, 1988.

[8] Hansen T. B., Yaghjian A. D., *Plane Wave Theory of Time-Domain Fields, Near-Field Scanning Applications*, IEEE PRESS, 1999.

[9] Devaney A. J., Wolf E., *Multipole Expansion and Plane Wave Representations of the Electromagnetic Field*, Journ. of Math. and Phys., vol. 15, 234-244, February 1974.

[10] Homepage of TICRA's software: http://www.ticra.com/script/site/page.asp?artid=27.

Paper V

APPLICATION OF THE SWE-TO-PWE ANTENNA DIAGNOSTICS TECHNIQUE TO AN OFFSET REFLECTOR ANTENNA

Cecilia Cappellin[1-2], Aksel Frandsen[1], Olav Breinbjerg[2]

[1] TICRA, Læderstræde 34, DK-1201 Copenhagen K, Denmark
[2] Ørsted•DTU, Technical University of Denmark, DK-2800 Kgs. Lyngby, Denmark

ABSTRACT

A new antenna diagnostics technique has been developed for the DTU-ESA Spherical Near-Field Antenna Test Facility at the Technical University of Denmark. The technique is based on the transformation of the Spherical Wave Expansion (SWE) of the radiated field, obtained from a spherical near-field measurement, to the Plane Wave Expansion (PWE), and it allows an accurate reconstruction of the field in the extreme near-field region of the antenna under test (AUT), including the aperture field. While the fundamental properties of the SWE-to-PWE transformation, as well as the influence of finite measurement accuracy, have been reported previously, we validate here the new antenna diagnostics technique through an experimental investigation of a commercially available offset reflector antenna, where a tilt of the feed and surface distortions are intentionally introduced. The effects of these errors will be detected in the antenna far-field pattern, and the accuracy and ability of the diagnostics technique to subsequently identify them will be investigated. Real measurement data will be employed for each test case.

Keywords: Antenna diagnostics, spherical near-field measurements, spherical wave expansion, plane wave expansion, offset reflector antenna.

1. Introduction

Electrical and mechanical errors in an antenna may seriously affect the antenna's performance. Though their presence is usually observed by anomalies in the antenna's far-field pattern, their identification is normally possible only through an analysis of the antenna's extreme near-field. The reconstruction of the extreme near-field on the basis of near- or far-field measurements is thus an essential step in antenna diagnostics.

Several non-invasive diagnostics techniques have been proposed over the years [1]-[3]: [1] computes the aperture field from planar near-field measurements, [2] studies and detects the errors caused by radome defects on basis of spherical near-field measurements while [3] reconstructs the induced currents on the surface of big reflectors starting from far-field data.

When the field is expressed as a SWE obtained from a spherical near-field measurement, as is the case at the DTU-ESA Spherical Near-Field Antenna Test Facility [4], the calculation of the extreme near-field is anyway not straightforward since the SWE is valid only outside the antenna minimum sphere of radius r_o, see Fig. 1.

One way to circumvent this limitation is to transform the SWE into the PWE, which is valid on any z-plane $z > z_o$, with z_o being the largest z-coordinate of the source; note that $|z_o| \leq r_o$, see Fig. 1. Once the PWE is known, the extreme near-field can be computed by an inverse Fourier transform (IFT) and then subjected to diagnostics. This constitutes the basis of the recently developed SWE-to-PWE antenna diagnostics technique [5]-[6]. The technique uses spherical near-field measurement data to compute the field on a plane located in the extreme near-field of the AUT, and provides a spatial resolution that may, in principle, exceed the traditional limit of half a wavelength.

The purpose of this work is to perform an experimental validation of the SWE-to-PWE antenna diagnostics technique under typical measurement conditions. To this end, we employ a cheap and simple commercially available offset reflector antenna for satellite TV reception, which in its nominal configuration already exhibits several

non-ideal characteristics. We then introduce three additional errors, viz. a tilt of the feed, a localized bump in the reflector, and a global distortion of the reflector surface. The near-fields are measured on a spherical surface, and transformed to the corresponding far-fields, where the effects of the errors are observed. The extreme near-field is then computed with the new antenna diagnostics technique with the purpose of identifying those errors.

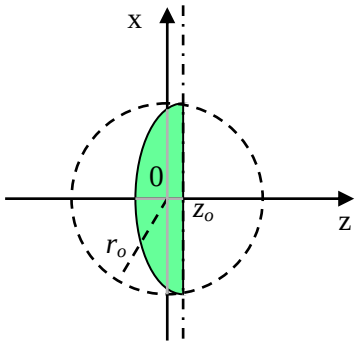

Figure 1. Spatial domains of validity of the SWE and PWE for a general antenna: the PWE is valid for $z > z_o$, the SWE for $r > r_o$.

The paper is organized as follows: In Section 2 the SWE-to-PWE diagnostics technique and its properties are briefly summarized, in Section 3 the offset reflector antenna is described, while the errors and the diagnostics results are presented in Section 4. All quantities are expressed in the S.I. rationalized system with the $e^{-i\omega t}$ time convention.

2. The SWE-to-PWE antenna diagnostics technique

We start by introducing the SWE of the electric field $\bar{E}$ radiated by an antenna circumscribed by a minimum sphere of radius r_o, [7], for $r > r_o$.

$$\bar{E}(\bar{r}) = \frac{k}{\sqrt{\eta}} \sum_{n=1}^{\infty} \sum_{m=-n}^{n} Q_{1mn}^{(3)} \bar{F}_{1mn}^{(3)}(\bar{r}) + Q_{2mn}^{(3)} \bar{F}_{2mn}^{(3)}(\bar{r}), \qquad (1)$$

where $Q_{1mn}^{(3)}$ and $Q_{2mn}^{(3)}$ are the expansion coefficients and $\bar{F}_{1mn}^{(3)}(\bar{r})$ and $\bar{F}_{2mn}^{(3)}(\bar{r})$ are the power-normalized spherical vector wave functions. The medium intrinsic admittance is η, k is the wave number, and $\bar{r}$ is the position vector expressed in terms of spherical coordinates (r, θ, φ) or rectangular coordinates (x, y, z). In practice, the n-summation of the SWE is typically truncated at $N = kr_o+10$ since this is sufficient for an accurate calculation of the far-field. The PWE of the same electric field $\bar{E}$ in the spectral k_xk_y-domain valid for $z > z_o$ is given by [8],

$$\bar{E}(x,y,z) = \frac{1}{2\pi} \int_{-\infty}^{\infty} \int_{-\infty}^{\infty} \bar{T}(k_x,k_y)\, e^{ik_z z} e^{i(k_x x + k_y y)} dk_x dk_y \qquad (2)$$

where k_x and k_y, are the spectral variables and $k_z = \sqrt{k^2 - k_x^2 - k_y^2}$. The plane wave spectrum for a given z-coordinate is $\bar{T}(k_x,k_y,z) \equiv \bar{T}(k_x,k_y)e^{ik_z z}$. The spectral domain is divided into two regions, the visible region, for $k_x^2 + k_y^2 \le k^2$, which contains the propagating plane waves, and the invisible region, for $k_x^2 + k_y^2 > k^2$, which contains the evanescent plane waves, see Fig. 2. The two variables k_x and k_y are real, while k_z is real in the visible region but purely imaginary with a positive imaginary part in the invisible region. In practice, the k_x- and k_y-integrals are truncated at finite values $\pm k_{xmax}$ and $\pm k_{ymax}$ respectively, providing a spatial resolution (δ_x, δ_y) in the aperture field equal to $\delta_x = \pi / k_{xmax}$, $\delta_y = \pi / k_{ymax}$. At the border between the visible and invisible regions $k_z = 0$ and the PWE generally possesses a singularity there [8].

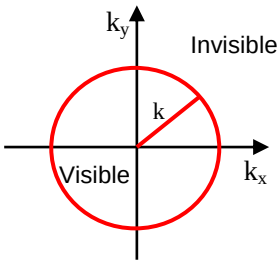

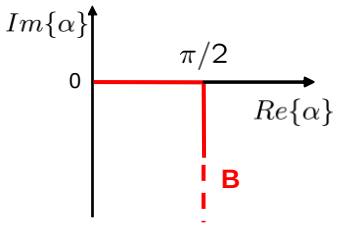

Figure 2. Visible and invisible regions of the spectral k_xk_y-domain, and B contour of the variable α.

It can be shown [5]-[6] that the SWE of Eq. 1 can be rigorously transformed into the PWE of Eq. 2, allowing the plane wave spectrum $\bar{T}(k_x, k_y, z)$ to be written as

$$\bar{T}(k_x,k_y,z) = \sum_{n=1}^{\infty}\sum_{m=-n}^{n} Q_{1mn}^{(3)}\bar{T}_{1mn}(k_x,k_y,z) + \\ + Q_{2mn}^{(3)}\bar{T}_{2mn}(k_x,k_y,z) \qquad (3)$$

where

$$\bar{T}_{1mn}(k_x,k_y,z) = \frac{e^{ik_z z}}{k_z}\frac{(-i)^{n+1}}{\sqrt{\eta}\sqrt{n(n+1)}}\bar{Y}_n^m(\alpha,\beta) \qquad (4)$$

$$\bar{T}_{2mn}(k_x,k_y,z) = \frac{e^{ik_z z}}{k_z}\frac{(-i)^{n}}{\sqrt{\eta}\sqrt{n(n+1)}}\hat{k}\times\bar{Y}_n^m(\alpha,\beta) \qquad (5)$$

with $\hat{k} = \bar{k}/k = (k_x\hat{x} + k_y\hat{y} + k_z\hat{z})/k$. The function $\bar{Y}_n^m(\alpha,\beta)$ is the vector spherical harmonics [5], $\alpha \in$ B, see Fig. 2, and is equal to $\alpha = \text{acos}(k_z/k)$, while $\beta \in [-\pi, \pi]$ and is equal to $\beta = \text{atan}(k_y/k_x)$. Eq. 3 shows that the plane wave spectrum on any z-plane $z > z_o$ can be expressed as a series of the same type and with the same Q coefficients of the SWE of Eq. 1, where the only difference lies in the basis functions that are now the vector spherical harmonics instead of the power-normalized spherical vector wave functions. The imaginary values of the angle α correspond to the invisible region of the k_xk_y-domain. Though the functions $\bar{Y}_n^m(\alpha,\beta)$ have an exponential growth in that region, it is important to note that the series of Eq. 3 is convergent in the entire spectral domain. Nevertheless, while the visible region of the spectrum reaches convergence with $N \approx kr_o$ terms, the invisible requires many more terms to compensate the exponential growth of the spherical harmonics [5]-[6]. In practice the finite dynamic range of the measurement system limits the measurement of these high order modes. However, it has been shown [6] that the recovery of the visible region and the singularity for $k_z = 0$, both correctly represented by the first $N \approx kr_o$ modes, provides accurate aperture fields that facilitate an effective diagnostics.

3. The offset reflector antenna: model and nominal configuration

The AUT is a 12 GHz offset parabolic reflector, defined in the *xyz*-coordinate system by a circular projected aperture of diameter D = 60 cm, a focal length f = 39 cm and a clearance d' = 9 cm, see Fig. 3. The feed is linearly polarized along x_f, where $x_f y_f z_f$ is the feed coordinate system, with its origin at the focus and with z_f pointing towards the center point on the reflector. We introduce two coordinate systems (CS): the measurement CS, $x_{meas}\, y_{meas}\, z_{meas}$, with its origin on the reflector aperture plane and the z_{meas}-axis normal to that and coinciding with the horizontal rotation axis of the measurement system, and the cut CS, $x_{cut}\, y_{cut}\, z_{cut}$, obtained by rotating $x_{meas}\, y_{meas}\, z_{meas}$ 26.5° around y_{meas}, and with z_{cut} thus aligned to the main beam direction.

The measurement set-up of the antenna in its nominal configuration is shown in Fig. 4. By simply rotating the Q coefficients of the SWE of the radiated electric field measured in the measurement CS, the Q coefficients of the SWE in the cut CS are easily obtained [7]. The amplitude of the transformed far-field pattern, in the cut CS, of the antenna in its nominal configuration is plotted in dB in Fig. 5, showing co- and cross-polar components according to Ludwig's 3rd definition [7], in the *uv*-space, normalized to the maximum value of the co-polar component.

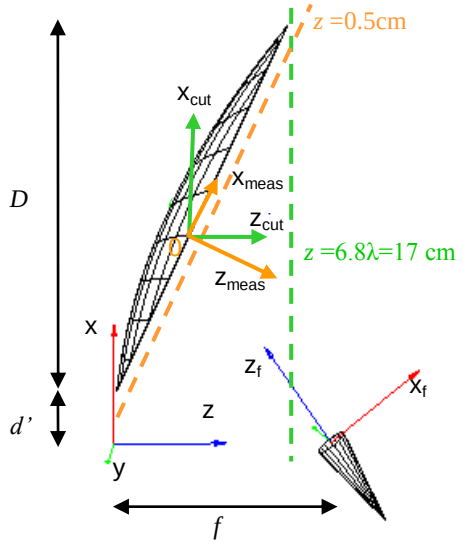

Figure 3. Offset reflector antenna: geometry and coordinate systems.

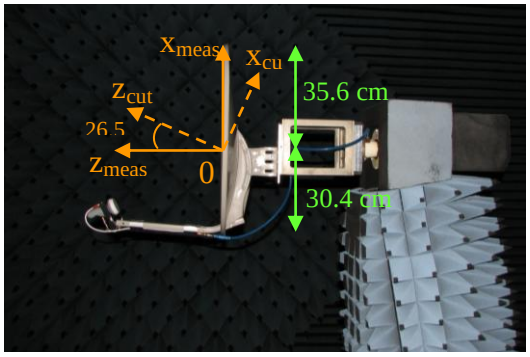

Figure 4. AUT on the measurement tower: geometry and coordinate systems.

From the Q coefficients the power spectrum $P_{rad}(n) = \frac{1}{2}\sum_{m=-n}^{n}\left|Q_{1mn}^{(3)}\right|^2 + \left|Q_{2mn}^{(3)}\right|^2$ has been found, see Fig. 6.

It is seen that the finite dynamic range of the measurement system allows the correct acquisition of N = 135 modes which, with $r_o \approx 18\lambda$, corresponds to $N = kr_o + 22$, and M = 120.

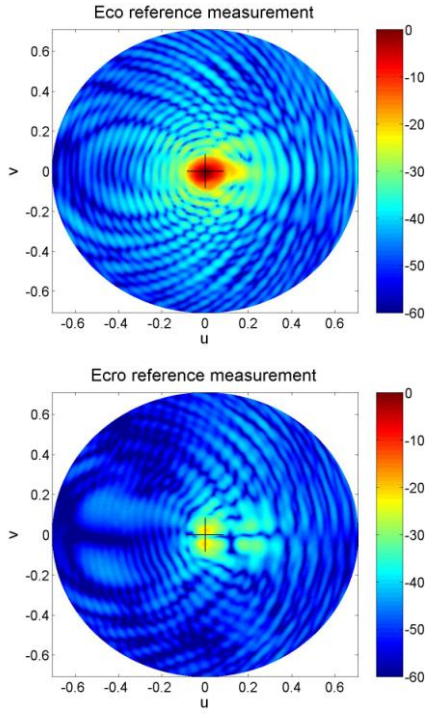

Figure 5. Amplitude of co- and cross-polar components in dB of the antenna far-field in its nominal configuration in the cut CS.

Truncating the mode spectrum at these two values, which will be used in all the subsequent investigated cases, retains more than 99.99% of the total radiated power. With these n- and m-truncations in the series of Eq. 3 it is expected to recover only the visible part of the plane wave spectrum and the singularity at $k_z = 0$. A calculation of the invisible region to improve the spatial resolution of the aperture fields is not possible here, since the number of available n-modes is not sufficient to reach convergence in the invisible region.

The Q coefficients of the SWE in the cut CS have thus been used to compute with Eq. 3 the plane wave spectrum $\bar{T}(k_x, k_y, z)$, in the [-3k, 3k] spectral domain, on the z-plane z = 17cm= 6.8 λ, see Fig. 3.

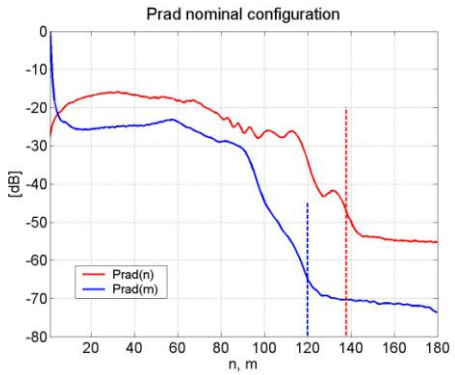

Figure 6. Power spectrum in the cut CS of the antenna in the nominal configuration and the truncation numbers *N*=135, *M*=120.

After replacing by zeros the values of the plane wave spectrum in the invisible region, the spectrum was inversely Fourier transformed obtaining the aperture field. Plots of the amplitude of the *x*- and *y*-components of the electric field (in dB scale and normalized to the maximum of E_x), and phase of the *x*-component are shown in Fig. 7 on the *z*-plane z = 17 cm in the cut CS, where the projected circular rim of the reflector is also indicated.

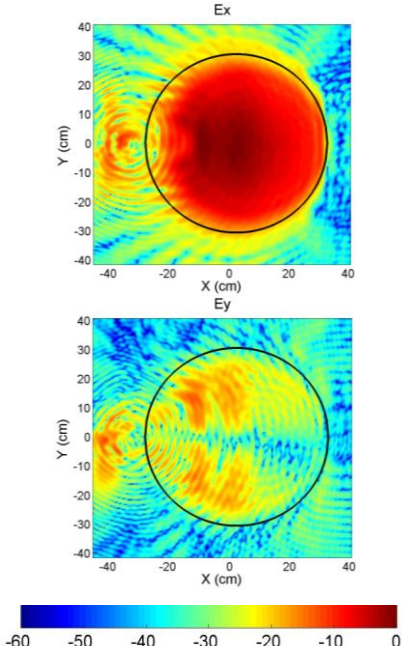

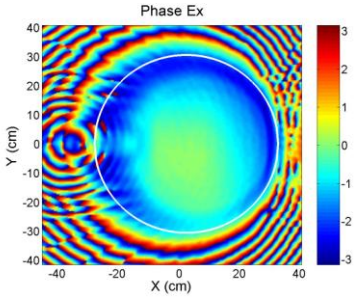

Figure 7. Amplitude of E_x and E_y and phase of E_x on *z*=17 cm, in the cut CS for the nominal configuration.

While the amplitude field distributions of E_x and E_y are almost symmetric around the *y*=0 axis, as expected, the phase distribution is not constant, as would be the case for an ideal parabolic reflector antenna, but shows a variation from the center of the aperture to the edge that reaches the maximum value of 2.4 rad. Thus, this reflector antenna – even in its nominal configuration – is far from ideal. By looking at the left side of the projected circular rim, we clearly distinguish the diffraction from the strut and the effect of the feed.

4. Antenna errors: measurements and diagnostics results

4a) Feed tilt

Feed tilts of 5º and 10º around the x_f –axis have been considered, see Fig. 8. The tilt of the feed causes an asymmetry of the cross-polar far-field which is detectable already for the 5º case but becomes more evident for the 10º case, see Fig. 9. The *Q* coefficients of the SWE in the cut CS have been used to compute the plane wave spectrum $\bar{T}(k_x, k_y, z)$ on the *z*-plane *z* = 17cm.

The amplitudes of the *x*- and *y*-components of the aperture field are shown in Fig. 10. When it is compared to Fig. 7, this clearly shows a tilt of the feed illumination towards the negative *y*-axis.

Figure 8. Offset reflector with a feed tilt.

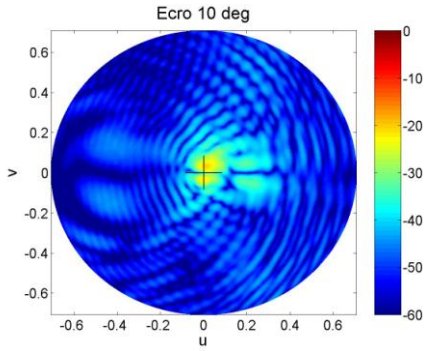

Figure 9. Amplitude of cross-polar component in dB of the antenna far-field for the 10º feed tilt case in the cut CS.

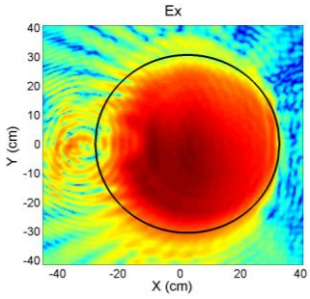

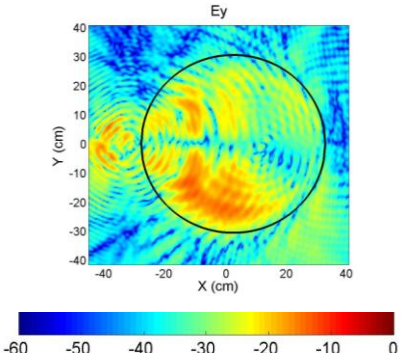

Figure 10. Amplitude of E_x and E_y on z = 17 cm, in the cut CS for the 10º feed tilt case.

4b) Gaussian bump

A metallic bump with the shape of a two-dimensional Gaussian function with peak and sigma both of 1 cm has been built and attached to the reflector surface, see Fig. 11. The co-polar component of the far-field pattern in the cut CS is shown in Fig. 12.

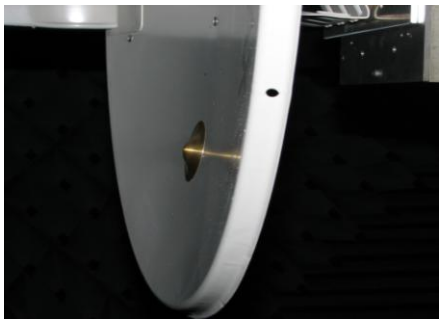

Figure 11. Offset reflector with a Gaussian bump.

While the shape of the main beam is similar to the one of the nominal configuration in Fig. 5, the structure of the side-lobes changes significantly. The same was noticed for the cross-polar component.

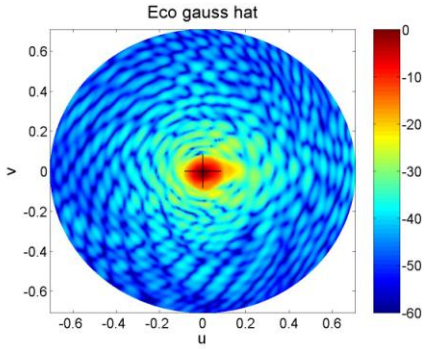

Figure 12. Amplitude of co-polar component of the antenna far-field for the Gaussian bump case in the cut CS.

The aperture field was then calculated on the z = 17 cm plane in the cut CS, see Fig. 13 (above). On that plane also the z-component of the field (not shown here) highlights the circular structure caused by the bump.

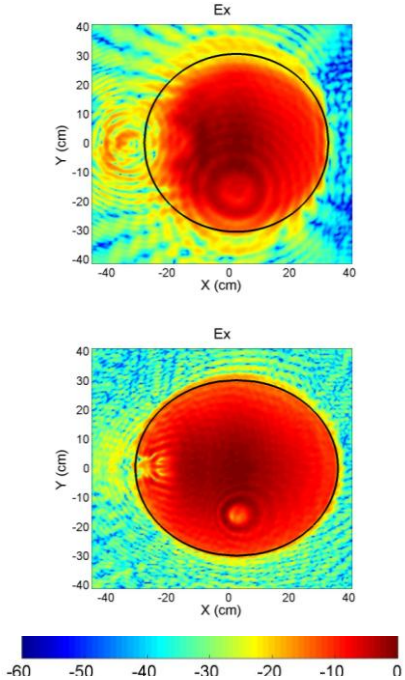

Figure 13. Amplitude of E_x on z = 17 cm in the cut CS (above), and on z = 0.5 cm in the measurement CS (below) for the Gaussian bump case.

Though the aperture illumination is now almost symmetric, when compared to Figs. 7 and 10, a circular structure of different amplitude is noticed for $x \approx 0$ cm and $y \approx$ -20 cm. The picture becomes more clear when the aperture field is computed in the measurement CS on z = 0.5 cm, see Figs. 3 and 13 (below), where the projected elliptical rim of the reflector is also indicated.

4c) Surface distortion

A surface distortion was finally introduced by randomly placing 21 dishes of aluminum each with a diameter of 5 cm and thicknesses of 2.5 mm, 1.5 mm and 1 mm (λ=2.5 cm) on the entire reflector surface, see Fig. 14. This serves as a model of slowly varying surface distortions.

Figure 14. Offset reflector with surface distortions.

The co-polar component of the far-field is shown in Fig. 15.

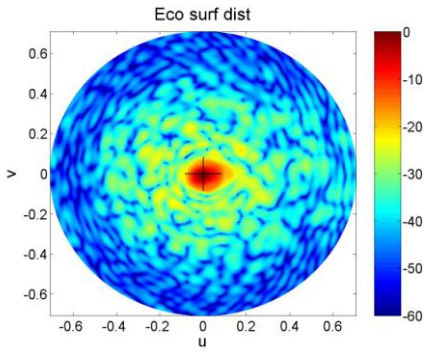

Figure 15. Amplitude of co-polar component of the antenna far-field for the surface distortion case in the cut CS.

It is seen that side-lobes of high amplitude appear all around the main beam region, which remains almost the same as for the nominal configuration of Fig. 5.

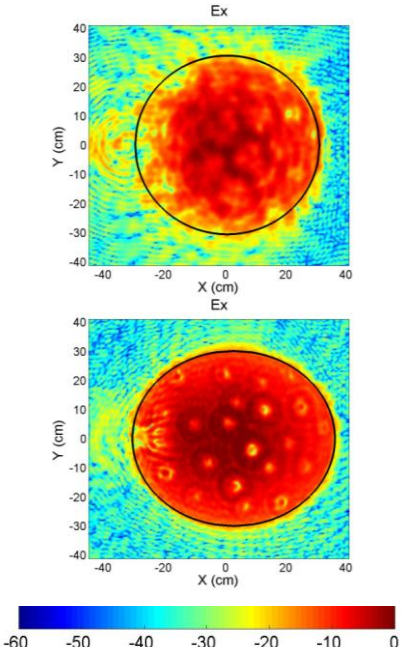

Figure 16. Amplitude of E_x on z = 17 cm in the cut CS (above), and on z = 0.5 cm in the measurement CS (below) for the surface distortion case.

The x-component of the aperture field is shown in Fig. 16, above at z = 17 cm in the cut CS, and below at z = 0.5 cm in the measurement CS. As for the Gaussian bump case, the distortions become more distinguishable on a plane closer to the reflector surface, in particular all 21 dishes, the thicker clearly, the thinner less strongly, are identified.

5. Conclusions

A diagnostics of a simple commercially available offset reflector antenna for satellite TV reception has been performed by applying the SWE-to-PWE antenna diagnostics technique. The diagnostics showed that the antenna in its nominal configuration already exhibited non-ideal properties. Even in the presence of these, a feed tilt and two different types of surface distortions, which were intentionally introduced and provided anomalies in the far-field pattern, were correctly and accurately identified. The investigation serves as an experimental validation of the SWE-to-PWE antenna diagnostics technique in the presence of typical measurement inaccuracies and a non-ideal AUT. Furthermore, it highlights the value and importance of applying different coordinate systems and projected aperture planes for the purpose of antenna diagnostics.

REFERENCES

[1] Kaplan L., Hanfling J. D., Borgiotti G. V., *The Backward Transform of the Near Field for Reconstruction of Aperture Field*, IEEE Ant. and Prop. Soc. Symp. Dig., 764 - 767, 1979.

[2] Joy E. B., Guler M. G., *High Resolution Spherical Microwave Holography*, IEEE Trans. Ant. Prop., vol. 43, 464 - 472, 1995.

[3] Rahmat-Samii Y., *Surface Diagnosis of Large Reflector Antennas Using Microwave Holographic Metrology: an Iterative Approach*, Radio Science., vol. 19, 1205-1217, 1984.

[4] Homepage of the DTU-ESA Facility: http://www.oersted.dtu.dk/English/research/emi/afg/dtu_esa_facility.aspx.

[5] Cappellin C., Frandsen A., Breinbjerg O., *On the Relationship between the Spherical Wave Expansion and the Plane Wave Expansion*, AMTA Europe Symposium, Munich, Germany, 2006.

[6] Cappellin C., Breinbjerg O., Frandsen A., *The Influence of Finite Measurement Accuracy on the SWE-to-PWE Antenna Diagnostics Technique*, EuCap, European Conference on Antennas and Propagation, Nice, France, 2006.

[7] Hansen J. E., "Spherical Near-Field Antenna Measurements", Peter Peregrinus Ltd. London, 1988.

[8] Hansen T. B., Yaghjian A. D., "Plane Wave Theory of Time-Domain Fields, Near-Field Scanning Applications", IEEE PRESS, 1999.

Paper VI

DIAGNOSTICS OF THE SMOS RADIOMETER ANTENNA SYSTEM AT THE DTU-ESA SPHERICAL NEAR-FIELD ANTENNA TEST FACILITY

C. Cappellin[1-2], A. Frandsen[1], S. Pivnenko[2], G. Lemanczyk[3], O. Breinbjerg[2]

[1]TICRA, Læderstræde 34, DK-1201, Copenhagen, Denmark
[2]Ørsted·DTU, Technical University of Denmark, DK-2800 Kgs. Lyngby, Denmark
[3]European Space Research and Technology Centre, Noordwijk, The Netherlands

Keywords: Antenna diagnostics, spherical near-field measurements, radiometer antenna, plane wave expansion, spherical wave expansion.

Abstract

The recently developed Spherical Wave Expansion-to-Plane Wave Expansion (SWE-to-PWE) antenna diagnostics technique is employed in an investigation of the antenna system in the Microwave Imaging Radiometer using Aperture Synthesis (MIRAS) for ESA's Soil Moisture and Ocean Salinity (SMOS) mission. The SWE-to-PWE antenna diagnostics technique successfully identifies the sources of the anomalies detected in 2 of the 138 MIRAS antenna far-field patterns that were measured during the on-ground calibration at the DTU-ESA Spherical Near-Field Antenna Test Facility in 2006. In addition to its obvious value for the SMOS mission, this investigation also provides an experimental validation of the SWE-to-PWE antenna diagnostics technique.

1 Introduction

The SMOS mission, scheduled for launch in 2008, is the latest Earth Observation Mission of the European Space Agency (ESA) [5]. Its purpose is to monitor the water cycle, the density of the seawater and the currents in the oceans to improve the knowledge of these phenomena and hence provide better weather and climate forecasts. A special radiometer, MIRAS, has been developed to capture the microwave radiation emitted from soil and ocean in the frequency band from 1.404 GHz to 1.423 GHz (L-band). In order to achieve the required spatial resolution, the radiometer consists of 69 independent dual-polarized receivers positioned on an 8 meter diameter Y-shaped support structure, that is folded during launch and un-folded once the satellite is in orbit. Each receiver includes a dual linearly polarized circular patch antenna.

For the purpose of accurately determining the soil moisture and ocean salinity, the radiometric signal processing requires an extremely accurate measurement of the receivers' antenna far-field patterns. A 1σ accuracy of 0.05 dB for the amplitude and 0.33° for the phase in a 70° angular region centred on the main beam direction was requested. The DTU-ESA Spherical Near-Field Antenna Test Facility at the Technical University of Denmark (DTU) [6] was selected to conduct the on-ground calibration of the MIRAS antenna patterns. After an investigatory study to improve measurement procedures and the measurement system during 2003 to 2005 [7]-[8], the final on-ground calibration measurements took place from November 2005 to July 2006, while the processing of the raw measurement data to determine the antenna far-field patterns was carried out in the fall of 2006.

During the last measurement series of the MIRAS, see Fig. 1, anomalies were detected in the antenna patterns of two MIRAS receivers.

In order to identify the source of these far-field anomalies a diagnostics of the two elements was performed based on the SWE-to-PWE antenna diagnostics technique [1]-[2]. The technique uses spherical near-field measurement data to compute the aperture field on a plane located in the extreme near-field of the antenna under test, and provides a spatial resolution that may, in principle, exceed the traditional limit of half a wavelength. The aperture plane was chosen to be positioned on the outside surface of the Kapton-Germanium protection layer which covers the complete MIRAS structure, see Fig. 1.

The purpose of this work is, besides being an important step in the MIRAS on-ground calibration, to provide an experimental validation of the SWE-to-PWE antenna diagnostics technique, when working in the presence of noise,

finite dynamic range, and other non-ideal phenomena typical of practical measurements.

Figure 1. Central part of the MIRAS, consisting of the hub and the three inner arm segments, on the tower of the DTU-ESA Spherical Near-Field Antenna Test Facility during the last measurement series.

The paper is organized as follows: in section 2 a summary of the SWE-to-PWE technique is provided, while in section 3 the two faulty elements are analyzed. Both the measured far-field patterns and the computed aperture field distributions will be shown for each of the two test cases, arriving at the identification of the antenna errors. All results are expressed in the S.I. rationalized system with the $e^{-i\omega t}$ time convention.

2 The SWE-to-PWE antenna diagnostics technique

Electrical and mechanical errors in an antenna may seriously affect the antenna performance, and while their presence is normally detected by anomalies in the measured far-field pattern, often only an analysis of the extreme near-field can facilitate the identification of those errors. However, the computation of the extreme near-field is generally not possible when the field is expressed as a SWE obtained from a spherical near-field measurement since the SWE is valid only outside the antenna minimum sphere of radius r_o, with r_o being the largest r-coordinate of the source. One way to overcome this limitation is to transform the SWE into the PWE which is valid on any z-plane $z > z_o$, with z_o being the largest z-coordinate of the source, see Fig. 2. Note that $|z_o| \leq r_o$. Once the PWE is known, the extreme near-field can be computed by use of the Fourier transform and then subjected to diagnostics.

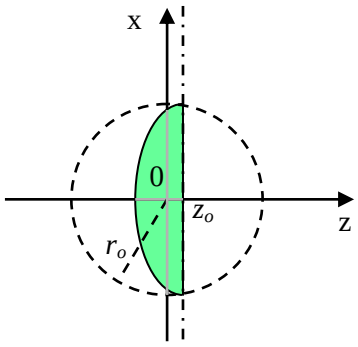

Figure 2. Spatial domains of validity of the SWE and PWE for a general antenna: the PWE is valid for $z > z_o$, the SWE for $r > r_o$.

To summarize the theory behind the SWE-to-PWE technique, we start by introducing the SWE of the electric field $\bar{E}$ radiated by an antenna circumscribed by a minimum sphere of radius r_o, [3], with $r > r_o$,

$$\bar{E}(\bar{r}) = \frac{k}{\sqrt{\eta}} \sum_{n=1}^{\infty} \sum_{m=-n}^{n} Q_{1mn}^{(3)} \bar{F}_{1mn}^{(3)}(\bar{r}) + Q_{2mn}^{(3)} \bar{F}_{2mn}^{(3)}(\bar{r}), \quad (1)$$

where $Q_{1mn}^{(3)}$ and $Q_{2mn}^{(3)}$ are the expansion coefficients and $\bar{F}_{1mn}^{(3)}(\bar{r})$ and $\bar{F}_{2mn}^{(3)}(\bar{r})$ are the power-normalized spherical vector wave functions. The medium intrinsic admittance is η, k is the wave number, and $\bar{r}$ is the position vector expressed in terms of spherical coordinates (r, θ, φ) or rectangular coordinates (x, y, z). In practice, the n-summation of the SWE is typically truncated at $N = kr_o+10$ since this is sufficient for an accurate calculation of the far-field. The PWE of the same electric field $\bar{E}$ in the spectral k_xk_y-domain valid for $z > z_o$ is given by [4],

$$\bar{E}(x,y,z) = \frac{1}{2\pi} \int_{-\infty}^{\infty} \int_{-\infty}^{\infty} \bar{T}(k_x,k_y)\, e^{ik_z z} e^{i(k_x x + k_y y)} dk_x dk_y \quad (2)$$

where k_x and k_y, are the spectral variables and $k_z = \sqrt{k^2 - k_x^2 - k_y^2}$. The plane wave spectrum for a given z-coordinate is

$\bar{T}(k_x,k_y,z) \equiv \bar{T}(k_x,k_y)e^{ik_z z}$. The spectral domain is divided into two regions, the visible region, for $k_x^2 + k_y^2 \le k^2$, which contains the propagating plane waves, and the invisible region, for $k_x^2 + k_y^2 > k^2$, which contains the evanescent plane waves, see Fig. 3. The two variables k_x and k_y are real, while k_z is real in the visible region but purely imaginary with a positive imaginary part in the invisible region. In practice, the k_x- and k_y-integrals are truncated at finite values $\pm k_{xmax}$ and $\pm k_{ymax}$ respectively, providing a spatial resolution (δ_x,δ_y) in the aperture field equal to $\delta_x = \pi / k_{xmax}$, $\delta_y = \pi / k_{ymax}$. At the border between the visible and invisible regions k_z = 0 and the PWE generally possesses a singularity there [4].

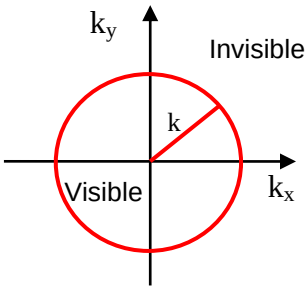

Figure 3. Visible and invisible regions of the spectral k_xk_y-domain.

It can be shown [1][2] that the SWE of Eq. 1 can be rigorously transformed into the PWE of Eq. 2, if the plane wave spectrum $\bar{T}(k_x,k_y,z)$ is written as

$$\bar{T}(k_x,k_y,z) = \sum_{n=1}^{\infty}\sum_{m=-n}^{n} Q_{1mn}^{(3)}\bar{T}_{1mn}(k_x,k_y,z) + Q_{2mn}^{(3)}\bar{T}_{2mn}(k_x,k_y,z) \quad (3)$$

where

$$\bar{T}_{1mn}(k_x,k_y,z) = \frac{e^{ik_z z}}{k_z}\frac{(-i)^{n+1}}{\sqrt{\eta}\sqrt{n(n+1)}}\bar{Y}_n^m(\alpha,\beta) \quad (4)$$

$$\bar{T}_{2mn}(k_x,k_y,z) = \frac{e^{ik_z z}}{k_z}\frac{(-i)^{n}}{\sqrt{\eta}\sqrt{n(n+1)}}\hat{k}\times\bar{Y}_n^m(\alpha,\beta) \quad (5)$$

with $\hat{k} = \bar{k}/k = (k_x\hat{x} + k_y\hat{y} + k_z\hat{z})/k$. The function $\bar{Y}_n^m(\alpha,\beta)$ is the vector spherical harmonics [1], with $\alpha \in$ B, see Fig. 4, equal to $\alpha = \text{acos}(k_z/k)$, and $\beta \in [-\pi, \pi]$ and equal to $\beta = \text{atan}(k_y/k_x)$.

Eq. 3 shows that the plane wave spectrum on any z-plane $z > z_o$ can be expressed as a series of the same type and with the same Q coefficients of the SWE of Eq. 1, where the basis functions are now the vector spherical harmonics. The imaginary values of the angle α correspond to the invisible region of the k_xk_y-domain. Though the functions $\bar{Y}_n^m(\alpha,\beta)$ have an exponential growth in that region, it is important to note that the series of Eq. 3 is convergent in the entire spectral domain.

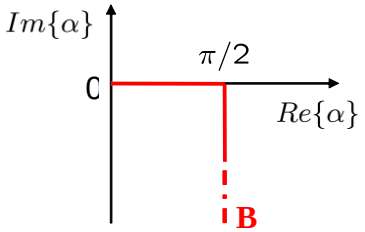

Figure 4. Domain of the variable α on contour B.

Nevertheless, while the visible region of the spectrum reaches convergence with $N \approx kr_o$ terms, the invisible generally requires many more terms to compensate the exponential growth of the spherical harmonics [1][2]. In practice, the finite dynamic range of the measurement system limits the measurement of these high order modes. However, it has been shown [1] that the recovery of the visible region and the singularity for $k_z = 0$, both correctly represented by the first $N \approx kr_o$ modes, provides accurate aperture fields that facilitate an effective diagnostics.

3 Faulty elements and diagnostics results

During the final calibration measurements of the MIRAS, see Figs. 1 and 5, anomalies were discovered in the far-field patterns of two receivers:

1) Port 1 of the receiver unit BC03 showed a high cross-polarisation in the φ = 90° plane.

2) Port 1 of the receiver unit A05 exhibited a noticeable frequency variation in all φ planes.

In order to identify the sources of those anomalies, the SWE-to-PWE diagnostics technique was applied and the aperture fields for these two receivers were computed on the z-plane placed on the surface of the Kapton-Germanium protection layer, see Fig. 1, located at z = -5mm in the measurement coordinate system. For reference, the diagnostics was also applied to the unit A01 (port 1) which did not present any anomalies. Its co-

and cross-polar far-field patterns (Ludwig's 3rd definition [3]) are shown in Fig. 6 for φ = 90º.

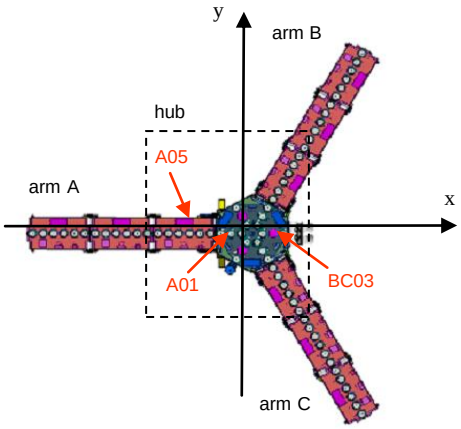

Figure 5. The MIRAS antenna system in the measurement coordinate system with the faulty units A05 and BC03 and the correct unit A01 indicated.

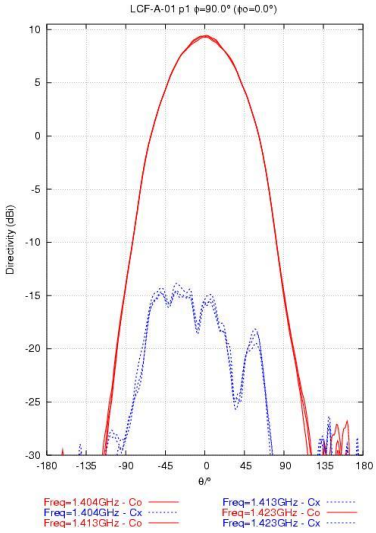

Figure 6. Far-field pattern of the receiver unit A01, port 1, for $\varphi = 90°$, showing correct co- and cross-polar components.

3.1 Element BC03

The far-field pattern of port 1 of the receiver unit BC03 in the φ = 90° plane is shown in Fig. 7: it exhibits a correct co-polar component, but an unusual high cross-polar level at all frequencies of interest when compared to the reference pattern of Fig. 6.

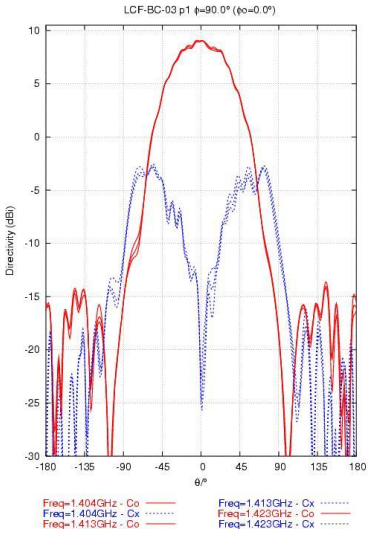

Figure 7. Far-field pattern of the receiver unit BC03, port 1, for $\varphi = 90°$, showing an unusual high cross-polar component.

From the Q coefficients of the SWE the power spectrum $P_{rad}(n) = \frac{1}{2}\sum_{m=-n}^{n} \left|Q_{1mn}^{(3)}\right|^2 + \left|Q_{2mn}^{(3)}\right|^2$ has been found, see Fig. 8.

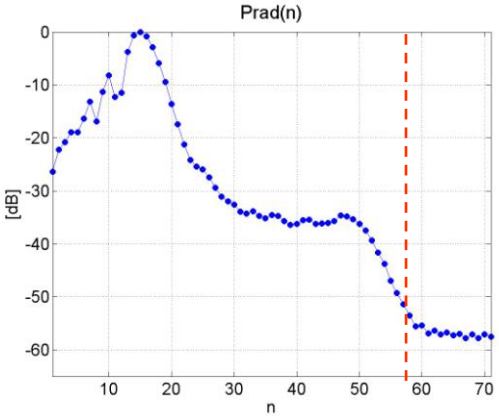

Figure 8. Power spectrum of the unit BC03 at f =1.423 GHz, and the truncation value N = 58.

It is seen that the finite dynamic range of the measurement system allows the correct acquisition of N = 58 modes which, at a frequency f =1.423 GHz and with r_o being equal to 9λ, corresponds to $N = 58 = kr_o+2$. With this n-truncation in the series of Eq. 3 it is expected to recover only the visible part of the plane wave spectrum and the singularity at $k_z = 0$. A calculation of the invisible region to improve the spatial resolution of the

aperture fields is not possible due to an insufficient number of *n*-modes. The plane wave spectrum $\bar{T}(k_x, k_y, z)$ has thus been calculated with Eq. 3, see Fig. 9 for a plot of the *y*-component in dB scale on the [-2*k*, 2*k*] spectral domain. It is possible to notice the recovery of the visible region and the singularity at k_z = 0, while it is evident that the convergence of points belonging to the invisible region is not reached yet. The invisible region is thus replaced by zeros and the spectrum is then inverse Fourier transformed to obtain the aperture field.

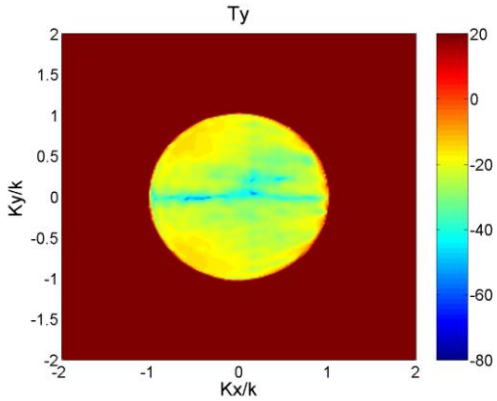

Figure 9. Amplitude of T_y, unit BC03, in dB on *z* = -5mm with *N* = 58: the visible region and the singularity are reconstructed, while the convergence in the invisible region is not reached for this value of *N*.

In Fig. 10 the cross-polar components E_y and E_z are plotted. It is possible to distinguish the radiation from the circular patch as well as the diffraction from the edges of the hub. Moreover, for both components the radiation from the patch shows asymmetries with respect to the axis parallel to the *y*-axis and passing through the center of the patch. It was thus concluded that the anomalies of the pattern in Fig. 7 were due to an error in the patch excitation, i.e., in the patch feed network. The unit BC03 was subsequently replaced by a new one and, after a new spherical near-field measurement, the aperture fields were calculated, see Fig. 11. It is noted that the patch excitation is now totally symmetric and the diffraction from the edges has decreased slightly with respect to the faulty element case shown in Fig. 10.

The circular ripples in the near-fields shown in Figs. 10 and 11 are artefacts caused by the truncation of the plane wave spectrum at the border of the visible region. This is the general consequence of a convolution with a sinc function in the transformed spatial domain. For high directive antennas, i.e., when the plane wave spectrum is highly concentrated inside the visible region and has low values at the border of the visible region, this ripple effect is negligible. For low directive antennas, i.e., when the plane wave spectrum is distributed on the entire visible region, this ripple effect becomes evident.

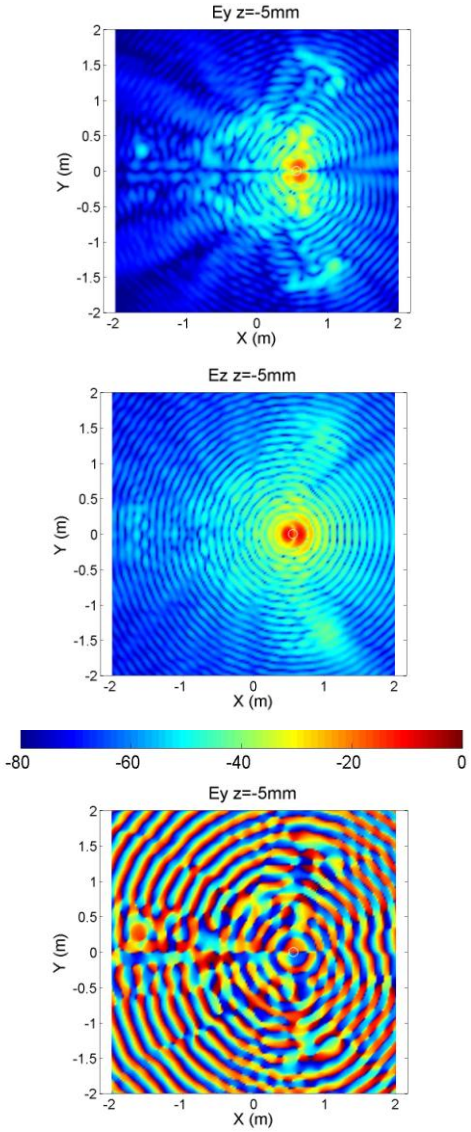

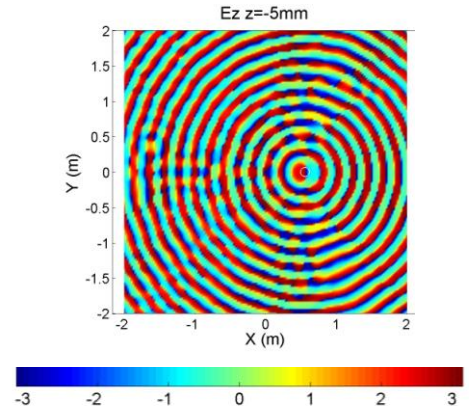

Figure 10. Amplitude in dB and phase in radians of E_y and E_z, unit BC03, on $z = -5\text{mm}$.

The artefact can however be reduced by use of windowing prior to Fourier transform; to this end a multitude of well-established signal processing techniques is available [9].

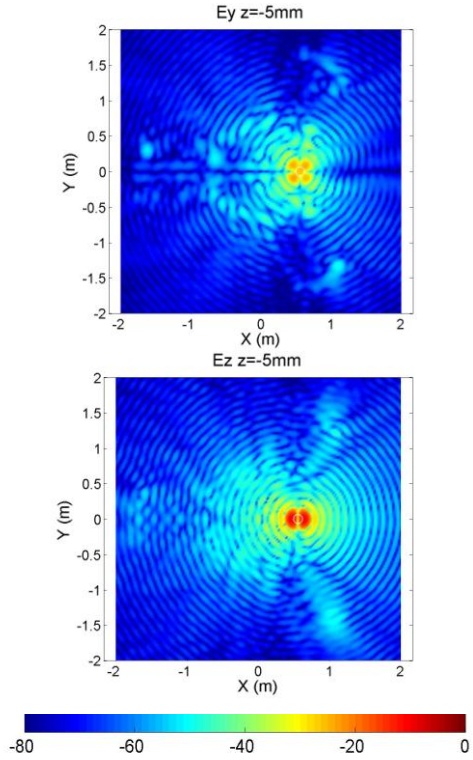

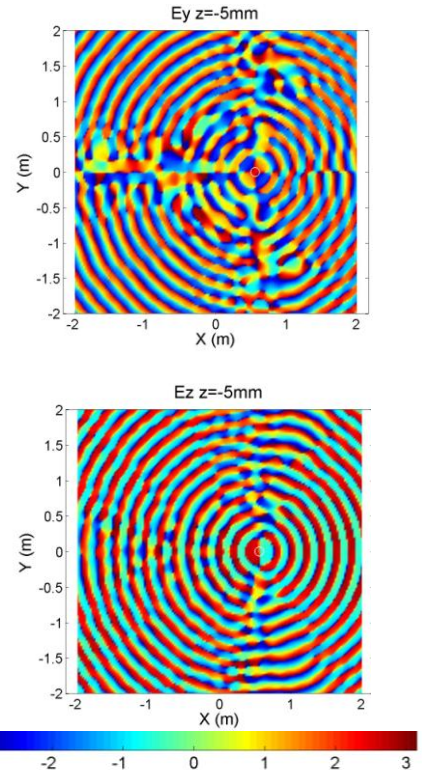

Figure 11. Amplitude in dB and phase in radians of E_y and E_z, unit BC03 replaced, on $z = -5\text{mm}$.

3.2 Element A05

The far-field pattern of port 1 of the receiver unit A05 in the φ = 0° plane is shown in Fig. 12: the co-polar component clearly shows an unusual frequency variation.

This anomaly was observed in all φ planes and in some of them also for the cross-polar component. In order to highlight and isolate the effect of the frequency variation, the diagnostics was also applied to the correct element A01. From the measured Q coefficients the power spectrum was computed and it was found that again a truncation of the n-modes at N = 58 was necessary for both elements. Following the same procedure used for the unit BC03, the spectra were computed on the [-2k, 2k] spectral domain with the use of the SWE-to-PWE transformation of Eq. 3 on the z-plane $z = -5\text{mm}$, and then inverse Fourier transformed. Again, for both units only the visible region and the singularity for k_z = 0 were recovered, while the entire invisible region did not reach the convergence with N = 58 and was thus replaced by zeros.

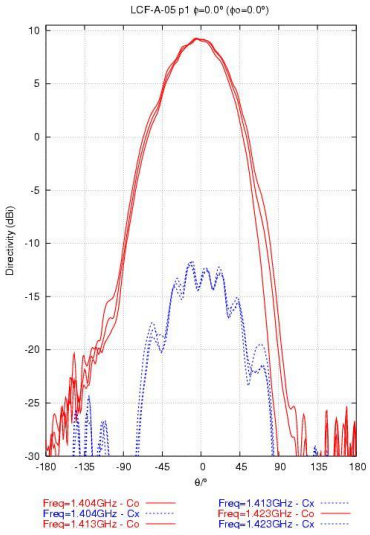

Figure 12. Far-field pattern of the receiver unit A05, port 1, for $\varphi = 0°$, showing an unusually large frequency variation.

In Fig. 13 the *y*-component of the aperture field of the faulty unit A05 is compared to the corresponding component of the correct unit A01 for the three frequencies of interest, f = 1.404 GHz, 1.413 GHz and 1.423 GHz. While the behaviour of the unit A01 remains constant with frequency, the unit A05 shows significant changes. In particular it is noticed that the field at the antenna itself is asymmetric and changes with frequency; furthermore, the diffraction from the hub edges decreases with increasing frequency. The same happens to the *z*-component, while it becomes less evident for the co-polar *x*-component. The same asymmetries were noticed also in the phase plots. Again, it was concluded that the anomalies detected in the far-field pattern were due to errors in the feed network.

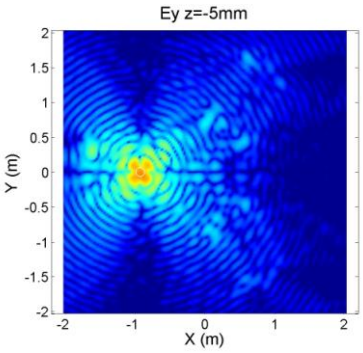

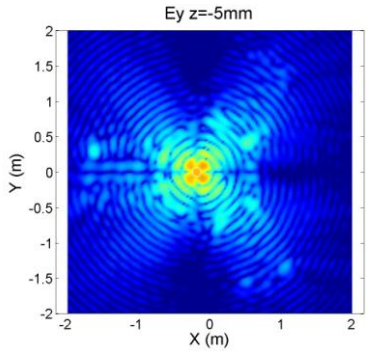

(a)

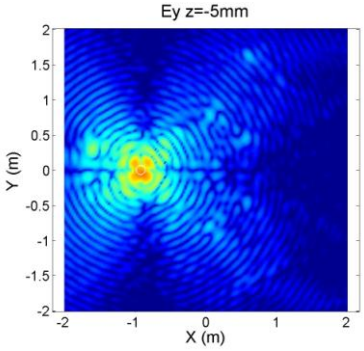

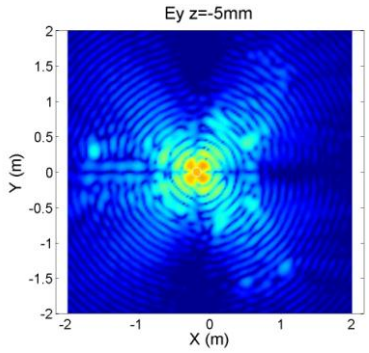

(b)

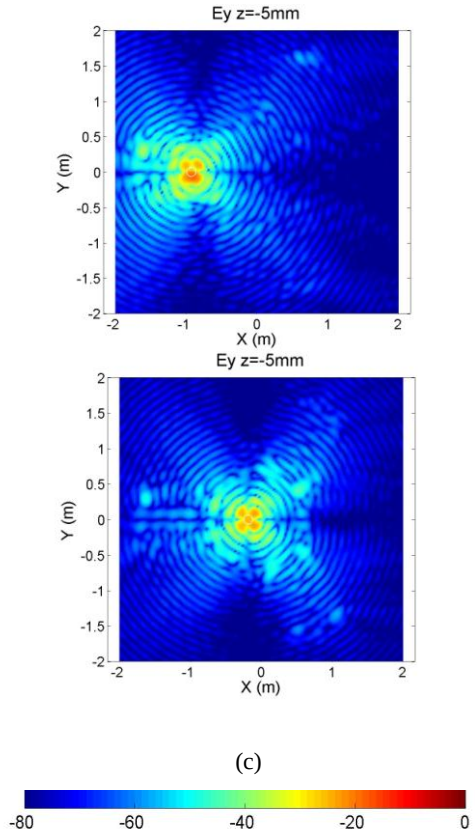

Figure 13. Amplitude of E_y in dB on the *z*-plane *z* = -5mm: above the unit A05 (faulty) below the unit A01 (correct): (a) f =1.404 GHz (b) f =1.413 GHz (c) f =1.423 GHz.

4 Conclusions

A diagnostics of two units of the SMOS MIRAS antenna system has been performed by applying the SWE-to-PWE antenna diagnostics technique to the measurements of the final on-ground calibration at the DTU-ESA Spherical Near-Field Antenna Test Facility. The diagnostics showed that the anomalies observed in the far-field pattern could be traced back to asymmetries and frequency variations in the extreme near-field of the two antenna elements. In both cases, it was concluded that errors were present in the feed networks of the units, for port 1 only, and the presence of such errors was later confirmed by an inspection of the antenna hardware. It is noticed, that the calculated aperture fields show not only the field radiated directly by the antenna unit but also quite clearly the diffraction from the edges and other structural components of the support structure.

The investigation presented here also serves as an experimental validation of the SWE-to-PWE antenna diagnostics technique in presence of typical measurement inaccuracies and highlights the importance of the analysis of the cross-polar components, in amplitude as well as in phase, for the purpose of antenna diagnostics.

References

[1] C. Cappellin, A. Frandsen, O. Breinbjerg. "On the relationship between the Spherical Wave Expansion and the Plane Wave Expansion", AMTA Europe Symposium, Munich, Germany, 2006.

[2] C. Cappellin, O. Breinbjerg, A. Frandsen. "The influence of finite measurement accuracy on the SWE-to-PWE antenna diagnostics technique", EuCap European Conference on Antennas and Propagation, Nice, France, 2006.

[3] J.E. Hansen. "Spherical Near-Field Antenna Measurements", Peter Peregrinus Ltd. London, 1988.

[4] T.B. Hansen, A.D. Yaghjian. "Plane Wave Theory of Time-Domain Fields, Near-Field Scanning Applications", IEEE PRESS, 1999.

[5] Homepage of the SMOS mission: http://www.esa.int/esaLP/LPsmos.html.

[6] Homepage of the DTU-ESA Facility: http://www.oersted.dtu.dk/English/research/emi/afg/dtu_esa_facility.aspx.

[7] S. Pivnenko, J. M. Nielsen, O. Breinbjerg. "Aspects of antenna pattern characterization of an L-band space radiometer", AMTA 2003, Irvine, California, 2003, 375-379.

[8] S. Pivnenko, J. M. Nielsen, O. Kim, O. Breinbjerg. "SMOS antenna measurements. Phase C/D investigatory measurements", Report. No: SO-TR-DTU-ANT-0004, 2 volumes, Technical University of Denmark, Ørsted-DTU, EMI, October 2005 (R 725).

[9] H. C. Stanwitz, R. J. Dallaire, J. R. Fienup. "Nonlinear apodization for sidelobe control in SAR imagery", *IEEE Trans. on Aer. and Elect. Syst.*, vol. 31, no. 1, 267-279, Jan 1995.